Theoretical and Experimental Aerodynamic Analysis For High-Speed Ground Vehicles

by

Ismail Haider Farhan, B.Sc, M.Sc.

A doctoral thesis

submitted in partial fulfilment of the requirements

for the award of

the degree of Doctor of Philosophy of the Loughborough University of Technology

May, 1991

SUPERVISORS : Professor J. J. McGuirk

F.G. Maccabee, M.Sc., D.C.Ae, C. Eng., A.F.R.Ae.S,

Department of Transport Technology

Loughborough University of Technology

DEDICATION

" To my mother "

DECLARATION

This thesis is the outcome of the research carried out by the author in the Department of Transport Technology at Loughborough University of Technology and represents the independent work of the author; the work of others has been referenced where appropriate.

The author also certifies that neither the thesis nor the original work contained herein has been submitted to any other institution for a degree.

Ismail Haider Farhan

ACKNOWLEDGEMENTS

I wish to express my great and most sincere thanks to my supervisors, Professor J.J. McGuirk and Mr. F. G. Maccabee for their guidance, and encouragement throughout the course of the research.

My thanks also due to my Director of Research Mr. L. R. Jenkinson for his valuable direction, comments encouragement and invaluable moral support. The assistance and advice of Professor N. Ashford and Professor F. D. Hales are appreciated and gratefully acknowledged.

I would like to extend my thanks to the administrative staff of the Department of Transport Technology for their help and care during my period of research, particularly Mrs. B. Moore and Mrs V. Grove.

I also wish to thank Mr. G. Gerrard and Mr. J. Harris of the computer centre of Loughborough University computer centre for their assistance.

Thanks also due to Mr. J. E. Ogendo for his discussions and suggestions on computer programming.

Special thank due to my wife Hana for her constant encouragement, patience and help during the course of the work. Thanks also to my sons Assel and haider and my daughters Hadiel and Zenab for their patience during the evenings and weekends that I was absent.

SUMMARY

An improved understanding of the aerodynamics of high-speed ground vehicles can lead to significant reductions in the energy consumption required for propulsion, an increase of vehicle cruising speed, and an increase in the safety and comfort of passengers. To contribute to these goals, this thesis employs theoretical and experimental techniques to investigate the air flow around a proposed geometry for a high-speed electromagnetic suspension (EMS) train. Train motion at normal cruising speed in still air and in crosswind conditions are studied, considering aerodynamic forces and moments, the wake in the lee side of the train and the turbulent boundary layer development.

The theoretical prediction work may be conveniently divided into two parts, for inviscid flow, and with viscous effects included. In the first, a numerical technique called the panel method has been applied to the representation of the body shape and the prediction of the potential flow and pressure distribution. Two computer programmes have been written, one for a single vehicle in the presence of the ground at different yaw angles, and the second for application to two body problems, e.g. a train passing a railway station or a train passing the central part of another train. Both programmes have been developed in fully three-dimensional form, but are currently based purely on the source distribution method. This limits the applicability of the method, in particular to small angles of yaw, but useful results are still obtainable. In the second part of the theoretical prediction work, two methods based on the momentum integral equations for three-dimensional boundary layer flow have been developed for use with the aforementioned potential flow analysis; these predict the development of the three-dimensional turbulent boundary layer (i) on the central section (for the analysis of crosswind conditions) and (ii) on the nose of the train.

The primary interest of the experimental programme was to provide qualitative and quantitative results for comparison with the theoretical predictions as well as to give insight into the flow behaviour around the train. The experimental tests also provided the first results for the influence of both stationary and moving ground planes on the

EMS train. Extensive wind tunnel tests were performed on four purpose-made models of the high-speed train to measure aerodynamic forces, moments and pressures to establish ground effect characteristics. The experimental results demonstrated the importance of ground clearance. Flow visualisation showed that the wake vortices were both stronger and larger in the presence of a ground. At small yaw angles ground clearance had little effect, but as yaw increased, larger ground clearance led for example to substantial increase in lift and side force coefficients. The wind tunnel tests also identified the differences between a moving and a fixed ground plane. The measured data showed that the type of ground simulation was significant only in the separated region.

A comparison of the results predicted using potential flow theory for an EMS train model and the corresponding results from wind tunnel tests indicated good agreement in regions where the flow is attached. For small yaw angles, not more than 15° , predicted pressure distributions reproduced measured behaviour. For greater angles, the shed vorticity (associated with flow separation) has a strong effect on the surface pressure field and this would have to be introduced into the panel method to improve prediction.

The turbulent boundary layer calculations for the train in a crosswind condition showed that the momentum thickness along the crosswind surface distance co-ordinate increased slowly at the beginning of the development of the boundary layer but then increased sharply at the side top roof on the lee side. The sharp increase is believed to indicate a tendency for flow separation as the solution procedure exhibits signs of failure in this region. Suggestions are made in the thesis for ways of improving both this and other aspects of the theoretical approach.

LIST OF CONTENTS

LIST OF FIGURES

LIST OF SYMBOLS AND ABBREVIATIONS

A	Area of a plane quadrilateral
A_{ij}	Normal component of velocity induced at the control point of the i-th element by a unit source strength at the j-th element
C_D	Drag coefficient
C_{Dc}	Corrected drag coefficient
C_L	Lift coefficient
C_p	Pressure coefficient
C_S	Side force coefficient
C_Y	Yawing moment coefficient
c_{fl}	Local skin friction coefficient
c_{f1},c_{f2}	Components of the local skin friction coefficient in an orthogonal curvilinear co-ordinate system
c_{fx},c_{fz}	Components of the local skin friction coefficient in a boundary layer co-ordinate system
d_e	Train height (a close approximation to the equivalent diameter)
D	Drag force
F	Entrainment function
H	Shape factor
h_1,h_2	Metric unit
i,j	Subscripts denoting quantities associated with i-th and j-th element respectively
K_1,K_2	Geodesic curvature of streamlines and lines orthogonal to them
l	The length of the model
L	Lift force
M_e	Mach number
$\mathbf{n}$	Normal unit vector
N	Number of elements distributed on the surface of a body
n_1	Index in power law representation of mean velocity profile

P	The static pressure in the fluid
$r_{(p,q)}$	Distance between the flow field point ,p, and the point ,q, where the source is located
r_o	Distance from a flow field point, where the potential and velocity components are evaluated, to the origin of the local co-ordinate system of an element
Re	Reynolds number based on equivalent diameter
R_m	The ratio between r_o and T_{max}
$R_{\theta 11}$	Reynolds number based on θ_{11}
s	Streamwise direction
s,h	Local co-ordinate system used in chapter three
S	Surface of the body about which the flow is computed
T_{max}	Maximum diagonal length of an element
$\mathbf{T}_n$	Normal vector to an element's diagonals
$\mathbf{T}_1,\mathbf{T}_2$	Element diagonal vectors
t	Time
$\mathbf{t}_1,\mathbf{t}_2$	Unit vectors in the plane of an element in the element co-ordinate system
u,v,w	Velocity components in an orthogonal curvilinear co-ordinate system
u',v',w'	Fluctuating velocity
U_e,V_e,W_e	Mean velocity components just outside the boundary layer
U ,V ,W	Components of a uniform onset flow in the reference co-ordinate system
U_s	Resultant velocity at the boundary layer edge
U_1,V_1,W_1	Mean velocity components in the chordwise and spanwise directions respectively just outside the boundary layer
v	Disturbance of the free stream velocity due to the presence of a body
V	Fluid velocity
V_{ij}	Velocity induced at the control point of the i-th element by a unit source density at the j-th element
V_x',V_y',V_z'	Velocity components in the reference co-ordinate system
V_x,V_y,V_z	Velocity components in the element coordinate system

V_∞	Freestream velocity
x	Chordwise surface distance
x/d_e	Longitudinal length to equivalent diameter ratio
X^i	Cartesian co-ordinate system in chapter nine
$X^{i'}$	Boundary layer co-ordinate system
X_o, Y_o, Z_o	Global co-ordinate of the element origin
X_n, Y_n, Z_n	Null point co-ordinate in reference co-ordinate system
Y	Yawing moment
Z	Ground clearance
Z/d_e	Ground clearance to equivalent diameter ratio

Greek symbols

α_C	Contour angle
β	Angle between the external streamline and the surface streamline
$\beta_j^{i'}$	Co-ordinate of covariant base vector
ρ	Air mass density
ν	Kinematic viscosity
Φ	Total potential function of the flow
ϕ	Potential function disturbance
ϕ_∞	Potential of a uniform onset flow
ψ	Stream function
σ	Source density
$\gamma_x, \gamma_y, \gamma_z$	Velocity direction cosines with respect to the co-ordinate axes
τ_1, τ_2	Components of the shear stress
τ_{w1}, τ_{w2}	Components of the wall shear stress
ξ, η, ζ	Orthogonal curvilinear co-ordinate
δ	Boundary layer thickness

δ_1 Streamwise displacement thickness given by

$$\delta_1 = \int_0^\delta [1 - \frac{U}{U_e}]\, d\zeta$$

δ_2 Crosswise displacement thickness expressed as

$$\delta_2 = \int_0^\delta [\frac{W}{U_e}]\, d\zeta$$

Δ_1, Δ_2 The displacement thicknesses in a boundary layer co-ordinate system

θ_{11} Streamwise momentum thickness given by

$$\theta_{11} = \int_0^\delta \frac{U}{U_e} [1 - \frac{U}{U_e}]\, d\zeta$$

$\theta_{12}, \theta_{21}, \theta_{22}$ Crosswise momentum thicknesses defined as

$$\theta_{12} = \int_0^\delta \frac{W}{U_e} [1 - \frac{U}{U_e}]\, d\zeta$$

$$\theta_{21} = \int_0^\delta - [\frac{WU}{U_e^2}]\, d\zeta$$

$$\theta_{22} = \int_0^\delta - [\frac{W^2}{U_e^2}]\, d\zeta$$

$\Theta_{11}, \Theta_{12}, \Theta_{21}, \Theta_{22}$ Momentum thicknesses (corresponding to above definitions) defined in the boundary layer co-ordinate system

$\int$	Integral
$\partial/\partial x$	Partial differential
d/dx	Total Differential
∇	Vector differential operator
Σ	Summation
$\iint$	Double integration
$\vert_s$	Quantities at the the surface

Abbreviations

APT	Advanced Passenger Train
ARC	Aeronautical Research Council
APT-P	Advanced Passenger Train P-type
EMS	ElectroMagnetic Suspension
HST	High Speed Train
SERC	Science and Engineering Research Council
TGV	Train a Grande Vitesse (High speed train)

CHAPTER 1
INTRODUCTION AND LITERATURE SURVEY

1.1 Introduction

This chapter provides a brief introduction to a proposed generation of lighter, high-speed passenger trains and some of the aerodynamic issues associated with their design. The aim of the work in this thesis is to contribute to the aerodynamic design of such trains by providing computer prediction procedures and experimental model data to aid the understanding and prediction of the surface air flows and pressure fields around these trains in motion. The chapter closes with a description of the intended scope of the research work.

1.2 High-Speed Train Transport

1.2.1 Importance of the Train Transport Mode

It may well be the case that in the near future high demands on, and the attendant congestion of, the air lanes for internal journeys in various countries (as well as between close neighbouring countries) will increase due to changes in life style. This has been brought about, in part, as a result of changes in attitudes in favour of air travel for visiting and working in other than one's country. An important contributing factor in some regions, notably the United States of America and the European Economic Community, is the ease with which one can cross state or national borders for these purposes. At present, and in the near future, travelling by air is costly due to high aeroplane and fuel prices, regular maintenance costs, operational and airport costs. In spite of its popularity, the aeroplane leads to a false sense of speed for medium distances. When we consider point of departure to point of destination trip time, the average speed is often less than 100 mph [1], and the trip is accompanied by frustrating ground connections, unpleasant transport mode mixes in the airport and the threat of delays or cancellations as a result of inclement weather. High demands and congestion in the air lanes can however be alleviated by employing high-speed trains, which are likely to be competitive for short journeys. High speed has two major advantages : first short transit time and second a smaller number of vehicles to provide a given traffic volume. Comfort, convenience, safety and speed, coupled with passenger services, provide a basis for a pleasant journey and have the potential to attract passengers to travel by train. With regard to the acceptance of this form of transport it is encouraging to note that the French railway claim that 1700 of the 40,000 passengers carried by their high-speed train (TGV) system today previously travelled by car or aeroplane [1]. Similarly, an opinion poll in West Germany to investigate public acceptance of an Inter-City Express (ICE) high-speed train was carried out after an experimental ICE-prototype with a speed of 317 km/h had been publicly introduced for about a year. In interviews with travellers who normally travelled by aeroplane or car 70% announced that they would consider using the ICE high-speed train instead of other forms of transport [2] . On some prime routes within mainland Europe high-speed trains can offer not only journey times comparable with air travel but considerably lower fares as well. For instance, for the Paris-Brussels route, plane travel (full economy, one way fare) costs £80 with a city centre to city centre travel time of 3 hours and 20 minutes. In contrast, the high-speed train alternative (second class, one way fare) costs £12 and takes 3 hours and 30 minutes. With such an alternative, high-speed train travel offers an attractive transport mode for the highly prized business traveller [1]. It is also worth noting that there is no transport mode that can deal with large passenger volumes as efficiently and effectively as the train. (Travel by road is not seen as an option due to growing road traffic demand and road congestion.)

1.2.2 High-Speed Train Using Maglev Contactless Support

Conventional trains with steel wheels running on rails for support and guidance are not considered suitable at high speed because of the excessive track maintenance and the generation of high and environmentally unacceptable noise levels. There is a high demand to design an alternative mass transport system capable of moving large numbers of people efficiently and economically at a much faster cruising speed than the traditional train. It is clear that the drawbacks of a wheel/rail friction driven system can be largely overcome by a contactless system, such as magnetic levitation (maglev), for which considerable research and development work has been undertaken in, for instance, Japan and West Germany. In the maglev-based contactless technology the weight of the vehicle is supported by the use of magnets instead of wheels. Since there is no need for the wheels and heavy bogies a major reduction in the weight of the vehicle as well as a lower vehicle height is possible, both of which give important technical and economic advantages. This contactless technology for support, guidance and propulsion involves essentially no mechanical friction and therefore no mechanical wear and tear and low noise levels [3].

In brief, maglev systems employ the attractive or repulsive forces between magnets to provide contactless vertical and possibly lateral support for a vehicle above a purpose-built guideway. In the case of the attractive mode of support the body of the train wraps around a T-shaped guideway. By controlling the strength of the electromagnet system at the base of the wrapped portion of the train, the force with which it attracts the magnets on the cross-bar of the guideway above it can be adjusted to support the weight of the train. For the repulsive mode of support the magnets at the base of the train are of like poles to those that face them at the base of a U-shaped guideway. In both support modes the propulsion and braking forces for the horizontal motion of the train are provided by an electric linear motor which utilises the electromagnetic coupling between the guideway and the magnets at the base of the train [4].

In this thesis the aerodynamics of a body design for a high-speed train envisaged for use with a maglev technique called the electromagnetic suspension system (EMS) is to be studied. In this suspension system, conventional electromagnets react attractively with a steel rail. The vehicle must therefore partly wrap around track. The system is inherently unstable, stability being achieved by active control of the magnetic current. The typical full scale clearance between magnet and track is 10 mm. More details of the precise EMS body shape of interest will be provided below.

1.3 Aerodynamics and High-Speed Train Design

1.3.1 Role of Aerodynamics in High-Speed Train Design

To design high-speed trains two basic technical issues should be considered, mechanical and aerodynamic. Mechanical issues concern the engines, brakes, transmission, track design and so on. Aerodynamic issues are concerned with the nature of the airflow around the train and its effect on the performance and stability of the train due to the resulting aerodynamic forces.

The increased demand to design faster and lighter trains has brought about a requirement for a better understanding of train aerodynamics, since the aerodynamic forces exerted on the surfaces of these new trains are greater and have more influence on such performance aspects as the ability to increase the speed of the train with less energy and passenger comfort at high speed. Also affected is the stability of the train; for example, the possibility of lighter trains being blown over in strong cross-winds (especially in an exposed location such as a bridge or embankment).

1.3.2 Some Basic Problems in the Aerodynamics of High-Speed Trains

The basic problems in the aerodynamic design of high-speed trains are ultimately concerned with the prediction of the overall aerodynamic forces and moments. This section reviews the important aspects of external aerodynamics of concern in the industrial design of high-speed trains. These main topics are :

1. *Drag in still air*

   As the speed at which trains are designed to operate increases, the aerodynamic forces become more important. Hara et al. [5] show that the aerodynamic resistance of a train increases with the square of its speed while the mechanical resistance increases linearly. In the case of conventional trains the aerodynamic resistance exceeds the mechanical resistance at about 200 km/h. Howarth [6] shows that the aerodynamic resistance for an eight-car Advanced Passenger Train (APT) exceeds the mechanical resistance at the lower speed of about 155 km/h. A typical inter-city passenger train at its maximum operating speed consumes approximately 75% [7,8] of the traction power available at the wheel overcoming aerodynamic resistance. It is therefore no surprise that reducing aerodynamic resistance is of major concern to railway engineers.

2. *The effect of mean and unsteady cross-winds on performance and stability*
Cross winds have a significant effect on the aerodynamic resistance as well as the potential to affect the stability of the train. In a cross-wind condition more energy will be required in order to maintain the speed of the train; for passenger trains the aerodynamic resistance increases at a rate of approximately 2-3% per degree of yaw angle up to 45° [7]. In the United Kingdom, over typical mainline routes, the daily average wind adds approximately 10% aerodynamic resistance to the no wind value; on a windy day the aerodynamic resistance increases by about 50%.

3. *Adjacent train and train track-side features interaction*
Problems of pressure waves and turbulence due to the unsteady side force that is generated when adjacent trains pass one another at high speed must be minimised. The pressure changes on the passing sides of the train are dependent on the clearance between the trains, train speed and nose shape [7,8]. Cases of adjacent trains passing each other (in the same or opposite direction) or passing a stationary object (e.g. a railway station) are all of interest.

The following section details the work which has gone on to provide a more detailed technical understanding of the basic train aerodynamics problems.

1.4. Literature Survey : Train Aerodynamics

Very little published research work is available in the open literature on the aerodynamic analysis, especially computational work, of full-scale or model trains. This situation seems to be due to two reasons: first, a high priority for the importance of aerodynamics in the design process has arrived later in the train industry than within the aerospace and automotive industries (only recently has attention been given to the aerodynamically more sensitive light and high-speed trains). Secondly, industrial confidentiality is a very sensitive issue, which leads to a lot of work being classified. In the last decade a fairly large body of literature has arisen concerning the aerodynamic problems of high-speed vehicles [9-15], of which discussions of train aerodynamics form a small part. The literature survey which follows covers a range of topics relevant to the subject matter of train aerodynamics (e.g. train in cross-wind conditions and at 0° yaw angle) and includes both theoretical and experimental work.

1.4.1 Early Work in Train Aerodynamics — Before 1960

Train aerodynamics, especially of aerodynamic drag, has been of interest to railways from the days of George Stephenson in the early 19th century. Measurements of the total resistance of trains were made using full-scale trains. From such studies the Count de Pambour reported (in 1835) a three-component equation for the resistance of a train in motion which has, in different forms, been used ever since in Britain, France and West Germany [16]. He proposed that the train resistance R on a train travelling at a speed V be expressed in the form

$$R = A + BV + CV^2 \qquad 2\text{-}1$$

where A, B and C are constants. This relation shows the linear and quadratic contribution mentioned above.

As early as 1847 Sir Henry Bessemer concluded from experiments to measure the air resistance, using a 1/6th scale model of a train, that the resistance may be reduced by modifications which may be viewed as early attempts at streamlining.

The use of experimental studies of full-scale and model trains started by early workers such as the above, has continued into the present century. The experimental methods, measurement tools and scope of work gradually became more sophisticated, including the use of wind tunnels and the associated measurement technology and the study of more specific areas of train aerodynamics e.g. effect of crosswinds on stability. However, the results for train drag essentially confirmed the early conclusion of a three-component equation and the need to consider the streamlining and quality of the surface finish. A reader interested in more about the early history of train aerodynamics may refer to references [17-19].

1.4.2 Recent Work in Train Aerodynamics — After 1960

In the late 1960's research at The Douglas Aircraft Company in the United States of America led to the development of a versatile numerical technique called the panel method to predict two- and three-dimensional potential flow (i.e. inviscid, irrotational). Although the technique was originally developed for applications in the aerospace industry it was recognised that it could also be employed in both automotive and high-speed train aerodynamics studies. In recent years there has been research work in United Kingdom Universities on train aerodynamics at the universities of Cambridge, Warwick, Loughborough and Nottingham. Almost all the work involved both wind tunnel tests and use of the above mentioned potential flow method. The real flow about a train is of course neither inviscid nor irrotational. The success of potential flow methods relies on the viscous effects being restricted to a small region (the boundary layer) in the immediate vicinity of the train, on the larger nlretical flow effects being introduced separately into the prediction method (e.g. embedded regions of validity). Accordingly, a few attempts have also been made to predict the train boundary layer effects, particularly in crosswind conditions. The work at Cambridge concentrated on the measurement and calculation of air flows for simple shapes about which the flow was likely to have some similarities with a real train. Specifically, the studies concerned the flow around slender bodies, see for example Stewart [20], Mair et al. [21] and Copley [22]. The latter presents some work using simplified Advanced Passenger Train (APT) shapes. At Warwick University there has been experimental wind tunnel work on maglev trains while at Loughborough the main work, led by F.G. Maccabee, was for APT train shapes and involved the prediction of three-dimensional potential flow and experimental wind tunnel tests. The work in the department of civil engineering of Nottingham university, led by C.J. Baker, was mainly experimental work and largely concerned with winds effects on the railway environment [23,24]. The following sections review the relevant work in these research areas mentioned above, viz : potential flow predictions, viscous boundary layer analysis and wind tunnel tests.

It is quite clear that the rail industry is the main body to benefit from research on train aerodynamics; it also possesses considerable practical experience which can give insight in the field of high-speed train aerodynamics and support research. Testing a train on an actual track and gaining field experience from such full-scale tests is very important to academic and industrial researchers. There is a considerable amount of published research work from industry. In particular, R.G. Gawthorpe of British Rail, has published a number of papers in the field which are rich in industrial experience. In reference [7] he covers the aerodynamics of trains in the open air. This gives a very good insight on how train drag is related to the speed of the train; presents tables for drag for different modern high-speed trains; gives industrial experience on train stability in high winds; discusses the environmental effects at the track side; and the passing of trains on adjacent tracks. In two other papers, Gawthorpe discusses the aerodynamics of a train with overhead line equipment [25] and [26] the aerodynamics of trains in tunnels; these are not of primary interest in the present work.

Peters[8] reviewed the aerodynamic problems of high-speed trains and the ways to solve these. He showed that by the use of modern aerodynamic design methods, new high-speed conventional train or maglev train can travel 50-100 km/h faster than the present trains without additional energy consumption

1.4.3 Panel Method for Potential Flow Prediction

The numerical solution of the potential flow problem using the panel method has received considerable attention from various researchers especially within the aerospace industry [27] where the method was originally developed when large-scale high speed computing facilities become available. The method is applicable to the analysis of inviscid flows over vehicles in subsonic or supersonic flight, high-speed ground vehicles and underwater marine applications, and for internal flows, such as those in wind tunnels or in ducts. The method has been applied successfully to a significant number of practical design problems; for example, the PANAIR panel method has been used to analyse the Boeing 737-300 take off high lift configuration in support of the aircraft's flight development phase during pre-certification flight tests [28]. Reference [29] is a recent comprehensive publication on potential flow computational methods applied in the aerospace industry. Hess [30,31] reviews the historical development of these methods and describes the considerable current activities together with a comprehensive bibliography.

The panel method has also been used in the automotive industry. As an example, Ahmed et al. [32] have used the panel method to predict the pressure distribution on a Volkswagen van, using a simplified geometry. The following sub-sections present a survey of the application of the two- and three-dimensional panel method in train aerodynamics.

1.4.3.1 Panel Method Prediction for Two-Dimensional Train Models

Attempts have been made by British Rail to calculate the velocities and hence pressure distribution around a train cross-section i.e. a two-dimensional model. Mahomedali [33] developed a procedure based on the panel method for calculation of potential flow around bodies of a circular shape. The ground presence was represented by an image of the body displaced by twice the ground clearance.

Johnston et al. [34] developed a two-dimensional, potential flow, panel-based method capable of predicting the unsteady interference pressure loading on either moving or stationary bodies of arbitrary shape due to the passage of a second body. These studies concluded that substantial aerodynamic interference loads may be expected under real train passage conditions. These loads, which are impulsive in nature, depend on the type of body geometry, the lateral distance between the bodies and the closing velocity. The panel method approach permits a useful way of assessing these loads in a qualitative way.

At Cambridge University Copley [22,35,36] has developed a quasi threee-dimensional approach using a two-dimensional panel method using distributed sources and discrete vortices embedded in the wake to evaluate the circumferential pressure distribution for a simplified train shape and for an APT cross-section shape. He found that for the case of large crossflow there was a significant improvement on the accuracy of the predictions when the source panel method was combined with discrete vortices embedded in the wake.

1.4.3.2 Panel Method Prediction for Three-Dimensional Train Models

Morrow [37] has written a computer programme to predict the potential flow around a fully three-dimensional train shape. Morrow used two numerical models, the first consisted of a circular cylinder with a paraboloid nose to represent the train and the second was taken from the geometry of an APT train. The predicted pressure distributions around the APT train were compared with the experimental results from a wind tunnel model carried out by Maccabee [38] at a tunnel speed of 27 m/s and a

Reynolds number of about 1.75×10^5 based on an equivalent model diameter. The results show reasonable agreement. Morrow also predicted the potential flow around a model of an APT power car for yaw angles 0°, 6°, 12° and 90°. He found that at zero yaw angle, with no ground simulation, a region of low pressure where C_p varied from -0.3 to -0.6, was predicted along the edge of the sloping nose. A further, slightly weaker low pressure region was predicted to occur near the joint line of the cab and the constant cross-section. Finally, the pressure on the underside of the body was slightly less than on the top side. He also investigated the positive and suction pressure induced at points on a station wall by a passing train and the pressure pulses experienced on the nose of an APT train when passing the central section of another train. This work indicated the promise of the approach, but ignored aspects such as ground effect and contains only minimal experimental verification.

1.4.4 Viscous Flow Effects on Trains

As mentioned earlier the importance of viscous flow in train aerodynamics is that it is undoubtedly a characteristic of real flows and its inclusion is a step towards realistic simulations of the actual flow around trains. Most of this type of work has been done experimentally using wind tunnels and full-scale track tests. There is little work in the open literature for practical methods to predict this type of flow, especially for flow around the nose of the train. Most of the research has concentrated on the three-dimensional analysis of the central part of the train (e.g. in crosswind conditions) due to the simple and constant shape of the train over this part of the train.

Lock et al. [39] review the development of boundary layer prediction techniques using the integral momentum and entrainment equations, for estimating viscous effects in external aerodynamics problems concerned with the practical design of aircraft wings. This approach has some application in the prediction of train boundary layer and is thus reviewed below. Note that since the boundary layers on both model and actual trains are turbulent no consideration of laminar boundary layer method is given.

1.4.4.1 Turbulent Boundary Layer Prediction for Crossflow Conditions

A large amount of work has been carried out in the aerospace industry to solve problems for three-dimensional turbulent boundary layers, for both incompressible and compressible flows, for infinite yawed wings and bodies. This is the type of approach that is typically used to predict the turbulent boundary layer on the central portion of the train in cross-wind conditions. A brief presentation of the previous work related to this type of prediction follows.

Smith [40] calculated the development of the turbulent boundary layer on an infinite yawed wing of given section, sweep and pressure distribution for a given Reynolds number, Mach number and stagnation temperature. He used the momentum integral and entrainment equations of the boundary layer to predict its development. The computed results were compared with experimental tests and the results were encouraging.

Ashill et al. [41] have modified the approach of Smith [42] for calculating the turbulent boundary layers on infinite yawed wings to allow for wing platform taper. They found that for flows on an infinite tapered-wing, their method gave boundary layer parameters (momentum thickness, shape factor) that were in good agreement with those of Smith's general method [40]. In common with its two-dimensional analogue, the modified method is simple, economic and robust (i.e may be applied to a wide range of wing flow without numerical problems) [40].

Cumpsty et al. [43] developed a method for calculating the three-dimensional turbulent boundary layers using the integral momentum equations in conjunction with an entrainment equation to be applied to infinite swept wings and the results obtained were encouraging.

Everitt [44] developed two methods for calculating the development of three-dimensional turbulent boundary layers on an infinite length yawed cylindrical body. The goal of Everitt being to apply the method for the aerodynamic analysis of the central portion of a train. The first method used the integral momentum and the continuity equations while the second makes use of the rate equation for turbulence kinetic energy.

It is noted from the above quoted references that the common approach to a turbulent boundary layer analysis is to employ the integral momentum equations and entrainment equation approach (such as that developed by Smith [40]) and to simplify it to, suit a special case (e.g. cylindrical body to represent central portion of a train) that approximates an application area of interest.

Copley [22,35,36] developed a computer programme for quasi three-dimensional turbulent boundary layer prediction for cross-flow in the central region of a train using the integral method of Smith [40] to calculate the development and subsequent primary separation of the boundary layer on a train.

1.4.4.2 Turbulent Boundary Layer Prediction on the Nose of the Train

The prediction of the three-dimensional turbulent boundary layer around the nose of trains is an important (e.g. to aid the prediction of train drag) and difficult aspect of railway aerodynamics. Until recent years there has been no serious attempt, as far as the author is aware, to predict the three-dimensional viscous flow on the nose of trains. This situation is due to a number of reasons :

1. The flow around the nose is a mixture of attached and separated flows which can lead to numerical instability in the solution method and causing solution failure in regions where the flow characteristics changes from attached to separated.

2. The need for practical methods for representing the complicated geometry of the surface of the train nose and the specification of the governing equations for three-dimensional turbulent boundary layers close to these arbitrary (i.e complex) shaped surfaces.

3. To solve the problem of aerodynamics in the nose of the train requires large-scale computing power both in terms of memory and computational speed to achieve worthwhile results.

There have been attempts in the aerospace and automotive industries to predict the development of the three-dimensional turbulent boundary layer using momentum integral and entrainment equations. Hirschel has used these equations to compute the turbulent boundary layer of a transport aeroplane [45], a helicopter, fuselage of a fighter [46] and on car bodies [47].

As part of the theoretical work of this thesis, an approach to the prediction of the three-dimensional boundary layer of Hirschel is to be employed to the nose of the train.

1.4.5 Wind Tunnel Experiments in Train Aerodynamics

The use of the wind tunnel to study the aerodynamics of trains started in the early 1920's. The wind tunnel was used to solve practical railway engineering problems by avoiding the complicated theoretical approach and the extensive and time consuming calculations involved. Even with the availability of modern large-scale computers wind tunnel tests are still one of the important tools used in investigations of train aerodynamics.

1.4.5.1 Measurements of Aerodynamic Forces, Moments and Pressure Distribution

With the increased use of high-speed trains in transport, attention has turned to the analysis of aerodynamic forces and moments, especially for drag reduction. It is noted that the majority of the drag optimisation studies in the railway industry are carried out experimentally in wind tunnels to aid the design of the shapes for trains.

A group of researchers at University of Warwick conducted a series of wind tunnel investigations of high-speed maglev trains. Howell et al. [48-49] performed a series of tests on maglev trains to measure the aerodynamic forces and moments when their test trains passed through crosswind gusts of variable width and speed. The tests showed that over the range of investigation the side force in the gust increased linearly with crosswind angle, whereas steady state wind tunnel measurements on the same model at yaw showed a non-linear increase of side force with yaw angle. The difference was believed to arise from the slow development of the viscous side force component in the gusts. The increase in lift obtained in the gust was found to be comparable to that measured in the wind tunnel at yaw although zero crosswind data differed from zero yaw results as a fixed ground was used in the wind tunnel. It was concluded that in terms of steady state stability the wind tunnel data were conservative in that both side force and lift were greater than the data obtained from the gust.

Howell et al. also [50,51] carried out a series of wind tunnel tests to investigate the aerodynamic forces and moments, pressure distribution with different ground simulations and different ground clearances for a maglev train model. They found that the effect of the ground simulation is negligible for all the aerodynamic forces and moments except for lift and drag forces.

Maccabee et al. [38] carried out two series of measurements of forces, moments and pressure distribution on APT train models. The first series covered tests on a relatively short model and the second on a model similar to a two-car train arrangement. In general the tests results were plausible and have a consistency and pattern of variation which is easily explicable. Thus, the side force coefficients (measured for an APT model with an effective length to diameter ratio of about 16.5) increased with the yaw angle. For a given angle of yaw (over the range of 0°-10°), the side force coefficients for the APT model with bogies were, always higher than those for the APT model without bogies.

Cooper [52] carried out a series of experimental tests on a 1/25 scale driving trailer to measure the aerodynamic forces and moments at yaw angles 0° to 40°. The results were on an overall accuarcy of about 5% with those obtained from 1/5 scale model. He also found that the effect of the value of the Re between 1×10^5 to 4×10^5 was small but the effect of the bogies was significant.

Cooper [53] also performed experiments in a 1/5-th scale model of an APT moving in a natural wind and recorded the variation with yaw of measured aerodynamic normal force, side force and overturning moment acting on the model train. The mean values of the measured aerodynamic forces and moments increased steadily with increasing yaw but showed no significant increase for yaw above about 50°.

The above literature survey indicates that over the last few decades experimental work on APT and maglev type train models in wind tunnel been carried out. The tests have been used to measure surface pressure distribution and aerodynamic forces and some studies have investigated the influence of ground effects. In this thesis similar experimental studies are to be performed to provide results for the new generation of proposed EMS train. These results are intended to serve two purposes: (i) make available experimental results for this new class of train shape; and (ii) provide qualitative and quantitative results to support the theoretical work of the thesis.

1.4.5.2 Flow Visualisation

Everitt [54] carried out a series of flow visualisation tests on an APT model to investigate the general features of the flow. The results showed that the flow around the train comprised regions of attached flow, separation and vortices. Three techniques were used namely, smoke, attached tufts, and Day-glo with yellow fluorescent pigment in powder form mixed with diesel oil. The test were performed for yaw angles between 0° and 90°.

Maccabee et al. [55] studied a series of flow visualisation tests on a 1.59 m long model of a APT-type train, equivalent to two cars with a total full-scale length of 40 m. The tests were carried out at a Reynolds number 3×10^6 based on the model length. The oil suspension technique was used with French chalk or Day-Glo phosphorescent paint in a silicone oil mix, to visualise the flow on the train surface. Some of these results were compared with the theoretical results of Morrow [37] for three-dimensional potential flow prediction. The results correlated reasonably well for pressure distribution where the flow was attached but the flow visualisation tests also indicated a region of vortex detachment from the upper part of the train nose.

Similar work using oil and tuft was conducted by Baker et al. [56] on a 1/35 scale representation of a two-car Derby Lightweight DMU. The Reynolds numbers were in the range $2.0\text{-}2.4\times10^5$ based on the main stream velocity and the height of the model. Three main flow regimes were discovered. For a yaw angle less than 5° the flow was attached to the vehicle except for a separation bubble around the front of the leading car and a separated region at the rear of the trailing car. For yaw angles more than 5° and less than 40° a system of inclined trailing vortices existed in the lee side of the vehicle. It was concluded that for a yaw angle more than 40° but less than 90° it was probable that vortices break away from the lee side of the train in a similar manner to that around a circular cylinder normal to the stream. These results indicate that for large yaw angles, the assumption of small regions of viscous effects close to the train is clearly invalid.

Copley also carried out a series of flow visualisation tests on an APT train model. He used the oil suspension technique, in this case using a mixture of titanium dioxide and oleic acid. The flow on the surface of the model was recorded using sheets of black self-adhesive plastic coated with the mixture. The tests were carried out at Reynolds number of 3.7×10^5 , based on the diameter of the cross section of the model and mainstream velocity, for yaw angles between 20° and 35°. A study of the oil flow pattern on the lee side of the model indicated that the main lee side attachment line oscillated in the axial direction in response to the vortices tearing away from the body surface.

Stewart [20] carried out a series of wind tunnel experimental tests, namely flow visualisation and pressure distributions measurements, to study the flow on a slender bodies at yaw. He investigated two types of bodies, one with circular cross-section and the other a square with rounded corners and found the same basic wake structure on the lee side of the body for both types of cross-sections studied. The wake structure comprised a steady arrangement of alternately signed trailing vortices, breaking away from successive points along the length of the body surface.

1.4.5.3 Ground Effect Studies

Ground effect studies in wind tunnels are concerned with the influence of ground clearance as well as the method used to simulate the ground (i.e. stationary or moving floor) on the air flow around the test model.

Early work on ground effects was principally concerned with the take-off and landing of aeroplanes. Researchers have employed several methods to investigate the ground effect which occurs during wind tunnel tests. Butler et al. [57] used a fixed plane to simulate the ground effect at low speeds in the wind tunnel. Bagley [58] found that the effect of the ground on the maximum lift coefficient of a wing was significant. The experience of experimentalists using wind tunnels in automotive aerodynamics suggests that the simulation of the ground using a moving belt is desirable. Thus, for example, Bearman et. al. [59] investigated the influence of using a moving floor on the wind tunnel simulation of road vehicles. The results of using a 1/3 scale model of a car at a normal ground clearance indicated that on using the moving floor simulation the drag measured on the model car was reduced by about 8% and the lift was reduced by approximately 30%.

In train aerodynamics work has been done to simulate the effect of the ground. Howell [49,50] found that the pressure at the nose of the train was the most significant response to changes in ground clearance and to modifications of the ground-plane boundary layer. Maccabee et al. [38] have measured aerodynamic forces and moments on an APT model for different ground clearances using a stationary and a moving belt. The results for the drag coefficient (in the case of the train model without bogies) with moving ground simulation were less than that for fixed ground simulation.

Diuzet [69] has used the moving belt to study a SNCF railway car underfloor for the reduction of aerodynamic drag (using 1/10 and 1/20 scale models). He found that the drag reduced with ground clearance for the fixed floor and remained constant for the moving floor.

1.4.6 Concluding Remarks

From the above literature survey on train aerodynamics, it is clear that most of the research on train aerodynamics has been carried out experimentally on conventional train shapes. There have been some attempts to predict the development of the turbulent boundary layers. For the reasons discussed above, there appears to have been no attempts, until recent years, to predict the three-dimensional viscous flow at the nose of the train.

With respect to potential flow analysis there appears to be no accessible programmes in the open literature for use as a tool in railway engineering design applications. For viscous flow studies there exists an approach which is similar to that adopted for aerospace problems to solve crossflow problems. However there are no readily available computer programmes for this approach for trains and the prediction of the viscous flow on the nose of the train has not yet been tackled seriously. Another conclusion arising from the literature survey is that there appears to be no readily available computational studies of the new generation of proposed high-speed trains, namely maglev trains, and there are also few reported attempts to study experimentally this type of high-speed trains.

The aim of this thesis is to provide a contribution to an understanding of the aerodynamics of the new generation of proposed high-speed trains. It attempts to achieve this by making readily available the results of theoretical and experimental studies on a maglev high-speed train model performed during the course of this work. The theoretical work provides computer programmes for the potential flow and turbulent flow analysis of such trains. The experimental work is employed to show the qualitative and quantitative form of the surface pressure distributions, flow field (using flow visualisation) and the measurements of aerodynamic forces for cases of different yaw angles with and without ground effects.

1.5 General Scope of the Thesis and Objectives of the Research

Emerging from the remarks in earlier sections, the objective of this project is to study the aerodynamic characteristics of high-speed ground vehicles typical of maglev systems; both experimental and theoretical techniques will be used. The current work is concerned especially with a study of an Advanced Ground Transport (AGT) type train of the Electromagnetic Suspension (EMS) configuration, which was proposed by the Science and Engineering Research Council (SERC) in 1978. This has has been selected as a typical high-speed configuration which has had little attention to date with respect to its aerodynamic characteristics.

For a wide range of aerodynamic problems concerned with the design of high-speed trains, satisfactory results may be obtained by a procedure which involves successive calculations of the external inviscid flow and of the turbulent viscous flow in the boundary layers and wake. In view of this, the study reported herein explores a spectrum of aerodynamic issues, ranging from computational methods to predict inviscid and viscous flow on an EMS high-speed train model to experimental work on models for comparison with the theoretical work. These provide test data to aid the understanding of air flows around EMS trains and hence contribute to the design of high-speed trains.

The basic blue-print of the EMS train configuration (see reference [61]) was obtained from the Research and Development Division, British Railway Board) : the train has a 55 m overall length, a 3.73 m overall body height and a 3.77 m overall body width and a 13 m^2 total cross-sectional area. Figure 1-1 shows a side elevation and a plan view of the basic profile of the EMS nose. It shows that the nose shape in side elevation is formed (for optical reasons) by a flat windscreen sloped at 45°. The nose has a width at its tip equal to that of the track width. Figure 1-2 shows a front view and cross-section of the train and shows the location of the suspension envelope. Figure 1-3 shows both side and top views.

The principal differences in the geometry (which can contribute to significant differences in the aerodynamic analysis) of the EMS train and present conventional high-speed trains may be summarised as follows :

1. Current conventional high-speed trains possess a nose with a rounded profile. This is in contrast to the EMS train which has a flat nose profile with sharp edges at its tip and sides. Figure 1-4 shows the basic nose profiles of the APT (Advanced Passenger Train) and ICE (Inter-City Express) trains.

2. The EMS train does not possess bogies and therefore has a smaller overall height from the ground. Its design has the same total included vehicle cross-section as conventional train cabin, and maintains standard cabin dimensions. The ground clearance for the EMS train is considerably smaller than for conventional high-speed trains.

3. The EMS train has an overall length that is shorter relative to its cross-section when compared to the conventional train.

From preliminary considerations of EMS train aerodynamics, two areas are believed to be of particular importance :

i. cross-flow, due to a high cross-wind, when the very light train is in danger of toppling over ;

ii. the high-speed cruise condition, when the aerodynamic yaw angle is close to zero, when the train drag becomes the dominant factor in deciding performance.

These two aspects form the main focus of interest in this thesis

The remainder of the thesis comprises seven chapters which are grouped into three consecutive parts, where each part reflects the focus of attention of the research. In brief, Part I comprises chapter two which considers the prediction of potential flow and the development, testing and application of a suitable prediction method; Part II consists of chapters three, four and five concerned with experimental work ; Part III (chapter six) contains the final topic concerned in the thesis, namely, turbulent boundary layer prediction procedures. The thesis concludes in chapter seven with a summary of achievements and suggestions for further work.

For inviscid flow prediction a numerical technique called the panel method is used. The method leads to the prediction of the pressure distribution around an arbitrary two- or three-dimensional non-lifting body. The panel method embodies a versatile and simple mathematical representation of a body shape and has been applied in this research to the high-speed train. This method can only be applied to predict flow for small yaw angles as it is based on inviscid flow theory only. Two computer programmes have been written by the author to predict the velocities and pressure distributions on the surface of an EMS train model for two- and three-dimensional incompressible potential flow.

Real flows are viscous, therefore research on this type of flow would be valuable to the development of methods that are to be of real practical use in the design of high-speed trains. Two techniques have been presented to predict the development of the turbulent boundary layer. For crossflow condition, a technique suitable for calculating three-dimensional turbulent boundary layers on the central portions of the train has been developed. Integral momentum and entrainment equations have been used in a chordwise and spanwise co-ordinate system. The method is capable of predicting the development of the turbulent boundary layer in cross-wind conditions. A technique suitable for computing the turbulent boundary layer at the nose for zero yaw angle has been used and based on a momentum integral method (in which a mixing length model is used together with a similarity solution to find families of both main-flow and cross-flow profiles). The continuity equation is used as a third equation to cover the entrainment case.

Experimental tests are needed for two main reasons : to investigate the flow field, so that its main features may be understood; to provide experimental data for comparison with the results predicted by theoretical work. The experimental work involved pressure distribution measurements, flow visualisation and the measurements of aerodynamics forces on models of the EMS train in wind tunnels.

For the pressure distribution studies, two series of tests in a wind tunnel using a tapped EMS model were carried out to measure the pressure distribution on the train surface at different yaw angles to help the understanding of the flow field around the train and to compare the experimental data with the three-dimensional potential flow prediction by the panel method. The first series of tests did not involve ground simulation. The second series of tests investigated the effect of the type of ground simulation for different yaw and ground clearance on the pressure distribution on the train surface.

The flow visualisation tests (using tuft and spinner, oil suspension and smoke visualisation techniques) were carried out on EMS models in order to : to understand the general features of the flowfield around the train; too investigate the separation regions; to investigate the vortices and the wake around the train; to study the simulation effect of the ground on the behaviour of the flow and to relate and compare the flow visualisation tests results with the potential flow predictions, pressure measurements and the aerodynamics forces tests results. The tests were performed at different yaw angles with and without the presence of the ground simulation.

Aerodynamic forces and moments (lift, drag, side force and yawing moment coefficients) were measured in a series of experimental tests for the following reasons : due to the little data that exists in the open literature, wind-tunnel tests were performed to determine aerodynamic forces and moments and make the results available in the literature; to investigate the effect of the ground simulation; to study the effect of different yaw angles and to relate the results with the flow visualisation test results, pressure distribution measurements and the predicted turbulent boundary layer predictions. These tests were carried out at different yaw angles with and without ground simulation.

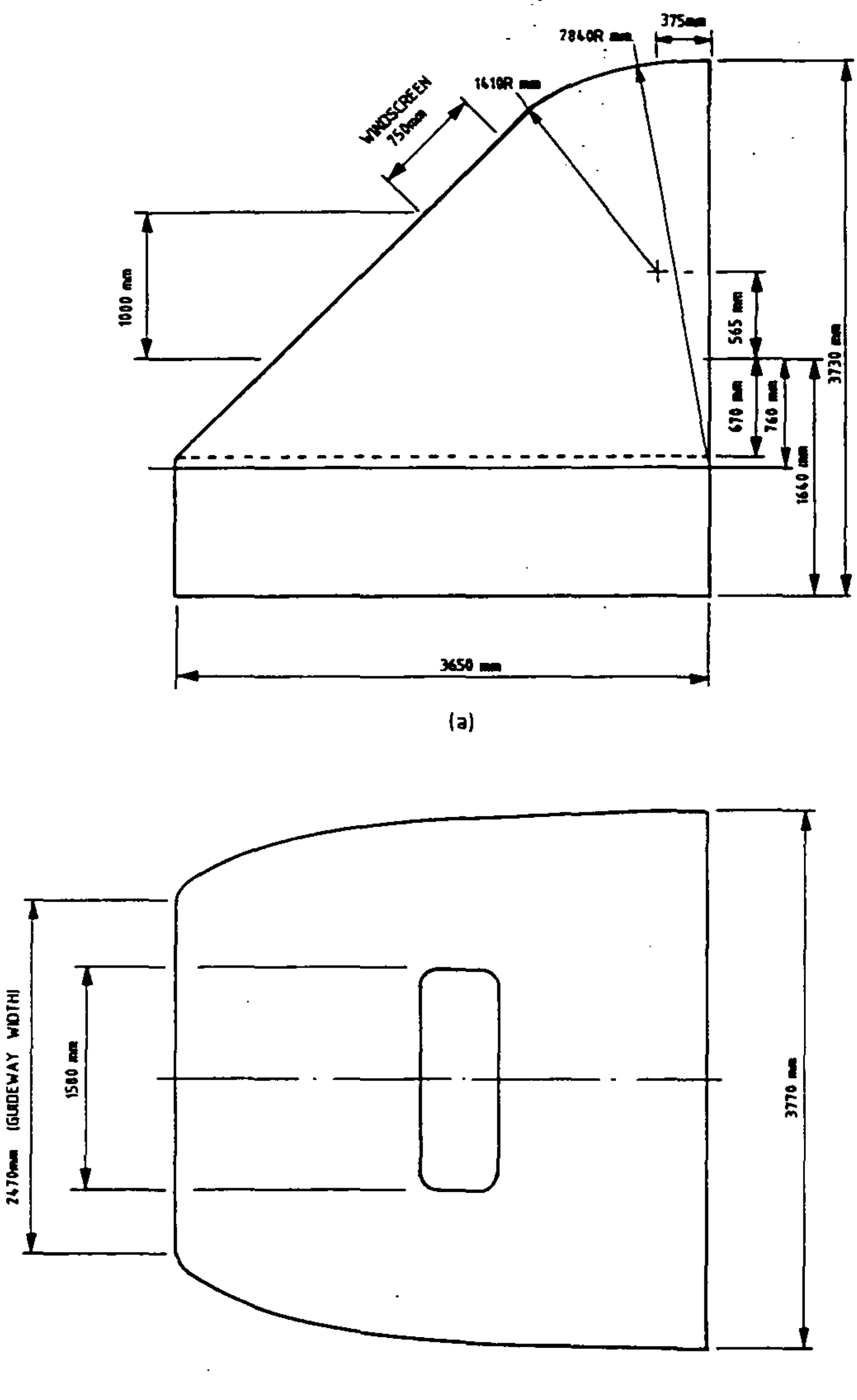

Figure 1-1 Basic nose profile for EMS train (Source ref. [6])
(a) cross-section on centre-line
(b) top view

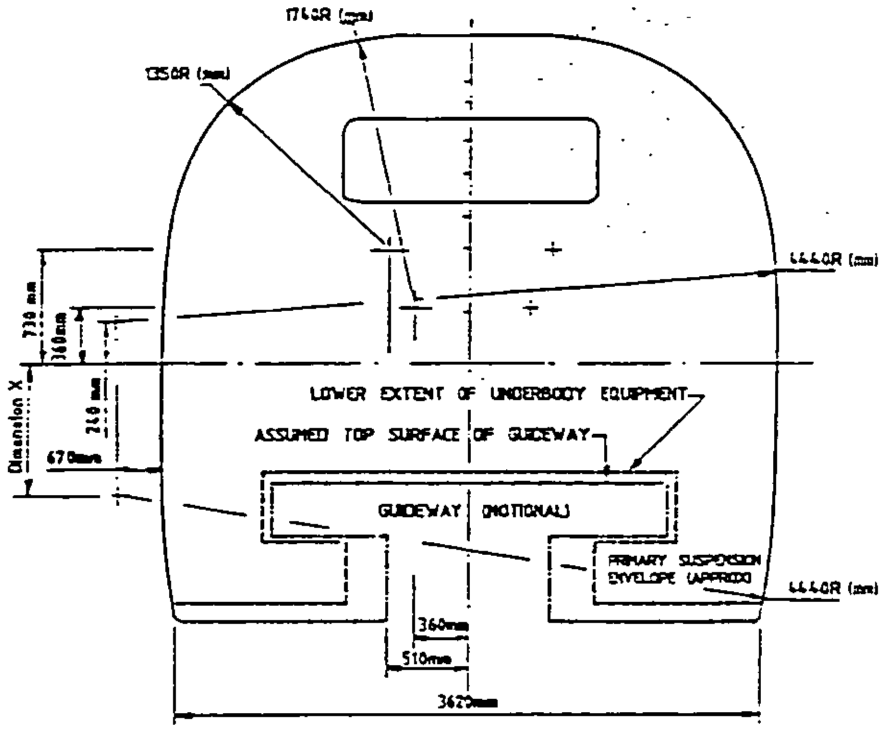

(a)

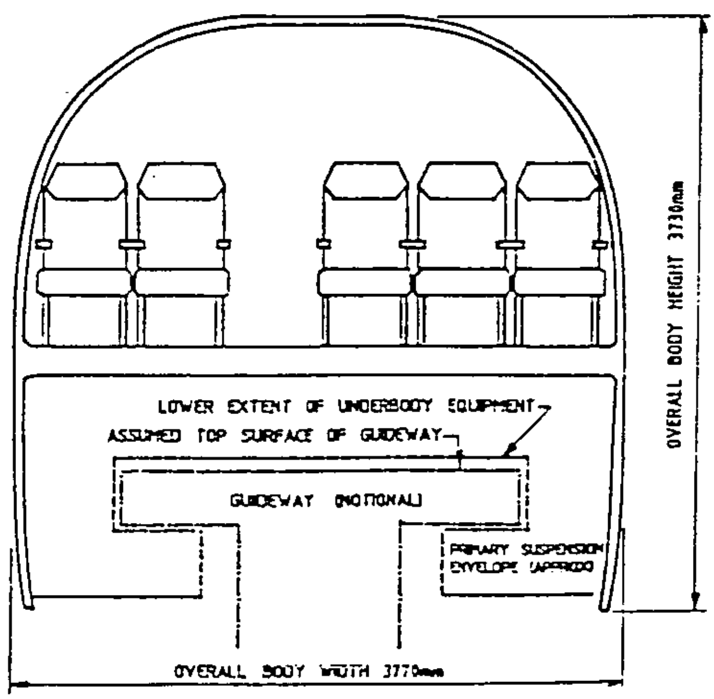

(b)

Figure 1-2 (a) Front view of an EMS train model

(b) Cross-section of an EMS train model

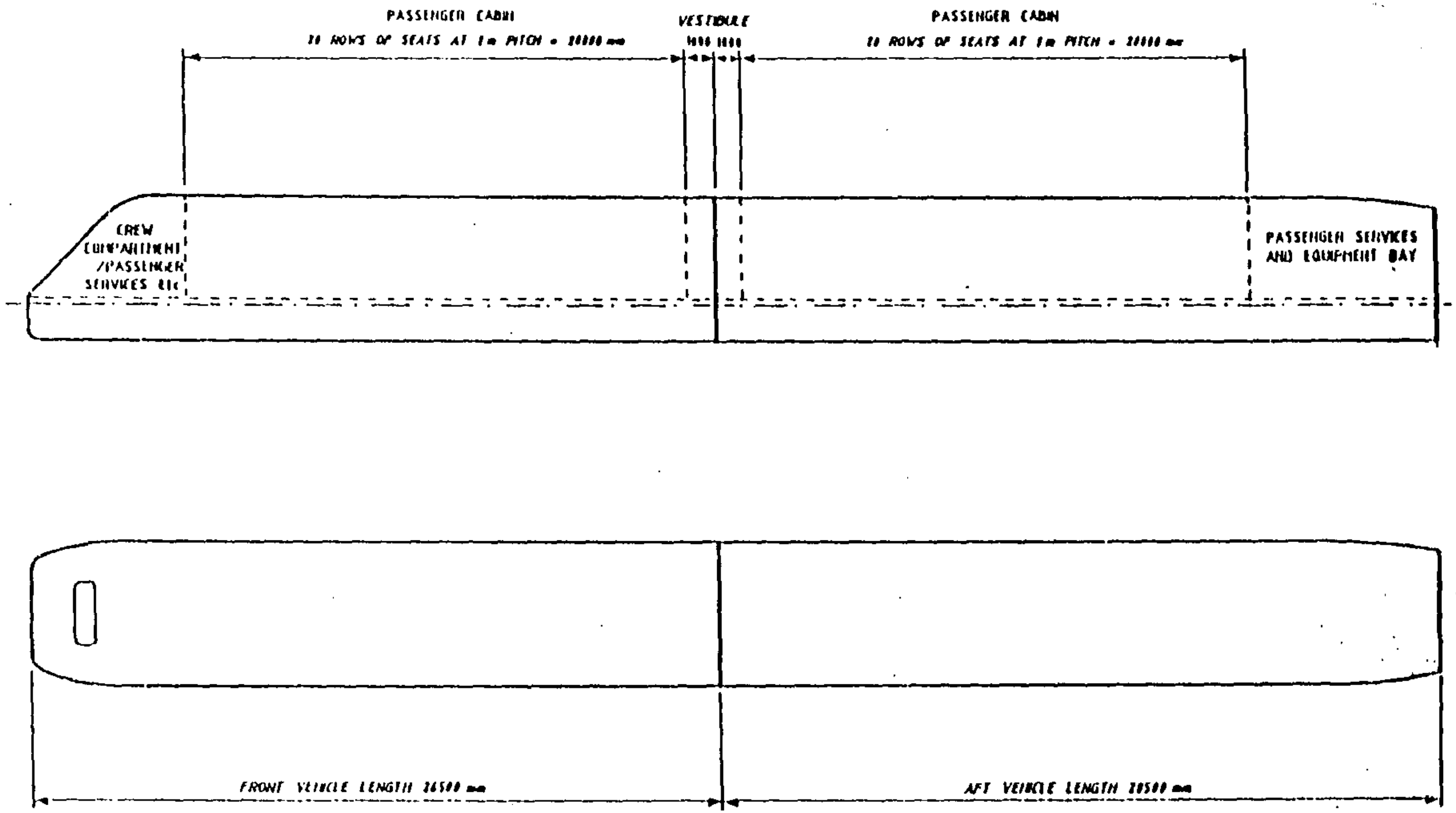

Figure 1-3 Basic configuration for EMS train (Source ref. [59])
(a) side view, (b) top view

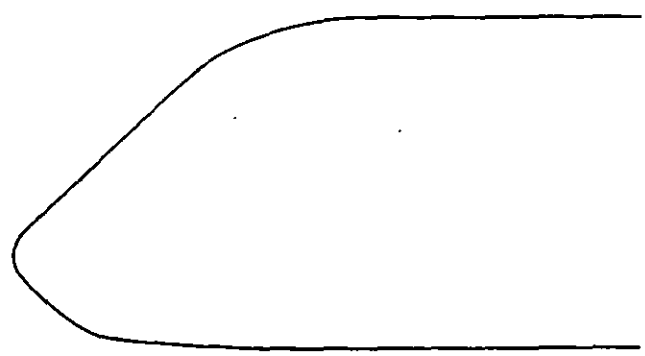

(a) APT nose shape profile

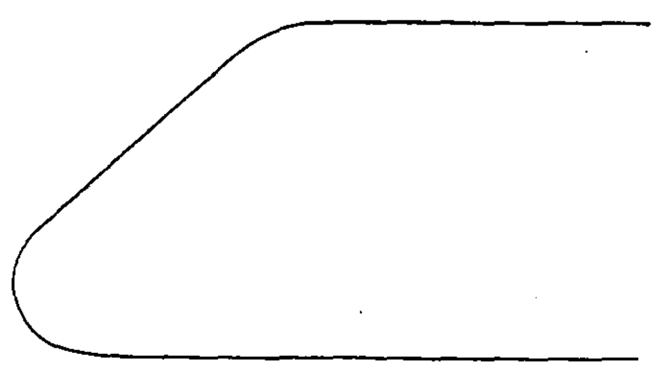

(b) ICE nose shape profile

Figure 1-4 Basic nose profile of two conventional trains

PART I : INVISCID FLOW PREDICTION ON EMS TRAIN

PART I

INVISCID FLOW PREDICTION ON EMS TRAIN

Part I describes the basic theory and demonstrates the capabilities of a practical numerical technique, called the panel method, for predicting three-dimensional inviscid potential flow over the surface of an industrial train design. Demonstrations of the capabilities of the numerical method are made by applying it to predict flow velocity and pressure distributions over a model of an EMS train for three situations of interest in railway engineering practice. The panel method is based on the theorems of potential flow, is quite general — for instance, it can cope with a body (or several bodies simultaneously) of arbitrary shape — and provided that the disturbance due to a body (or bodies) immersed in a fluid is a potential flow, does not employ any simplifying assumptions. Briefly, the panel method works by assuming a distribution of source density over the surface of a body and then solves for the distribution that makes the normal component of fluid velocity zero on the body surface in the presence of a given freestream flow.

Two computer programmes based on the panel method have been developed to predict the velocity and pressure distributions on the surface of an EMS train model. It is these computer programmes that have been employed to demonstrate the capabilities of the panel method by predicting the velocity and pressure distribution on the surface of a model of an EMS train, and in particular for the three situations Ú (1) train travelling at a constant speed in the open air for various angles of yaw, (2) train passing a railway station, and (3) a train passing another similar train on an adjacent track.

Part I consists a single chapter, chapter two and associated appendices (Appendix A and B).

CHAPTER 2

THREE-DIMENSIONAL POTENTIAL FLOW PREDICTION ON AN EMS TRAIN MODEL

2.7 A Comparison of Predicted Distribution of Pressure Coefficient on EMS and Conventional Train Shapes.

2.8 Concluding Remarks

2.1 Introduction

The use of modern large-scale computers in external aerodynamics theory has seen a trend in recent years towards numerical methods and computer programmes suitable for flow field analyses of complete aircraft [62,63]. This research success in the aeronautical industry has resulted in the development of practical numerical techniques and has encouraged researchers investigating design and performance issues of high-speed ground vehicles to undertake the analysis of the flow on high-speed ground vehicles, especially for high-speed trains. Such an approach is important and essential due to its potential for accuracy, economic cheapness and ability to give more details when compared to, say, experimental methods. As far as the author is aware theoretical work involving the prediction of comprehensive air flow data for high-speed trains is still in the early stages (view based on the apparent lack of relevant published work in the open literature).

In this chapter an attempt is made to apply the basic theory and features of a numerical technique called the panel method, due to Hess and Smith [64], to predict the three-dimensional potential flow on the surface of an EMS train. The chapter demonstrates the use of the panel method by describing a computer programme written by the author and applied to an EMS train model to predict the velocity and pressure distribution on the train surface. Two areas of application in industrial train design practice [65] are addressed, namely : (1) the study of the aerodynamic effects on a train travelling in the open air, and (2) the interference effect due to the passage of a high-speed train on the environment near the tracks, i.e. by-standers, buildings or other trains. The latter case includes an EMS train passing a railway station model and an EMS train passing the central section of an adjacent EMS train. For high-speed trains the pressure pulses produced in train-passing situations can be substantial [65] and if not catered for may result in, for example, a serious risk of people (both by-standers at train stations or trackside workers) being blown over. Appendix A describes a two-dimensional version of the panel method developed as a computing exercise prior to the work of this chapter. An illustration of the two-dimensional results is given in sections 2.5 and 2.6.

In industrial practice a significant number of the problems of interest in external aerodynamics require the solution for the flow on the surface of one or more bodies. The panel method, as originally published [64] and as employed in this chapter, can cater for the above mentioned surface-based problem of external aerodynamics but for a restricted class of flow — namely steady, incompressible, inviscid, non-lifting potential flow. Accumulated engineering experience in aerodynamics suggests that for many problems of interest the effect of viscosity can be neglected or at least as a first approximation results of an inviscid flow analysis are satisfactory except at points of flow separation and in wake regions. They also serve as a useful input to first calculations of viscous effect (inviscid/boundary layer interaction). Aerodynamic forces such as drag, of course, cannot be predicted correctly. The effect of viscosity, separation regions, wakes and boundary layer analysis, will be studied in this thesis both experimentally and theoretically in later chapters. The compressibility effect has been neglected since the EMS train cruising speed will be subsonic and at a low Mach number (less than approximately 0.3). The non-lifting assumption is discussed more fully below.

The panel method for flow velocity is based on the theorems of potential flow. The method employs a source distribution on the surface of the body and solves for the distribution that makes the normal component of fluid velocity zero on the body surface in the presence of a given freestream flow (assuming that the body surface is solid). The panel method is quite general and provided that the disturbance or perturbed flow due to the bodies is a potential flow, does not use any simplifying assumption. Thus a body under investigation need not be slender, nor do the perturbation velocities due to the body need to be small. Exterior and interior flows can be calculated and flow interference problems due to several bodies may be studied without difficulty as will be shown later in section 2.6.

In practice the technique first starts by approximating the body surface by a number of flat surface elements (panels) with dimensions that are small in comparison with that of the body, see Figure 2-1 in which the sample three-dimensional body is approximated by a surface distribution of small plane quadrilaterals. On each of these surface elements a control point is selected at which the velocities and pressures on the surface of the body are to be evaluated. Figure 2-2 shows a practical industrial example of a panel method approximation to a fully three-dimensional representation of an aircraft [30] and Advanced Passenger Train (APT) [37]. The representation of the aircraft employs 2700 elements.

Once the approximation to the body geometry has been made the panel method then proceeds to simultaneously adjust the source densities on the entire set of surface elements in such a manner that the prescribed normal-velocity condition is complied with at all control points. Briefly, the procedure is as follows. The surface source density is assumed to be a fixed value over each element (the value may be different for different elements) and the number of unknown source strengths is thus equal to the number of elements. This assumption of a constant source density over a planar surface element is used to classify this panel method approach as a "first-order" panel method. The fluid velocities induced by each element at the other elements' control points are then calculated. Now, the prescribed boundary conditions require that the normal velocity at each control point due to the entire source distribution be the negative of the normal component of the main stream flow there, so that the total normal velocity is zero. These requirements for the induced velocities and surface normal boundary condition are expressed as a set of linear algebraic equations for the unknown source strengths. Once the source strengths are computed, then the velocities and pressure at any point either on the surface or in the free stream can be evaluated. For the basic theory of three-dimensional panel method the reader may refer to [66-69]. The accuracy of the panel method clearly depends on the number of the elements distributed on the surface of the body; the more elements, the better the accuracy of the solution.

The aims of the work presented in this chapter were the following :

1. To use the source panel method to compute the velocity and the pressure distribution on the surface of the EMS train model in three-dimensions.

2. To demonstrate the potential of the three-dimensional panel method as well as provide insight to the flow behaviour of some practical railway engineering problems, for example when the EMS train model passes a railway station and when an EMS train passes an adjacent EMS train model.

3. Accumulate experience in the prediction of sufficiently accurate velocities on the surface of the EMS train model with the objective of employing these as input to a method for calculating the evolution of the three-dimensional turbulent viscous boundary layer on the train surface (see later chapters).

This chapter has six remaining sections. Section 2.2 is concerned with the limitations of the panel method as used in this chapter. This is then followed by a combined qualitative and quantitative description of the theory and practical realisation of the first-order panel method in section 2.3. Section 2.4 presents a computer programme developed by the author and based on the adopted panel method. Section 2.5 describes the numerical test cases used to check the correctness of the computer programmes for both two-dimensional and three-dimensional cases. Section 2.6 then discusses the application of these computer programmes to several problems of interest in railway engineering. As a further example of the usefulness of the current method, section 2.7 presents a comparison of the predicted distributions of pressure coefficient over an EMS and conventional train model. The chapter then closes with concluding remarks in section 2.8.

2.2 Limitations of Potential Flow Using the Panel method with source Distribution

A few introductory remarks on the basis of the panel method are made before the main limitations of the adopted method are outlined. The limitations are highlighted by considering both the simplifications made to the real flow problem (physics) and limitations due to the numerical approximations inherent in the panel method (numerical discretization of the body by a finite number of panels).

Lamb [70] has shown that for a single-valued potential flow over a closed surface, the potential function at an external field point can be represented by the surface integral of a distribution of sources, doublets or closed vortex filaments on the closed surface. For a complicated surface geometry, such as in industrial high-speed train design, it is difficult to find a closed form solution to the surface integral equation. The panel method for the numerical evaluation of the surface integral equation is based on approximating the body surface by many planar panels and then placing source, doublet or vortex filaments on these panels. It is then possible to express the resulting integral equation and associated boundary conditions as a set of algebraic equations which are easier to solve.

Various panel method techniques are in use according to the type or combination of the possible singularity functions, i.e. source, doublet or vortex filament, on the surface of the body to meet a specific geometry and flow type of interest. The classic paper on the source panel method is the one by Hess and Smith [64]. This described what is now termed as a first-order panel method because a constant source distribution is assumed to exist over each panel that is employed to approximate the body surface. It is noted that the value of the source distribution can vary from panel to panel including adjacent ones. Since the method employs only a source distribution it may be shown that it is applicable only to non-lifting flows. This and other limitations, together with their relevance to the train aerodynamics of interest will be discussed later in this section.

The panel method is also capable of predicting three-dimensional lifting flows provided suitable singularity functions are employed in the formulation . The first such panel method was the technique developed by Rubbert et al. [71] in 1968, based on the addition of a constant dipole distribution to the constant source distribution over the panels on the wing camber surface. Maskew [72] and Giesing [73] developed a panel technique based on the distribution of a quadrilateral vortex "ring" on the surface and in the wake behind the body to predict the potential flow for lifting bodies such as a thin wing. Finally, Petrie [69] used constant source panels and constant doublet panels placed together on the surface of the body. This technique is able to predict the vorticity and source distribution of a thick wing lifting configuration. This method has been developed for applications to complex aircraft configurations but in general requires considerable computer storage and running time and can be expensive to apply [74].

In order to increase the accuracy for a given panel mesh distribution various researchers have developed higher-order formulations of the panel method. There are many variants of these higher-order and a discussion of these techniques is beyond the scope of this work. For readers with more interest in such techniques Giesing [73] made a short survey of the development of the vortex and doublet lattice method for lifting bodies while Morino [29] and Hess [31] reviewed the historical development of the panel method.

The panel method adopted here employs just a source distribution on the body surface of interest and has associated limitations. The limitations have been divided into two categories, (1) those that involve simplification to the flow physics, and (2) those related to the numerical approximation of the problem. Some remarks are provided here which clarify these limitations, their impact on the current flow pattern, and justify the currently selected method.

Category 1 limitations

1. The panel method is based on the assumption of inviscid potential flow and cannot therefore predict the development of the boundary layer and possible separated flow regions which may occur in viscous flow.

   High-speed trains have extensive boundary layer regions on nose, central body and rear of the train and possible separation zones on both nose and bluff trailing end. As a consequence the predictions of the panel method alone will be in error, to significant extent in regions of flow separation. There is however no reliable general technique for modelling and predicting three-dimensional boundary layer growth and three-dimensional separation for high-speed ground vehicles. In spite of this, the combination of a panel method and a three-dimensional boundary layer method can produce useful results, at least for the attached regions of the flow. Experiments will certainly be required for the foreseeable future to examine three-dimensional separation effects.

2. In practice vortices observed in the lee side of trains have a large effect on the pressure distribution on the train, and hence the overall aerodynamic forces [36]. Side force and rolling moment, for example, depend largely on the formation of these vortices. Copley observed that as the yaw angle increased, so did the side force due to the growth in the lee side vortices.

   Cooper [53] performed tests on a moving 1/5 scale model of an APT in natural wind and found that the trend of the aerodynamic forces displayed an increase with increasing yaw angle, reaching maximum at about 50° yaw and remaining essentially at this value for larger angles of yaw. At low yaw angle, less than 15°, Stewart [20] found that lee side vortices could not be clearly identified and that the aerodynamic side force was negligible. These studies suggest that for yaw angles above 15° the presence of the vorticity in the lee side of the train must be included. Therefore the adopted panel method (which employs *only a source* distribution) is clearly inadequate for the accurate calculation of the aerodynamic forces (particularly side force, and overturning moment) on a train travelling at a yaw more than 15°. However, a source panel prediction will still be of interest for cases close to zero yaw, particularly as as an input to a viscous calculation to study, for example, the effect of nose shape on boundary layer growth, as stated above.

3. The above limitation is linked to the more general constraint that a pure source panel method is incapable, for the case of an isolated body in free air, of predicting a net force perpendicular to the onset flow, since the technique does not admit any net circulation. For a train close to the ground, some lift normal to the ground may be predicted, but the all-important 'lift' force parallel to the ground will still be absent. However, for small yaw angles it was felt that a source distribution solution was still worthwhile. In potential flow lift is the result of circulation around a body, thus the potential flow for lifting bodies may be computed by distributing vorticity on the surface and in the wake of the body. It is possible to extend the current panel method to handle the lift case by adding to the free stream and the source distribution a piecewise constant doublet distribution or vorticity on a sheet positioned in the body and in the wake. Hence, the current work may be viewed as a first step in developing a method which can be extended to the lifting case in the future.

Category 2 Limitations

1. A discontinuous source density distribution is present over the surface of the body. This is because the source density is assumed to be constant over each panel (irrespective of the source density on adjacent or other panels), therefore step jumps in the values of source density at the boundary of two panels is possible.

2. Gaps are present in the discretized representation of the actual body surface as flat panels. For a body of arbitrary shape it is not possible to arrange the quadrilaterals so that all four vertices of each panel match the vertices of adjacent panels, that is the approximating surface of panels has gaps and is therefore not strictly impermeable.

3. Quantities such as velocities and pressures on the body can be usefully evaluated only at the control points of each panel (that is, only at the points at which the normal boundary conditions were matched). This makes accurate streamline tracing difficult since some streamlines may apparently pierce the approximating surface.

All the above disparities may be reduced by increasing the number of panels employed in the representation of the body or its parts.

2.3 Description of a First-order Three-dimensional Panel Method

This section provides an overview of the basic theory and practice in the realisation of a first-order panel method for the numerical analysis of three-dimensional external incompressible potential flows over three-dimensional bodies with arbitrary shapes. The section is divided into six parts. The first part, section 2.3.1, presents the principal normal velocity boundary condition at the surface of a body employed by the panel method. The second part (section 2.3.2) essentially quotes the governing integral-equation, involving the assumed distribution of source density on the body surface and the appropriate normal velocity conditions on the body surface, for the external flow. It then describes how this equation may be expressed as a system of linear algebraic equations for the unknown source densities applied to each of the approximating plane quadrilateral surface elements which idealise the body surface. Section 2.3.3 describes the computational procedure for evaluating the coefficient of pressure, C_p, for cases of unsteady flow such as when two trains pass on adjacent tracks. The final three parts provide a review of how the planar quadrilateral surface element is defined geometrically and manipulated to obtain expressions for each surface element's influence on the disturbance potential function at an external flow field point, and where simplifications may be made to reduce computing costs but not affect the accuracy. The choice of control point for imposition of the normal velocity boundary conditions on the body surface on these surface panels is also discussed.

2.3.1 A Normal Velocity Boundary Condition in Potential Flow

The governing equations for incompressible inviscid flow, when body forces are neglected, take the form of the Eulerian equations of motion, written in vector form as : -

$$\frac{\partial V}{\partial t} + (V \cdot \nabla)V = -\frac{1}{\rho}\nabla P \qquad 2\text{-}1$$

where

$\mathbf{V}$ fluid velocity vector

P pressure

ρ mass density

t time

the continuity equation for steady incompressible flow takes the form : -

$$\text{div}\,(\mathbf{V}) = 0 \qquad 2\text{-}2$$

Equations (2-1) and (2-2) hold for exterior flow on and off the surface of a body and in the case of a moving body immersed in a fluid, these equations need certain boundary conditions for their solution. One of the boundary conditions is based on the requirement that the total normal velocity at any point on the body surface, must be zero, provided there is no suction or blowing at the body surface. This condition is implied in equation (2-3) below which specifies the boundary conditions over the surface of a body. F is zero for a solid object, or equal to a prescribed normal velocity in the case of suction or blowing :

$$\mathbf{V}\cdot\mathbf{n}\big|_S = F \qquad 2\text{-}3$$

$\mathbf{n}$ is the unit outward normal vector at a point on the surface of the body, and

F denotes the presence of a prescribed normal velocity.

Now, the velocity field $\mathbf{V}$ on the surface of the body consists of the vector sum of two components, a freestream and a disturbance component, and may be expressed as : -

$$\mathbf{V} = \mathbf{V}_\infty + \mathbf{v} \qquad 2\text{-}4$$

where

V_∞ is the free stream velocity field, and

v is the disturbance to the freestream velocity field due to the presence of the body.

The only requirement on V_∞ is that it is an incompressible flow. However, for a potential flow, it is required that the disturbance velocity v be irrotational, and v may then be expressed as the negative gradient of a potential function ϕ, namely

$$v = -\nabla\phi \qquad 2\text{-}5$$

Thus, using equations (2-4) and (2-5), the boundary condition for the normal velocity at a point on the surface of the body expressed by equation (2-3) may be written in terms of the potential function as

$$\nabla\phi.n\Big|_S = \frac{\partial\phi}{\partial n}\Big|_S = V_\infty \cdot n - F \qquad 2\text{-}6$$

2.3.2 Derivation of the Governing Equations

The three-dimensional panel method described here approximates the surface of a body using planar quadrilateral surface elements as shown in Figure 2-1. The points that are used to form the planar surface elements are associated in groups of four and are distributed over the surface of the actual body. These points may be obtained for example from engineering drawings or computer-aided drafting, geometry modelling or finite element programmes used in the design process. Since four points do not necessarily lie on a single plane the panel method's approximating plane for each planar surface element is defined to pass through the centroid of the associated four data points on the body surface and its outward unit normal is derived from the vector cross-product of the two diagonals formed from the four data points, as alluded to in Figure 2-1. The corners of the surface element of interest are then simply defined as the projections of the four data points on the above plane.

A consequence of the above method of forming the panels is that the sides of adjacent panels do not, in general, coincide; this means that there are "gaps" between panels. However, the errors introduced by this mismatch of adjacent panel edges are usually negligible in comparison with those resulting from the basic approximation of the surface of a body by plane panels over which a constant source density is assumed to exist [64]. This remark holds provided that the size of the "gaps", as measured by the distance the input points need to be projected to place them on the plane of the panel, is small in comparison with the dimensions of the element — a situation which can be expected to hold for reasonable distribution of input points on the body. In practice such distributions may be quickly achieved by experience. Thus, for example, elements should be concentrated in regions where the body geometry — as measured by, say, curvature— changes rapidly with distance or where the flow properties (and in particular the source density) are expected to vary rapidly.

Consider a unit point source located at a point q, with co-ordinate (x_q,y_q,z_q) in a typical panel, on the surface of a body and a point p, with co-ordinate (x,y,z), in the flow field, see Figure 2-3. The potential, ϕ_p, at the field point p due to the source point q on the body surface is given by the expression

$$\phi_p = \frac{1}{r_{(p,q)}} = \frac{1}{\sqrt{(x-x_q)^2 + (y-y_q)^2 + (z-z_q)^2}} \qquad 2\text{-}7$$

where

$r_{(p,q)}$ is the distance between the flow field point, p(x,y,z), and the point q (x_q,y_q,z_q) where the source is located

Lamb [70] (Article 52) and Kellogg [75] (chapter eight, Theorem VIII and IX) show that for a single-valued potential flow over a closed surface the potential function at an external field point can be represented by the surface integral of a distribution of sources.

Thus the potential , ϕ_p, at the above mentioned flow field point p, due to the source distribution on the whole surface S may, see Figure 2-1, be written

$$\phi_p = \iint_S \frac{\sigma_{(q)}}{r_{(p,q)}} dS \qquad 2\text{-}8$$

where

$\sigma_{(q)}$ is the source density at a point q on body surface, and the remaining symbols are as defined in equation (2-7)

The boundary condition that must be complied with by the source density $\sigma_{(q)}$ is that the total of the normal perturbation velocity at any point on the body surface together with the undisturbed free stream flow component, must equal the prescribed normal velocity component F,

$$\nabla \phi . n = \frac{\partial \phi}{\partial n}\Big|_S = V_\infty . n - F \qquad 2\text{-}9$$

That is, the surface source density $\sigma_{(q)}$ of equation (2-8) must satisfy the surface normal-velocity boundary condition expressed by equation (2-9). In principle this requires that the derivative of the integral of equation (2-8) with respect to the outward normal at a sample field point p on the body surface be evaluated. However, some care is required since such a spatial derivative of this integral becomes singular as a given field point p approaches the surface of the body.

It can be shown, e.g., by Kellogg [75], (chapter eight, Theorem VI), that the normal velocity induced when the field point p lies on the body surface exists, is finite and may be obtained by a limiting process that approaches the surface as

$$2\pi\sigma_{(p)} - \oiint_S \sigma_{(q)} \frac{\partial}{\partial n} \left(\frac{1}{r_{(p,q)}}\right) ds \qquad 2\text{-}10$$

where

$\sigma_{(p)}$ is the value of the source density at the field point p on the body surface.

$\sigma_{(q)}$ is the value of the source density at point q on the body surface and which does not coincide with p.

$\frac{\partial}{\partial n}$ represent partial differentiation in the direction of the outward normal to the body surface of the point p.

Thus the governing integral equation for flow at the surface of the body is obtained by substituting expression (2-10) for the induced surface normal velocity into the left-hand side of equation (2-9) for the prescribed surface normal velocity and results in an expression of the form

$$2\pi\sigma_{(p)} - \oiint_S \frac{\partial}{\partial n}\left(\frac{1}{r_{(p,q)}}\right)\sigma_{(q)}\, dS = -n_{(p)}.V_{\infty} + F \qquad 2\text{-}11$$

Equation (2-11) is then the governing integral equation for the source distribution on the surface of the body which ensures that the normal component of fluid velocity on the body surface takes on the prescribed value F in the presence of the freestream flow V_{∞}. Appendix A describes a suitable numerical method for evaluating and solving the integral equation (2-11) for the special case of two-dimensional potential flow, here remarks are restricted to solution for three-dimensional potential flows.

The solution of the above analytic integral equation (2-11), is approximated numerically in the panel method by discretising the body surface into a number ,N, of quadrilateral panels whose corner points are derived from the geometry of the body as described above ; an unknown constant value of source density is then assigned to each surface panel, a constant value being assumed for each panel element. This means that there are as many unknown source densities as there are panel elements. On each panel a control point is chosen at which the surface normal-velocity condition embodied in equation (2-11) is to be satisfied. Consider the expression corresponding to the governing equation (2-11) at the i-th control point due to the j-th panel element. When i=j, the left hand side of equation (2-11) consists only of the term $2\pi\sigma_{(i)}$. For the case when i is different to j , only the integral term contributes to the left-hand side of equation (2-11). (It is also to be noted that for a constant source density, the σ term may be taken outside the integral whose value thus depends only on the geometry of the panel element ; this point is to be covered in a later section when this integral is evaluated analytically equation (2-11)). The application of equation (2-11) to each panel element results in a set of N simultaneous linear algebraic equations (in this work the prescribed velocity F is zero i.e there is no suction etc.). In summary form (see reference [64]) : -

$$\sum_{j=1}^{N} A_{ij}\sigma_j = -\mathbf{n}_i \cdot \mathbf{V}_\infty \qquad i=1,2, .., N \qquad 2\text{-}12$$

where

σ_j is the unknown source density on the j-th panel element.

$\mathbf{n}_i$ in the outward normal to the body surface at the i-th control point

$$A_{ij} = \mathbf{n}_i \cdot \mathbf{V}_{ij} = \begin{cases} 2\pi\sigma_i & \text{when } i=j \\ \iint_s \frac{\partial}{\partial n}\left(\frac{1}{r_{(i,j)}}\right) ds & \text{when } i\neq j \end{cases}$$

A_{ij} is an element of the matrix of influence coefficients and represents the component of the flow velocity normal to the i-th element induced by a unit source density on the j-th element.

$\mathbf{V}_{ij}$ the velocity induced at the i-th control point due to the j-th panel element.

The values of the source densities, σ, can now be obtained as the solution of this set of simultaneous equations. Once the equations have been solved for the unknown source densities, the velocity at the i-th control point may be calculated as :

$$\mathbf{V}_i = \mathbf{V}_\infty + \sum_{j=1}^{N} \mathbf{V}_{ij}\sigma_j \qquad 2\text{–}13$$

and the pressure coefficient, C_p, at any point i is

$$C_p = 1 - \frac{V_i^2}{V_\infty^2} \qquad 2\text{-}14$$

where

V_i is the magnitude of $\mathbf{V}_i$

V_∞ is the magnitude of $\mathbf{V}_\infty$

2.3.3 Calculation of C_p for Cases of Unsteady Flow

When two trains pass or overtake each other on adjacent tracks, unsteady pressure fields are created around them. These pressures impose loads which differ in nature and magnitude considerably from those on the single train. Important implications of the unsteady loads (whose severity depends upon the difference in speed of the two trains) are effects on stability, travel trajectory and passenger comfort. The relation for C_p stated above (2-14) requires modification in this case because (2-14) is based on the steady form of Bernoulli's equation. In the framework of potential theory the passing or overtaking problem has been treated as a quasi-steady flow as follows [34,37]. An approximation for the solution of the continuous unsteady flow involved during the passing of two trains, each travelling with constant but different speeds, is found numerically by discretising the continuous problem and replacing it as a finite number of steps in time between which the relative position of the trains change. In this approach, the time between a change in vehicle position and the moment its effect is felt throughout the flow field is assumed to be negligible. This is permissible with vehicle speeds which lie substantially below the speed of sound, which is the speed with which a pressure pulse travels in air. Further, the unsteady pressure field is determined from the solution of an unsteady form of Bernoulli's equation by adding to the steady flow from a time derivative of the potential function $\partial\phi/\partial t$, see [34]. This time derivative is obtained, for example, at a given point on a vehicle surface by evaluating the difference in the values of the potential function for the two consecutive locations of the given point and dividing the result by the time needed to traverse the relative distance between them. In this way unsteady solutions for any speed difference between the two trains can be generated from the basic steady solutions.

The general Bernoulli equation for unsteady flow can be written as

$$\frac{P}{\rho} + \frac{1}{2}V^2 - \frac{\partial\phi}{\partial t} = \frac{P_\infty}{\rho} + \frac{1}{2}V_\infty^2 \qquad 2\text{-}15$$

with the related coefficient of pressure given by

$$C_p = \frac{P - P_\infty}{\frac{1}{2}\rho V_c^2} = \frac{V_\infty^2}{V_c^2} - \frac{1}{V_c^2}(V^2 + 2\frac{\partial\phi}{\partial t}) \qquad 2\text{-}16$$

(the velocity V_c is used to non-dimensionalise the pressure, see below for more details)

and the solution for steady flow is obtained when $\partial\phi/\partial t = 0$ and V_c=V.

To illustrate the basic elements in the practical computation of the time-derivative component $\partial\phi/\partial t$, consider two trains A and B passing each other on adjacent tracks (see Figure 2-4) where

x	=	Distance from the centre of train B to the tip of the nose of train A.
x_o	=	the x-distance at time t=0
V_A	=	Velocity of train A
V_B	=	Velocity of train B
V_c	=	Closing velocity, i.e. velocity of train A relative to train B
Δy	=	Lateral separation of train A, B : an implicit spatial quantity in the theoretical derivation

The closing velocity, V_c, at which train A travels relative to train B is, for trains approaching each other,

$$V_c = |V_A| + |V_B|$$

and the relative distance of the tip of train A from the centre of train B varies with time, t, as

$$x = x_o - V_c \cdot t$$

from which it follows that

$$\frac{dx}{dt} = -V_c$$

and the time derivative for the potential function ϕ is obtained from the above result for dx/dt and

$$\frac{\partial \phi}{\partial t} = \frac{\partial \phi}{\partial x} \cdot \frac{\partial x}{\partial t} \qquad 2\text{-}17$$

that is

$$\frac{\partial \phi}{\partial t} = -V_c \frac{\partial \phi}{\partial x} \qquad 2\text{-}18$$

By computing the values of the potential function ϕ for at least one station with a relative displacement, Δx, from the station x then $\partial \phi / \partial x$ is obtained using a simple finite difference expression. The magnitude of Δx depending on the time-step employed in the calculation,

2.3.4 A Planar Quadrilateral Panel Element and its Local Co-ordinate System

This section describes briefly the formation of the plane quadrilateral surface panel elements used in the approximation of the body surface and the formation of the transformation matrix required to map points from the global (cartesian) co-ordinate system on to the panel element's local (cartesian) co-ordinate system. In order to determine the flow about an arbitrary body it is convenient to employ a single global coordinate system to specify the geometry of the body and its surrounding space and a set of local co-ordinate systems, one for each panel, to specify details local to each panel. The local co-ordinate system is fixed in the plane surface of the corresponding panel element.

Let the global position vectors of four data points on the surface of an arbitrary body which are to be associated with , say the i-th element (refer to Figure 2-5) be $\mathbf{x}_{1i}$, $\mathbf{x}_{2i}$, $\mathbf{x}_{3i}$ and $\mathbf{x}_{4i}$.

Then the transformation matrix, **R**, may be expressed as, see Appendix B

$$R = \begin{bmatrix} a_{11} & a_{12} & a_{13} \\ a_{21} & a_{22} & a_{23} \\ a_{31} & a_{32} & a_{33} \end{bmatrix} \qquad 2\text{-}19$$

where the components of the transformation matrix derived from the component of the vectors $\mathbf{t}_1$, $\mathbf{t}_2$ and **n**, (see Appendix B) may be written as

$$\begin{array}{lll} a_{11} = t_{1x} & a_{12} = t_{1y} & a_{13} = t_{1z} \\ a_{21} = t_{2x} & a_{22} = t_{2y} & a_{23} = t_{2z} \\ a_{31} = n_x & a_{32} = n_y & a_{33} = n_z \end{array}$$

Thus to transform, for example, a point specified in global co-ordinates to its corresponding value in a panel element's local co-ordinate system, only **R** and the position vector (in the global system) of the origin (centroid) of the element $\mathbf{V}_o$ are required. To transform a point with position vector $\mathbf{V}_r$ in the global co-ordinate system to its corresponding value $\mathbf{V}_e$ in a panel element local co-ordinate system requires the operation

$$\mathbf{V}_e = \mathbf{R}\,(\mathbf{V}_r - \mathbf{V}_o) \qquad 2\text{-}20$$

2.3.5 Exact and Approximate Induced Velocity at a Field Point Due to a Constant Source Distribution on a Planar Quadrilateral Element

In this section the exact and approximate formulae for the velocity induced at a point in the flow field due to a planar quadrilateral panel element on which there exists a constant source density with a unit value are presented. For a planar panel element of this type, it is possible to determine its pertrutbation potential (see equation (2-8)) as the product of the value of the constant source density and an integral that depends only on the geometry of the panel and can be evaluated analytically. Expressions so calculated for a quadrilateral panel are of use in the panel method; hence their discussion here. It is of further interest to reduce computing costs in the calculation of these analytic integrals. Thus the conditions for, and associated simplified expressions suitable for good approximating formulae for these integrals are also described.

A. Exact solution

Consider a point p in the flow field with element local co-ordinate (x,y,z) and a quadrilateral plane A which lies in its local co-ordinates system's x-y plane and has a surface source density equal to unity. Then the potential, ϕ, at this point p with co-ordinate (x,y,z) due to a source point at point q with element local co-ordinate $(\xi,\eta,0)$ is given by, see Figure 2-6

$$\phi = \oint_A \frac{1}{r_{(p,q)}} dA = \oint_A \frac{d\xi d\eta}{\sqrt{(x-\xi)^2 + (y-\eta)^2 + z^2}} \qquad 2\text{-}21$$

and the components of the velocity (in the element local co-ordinate system) at p are given by

$$V_x = -\frac{\partial\phi}{\partial x} = \oint_A \frac{(x-\xi)d\xi d\eta}{r^3} \qquad 2\text{-}22$$

$$V_y = -\frac{\partial\phi}{\partial y} = \oint\!\!\!\oint_A \frac{(y-\eta)d\xi d\eta}{r^3} \qquad 2\text{-}23$$

$$V_z = -\frac{\partial\phi}{\partial z} = \oint\!\!\!\oint \frac{z d\xi d\eta}{r^3} \qquad 2\text{-}24$$

For a flat panel the integration of equations (2-22), (2-23) and (2-24) can be obtained analytically to yield the exact velocity induced by the panel. If the four corner points of the panel are (ξ_1,η_1), (ξ_2,η_2), (ξ_3,η_3) and (ξ_4,η_4), see Figure 2-6, then the components of the induced velocity are given in [64] as

$$V_x = \frac{\eta_2-\eta_1}{d_{12}} \ln\left[\frac{r_1+r_2-d_{12}}{r_1+r_2+d_{12}}\right] + \frac{\eta_3-\eta_2}{d_{23}} \ln\left[\frac{r_2+r_3-d_{23}}{r_2+r_3+d_{23}}\right] + \frac{\eta_4-\eta_3}{d_{34}} \ln\left[\frac{r_3+r_4-d_{34}}{r_3+r_4+d_{34}}\right]$$
$$+ \frac{\eta_1-\eta_4}{d_{41}} \ln\left[\frac{r_4+r_1-d_{41}}{r_4+r_1+d_{41}}\right] \qquad 2\text{-}25$$

$$V_y = \frac{\xi_2-\xi_1}{d_{12}} \ln\left[\frac{r_1+r_2-d_{12}}{r_1+r_2+d_{12}}\right] + \frac{\xi_3-\xi_2}{d_{23}} \ln\left[\frac{r_2+r_3-d_{23}}{r_2+r_3+d_{23}}\right] + \frac{\xi_4-\xi_3}{d_{34}} \ln\left[\frac{r_3+r_4-d_{34}}{r_3+r_4+d_{34}}\right]$$
$$+ \frac{\xi_1-\xi_4}{d_{41}} \ln\left[\frac{r_4+r_1-d_{41}}{r_4+r_1+d_{41}}\right] \qquad 2\text{-}26$$

$$V_z = \tan^{-1}\left[\frac{m_{12}e_1-h_1}{zr_1}\right] - \tan^{-1}\left[\frac{m_{12}e_2-h_2}{zr_2}\right] - \tan^{-1}\left[\frac{m_{23}e_2-h_2}{zr_2}\right] - \tan^{-1}\left[\frac{m_{23}e_3-h_3}{zr_3}\right]$$
$$+ \tan^{-1}\left[\frac{m_{34}e_3-h_3}{zr_3}\right] - \tan^{-1}\left[\frac{m_{34}e_4-h_4}{zr_4}\right] + \tan^{-1}\left[\frac{m_{41}e_4-h_4}{zr_4}\right] - \tan^{-1}\left[\frac{m_{41}e_1-h_1}{zr_1}\right] \qquad 2\text{-}27$$

where

$$d_{12} = \sqrt{(\xi_2 - \xi_1)^2 + (\eta_2 - \eta_1)^2}$$

$$d_{23} = \sqrt{(\xi_3 - \xi_2)^2 + (\eta_3 - \eta_2)^2}$$

$$d_{34} = \sqrt{(\xi_4 - \xi_3)^2 + (\eta_4 - \eta_3)^2}$$

$$d_{41} = \sqrt{(\xi_1 - \xi_4)^2 + (\eta_1 - \eta_4)^2}$$

$$m_{12} = \frac{\eta_2 - \eta_1}{\xi_2 - \xi_1} \qquad m_{23} = \frac{\eta_3 - \eta_2}{\xi_3 - \xi_2}$$

$$m_{34} = \frac{\eta_4 - \eta_3}{\xi_4 - \xi_3} \qquad m_{41} = \frac{\eta_1 - \eta_4}{\xi_1 - \xi_4}$$

$$r_k = \sqrt{(x-\xi_\kappa)^2 + (y-\eta_\kappa)^2 + z^2} \quad , \quad k=1,2,3,4$$

$$e_k = z^2 + (x-\xi_\kappa)^2$$

$$h_k = (y-\eta_\kappa)(x-\xi_k) \quad , \quad k=1,2,3,4$$

B. Approximate solution

The exact solution for the induced velocity components in the cartesian x-, y- and z-directions due to a planar quadrilateral panel element given by the equations (2-22), (2-23) and (2-24) respectively are complicated because they include the effect of all the details of the panel shape, and the expressions are (due to the need to evaluate logarithms, inverse tangents and square roots) quite time-consuming to compute. It can be shown [76] that the formulae for the exact solution are unnecessarily complicated when the field point at which induced velocity is required in the flow field is sufficiently far from the panel, because the details of the panel shape are then unimportant. The induced potential and velocity in this case depend mainly on certain overall parameters that characterise the shape of the body, and an approximation can be used to reduce the computing cost. The commonly used technique is based on a so-called *multipole expansion* and the approximate expressions for the components of induced velocities given by equations (2-22), (2-23) and (2-24) can be written [64] as

$$V_x = -\frac{\partial \phi}{\partial x} = -[Aw_1 + \frac{1}{2} I_{xx} w_4 + I_{xy} w_5 + \frac{1}{2} I_{yy} w_6] \qquad 2\text{-}28$$

$$V_y = -\frac{\partial \phi}{\partial y} = -[Aw_2 + \frac{1}{2} I_{xx} w_5 + I_{xy} w_6 + \frac{1}{2} I_{yy} w_7] \qquad 2\text{-}29$$

$$V_z = -\frac{\partial \phi}{\partial z} = -[Aw_3 + \frac{1}{2} I_{xx} w_8 + I_{xy} w_7 + \frac{1}{2} I_{yy} w_{10}] \qquad 2\text{-}30$$

where

$$r_o = \sqrt{x^2 + y^2 + z^2}$$

$$P = y^2 + z^2 - 4x^2$$

$$Q = x^2 + z^2 - 4y^2$$

$$w_1 = -x\, r_o^{-3}$$

$$w_2 = -y\, r_o^{-3}$$

$$w_3 = -z\, r_o^{-3}$$

$$w_4 = 3x\,(3P + 10x^2)\, r_o^{-7}$$

$$w_5 = 3y\, P\, r_o^{-7}$$

$$w_6 = 3x\, Q\, r_o^{-7}$$

$$w_7 = 3y\,(3Q + 10y^2)\, r_o^{-7}$$

$$w_8 = 3z\, P\, r_o^{-7}$$

$$w_9 = -\,15\, x\, y\, z\, r_o^{-7}$$

$$w_{10} = 3\, z\, Q\, r_o^{-7}$$

$$I_{xx} = 1/12\,(\xi_3 - \xi_1)\,[\,\eta_1(\xi_4 - \xi_2)(\xi_1 + \xi_2 + \xi_3 + \xi_4) + (\eta_2 - \eta_4)(\xi_1^2 + \xi_1\xi_3 + \xi_3^2) + \xi_2\eta_2(\xi_1 + \xi_2 + \xi_3) - \xi_4\eta_4(\xi_1 + \xi_3 + \xi_4)]$$

$$I_{xy} = 1/24\,(\xi_3 - \xi_1)\,[\,2\xi_4(\eta_1^2 - \eta_4^2) - 2\xi_2(\eta_1^2 - \eta_2^2) + (\xi_1 + \xi_3)(\eta_2 - \eta_4) + (\xi_1 + \xi_3)(\eta_2 - \eta_4)(2\eta_1 + \eta_2 + \eta_4)$$

$$I_{yy} = 1/12(\xi_3 - \xi_1)(\eta_2 - \eta_4)\,[(\eta_1 + \eta_2 + \eta_4)^2 - \eta_1(\eta_2 + \eta_4) - \eta_2\eta_4)$$

If the field point at which it is required to determine the induced potential or velocity is further from the centroid of a panel element than approximately four times the largest dimension of the element then the element may be approximated to good degree of accuracy by a point source plus a point dipole placed at the element's centroid (see reference [64]) . Since the dipole moments of the quadrilateral with respect to the element's origin (i.e the location of its centroid in the element's local co-ordinate system) are zero then the approximated velocity components are as given by equations (2-28), (2-29) and (2-30). By retaining the first terms only, to reduce the computation time but still retain a good degree of accuracy, the above equations may be written in the element local co-ordinate system as

$$V_x = A\, r_o^{-3}\, (x_n - x_o) \qquad 2\text{-}31$$

$$V_y = A\, r_o^{-3}\, (y_n - y_o) \qquad 2\text{-}32$$

$$V_z = A\, r_o^{-3}\, (z_n - z_o) \qquad 2\text{-}33$$

where x_n, y_n and z_n are the element local ordinates of the panel element control point which is referred to as the null point. The null point is described next

2.3.6 Determination of the Null Point of a Planar Quadrilateral Panel Element

The null point is the point of a quadrilateral element at which the induced velocities are to be computed (and also the point where the surface normal-velocity boundary conditions are to be applied) and is thus called because it is the point where the element itself induces no velocity in its own plane. The co-ordinates (x,y) of the null point in the element co-ordinate system are obtained from the solution of the nonlinear equations :

$$V_x(x,y) = 0 \qquad 2\text{-}34$$

$$V_y(x,y) = 0 \qquad 2\text{-}35$$

where V_x and V_y are the velocities given by equations (2-25) and (2-26). These equations are solved by an iterative procedure which utilises analytic expressions for the derivatives of V_x and V_y, as in reference [64].

2.4 Computer Programme

The principal aim of this section is to describe the essential computational details of the computer programme written during the present work capable of predicting three-dimensional incompressible potential flow on high-speed ground vehicles, and applied to an EMS train model. The section includes remarks on how to define the shape of the body to be analysed; a summary of the computing procedure and a general description of the computer programme.

2.4.1 Defining the Shape of the Body Surface

The basic input to the computer programme for predicting three-dimensional potential flow consists of the body surface about which the flow is to be computed. The body is defined by a set of input points in the global cartesian co-ordinate system. The points are placed in groups of four and connected by straight lines to produce quadrilateral peripheries which in general are not planar. In the present work the set of input points for an EMS model are obtained from the blue-print drawing produced by British Rail [61] . A simple computer programme has been written to generate the body surface configuration panels in three dimensions with each node defined by a three-dimensional co-ordinate. It is important to draw and inspect the geometry generated for the body before proceeding further to insure that all the co-ordinates and the panels generated are correct and well proportioned. A software package for finite element modelling and analysis (PAFEC [76]) has been used to draw the element distribution on the surface of the body ; this helps to check the element formation, distributions and node positions, and thus allows the geometry of the EMS train model to be checked. The first step before proceeding to the computation is to inspect the body surface for symmetry, because if the body has planes of symmetry only the non-redundant portion of the body need be input. The other portions are generated by reflecting the input in the plane of symmetry. Reflection planes are useful in reducing storage requirements and computing time, bearing in mind that for a ground vehicle an image model beneath the vehicle makes the problem symmetric with respect to the ground plane. The second step is to approximate the basic portion of the body by a set of cartesian co-ordinates lying on the surface of the body and to join these points by straight lines to form the elements. The element distribution on the surface of the body should be concentrated in regions where the freestrean flow perturbation are expected to be high and sparsely distributed in regions where this is expected not to be so. Thus, for an EMS train model most of the elements should be distributed over the nose and just behind it, where it is joined to the main body of the train. The elements should be quadrilateral, however a triangular element can be formed if required as a degenerate quadrilateral by choosing one vertex of the quadrilateral element to lie midway along a side of the triangle or by enforcing the last two vertices to coincide (the latter method is preferable, see Figure 2-7). When all the element generation on the surface of the body is complete the model is plotted to ensure that all the elements generated are correct and well defined.

2.4.2 Description of the Computing Procedure for External Flow

In this section a brief summary is presented of the principal details of the panel method used to compute the three-dimensional potential flow velocity and pressure on the surface of an EMS train model for different flow situations. As the method closely follows that of Hess et al. [64], the presentation here is in a somewhat abbreviated form.

The first step is to determine the velocity induced at each point due to a unit source strength present at each element on the surface of the body. In the description that follows it is convenient to consider the velocity induced at the i-th point due to the j-th element. Before it is possible to determine the velocity that this element induces at the i-th point we must find the distance between the point i and the source point in the element j. This is to establish the computationally cheapest formulae to use for good accuracy.

Assuming that all the element properties in its local co-ordinate system are known (see Appendix B), the first step is to compute the distance (r_o) between the null point (x_n,y_n,z_n) of the i-th element and the origin (x_o,y_o,z_o) of the j-th element :

$$r_o = \sqrt{(x_n - x_o)^2 + (y_n - y_o)^2 + (z_n - z_o)^2}$$

Then the ratio between r_o and the maximum diagonal length of the j-th element, T_{max}, (see section 2.3) is

$$R_m = \frac{r_o}{T_{max}}$$

The value of R_m is then compared with a prescribed number, which is customarily set equal to 4, see [64], or another number usually determined by user experience (this prescribed number does not effect the accuracy of the results in any significant way but is chosen to reduce the CPU time).

If $R_m > 4$ then the j-th element is approximated by a point source at its origin (i.e. its centroid) of its local co-ordinate system and the velocities it induces at the i-th point can be calculated using equations (2-31), (2-32) and (2-33) which are good approximate solutions.

If $R_m < 4$ then R_m is further compared with another prescribed number (namely, 2.45 (see reference [64])) and for the same reasons explained earlier i.e CPU time reduction) a further two stage approximation is implemented.

If $R_m \geq 2.45$ then the j-th element is approximated by a point source plus a point of a quadripole at the origin of its co-ordinate then equations (2-28),(2-29) and (2-30) can be used to calculate the induced velocity.

If $R_m < 2.45$ then the exact formulae (2-25), (2-26) and (2-27) are used to calculate the velocity.

In all the above cases the calculated velocities are then transformed from the element co-ordinate system to the global co-ordinate system.

When all the velocities have been calculated i.e for all combinations of points i and element j , then the components, V_{ij}, of the velocity matrix [V] are known. The normal velocity induced at the null point of the i-th element is obtained by taking the dot product of the induced velocity vector of the i-th element $\mathbf{V}_{ij}$ and the unit normal vector $\mathbf{n}$ of the i-th element

i.e

$$A_{ij} = \mathbf{n}_i \cdot \mathbf{V}_{ij} \qquad 2\text{-}36$$

The normal component of the onset flow, $\mathbf{V}_{\infty n}$, at the i-th null point is the dot product of the normal unit vector, $\mathbf{n}_i$, and the onset flow velocity, $\mathbf{V}_\infty$, i.e

$$\mathbf{V}_{\infty n} = \mathbf{n}_i \cdot \mathbf{V}_\infty \qquad 2\text{–}37$$

The total normal velocity at the i-th point is obtained by a sum of equations (2-36) and(2-37), in other words at all control points on the approximating body surface the velocity component normal to the surface of the body is to be desired zero, that is

$$\sum_{j=1}^{N} A_{ij}\sigma_j = -\mathbf{n}_i \cdot \mathbf{V}_\infty \qquad i=1,2,\ldots,N \qquad 2\text{-}38$$

The only unknowns in the equation (2-38) are the source strengths σ_j. Equations (2-38) represents a set of simultaneous linear algebraic equations with N unknown source strengths. When the solution to this system of equations is found, the velocity at the i-th point is found by

$$\mathbf{V}_i = \sum_{j=1}^{N} \mathbf{V}_{ij}\sigma_j + \mathbf{V}_\infty \qquad 2\text{–}39$$

i.e. summing the velocities induced at it by all the other elements including itself and superimposing the onset flow. Finally, the pressure coefficient at the field point i is

$$C_P = 1 - \frac{V_i^2}{V_\infty^2} \qquad 2\text{-}40$$

2.4.3 General Description of the Computer Programme

A computer programme called POTOFLO based on the theory described in sections 2-3 has been developed for predicting the three-dimensional incompressible potential flow around an arbitrary shape. This is capable of representing the body surface and determining the source strengths, velocity and pressure coefficients at each null point of the panel elements. A brief description of the programme POTOFLO is presented in this section. Programme POTOFLO, whose block diagram is shown in Figure 2-8, accepts input data which includes the number of panels that cover the surface of the body and the co-ordinates of their vertices and the yaw angle. The programme analyses all the elements in turn. For each element the induced velocity at the null point due to the other elements is computed. The programme starts by calling subroutine LCHECK which checks that the ratio of the element diagonals, or altitude to the base for a triangle panel, does not exceed a value of thirty to ensure that the procedure for calculating the null point will converge. Then the programme starts to generate the element co-ordinates, in the element local co-ordinate system; the associated transformation matrix; the normal unit vector for the element; the centroid of the element and the length of the longer diagonal of the element. Subroutine NILP is then called : it uses an iterative procedure mentioned in sub-section 2.3.6 to find the co-ordinates of each null point in the global co-ordinate system. The computation then proceeds to call VELCAl, determines the velocity vector by calculating the velocity induced at the i-th element due to a unit source strength at the j-th element using the procedure discussed in sub-section 2.3.5. The resulting system of simultaneous linear algebraic equations is solved numerically by subroutine SOLEQ. The source strengths are then known, and the programme then calculates the velocities and pressure coefficients.

2.5 Test Problems

This section describes the results for some test problems employed to check the functionality of the computer programmes developed for predicting potential flow using the panel method. Initial tests were made for two-dimensional flows using a convienient modification of the method described above (see Appendix A) ; this code was then extended to the full general method of section 2.3 to allow three-dimensional flow to be simulated. The computer programme for two-dimensional flow is named TWODP and that for three-dimensional flow is POTOFLO. The remainder of this section is in three parts. The first two sections 2.5.1 (flow past a single cylinder) and 2.5.2 (two cylinders passing each other), concern test problems involving programme TWODP while the last part in section 2.5.3 (pressure distribution on sphere) concerns programme POTOFLO.

2.5.1 Flow Past a Single Cylinder

Programme TWODP for two-dimensional flow has been applied to the potential flow over a single cylinder for which there is a well known exact analytical solution.

The potential flow pressure distribution on an isolated single cylinder moving in a fluid is well established theoretically. For a single cylinder in potential flow, moving with a velocity of magnitude V_∞, the velocity at any point on the surface of the cylinder is $2V_\infty \sin\theta$ [77] and the pressure coefficient is given by

$$C_p = \frac{P - P^2_\infty}{\frac{1}{2}\rho V^2_\infty} = 1 - 4\sin^2\theta \qquad 2\text{–}41$$

where

θ is the angle measured between the direction of the parallel flow, and the point of interest on the surface of the cylinder and

P is the pressure at the point of interest

This analytical solution is shown together with the corresponding results predicted by the computer programme TWODP in Figure 2-9. For the test, a single circular cross section cylinder with a unit radius and a unit free stream velocity has been used. The surface of the cylinder was divided into 20 elements in the first instance of the test and 40 elements in the second instance. Both discretisations gave essentially identical solutions for the pressure field and the figure shows results for 40 elements. The velocities and the pressure were evaluated by TWODP at the centre of each of the elements. It is seen that the agreement between the analytical and TWODP prediction are, as expected for this simple case, excellent.

2.5.2 Two Cylinders Passing Each Other

The computer programme TWODP has also been tested for the case of two bodies moving relative to each other. This tests the quasi-steady method described above for calculating C_p coefficients under transient conditions. Here, the case of two right circular cylinders passing each other with their centres located on parallel lines has been chosen to check the accuracy of the programme. This problem has previously been investigated by Kawaguti [78]. As a first approximation he replaced the cylinders by doublets then, by considering the images of these doublets in the two cylinders, he proceeded to a higher order approximation. He arrived at a series solution by summing the potential due to each of the doublets and their images. The accuracy of the solution depends on the number of the terms of the series considered; he gave the solution to a fifth order approximation. The programme TWODP has been applied to the same problem. Figure 2-10 shows the time history of pressure at point A on one of the cylinders, see Figure 2-10, when the two circular cylinders have the same radius a. The Figure shows good agreement between the current panel method and the Kawaguti results. It can be seen that ut/a=0 is a critical point and the curve shows a large interference effect when the two cylinders are close together. This demonstrates the ability of the quasi-steady approximation to solve this type of unsteady problem and provides confidence in the method's possible use to solve EMS train problems.

2.5.3 Pressure Distribution on a Sphere

The three-dimensional version of the method, embodied in programme POTOFLO has been applied to predict the three-dimensional potential flow around a body for a flow with a well known analytic solution in order to evaluate the accuracy of its computed pressure coefficients before proceeding with predictions involving the EMS train model. The flow around a sphere was chosen as the basic three-dimensional test case.

The potential function for axisymmetric irrotational flow past a sphere is a combination of a doublet and uniform flow [77]. The pressure coefficient on the surface of the sphere may be written [77] :

$$C_p = 1 - \frac{9}{4}\sin^2\theta \qquad 2\text{–}42$$

where

θ is the angle measured from the direction of the parallel flow to a point on the surface of the sphere, as indicated in Figure 2-11.

A series of numerical computations have been performed for this case using various numbers of elements to approximate the surface to examine numerical accuracy aspects. The distribution of the elements in all cases is similar to that shown in Figure 2-12. The results for two cases are shown in Figures 2-13 and 2-14. The first case used 100 elements and three reflection planes, while the second case used 169 elements and three reflection planes (these are equivalent to approximating the entire surface of the sphere by 800 and 1352 elements respectively). The Figures show the comparison of the analytic solution, (equation 2-42), and the POTOFLO predicted pressure coefficient versus the angle for an onset flow parallel to the x-axis for points in the xz and xy plane, see Figure 2-11. Both sets of results computed by programme POTOFLO are in good agreement with the analytic results and give a maximum error of 0.01%. Figure 2-15 presents results for conditions similar to those of Figures 2-13 and 2-14 except that the onset flow is parallel to the y-axis and the results are for flow at points in the yz plane, see Figure 2-11. The computed results and the analytical results are again in good agreement. These tests provide confidence that the three-dimensional method has been coded correctly.

Before applying the programme to a train case it is useful and interesting to compare a sample of results from the computer programme POTOFLO and the computer programme used by Morrow [37], in order to gain some idea of their relative accuracy. The results of the pressure coefficient distributions calculated by both computer programmes have been compared for the flow over a sphere. For this comparison 81 basic elements and three reflection planes (the element distribution on the surface of the sphere is similar to that shown in Figure 2-12). This element distribution is similar to that used by Morrow [37] and is equivalent to approximating the entire surface of the sphere by 648 elements. The predicted results were for a freestream parallel to the x-axis. Figure 2-16 and Figure 2-17 show the variation of the predicted pressure distribution with angle θ on the surface of the sphere for the x-y and y-z planes, respectively. The Figures show that, for this test case, although both results lie close to the analytical solution, the results predicted by the programme POTOFLO are more accurate than those predicted by the programme used by Morrow particularly at large values of θ because the numerical techniques used to find the control points and to solve the simultaneous equations are different.

2.6 Applications

The application of the tested computer programmes for two- and three-dimensional potential flow to problems of interest in railway engineering are presented in this section. Section 2.6.1 discusses the application of the two-dimensional flow programme TWODP to the prediction of pressure pulses when two bodies of non-simple shape pass each other. The remaining parts, section 2.6.2-2.6.4, concern the use of programme POTOFL to predict the three-dimensional pressure distribution on the surface of EMS train models in typical cases found in practice. These include an EMS model in open air (section 2.6.2) an EMS model passing a railway station (section 2.6.3) and an EMS train model passing the central section of another EMS train model (2.6.4). The latter two applications have been chosen to evaluate and demonstrate to the reader the capability of the computer programme POTOFLO to predict not only potential flow on a single body but also its capability for multi-body problems.

2.6.1 Pressure Pulses when Two Bodies are Passing Each Other

The two-dimensional computer programme TWODP for potential flow, has been used to study numerically the case where two bodies are considered to be moving past each other with equal and opposite velocities, V_A and $-V_B$. In this case the pressure pulse is predicted for the point designated a located on the front of body A and facing body B, see Figure 2-18. The two-dimensional idealisation for each body is taken as being the plan view contour of an EMS train shape as shown in Figure 2-18. It must be emphasised however that the two-dimensional assumption means that the results of this section must be interpreted with some caution since the pressure pulses on real three-dimensional shapes will be different to those on infinite long two-dimensional shapes whose cross-section has the same plan view. These results form at best an extreme estimate and are included more for illustrative purposes. A total of 200 elements have been used to simulate the two trains (100 elements per plan profile). Figure 2-19 shows the time history of the pressure wave predicted by TWODP at point a. When the effect of B is weak the value of C_p at point a was -0.6. As the two bodies approach each other, at a rate depending on the closing velocity, the mutual interference due to the two bodies begins to relieve the suction pressure. As the head of body B passes point a on body A, this relief effect decreases until, by the time the two bodies completely overlap each other, the suction pressure has again increased reaching a peak C_p value of nearly -1.5. As stated above, these results are of interest only as a precursor to performing this type of calculation for a real three-dimensional train shape.

2.6.2 EMS Train Model in the Open Air

The first application of the computer programme POTOFLO was to predict the three-dimensional pressure distribution on the surface of an EMS train model moving in open still air. The external surface of the model was obtained from the basic layout drawing proposed by Science and Engineering Research Council and the British Railway Board, [61] and is shown in Figures 1-1, 1-2, and 1-3.

To simplify the presentation of the results obtained by the computer programme POTOFLO on the EMS train model, the model has been divided into thirteen sections as identified by the letters, A to M, each section representing an x/d_e ratio where x is the distance along the train centre-line from the tip of the nose. If $x/d_e<1.0$ the term, ***nose region*** will to be used, if $1.0>x/d_e>2.0$ the term ***after the nose*** is employed, and if $x/d_e>2.0$ the term ***far away from the nose*** is applied, see Figures 2-20, 2-21, 2-22 and table 2-1.

Working from the dimensions given on the drawing, a set of 563 elements was chosen to cover one-quarter of the surface of the model as shown in Figure 2-21. Three reflection planes were used to generate a full EMS train model including an image model beneath it to simulate the ground. The POTOFLO programme was then used to compute the potential flow at five different yaw angles (0°, 5°, 10°, 15° and 90°).

Figure 2-23 shows the pressure coefficient distribution near the centre line of an EMS model for zero yaw angle. It is seen that significant changes in pressure coefficient occur at the nose region, namely on the sections A, B, C and D of the model, as expected, see Figure 2-22. These sharp changes in the pressure values at the nose may be expected in the real case to lead to separation on the top of the roof of the train and on the tip of the nose. Moving away from the nose of the train the negative value of the pressure coefficient increases to a value close to atmospheric pressure (this leads to the expectation that the flow may well be attached throughout this region).

Figures 2-24 and 2-25 show the pressure coefficient for selected sections (A, B and C) in the nose region (i.e $x/d_e<1.0$) at zero yaw angle, see Figure 2-22. The Figures indicate that the changes of pressure coefficient in these sections are significant at the top of the nose and they imply regions of significant adverse pressure gradient exist ; these are also significant on the side corner of the nose (clearly due to sharp corners on the side and shoulder of the nose).

Figure 2-26 shows the pressure coefficient distribution on the region defined as after the nose. The Figure shows that the significant changes in pressure coefficient occur only on the top side of the cross-section.

Figure 2-27 shows the pressure coefficient far from the nose. No significant changes in shape occured as we move away from the nose, the suction values of pressure are gradually relieved, moving closer to atmospheric pressure.

The effect of yaw angle on the pressure coefficient is included in Figures 2-28-2-30 for two yaw angles, 0° and 15°. Figure 2-28 presents results for a centre-line axial profile, while Figure 2-29 and 2-30 indicate circumferential changes. The Figures at yaw angle show that the influence of the yaw angle, i.e. cross flow, is quite strong on the nose and in the after nose region, leading generally to a strengthing of sunction peaks, and even steeper local pressure gradient. It can also be seen that all the significant variation in the pressure occurs on the nose region. As the yaw angle increased a strong suction is noticeable on the upper edge of the lee side on the nose and after nose regions. There is no significant changes far away from the nose. A discussion on the accuracy of these results is defered until after the experimental work has been described.

2.6.3 EMS Train Model Passing a Railway Station Model

The computer programme POTOFLO has also been used for a case where an EMS train passes a simple model of a railway station to predict the pressure surges induced at the station wall, on the train and at various intermediate locations. This analysis has been undertaken to demonstrate the capability of the computer programme POTOFLO to predict unsteady pressure fields in this important example of a railway engineering problem.

The railway station is represented by a block 7m high and 4m wide with a platform 0.9 high and 7.5m long and 1.5m from the the track centre line. Figure 2-31 shows the element distribution on the surfaces of both the train and the railway station. The element distribution is concentrated in the region just ahead and behind the nose of the train and the centre of the station where the pressure is expected to vary rapidly. In actual practice as a train passes a railway station, the train and the railway station are moving relative to each other. In this work both the train model and railway station model are taken to be stationary with respect to the air stream. This is valid because when viscous boundary layers are absent the effect on the pressure distribution on the train nose due to an adjacent infinite constant cross-section body in motion is the same irrespective of the state of motion of the constant cross-section body. The total number of elements used is 760 with two reflections planes; one to simulate the ground and the other to provide the other half of the train. The results of the computations at section D, where the pressure is expected to vary rapidly, see Figure 2-31, are shown in Figure 2-32. The results show the ΔC_p values experienced at several points on the station model and on the train model. The Figure shows a considerable change in the ΔC_p closer to the train. A comparison of this results with a similar problem predicted by

Morrow shows (but for an APT shape [37]) that the both results have the same trend but the EMS shape provides a higher pressure difference close to the track centre line, due to the shape of the cross section of the EMS train while there is no significant change far away from the track centre line and on the wall surface of the station. The prediction shows that more significant pressure coefficient changes occur on the surface of the EMS model. The pressure values are less at the station walls and far away from the track centre line; and the pressure increases as the height above the station increases and that due to the pressure on the nose region is changed; the effect of this changes is not significant far away from the nose. These changes exert an effect on the train forces during passing, these results are beleieved to be reliable because the Morrow results, to which they are very similar, have been compared with full scale tests by another author [65].

2.6.4 EMS Train Model Passing the Central Section of Another EMS Train Model

The computer programme POTOFLO has also been applied to predict the pressure pulses experienced on the sides of an EMS train model caused during the passage of the central section of another EMS train model moving in the opposite direction. This problem has been chosen because it is an important element in the design studies carried out in railway engineering and to demonstrate the capability of the computer programme POTOFLO to solve this class of problem. A set of 700 elements (using just one reflection plane, to include the image model used to simulate the ground) was established to simulate the surface of the two train models, see Figure 2-33. It can be seen from the Figure that more elements were concentrated opposite to the nose and on the nose. This gives better resolution of the pressure variation caused by the nose. Both models are again considered stationary relative to the air stream (see section 2.6.3 where the validity of this approach is discussed).

Figures 2-34 and 2-35 show the variation of pressure coefficient at points A and B, see Figure 2-33. For point A the C_{pmax}= 0.2 and C_{pmin}= -0.2 and for point B the C_{pmax} =

0.19 and C_{pmin}=-0.18. Thus the peak-to-peak measure of the maximum pressure pulse experienced on the side of an EMS model caused by a long EMS model section is approximately 0.40. The magnitude of these peaks, and their duration in time would be invaluable in design studies of passing trains. Comparing the results of Figures 2-34 and 2-35 with those predicted in two-dimensions, Figure 2-19, it is seen that the results of the two-dimensional analysis at a point on the train side display suction higher than those predicted in the three-dimensional results.

2.7 A Comparison of Predicted Distribution of Pressure Coefficient on EMS and Conventional Train Shapes

It is important and of technical interest to compare the pressure coefficient distribution predicted by the present three-dimensional potential flow theory on the EMS train shape with that predicted for a conventional train shape to compare the flow behaviour on both models. This is done in the present section for the EMS shape and an APT shape, considered to represent a more conventional train profile.

Figure 2-36 compares the basic nose profile and element distribution of both EMS train and APT train. The main differences between the two train shapes are the EMS train model has a nose profile slope and sharp edges at the tip and along the side of the nose. Figure 2-37 forms the basis of a comparison of the predicted pressure coefficient distribution on the centre lines of a half-length EMS train and Advanced Passenger (APT) train models (the latter predicted by Morrow [37]). This Figure shows that for both trains most of the changes in the pressure coefficient occurs on the nose of the trains. The Figure also shows that as the flow moves far away from the nose the negative values of the pressure coefficient increase to approach the atmospheric pressure. It is also to be noted from this Figure that the negative values of pressure coefficients dropped on the nose of EMS train model more rapidly than those on the nose of the APT train is due to the presence of the sharp edges on the nose of the EMS train model.

2.8 Concluding Remarks

Summarising remarks from the two-dimensional potential flow method predictions .

1. A two-dimensional panel method capable of predicting inviscid flow over bodies was developed as a precursor to writing the full three-dimensional programme this two-dimensional programme was used as a development exercise and as a test for the prediction in three-dimensions.

Concluding remarks which emerge from the experience obtained by employing the panel-based numerical method for three-dimensional incompressible potential flow on EMS train model may be summarised as follows :

1. Most of the variations in the distribution of pressure coefficient, C_p, occur near the nose of the train, see Figures 2-23 to 2-30. Some of these pressure changes correspond to regions of large adverse pressure gradients. The nose region is thus expected to be a region of separated flow in the real case (a belief that needs to be confirmed and quantified experimentally, to be discussed latter in this thesis).

2. As the transverse section considered moved further down the train, the suction pressures reduce; there is no significant change in the pressure coefficient after about 1.1 equivalent diameters, see Figures 2-23 to 2-30. This suggests that the flow is attached far away from the nose (this again should be confirmed experimentally.)

3. The effect of yaw angle is significant on the nose and just after the nose, and is not significant far away from the nose. The suction in the lee side of the train is increased as the yaw angle increased. Only yaw angles up to 15° could be considered with the current method due to the limitations of this method as explained earlier. The effect of yaw angle is significant in the nose and after nose regions and

a strong suction was noticeable on the upper edge of the lee side of the train. The effect of the yaw is not significant far away from the nose.

4. The computer programme POTOFLO was demonstrated to be applicable in a wide variety of practical railway engineering problems (including some unsteady problems) and gave some encouraging results.

A series of wind tunnel tests are necessary to measure the pressure distribution on the surface of the EMS train model to check the validity and accuracy of the predicted pressure distribution using the panel method, these tests will be presented in a later chapter.

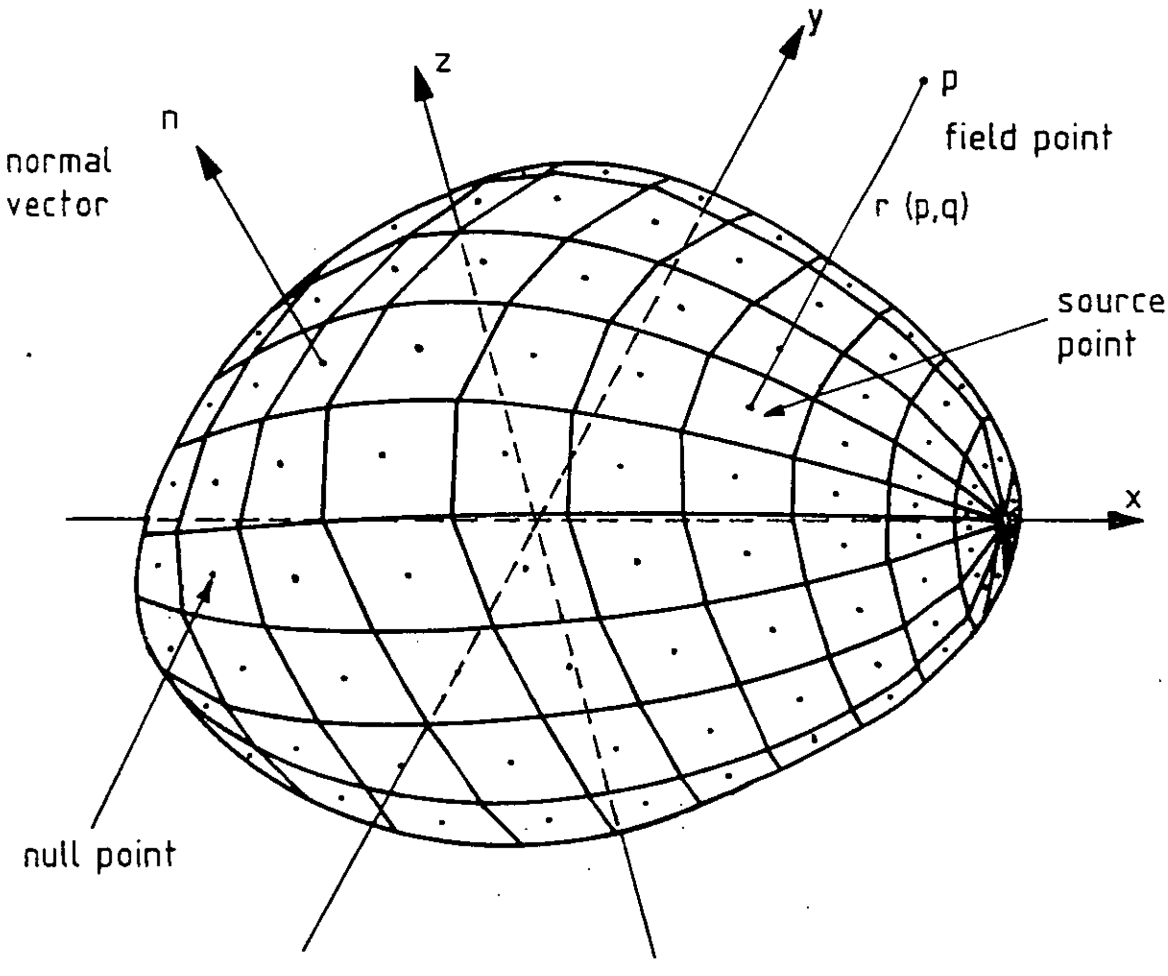

Figure 2-1 Approximation to panel distribution on an arbitrary shape

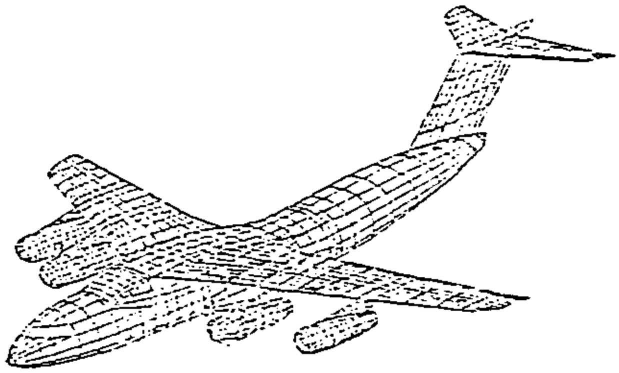

(a) Element distribution on an aircraft
(ref. [40])

(b) Element distribution on an APT train
(ref.[41])

Figure 2-2 Some practical bodies approximated by sets of panel elements.

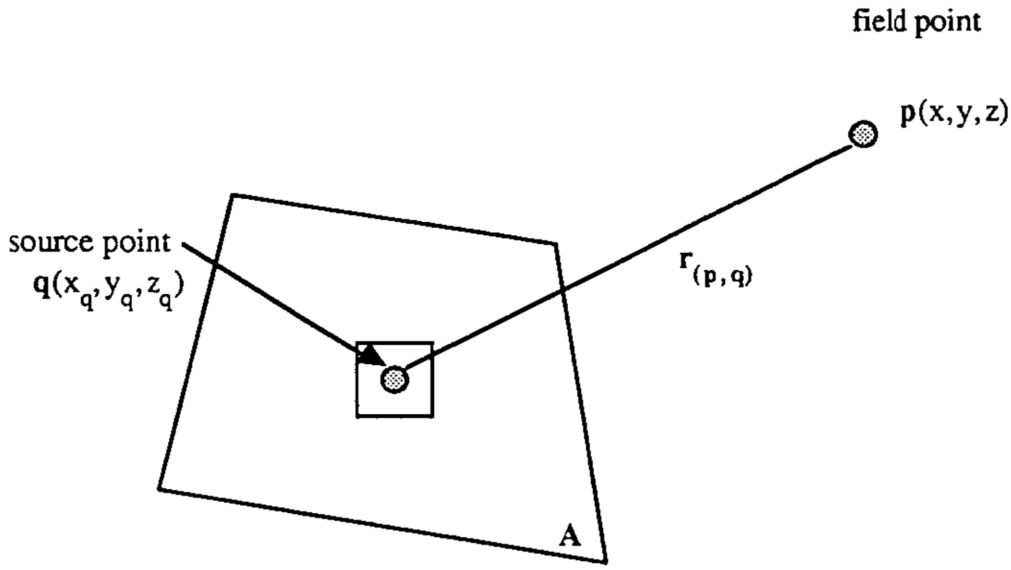

Figure 2-3 A plane quadrilateral source element in an approximated surface

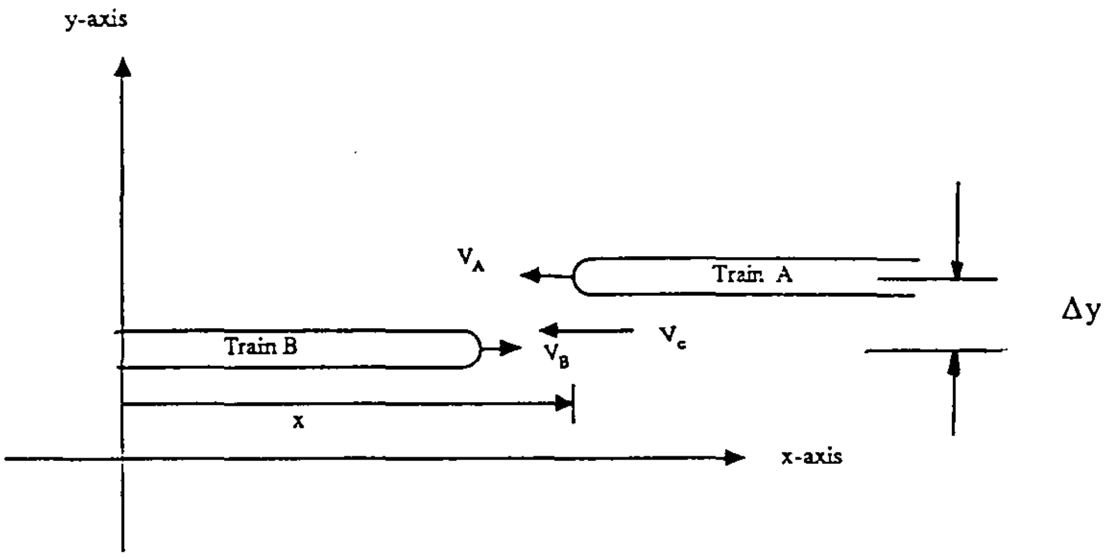

Δy = Lateral separation of train A and B

Figure 2-4 Two EMS trains passing each other

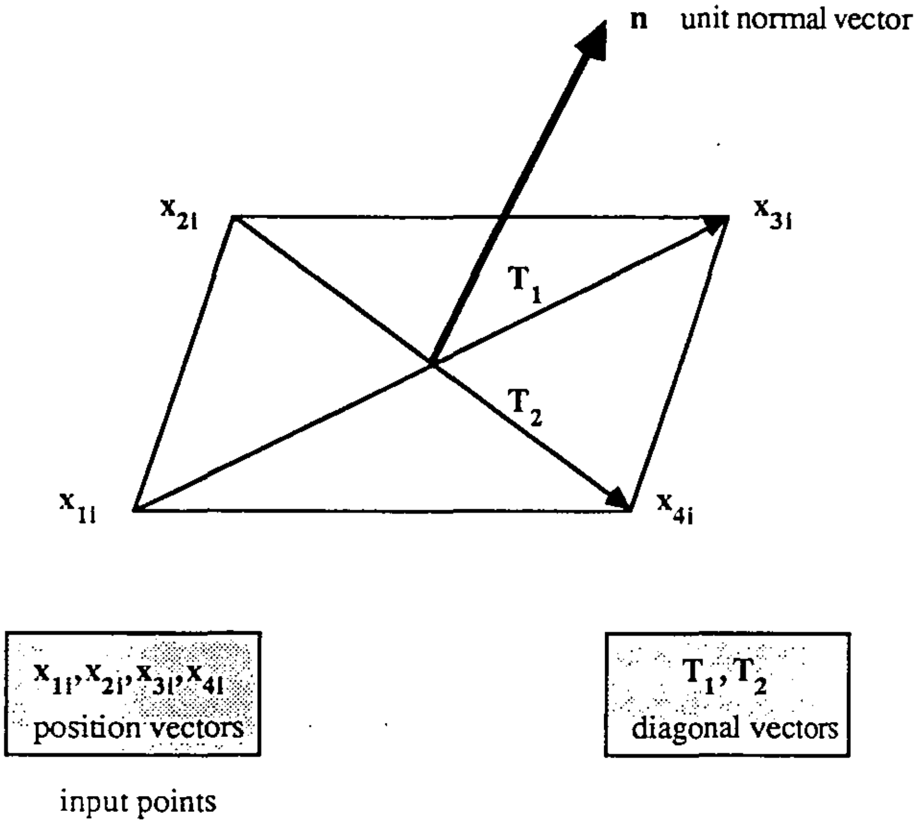

Figure 2-5 The formation of a planar panel element from four input points

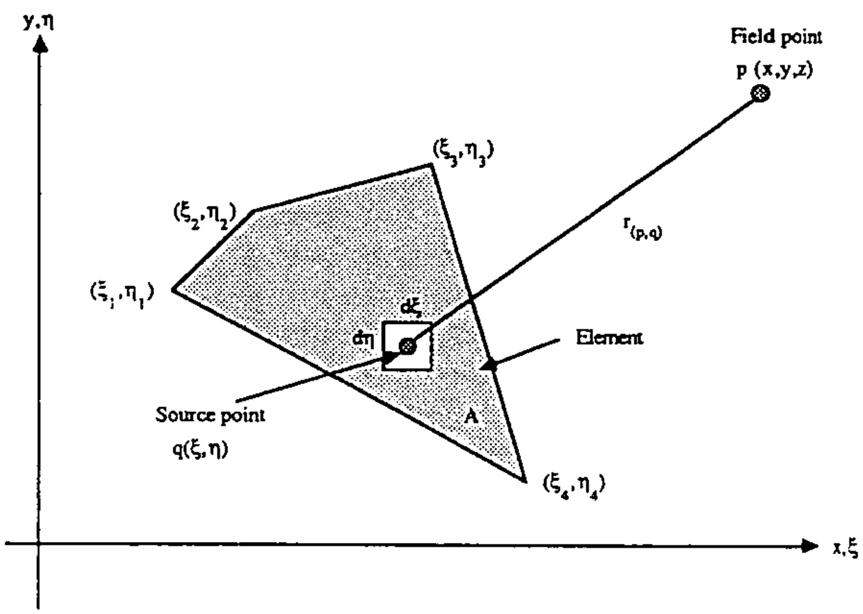

Figure 2-6 Element corners, field point and source point in local co-ordinate system

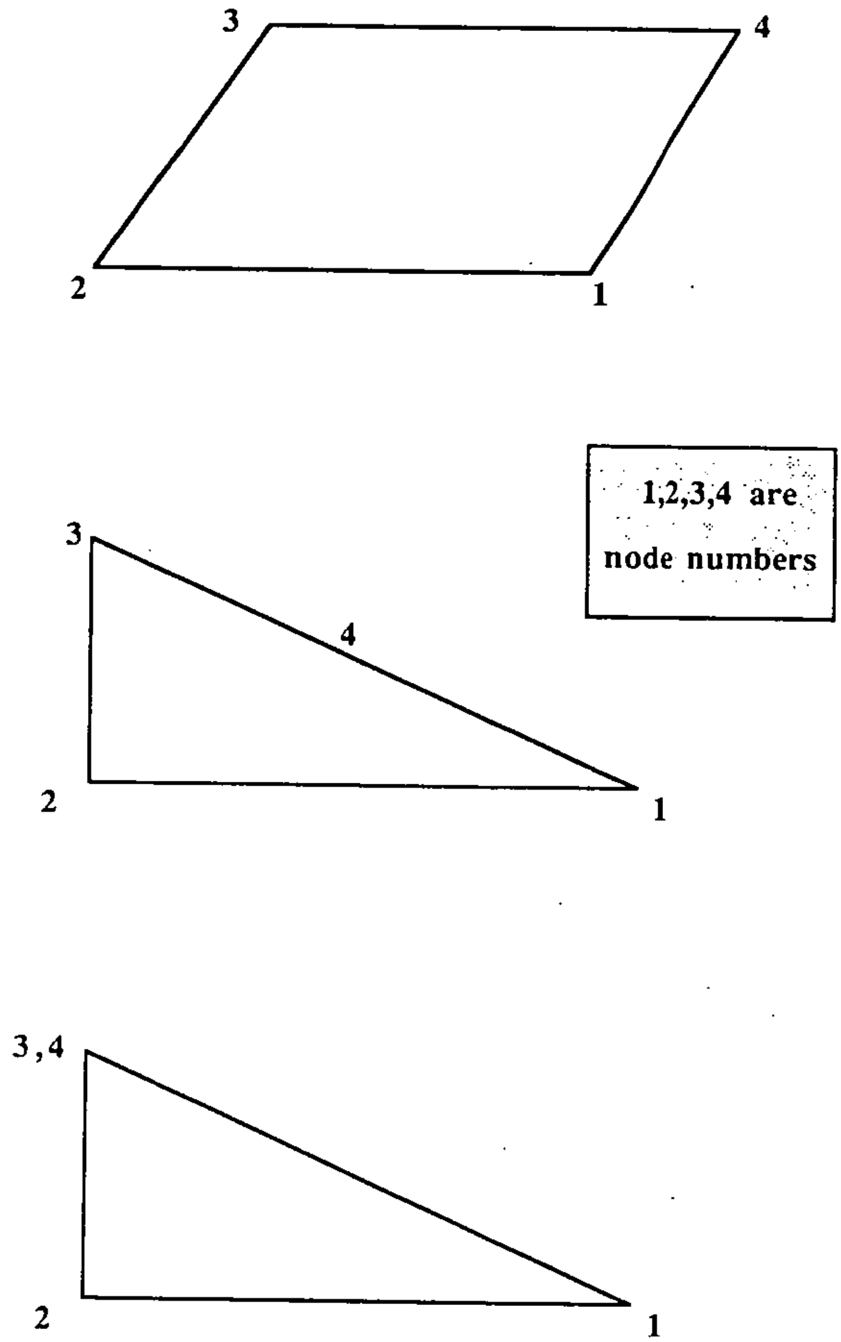

Figure 2-7 The location of input points (nodes) to form a quadrilateral element, with alternative choices for triangular elements

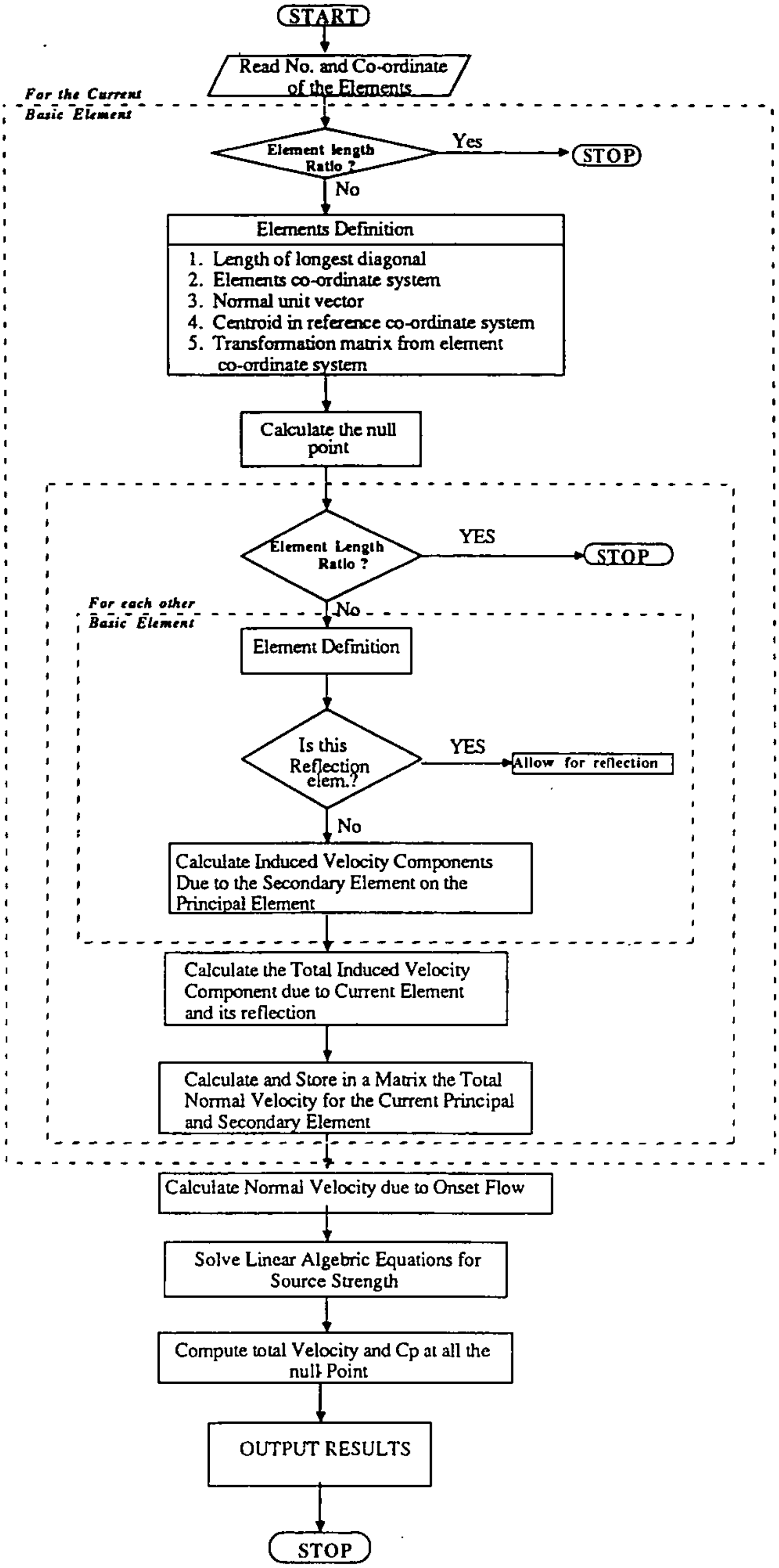

Figure 2-8 Block diagram for programme POTOFLO

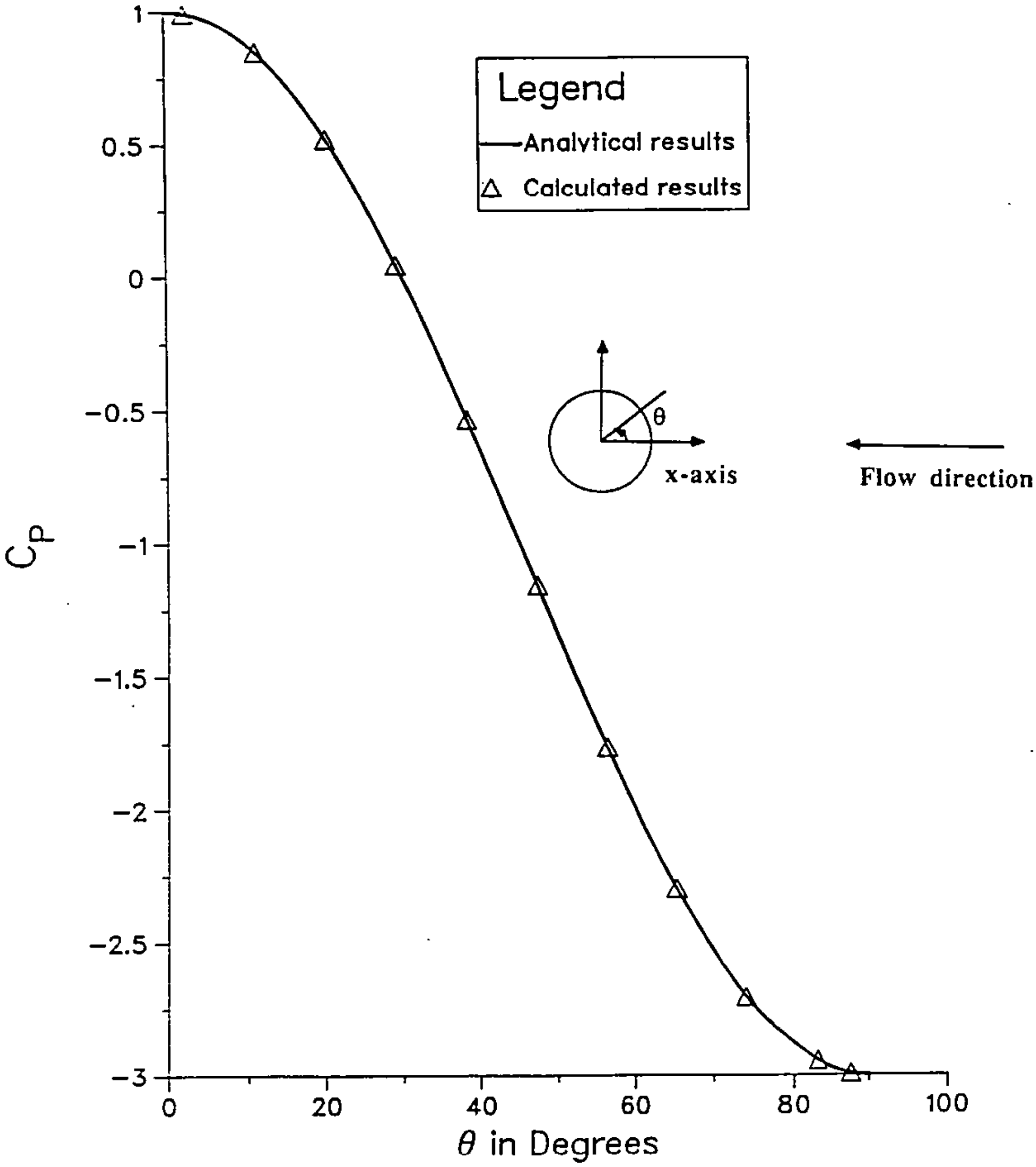

Figure 2-9 Comparison of analytic and panel-method predicted pressure coefficient on a cylinder for an onset flow parallel to the x-axis

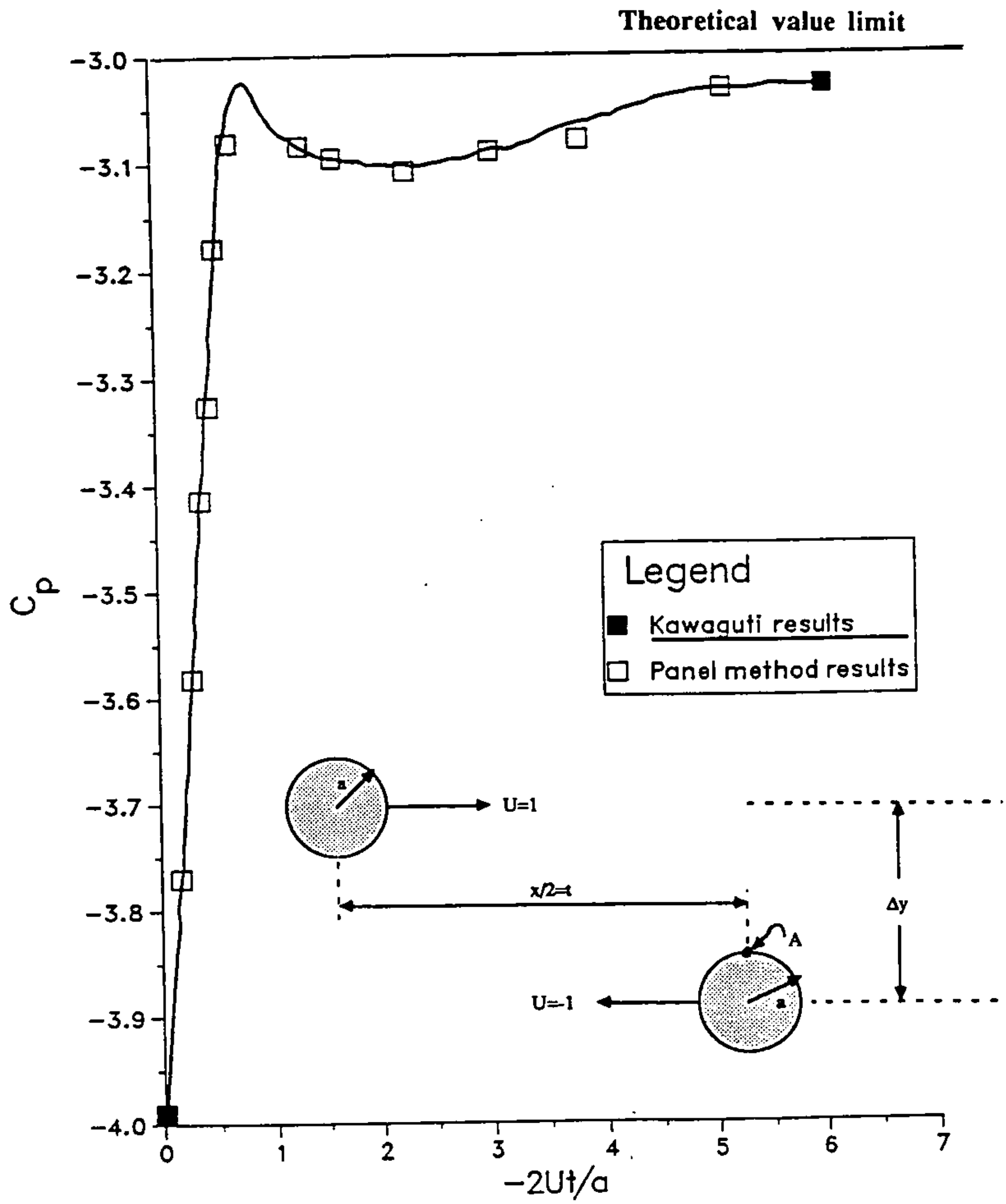

Figure 2-10 Pressure pulses of point A when two cylinders are passing each other.

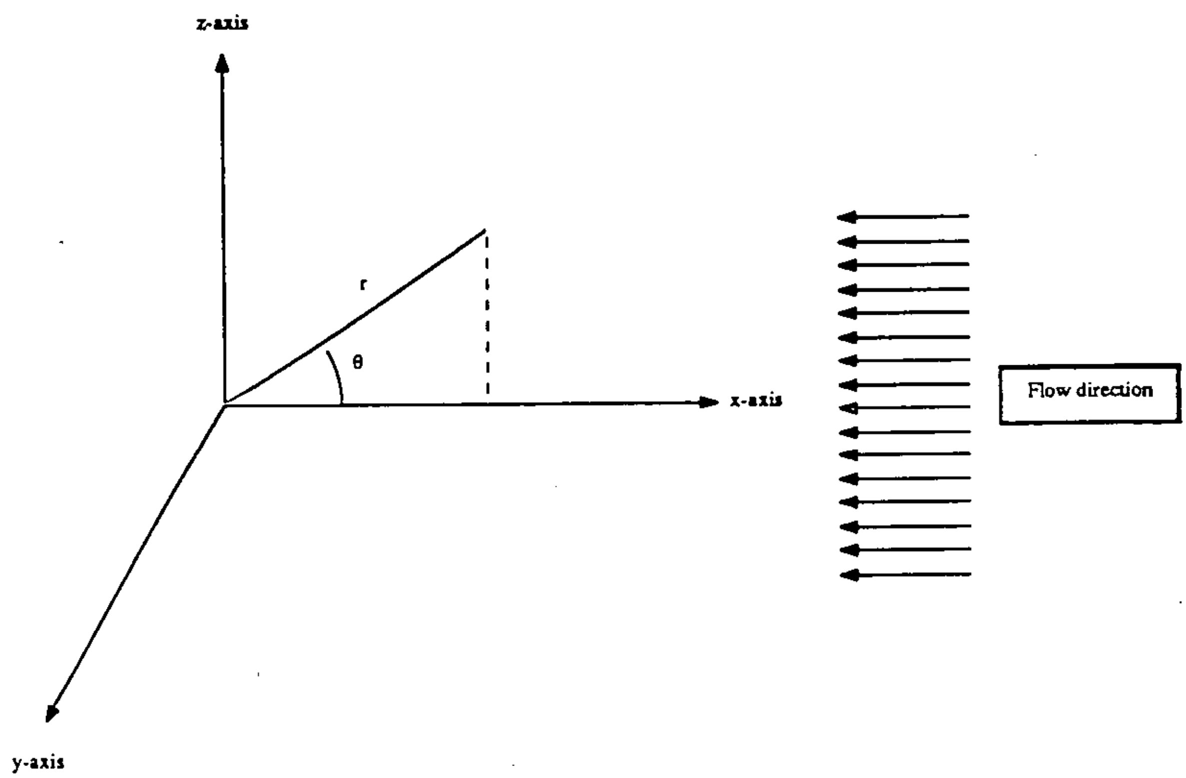

Figure 2-11 Co-ordinate definition for a flow passing a sphere

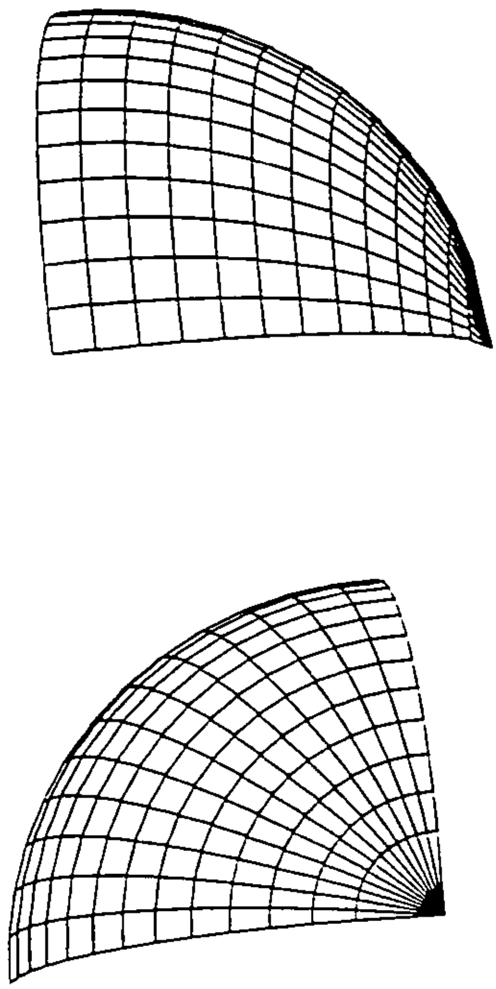

Figure 2-12 Panel element distribution on quadrants on the surface of a sphere

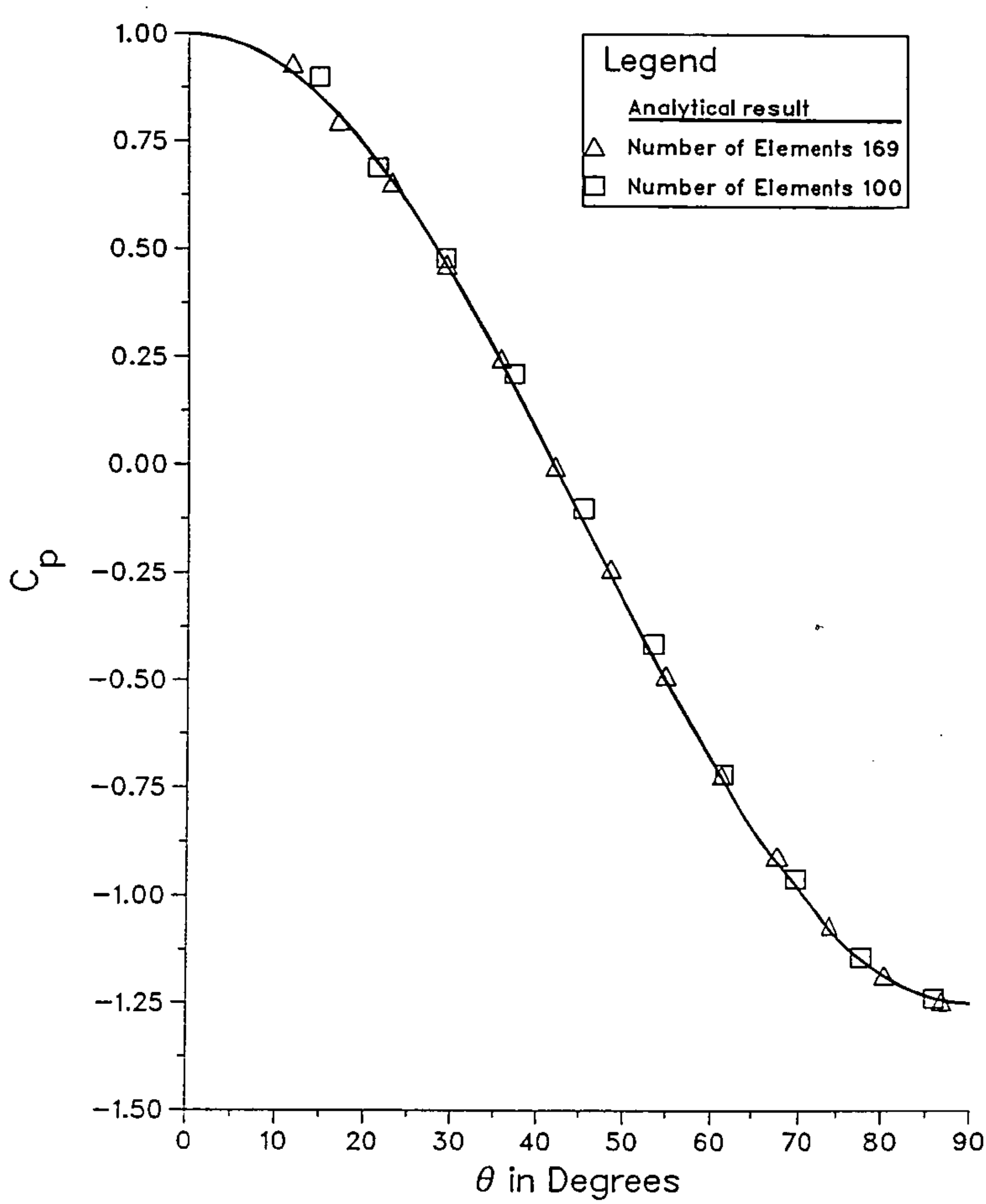

Figure 2-13 Comparison of analytic and panel-method predicted pressure coefficient on a sphere for an onset flow parallel to the x-axis, on the xz-plane

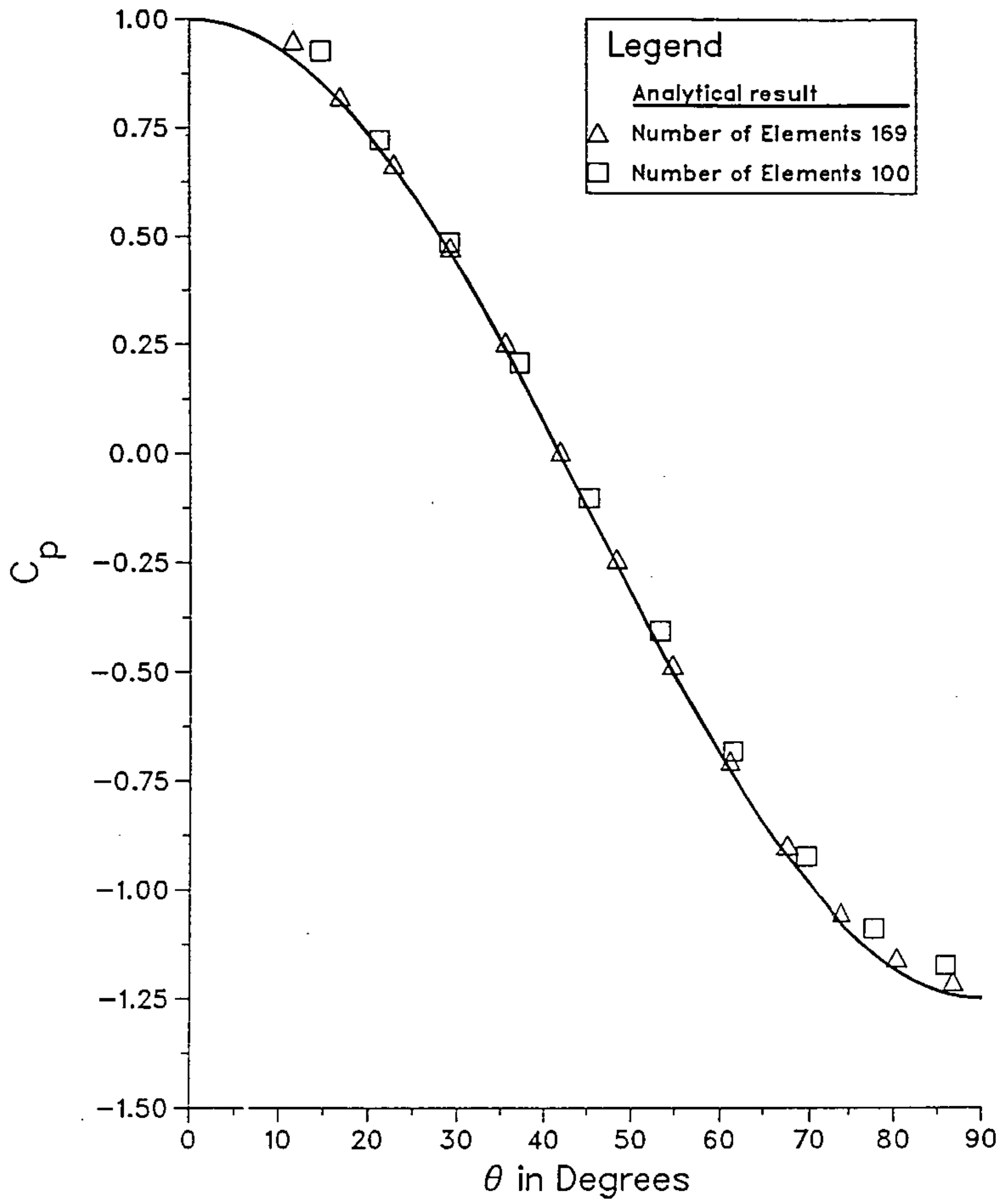

Figure 2-14 Comparison of analytic and panel-method predicted pressure coefficient on a sphere for an onset flow parallel to the x-axis, on the xy-plane

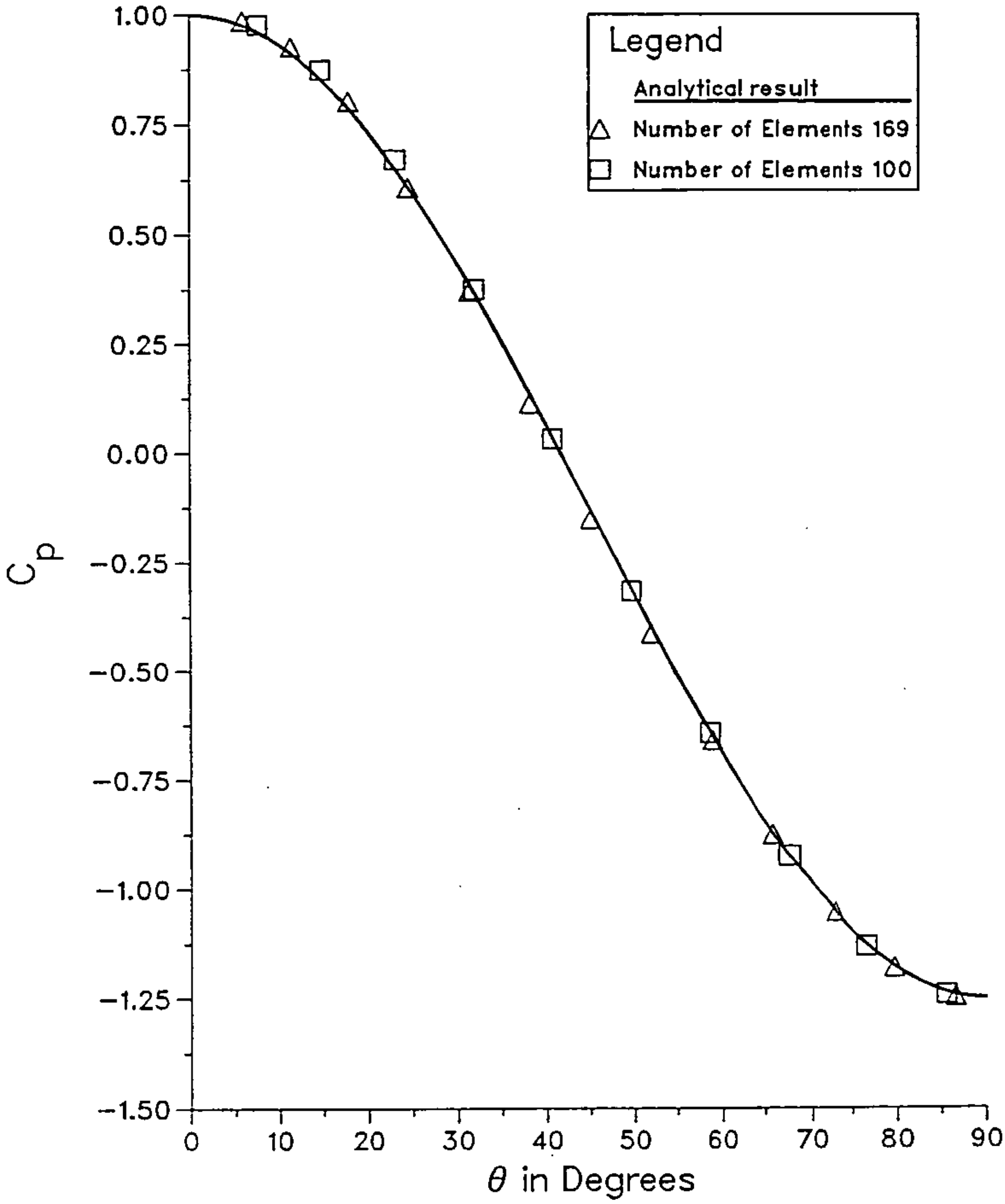

Figure 2-15 Comparison of analytic and panel-method predicted pressure coefficient on a sphere for an onset flow parallel to the y-axis, on the yz-plane

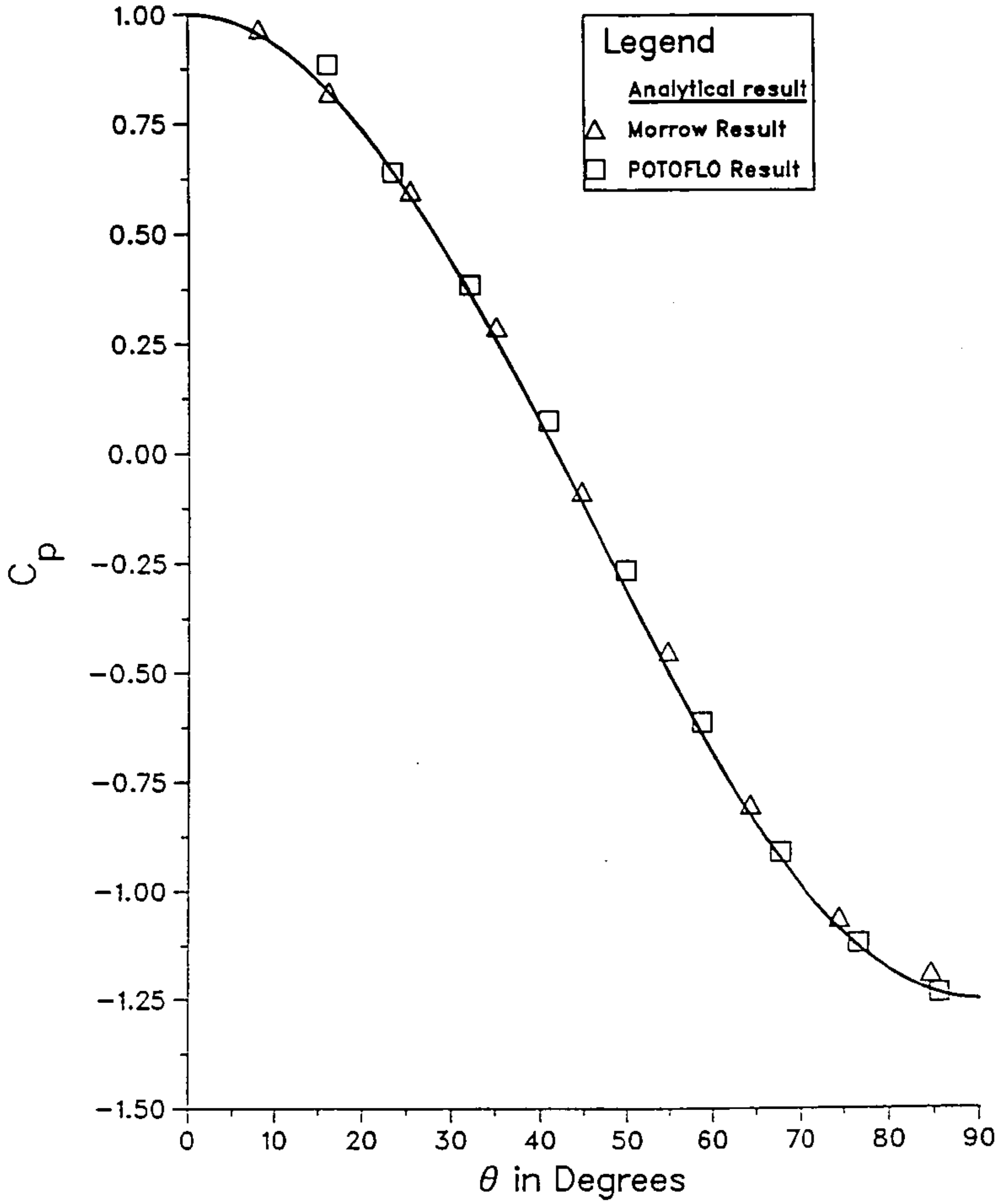

Figure 2-16 Comparison of analytical and Panel-Method based Morrow and POTOFLO results for predicted pressure coefficient on a sphere for an onset flow parallel to the x-axis, on the xy-plane

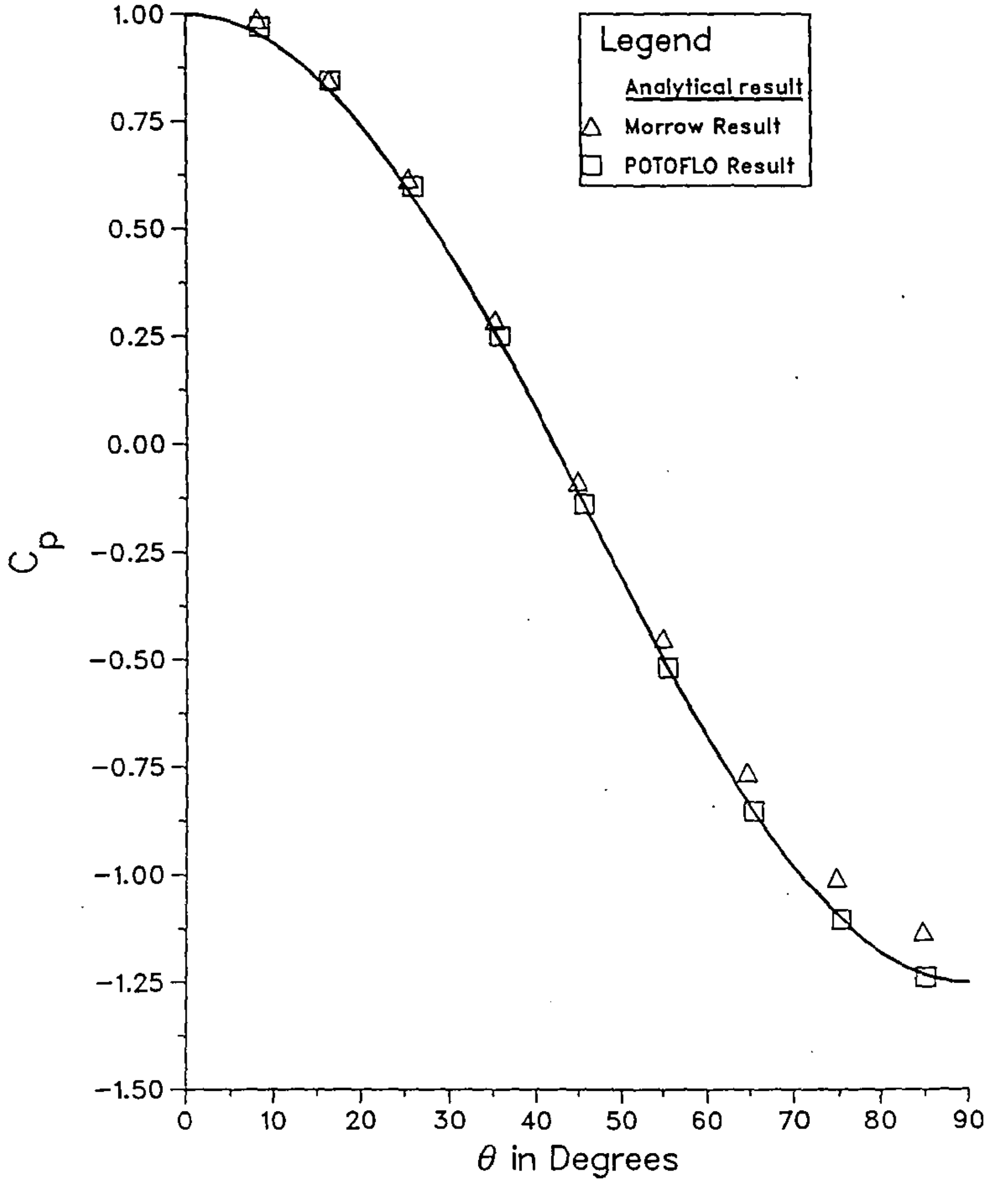

Figure 2-17 Comparison of analytical and Panel-Method based Morrow and POTOFLO results for predicted pressure coefficient on a sphere for an onset flow parallel to the x-axis, on the xz-plane

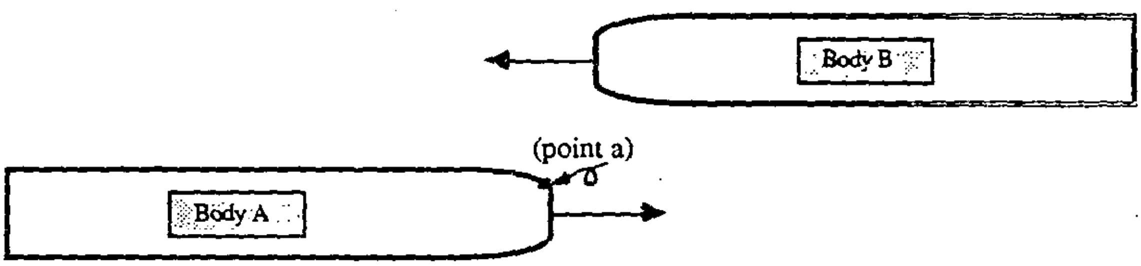

Figure 2-18 Two two-dimensional bodies passing each other. Showing the point a on body A at which pressure pulses are predicted using programme TWODP

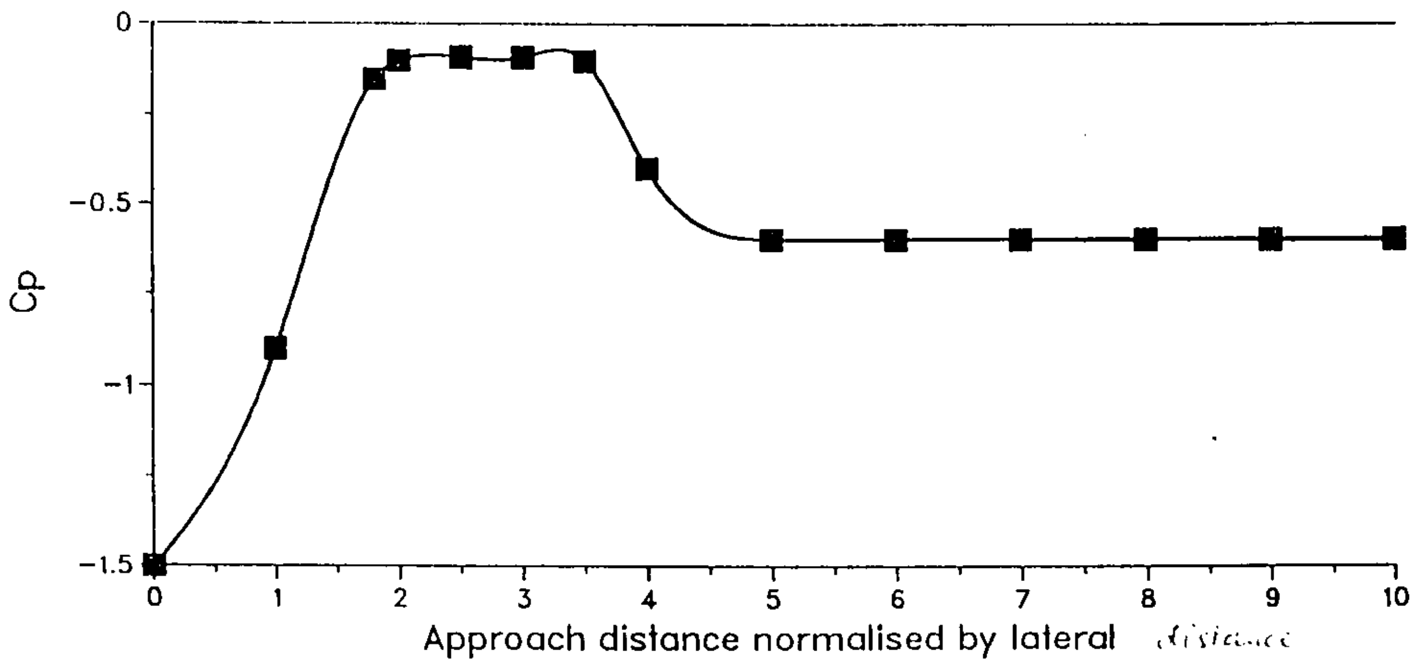

Figure 2-19 Time history of pressure at point a when two bodies are approaching with equal and opposite direction.

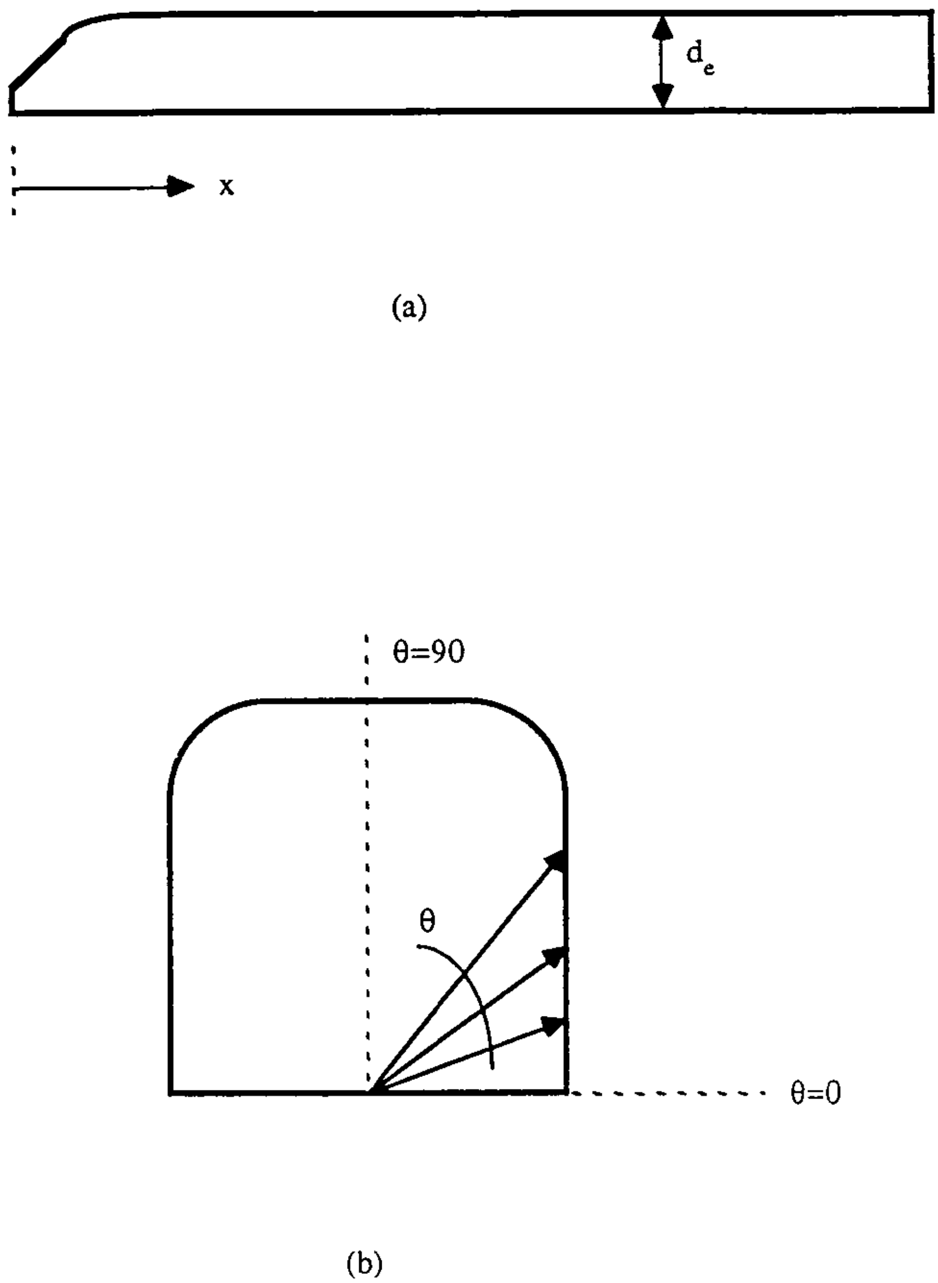

Figure 2-20 Basic parameters used to identify positions along the longitudinal section (a) and transverse section (b) on EMS train model

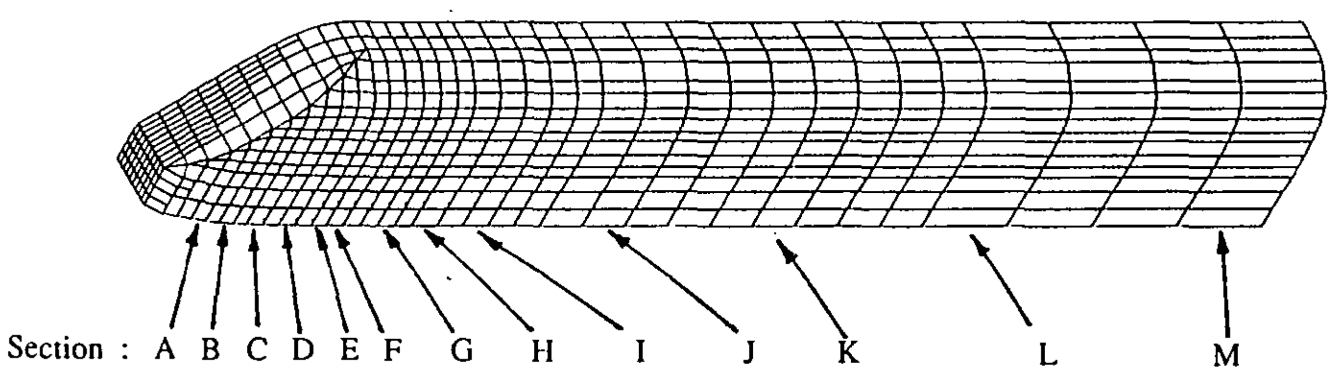

Figure 2-21 Panel element distribution on the surface of an EMS train model and showing a classification scheme using a single letter for cross-sections along the train.

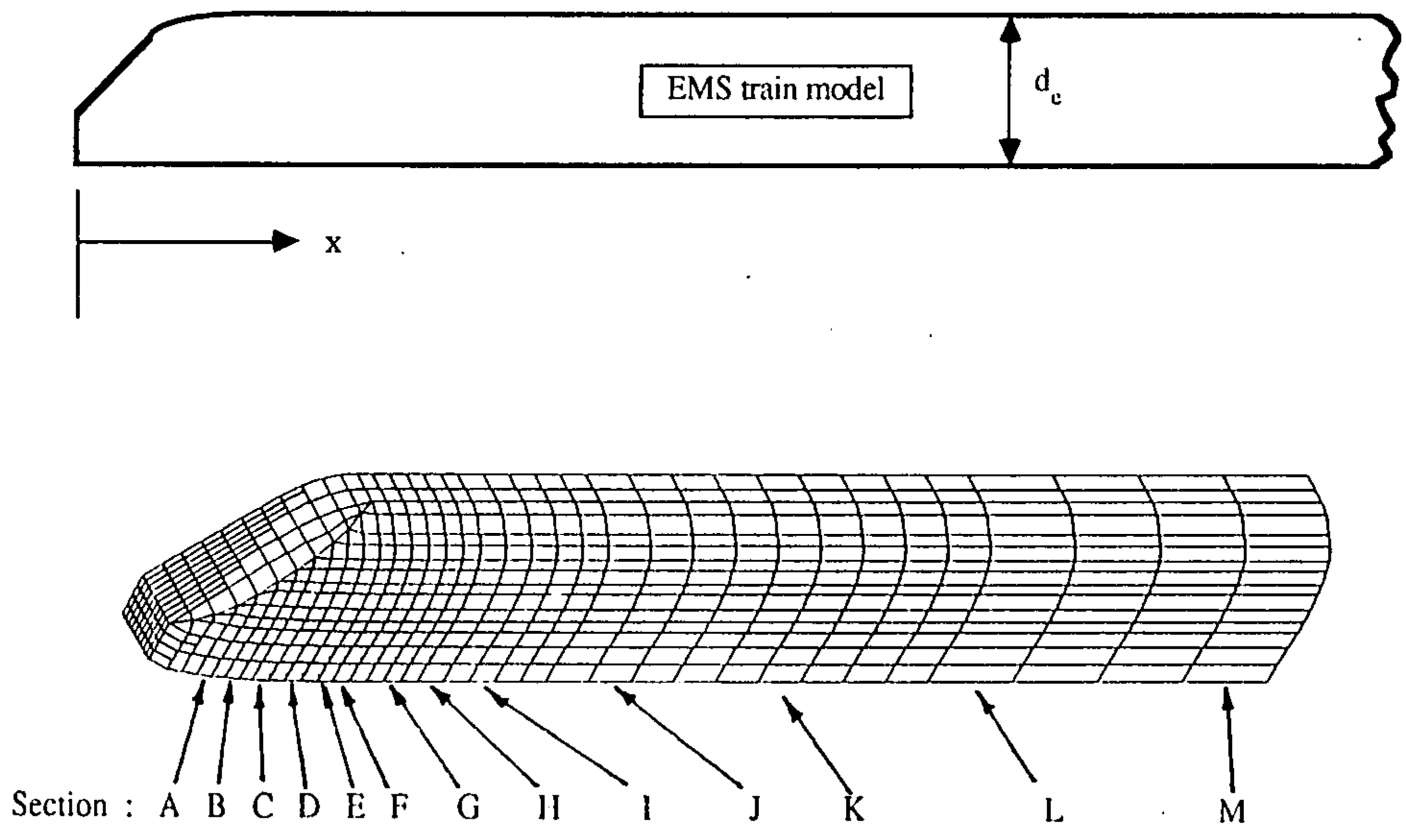

Section	x/d_e
Nose region	
A	0.28
B	0.45
C	0.62
D	0.72
After nose region	
E	1.0
F	1.12
G	1.44
H	1.68
I	2.00
Far from the nose	
J	2.80
K	3.60
L	5.0
M	6.7

Figure 2-22 Classifications details of, sections, regions and dimensions of an EMS train model for use

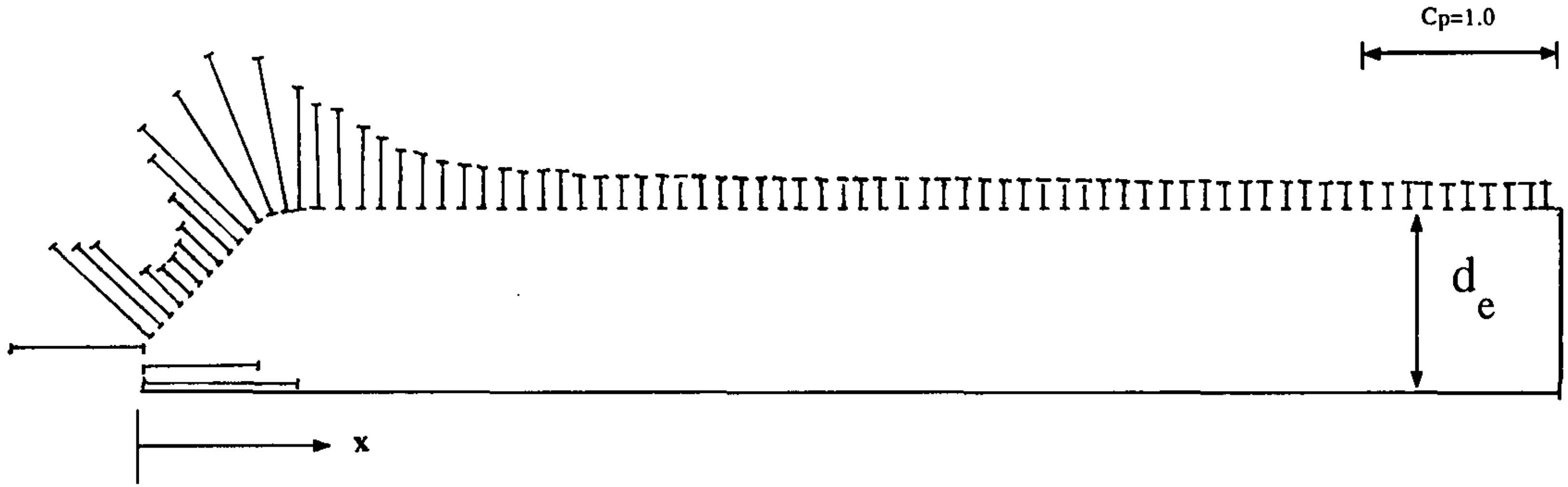

Figure 2-23 Pressure coefficient distribution close to the centre-line of an EMS train model at zero yaw angle. Panel element distribution shown by dashed train profile.

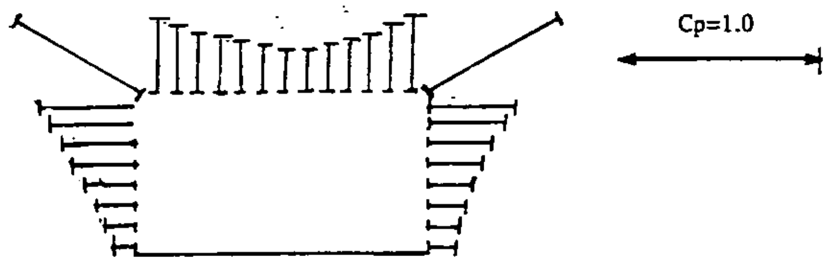

Cross section A

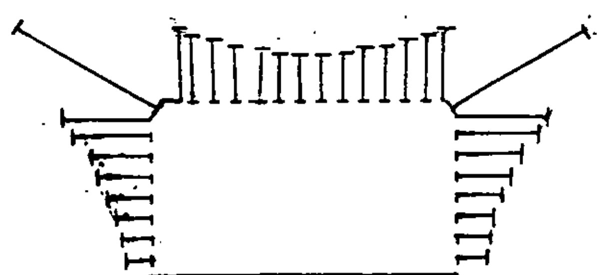

Cross section at section B

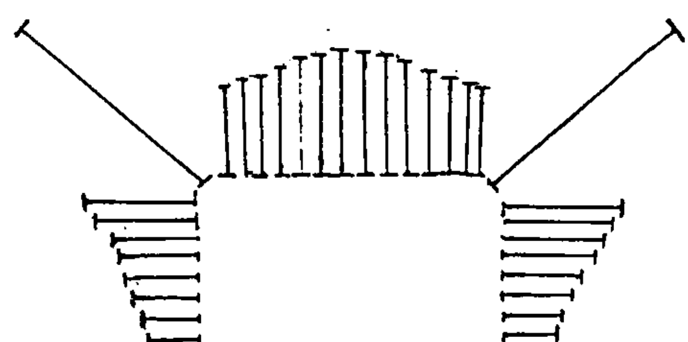

Cross section at section C

Figure 2-24 Circumferential pressure distribution for an EMS train model on sections A, B and C at zero yaw angle (see Figure 2-22).

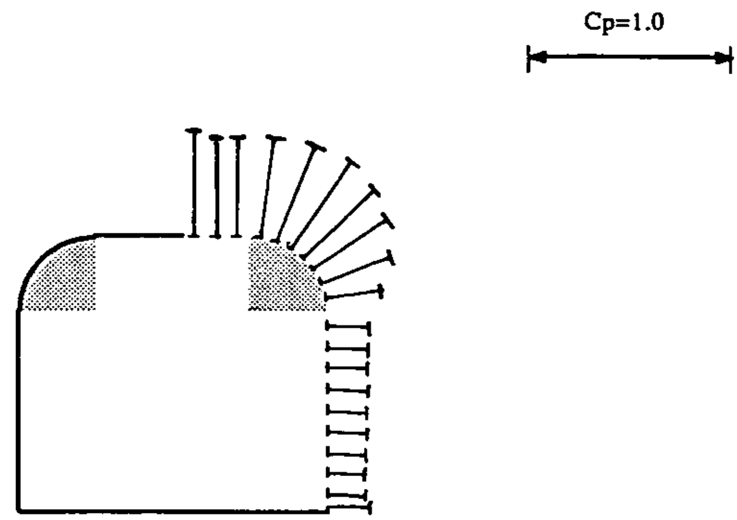

Cross section at section D

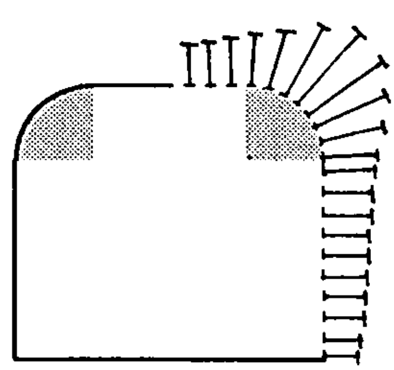

Cross section at section E

Figure 2-25 Circumferential pressure distribution for an EMS train model on section D and E, at zero yaw angle (see Figure 2-22). Panel element distribution shown by dashed train profile.

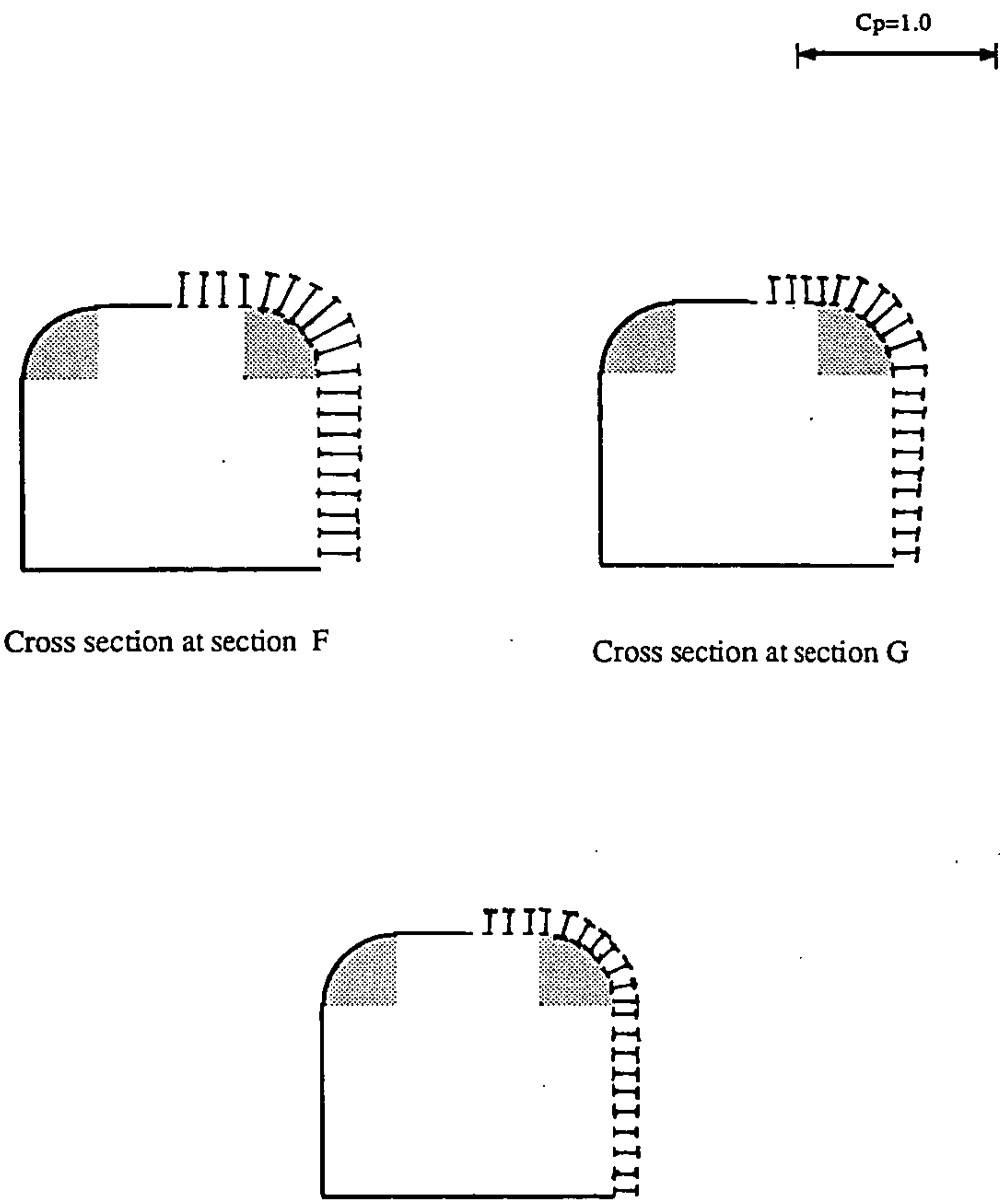

Cross section at section F

Cross section at section G

Cross section at section H

Figure 2-26 Circumferential pressure coefficient distribution for an EMS train model on sections F, G and H (see Figure 2-22) (after the nose).

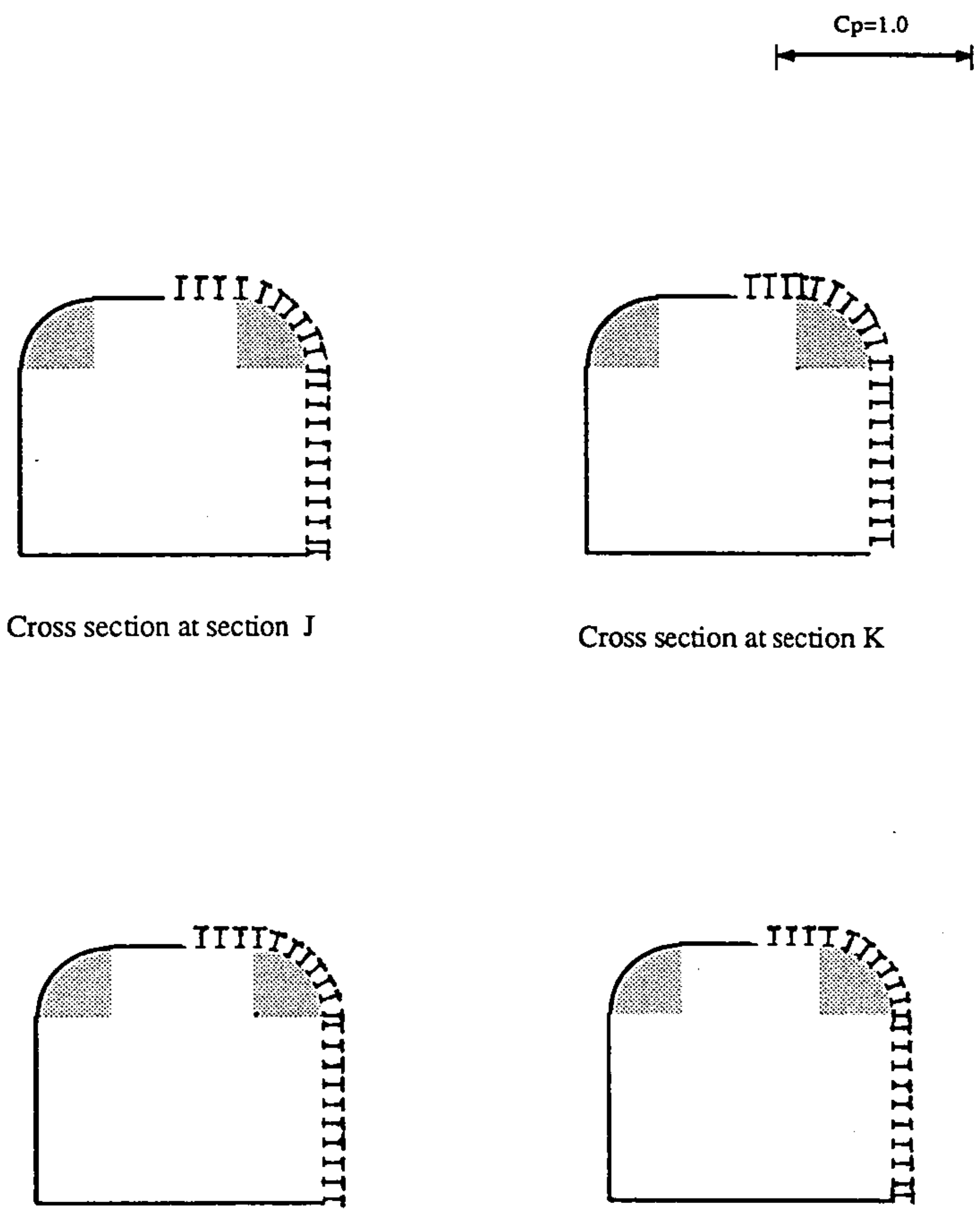

Figure 2-27 Circumferential pressure coefficient distribution for an EMS train model on sections J, K, L and M (see Figure 2-22)

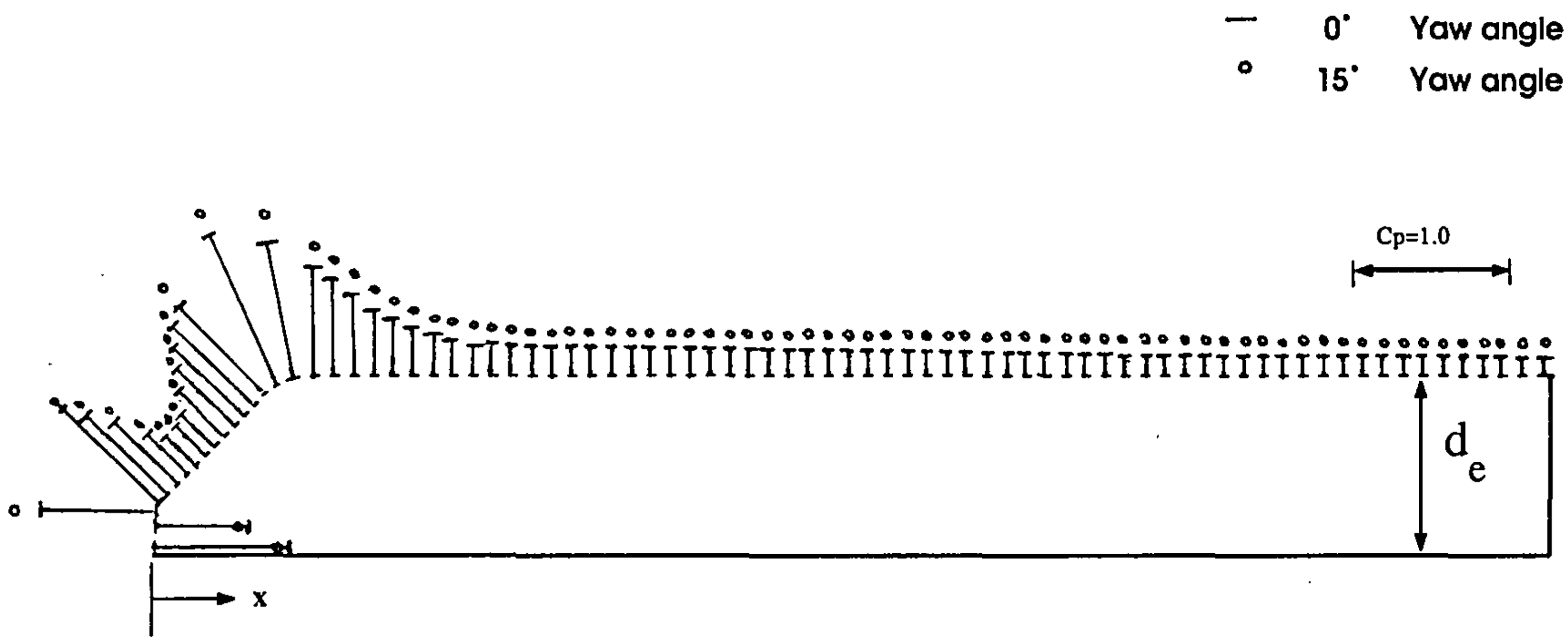

Figure 2-28 Pressure coefficient distribution close to the centre-line of an EMS train model at two different yaw angles. Panel element distribution shown by dashed train profile.

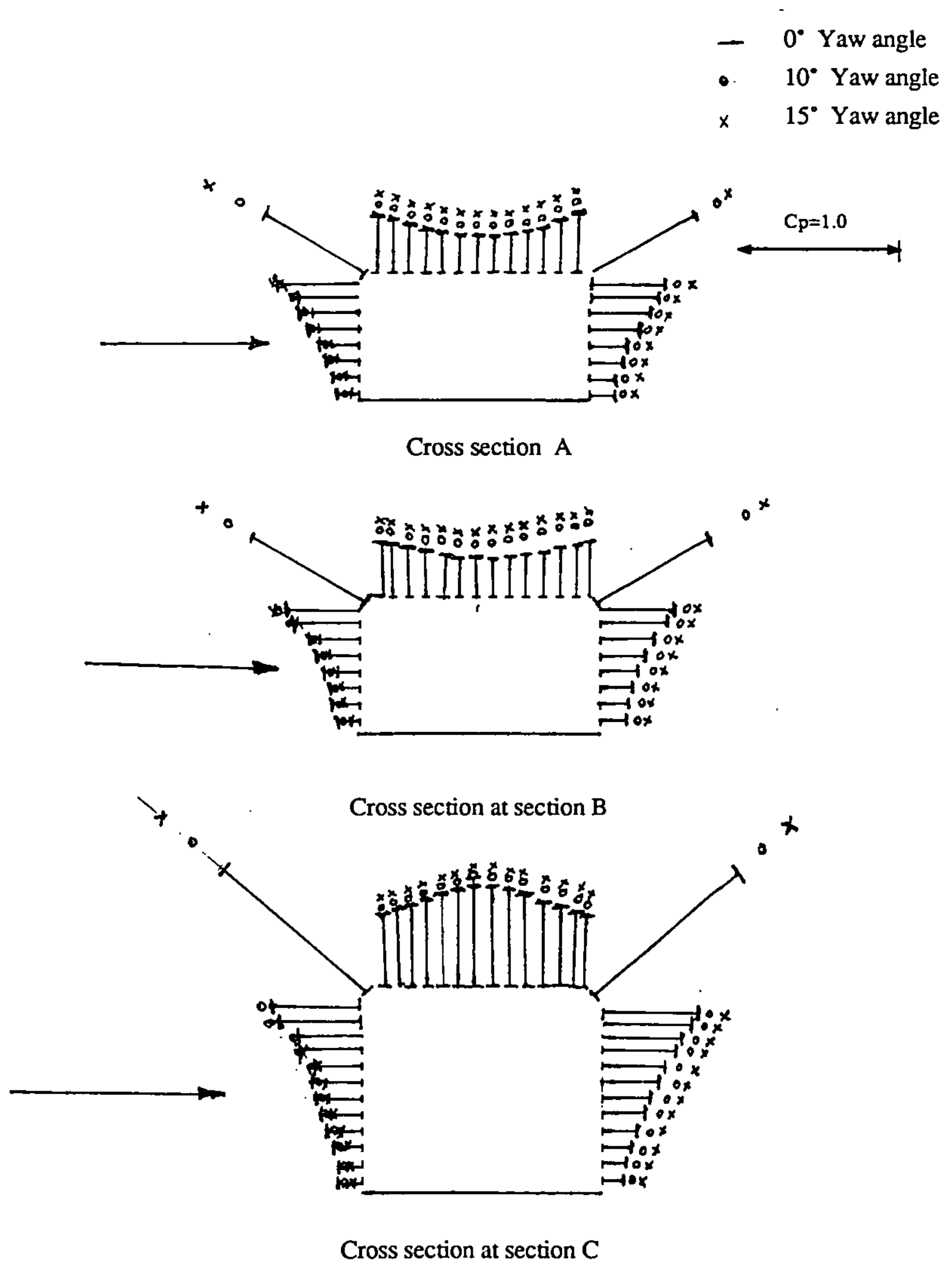

Figure 2-29 Circumferential pressure distribution for an EMS train model on sections A, B and C at different yaw angles (see Figure 2-22)

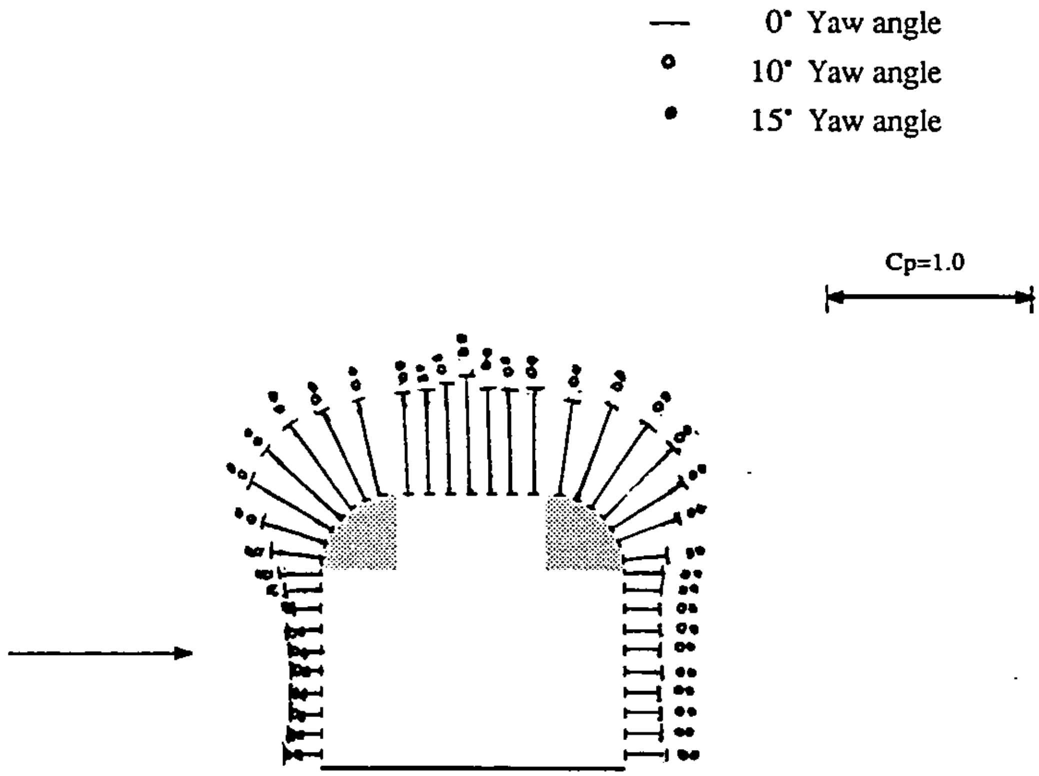

Cross section at section D

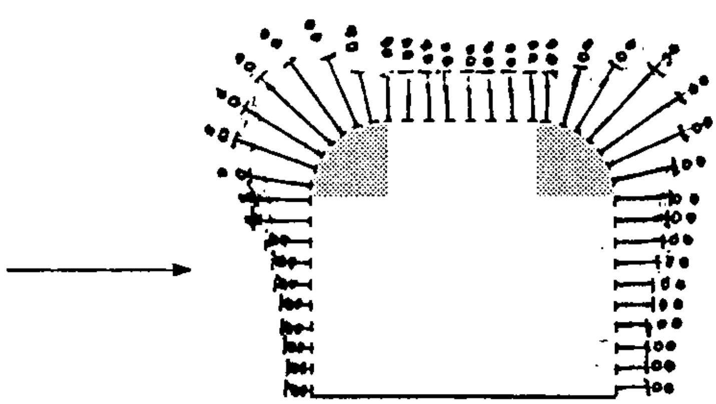

Cross section at section E

Figure 2-30 Circumferential pressure distribution for an EMS train model on section D and E at different yaw angles(see Figure 2-22)

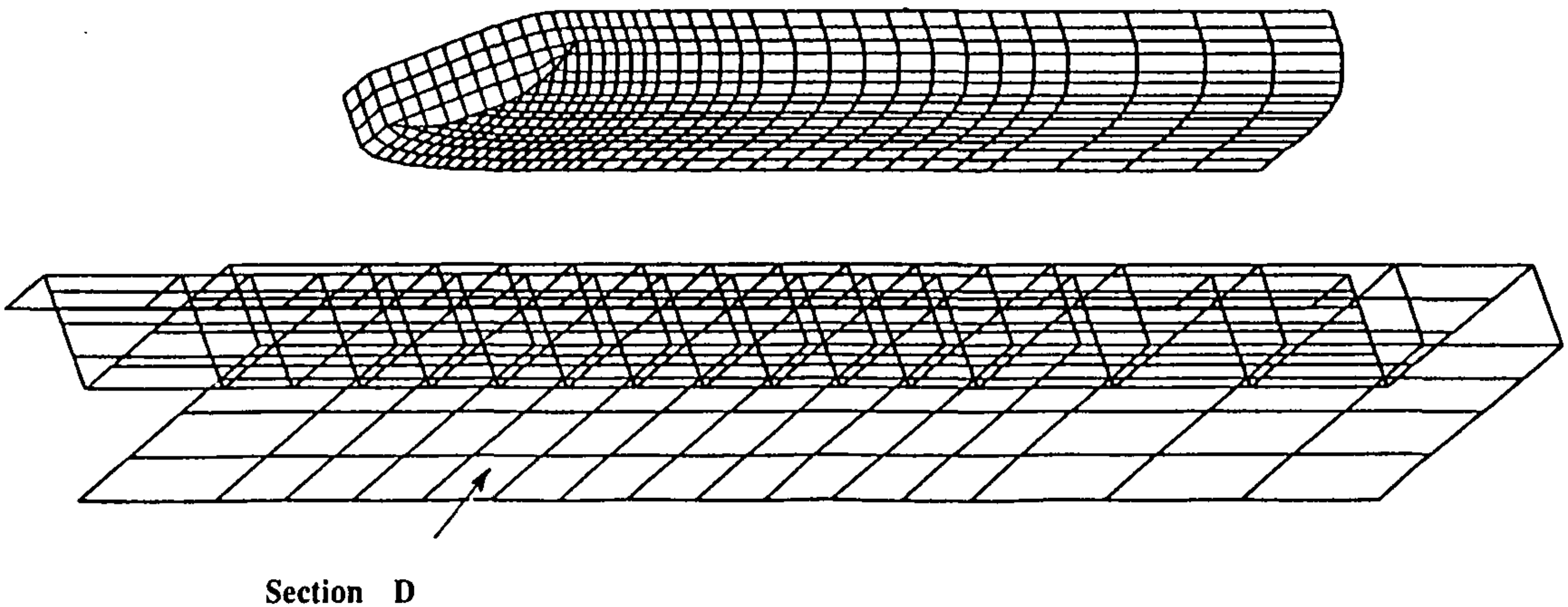

Figure 2-31 Panel element distribution on the surface of an EMS train half-model passing a railway station model.

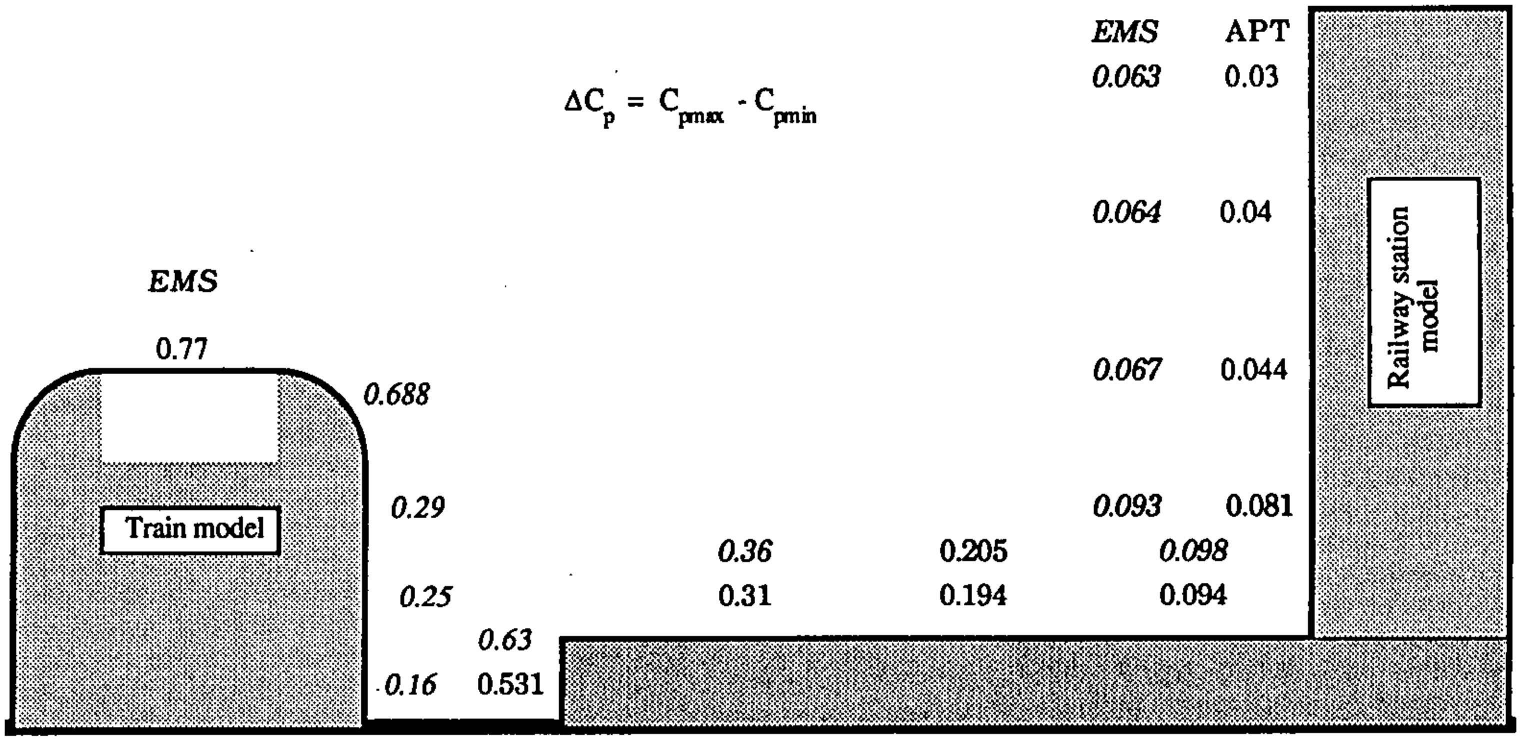

Figure 2-32 Comparison of pressure pulses when EMS and APT train models pass a railway station model at section D, (see Figure 2-31). The Figure shows the pressure pulses for both trains on the railway station and the pressure pulses on EMS train model only.

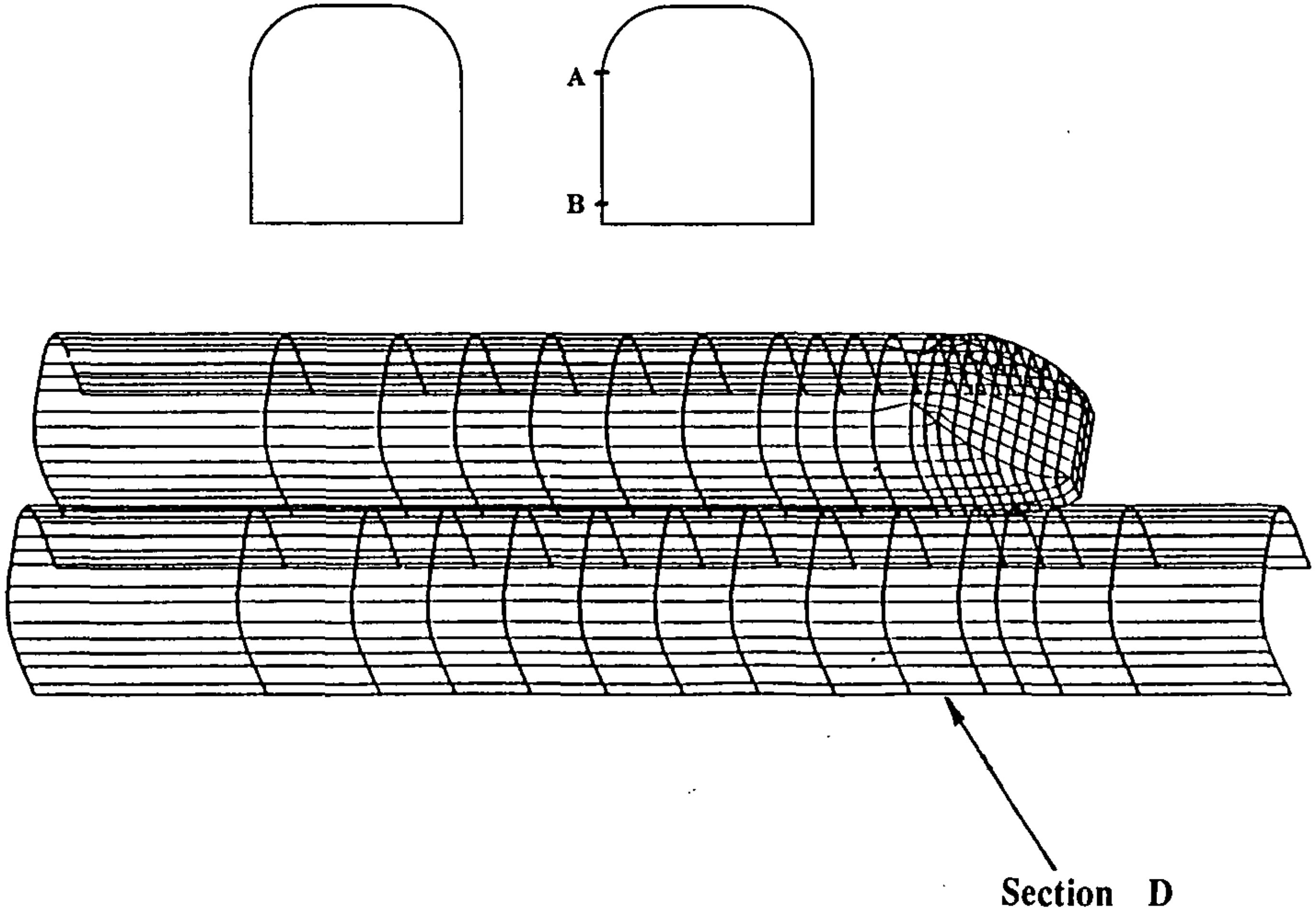

Figure 2-33 Panel element distribution on the surface of an EMS train model passing central part of another EMS train.

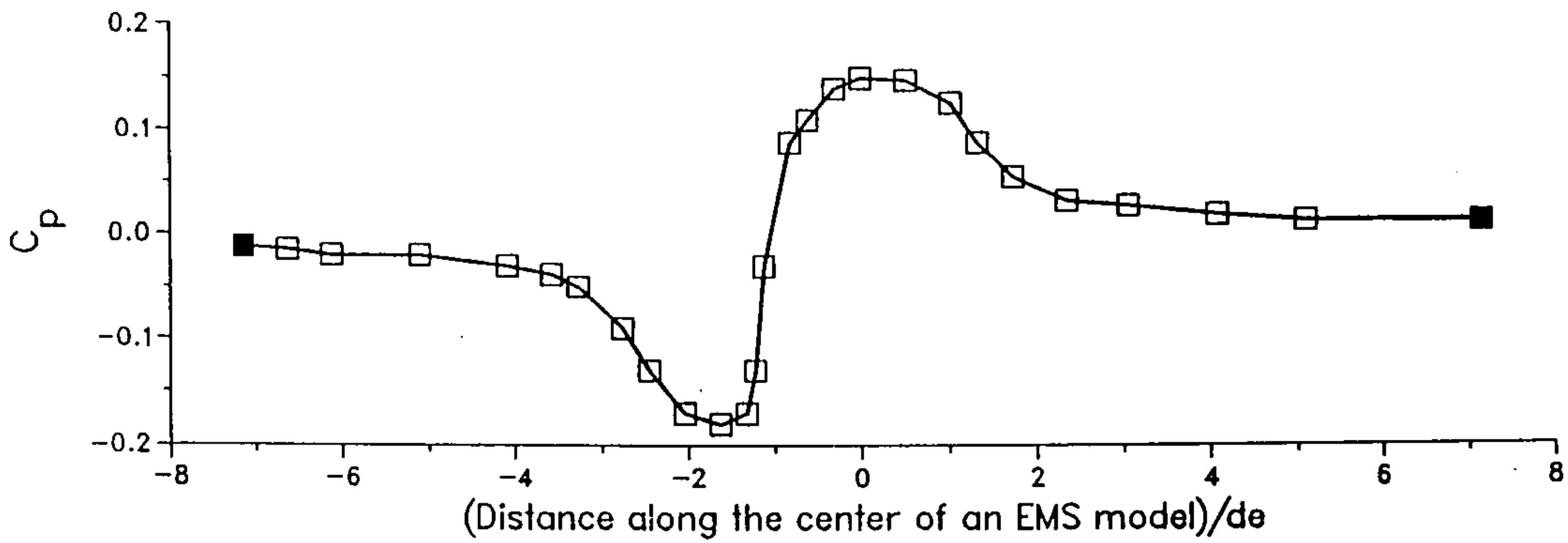

Figure 2-34 Pressure pulses at point A on the side of an EMS train in the presence of another EMS train along side it

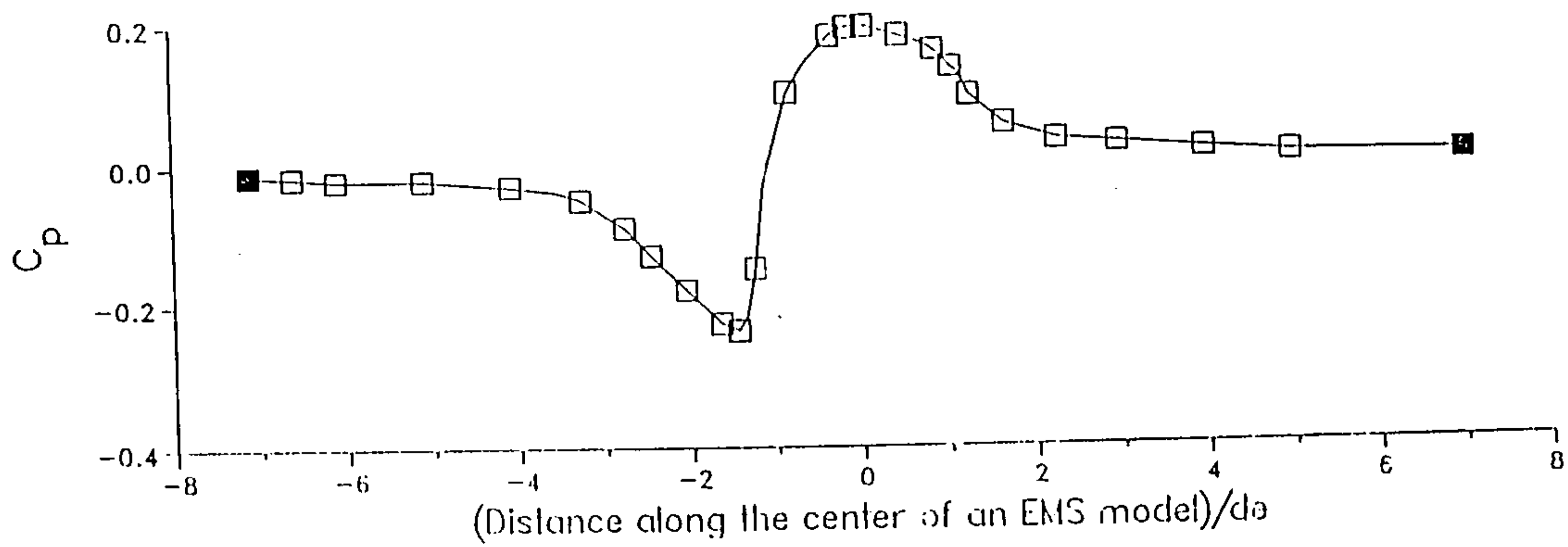

Figure 2-35 Pressure pulses at point B on the side of an EMS train in the presence of another EMS train along side it

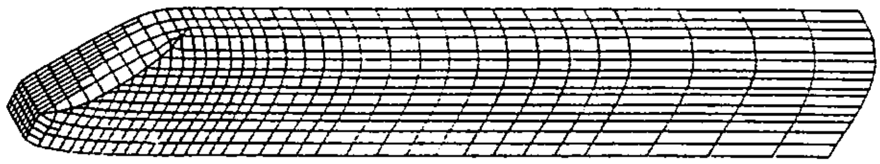

(a) EMS model

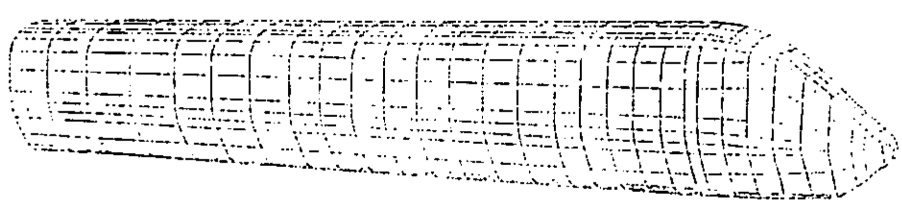

(b) APT model

Figure 2-36 Elemental surface source distribution, on the surface of an EMS train and APT models

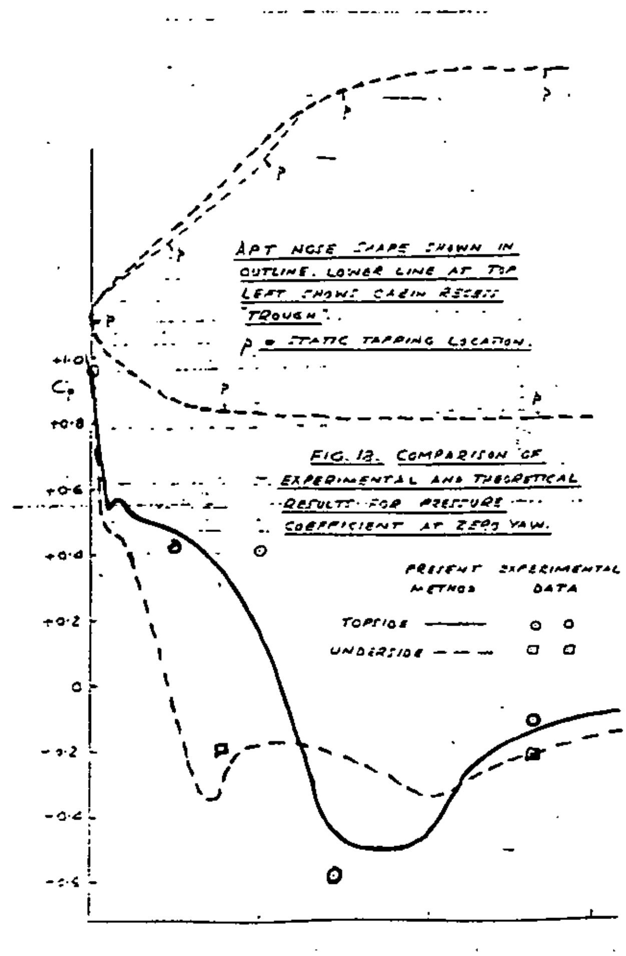

APT result [38]

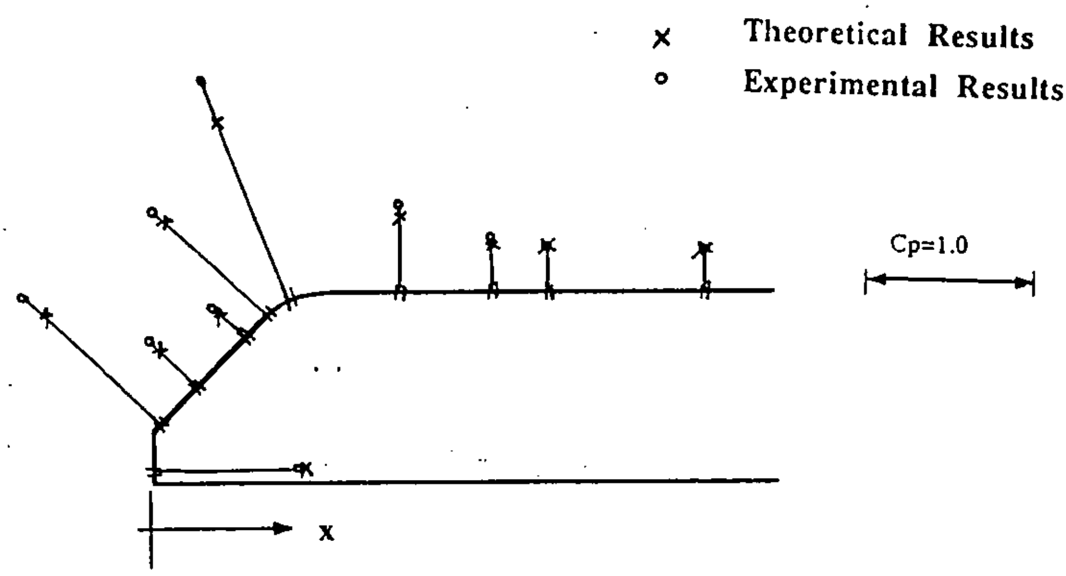

Figure 2-37 Pressure distribution close to the centre-line for an APT train model and EMS train model at 0° yaw angle

Nose region	
Section	x/d_e
A	0.28
B	0.45
C	0.62
D	0.72

After nose region	
Section	x/d_c
E	1.00
F	1.12
G	1.44
H	1.68
I	2.00

Table 2-1 A classification scheme for regions of an EMS train model

Region far from the nose	
Section	x/d_e
J	2.80
K	3.60
L	5.00
M	6.70

Table 2-1 Cont.

PART II : WIND TUNNEL TESTS ON EMS TRAIN MODELS

PART II

WIND TUNNEL TESTS ON EMS TRAIN MODELS

In Part I a numerical approach for the prediction of three-dimensional inviscid potential flow was employed to predict the pressure distribution over the surface of an EMS train. In practice the flow over a real (or model) EMS train is viscous and therefore a series of experimental tests were performed to investigate the flow field so that its main features could be identified and investigated, and to provide experimental data for comparison with corresponding results predicted numerically based on inviscid potential flow theory of Part I.

Three series of wind tunnel tests, using a number of scale models of the EMS train, were conducted for different angles of yaw, types of ground simulation and ground clearances and were as follows

(a) **Pressure measurements**

Tests were performed to measure the pressure distribution on the surface of the train model. These form a direct check on the predicted values.

(b) **Flow visualisation**

A series of flow visualisation tests has been carried out on the EMS train models to study the flow features on and around the models as well as investigating the vortices and wake observed on the lee side of the train. These form an initial estimate of the magnitude and location of viscous effects as identified by separation zones and vortices.

(c) **Aerodynamic forces and moments**

Aerodynamic lift, drag, side force and yawing moment have been measured. These are the most direct and useful quantities for design purposes and have not previously been reported for an EMS shape.

The remainder of this introduction to the experimental work of Part II of the thesis, consists of a discussion of factors — such as the influence of Reynolds number — which need to be considered as part of any investigation involving the use of scale models in wind tunnels to ensure the results are representative of full scale conditions. The main body of Part II comprises three chapters, as follows. Chapter three is concerned with the measurements of pressure distribution on an EMS train model. Chapter four deals with flow visualisation tests on EMS train models. Chapter five describes the tests and results from the wind tunnel measured aerodynamic forces and moments. Part II then concludes with a general discussion of all the wind tunnel tests.

The experimental results presented in Part II were obtained solely from conventional steady flow wind tunnel tests using simple 1/25-th and 1/63-th scale models of a proposed EMS train. These models retain the basic geometry of the train profile and take the form of a continuous slender body with a nose and the cross-sectional shape of the proposed train. To aid the engineering assessment of the test results, some of the main factors that need to be considered for relevant scale model tests, are outlined next. The discussion which follows is not intended to be exhaustive, but to provide a basic list of factors typically taken into account for the actual tests or borne in mind when assessing test results. The factors mentioned below may be grouped into three categories :

(i) air flow environment

- influence of Reynolds number
- nature of incident freestream, i.e.
  - — sheared incident airflow due to atmospheric boundary layer
  - — unsteady flow of natural freestream

(ii) degree of detail in model train

- intercarriage gaps
- underbody blockage due to train track

(iii) Presence of the ground

- modelling of ground, i.e.
  - — fixed ground simulation
  - — moving ground simulation
- effect of proximity of the ground

1. Reynolds Number effect

Previous work on wind tunnel tests on slender bodies Stewart [20] and train models Gould [79] suggest that useful results for overall pressure distributions and aerodynamic forces on trains can be obtained using scale models above a Reynolds number, based on body height, of about 2×10^5. Extensive experimental tests on long slender train-like bodies at yaw Stewart [20] showed — for the case of a cylinder with a train-like cross-section shaped as a square with rounded corners — that at low Reynolds number, the flow is attached at the windward side of the model and separated at the roof of the windward corner, denoted by the letter S, [20], see Figure P2-1. In this case the flow does not reattach and forms a wake in the lee side of the model. As the Reynolds number of the flow is increased the flow becomes reattached at some critical Reynolds number forming a separation bubble denoted, S_a, see Figure P2-2. The value of the critical Reynolds number depends upon the yaw of the model. At high Reynolds number this bubble is suppressed and the flow over the windward side and roof is fully attached. Further increase in Reynolds number can be expected to have little effect on the overall pressure distribution [20]. Since it impossible to achieve Reynolds numbers of the right magnitude for a real train, i.e. Re of approximately 10^7, the best that can be done is to choose a Reynolds number which will give an attached flow over the windward side and roof of the model. If this is achieved then flow should closely resemble that at the high Reynolds number more typical of a real train. This is because as mentioned above, increases in Reynolds number following the occurrence of attached flow on the roof and the windward side of the train have very little effect on the overall aerodynamic forces. It is noted that Gould [79] performed wind tunnel tests on a scale model of an APT train at 90° yaw and his results indicated also that there is no significant Reynolds number effect above a Reynolds number of about 2×10^5. In the present thesis a flow Reynolds number of 4.37×10^5 was employed in all wind tunnel tests, except for the flow visualisation tests which employed the smoke technique where the available facilities restricted the maximum usable Reynolds number to 2.0×10^4

2. **Atmospheric Boundary layer**

A feature of natural air flow which is not satisfactorily simulated in a modest conventional wind tunnel is the earth's atmospheric boundary layer. The wind tunnel tests have a uniform freestream flow on the train, apart from the boundary layer over the ground board, while in reality the real train will have a sheared approach flow due to the presence of the atmospheric boundary layer, see Figure P2-2. Therefore to achieve a totally realistic simulation of a real train, a simulation of the atmospheric boundary layer in wind tunnel tests may be needed. For the present tests, this aspect has been neglected, due to wind tunnel facility constraints.

3. **Unsteady Flow effect**

The wind incident on the model is steady whereas that for a real train is highly unsteady. This unsteadiness results from two effects: first, the wind naturally tends to gust, and, second, the topography of the terrain through which the train passes (e.g. trees cuttings,...etc), produces flow disturbances. In this work, the unsteady flow effect was not included.

4. **Intercarriage gaps**

In the real case there will be gaps between the carriages and these gaps influence the flow field around the train. The wind tunnel test models are continuous and thus not subject to these disturbances.

5. **Ground effect**

A real train moves relative to the ground while in wind tunnel tests the train model does not. The relative motion results in a complicated sheared flow between the train and the ground. Ground effect studies are concerned with the flow velocity and pressure changes due to the ground interference. In this work both a stationary and moving belt were used to study the ground effect.

In summary then, the experiments to be reported here have concentrated on simulation of realistic train shapes, flow Reynolds numbers and ground effects, whilst unsteady and onset flow boundary layer profile effects have been excluded.

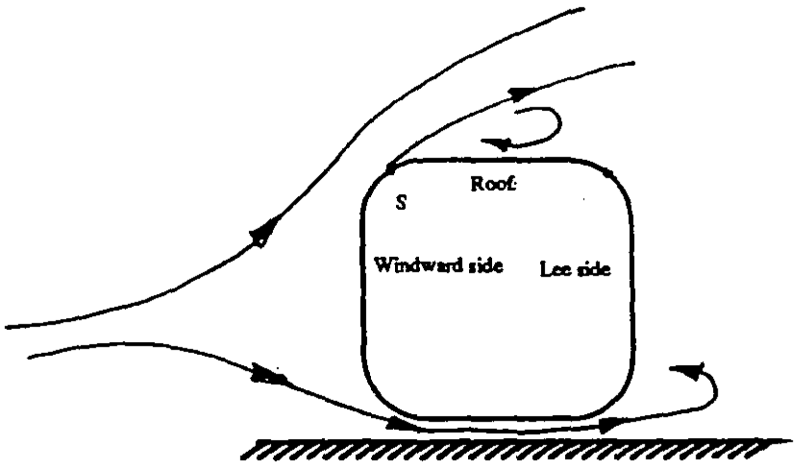

(a) Separation without reattachment

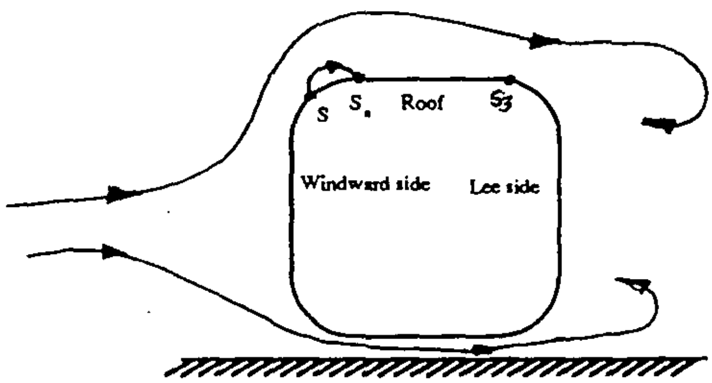

(a) Separation with reattachment

Figure P2-1 Reynolds number effect (Source ref. [20])

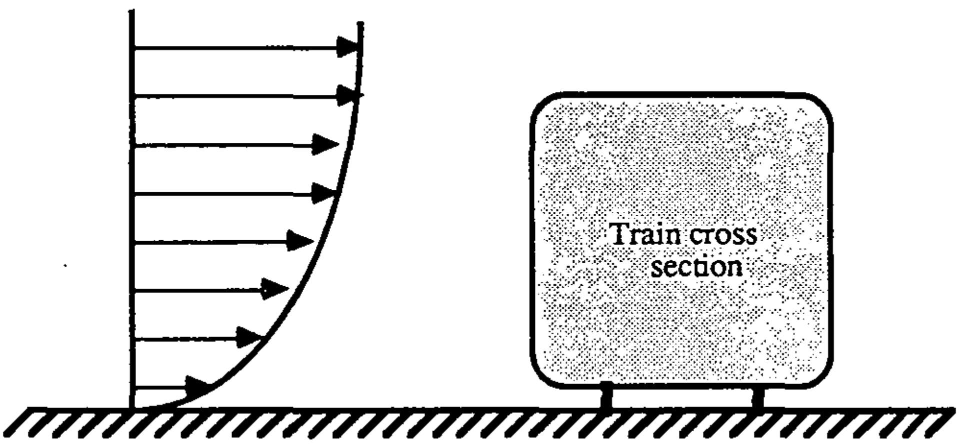

Figure P2-2 Atmospheric boundary layer

CHAPTER 3
PRESSURE DISTRIBUTION MEASUREMENTS ON AN EMS TRAIN MODEL

3.1 Introduction

This chapter reports on wind tunnel experimental measurements of pressure distribution over the surface of an EMS train model, to provide a check on the accuracy of the pressure distributions predicted by the panel method. The experimental programme was performed in an environmental wind tunnel using a 1/25 scale, tapped EMS train model for various yaw angles. The effect of the type of ground simulation, i.e. the use of a moving or a stationary belt to simulate the ground, for different ground clearances was also investigated. Some of the measured pressure distributions have been compared with corresponding theoretical results.

The main body of the chapter is in seven sections. Section 3.2 specifies how ground effects have been incorporated into the experimental tests. The experimental wind tunnel used is the subject of section 3.3 and section 3.4 describes the EMS train model. The test method is then presented in section 3.5 and the results follow in section 3.6. Section 3.7 compares the experimental results with potential flow predictions and the chapter closes with concluding remarks in section 3.8.

3.2 Ground Simulation

When a vehicle moves very close to the ground the flow about it is modified by the presence of the ground which can significantly influence the air movement and accordingly the aerodynamic forces. The influence of the ground on the moving body is generally called *ground effect.*

An important aspect of the experimental aerodynamics of high-speed ground vehicles is how the effect of the ground should be considered. This is a problem that has been discussed for a number of decades, and researchers have employed several methods to investigate the ground effects which occur during wind tunnel tests. Reference [80] is the proceedings of a recent conference on the effect of the ground on high-speed vehicles.

This section presents a brief description of the two wind tunnel ground simulation technique used — the fixed and moving belt.

Fixed ground plane

In the fixed ground plane technique, the ground is simulated by a fixed board mounted in the wind tunnel working section, parallel to the existing tunnel floor. This is the most widely used method in automotive tests and is perhaps the simplest. The main objection to this method is that the boundary layer conditions are not simulated exactly : this is because in practice when a vehicle is moving along the ground in still air, there is no boundary layer on the ground. However, the flow conditions under the vehicle are not the same when the model is in the wind tunnel on a fixed ground-plane, when a boundary layer development becomes unavoidable. This problem can minimised by, for example, careful design of the ground plane and by keeping the surface smooth and clean [81]

Moving belt

This method uses a moving belt placed under the model being tested to simulate the ground. In this arrangement both the air stream and "ground" are moving relative to the model in order to simulate the vehicle moving relative to the air and ground in practice. This method reduces further boundary layer development when the belt moves at the same speed as the air, so the speed of the belt must be carefully controlled. The driving cylinder must be heavy to prevent deflection and perfectly aligned to keep the belt on track. The removal of the boundary layer altogether ahead of the belt must be done carefully to prevent over correction. The belt must not flap and flutter. The design used satisfied these constraints.

3.3 Environmental Wind Tunnel

The pressure measurement tests were performed in the environmental wind tunnel of the Department of Transport Technology at Loughborough University of Technology. This wind tunnel has two fan speeds, a low speed and a high speed, and a variable fan blade pitch angle is used to provide a range of wind speeds. The calibration of the wind tunnel, to establish the velocity profile at various speeds and heights above the wind tunnel wall with both a moving and a stationary belt, and the relation of the air speed to vane angle, was discussed in reference [82].

Tunnel working section

Width	:	1.60 m
Height	:	1.0 m
Length	:	4.70 m
Maximum speed	:	30 m/sec
Longitudinal turbulence	:	0.5-0.7% at measurements section

The environmental wind tunnel is fitted with a moving belt to simulate the ground and this is discussed next.

Moving Belt

Figure 3-1 shows the layout of the working section of the environmental wind tunnel fitted with a moving belt which is co-axial with the air stream. The belt, which runs on transverse rollers fitted at its ends, is coated with a plastic to provide a smooth surface. The moving belt speeds are controlled manually and can be made equal to the main stream velocity.

Moving belt dimensions

Width : 0.90 m

Length : 2.45 m

3.4 EMS Test Model

A 1/25 scale EMS train model was made to the requirements of the Science and Engineering Research Council [61], as discussed in chapter one. The model was constructed from wood, with a removable wooden bottom to fit a scanivalve inside the model, and possessed a hole through its centre line to fix it in the wind tunnel and allow the connection of electrical wires. The model was pressure-tapped , a total of 46 taps each comprising a 1.8 mm outside diameter brass tube were fitted into the surface of the model. Figure 3-2 shows the EMS train model in the environmental wind tunnel. The distribution of the taps is shown in Figure 3-3 in which they are shown numbered from 0-45 inclusive. Due to symmetry, only one side of the model needed to be tapped and the distribution of the taps was concentrated in the nose region of the model, the region of most interest. The model had the following overall dimensions :

Length : 2.25 m

Height : 0.149 m

Width : 0.151 m

3.5 Test Method

It was considered worthwhile to conduct a comprehensive examination of the train model surface pressure distribution (i) for comparison with corresponding theoretical results predicted by the method of chapter two and (ii) to provide a source of data on the EMS type shape, not currently available in the open literature.

The experimental programme was carried out in the environmental wind tunnel described earlier. The tapped EMS train model was set up in the wind tunnel with the help of rod supports as shown in Figure 3-1, with the capability of changing ground clearance and yaw angles. The scanivalve was mounted inside the model and fixed at the centre of the model. The experimental setup allowed the measurement of the pressure value at each tap sequentially. The tests have been carried out with a Reynolds number, based on the main stream velocity and equivalent diameter of the model cross section, of 4.37×10^5.

3.6 Test Results

3.6.1 Pressure Distribution for an EMS Train Model

Figure 3-4 shows the variation of pressure coefficient close to the centre line (at tap numbers 0, 2, 4, 6, 8, 10, 26, 32, 36, 37, 38, 39 and 40, see Figure 3-3) of the EMS train model. The model is at zero yaw angle and has a ground clearance $Z/d_e = 0.125$, this value has been chosen because it is close to that occurring in the real train. The locations of the taps are marked on the profile of the longitudinal section of the EMS train model in the figure. It is seen that the most significant variations of the pressure coefficient occur at the nose of the train, while there are no major changes over the region far away from the nose. A double peaked profile, corresponding to the two corners of the sloping front face, was observed, as in the predicted shape of the previous chapter, but further comparisons between predictions and measurements are reserved for later. Regions of steep adverse pressure gradients are identifiable in these corner peak zones which will clearly have implications for viscous boundary layer separation. Figure 3-5 shows the pressure coefficients (which are all negative) for the same conditions at sections A, B and C which are at the nose of the train(see Figure 3-3). It is clear that significant changes in the value of the pressure coefficient occur at the nose, particularly at the sharp sided corners (e.g. taps numbers 12, 14 and 17). Figures 3-6 and 3-7 illustrate the pressure coefficient in sections D, F, H and L (see Figure 3-1). It is noted from these results that the only large circumferential changes occur at the top of the nose (section D), while no major variations around the train cross-section are observed in later section ; this indicates that as we move away from the nose the changes in pressure coefficients are very much reduced. These observations on the locations of large, and adverse pressure gradient zones, leads to the expectation of a separated flow region at the top of the nose as well as on the edge corner, i.e. the shoulder, of the nose (this needs to be confirmed by, for example, flow visualisation tests, see chapter four).

3.6.2 The Effect of Ground Clearance

A series of tests was carried out at different ground clearances, the values being chosen to move further away from the ground than the standard case to investigate the influence of ground effect on the measured pressure coefficient of an EMS train model. In Figure 3-8 the pressure coefficient values close to the centre line of the model are plotted for different ground clearances at zero yaw angle. No major pressure changes are evident with changes in ground clearance especially far away from the nose. The single identifiable trend is for slight increases in the suction pressures as the ground clearance grows. Figure 3-9 shows similar trends for pressure coefficient with ground clearances at sections D and F. Figures 3-10 and 3-11 underline the small influence of ground clearance over the range studied for a number of individual tappings selected to be those thought to be most sensitive to this effect significant variations. A detailed examination of ground clearance effects would have required pressure measurements underneath the model ; however the present results do show very little effect of ground clearance on the upper train surface.

3.6.3 The Effect of Yaw Angle

The pressure distribution close to the centre line of an EMS train model at different yaw angles is shown in Figure 3-12. The Figure shows that, not surprisingly, the major variations in pressure occur at the nose of the model. 8° of yaw gives rise to substantial increases in suction pressure. Figures 3-13 and 3-14 show the variation of pressure coefficient around sections A, B, C, D, F, H and L for different yaw angles. The impact effect on the windward side has led to a reduction in suction pressures over most of the train side surface, but an increase in these pressures near the train corner, presumably associated with the strong skewed flow slanting across the roof. The asymmetric distribution brought about by yaw seem to take some distance to become fully established, the strongest asymmetric being observed at sections F to H.

Figure 3-15 and 3-16 shows the effect of yaw angle on the pressure coefficient for individual tappings (ground clearance still $Z/d_e = 0.125$). It is clear that there are no major changes in pressure coefficient at the tappings far removed from the nose (numbers 32 and 36 in Figure 3-15) nor at points near the train centre line and stagnation point (numbers 1 and 8). Most of the major changes are induced at the side edge corner as shown in Figure 3-16. As mentioned above, increased suction pressures are generally observed, with only tap 17 departing from this trend. These larger suction pressures are likely to be associated with vortex formation on the side corners due to the yaw.

3.6.4 The Effect of Ground Simulation

A series of tests was also carried out on the tapped model with a stationary and a moving belt to investigate the effect of the type of ground simulation on the pressure coefficient at different ground clearances and at different yaw angles. Figure 3-17 shows the results for the train centre-line. The Figure shows that a moving belt gives a pressure coefficient that is higher by about 5% than that measured with a stationary belt. This is believed to be because the moving belt draws more air under the train model lowering pressures on its under surface. No major pressure coefficient differences arise for any of the tested tappings when using a moving belt for the taps far away from the nose, see Figure 3-18.

3.7 Comparison of the Experimental Results with Theoretical Potential Flow Predictions

A comparison of the measured and the numerically predicted values of the pressure coefficients close to the centre line of the front and roof surface of the tapped EMS model is shown in Figure 3-19. In general, the agreement is reasonable. Thus, qualitatively it can be seen that apart from the two suction peakes associated with the sharp corners both the experimental and the theoretical results have similar magnitudes and show similar trends in their variation over the surface. The agreement is best at points downstream of the nose where the theoretical results have slightly smaller suction pressures than the experimental results. Further examples of the quality of agreement between theory and experiment for the pressure variations around the train cross-section are presented in Figures 3-20 and 3-21. At sections D and F, located just downstream of the nose, the trend of the predicted results is fair bearing in mind the underprediction of the suction peakes mentioned above further downstream at sections H and L, the agreement between the two results is very good.

In summary, the agreement between the predicted results for pressure coefficient and the measured values is very good far away from the nose, i.e when the flow is expected to be fully attached in practice. The differences occur in the roof and shoulder of the nose and this is certainly due largely to the neglect of viscous effects in particular separation regions which cannot be predicted by potential flow theory.

3.8 Concluding Remarks

A series of wind tunnel tests were carried out on a 1/25 scale EMS train tapped model to measure the pressure distribution on the model at different yaw angles and different ground clearances. These results were used to help determine the validity and accuracy of the predictions of the computer programme based on the panel method for three-dimensional potential flow (chapter two). The main concluding remarks from these tests and their comparison with theory may be presented as follows :

Comparisons With Predicted Results

There is a reasonable level of agreement with the predicted pressure coefficient using the panel method for three-dimensional potential flow described in chapter two. The agreement is very good far away from the nose but is only qualitatively accurate at the nose. At the nose the disparity in the experimental and theoretical results is largely due to the neglect of viscous effects in the theoretical method. The major viscous effect is to cause separation in the corner edge (shoulder) and the roof of the nose. The good agreement between theory and experiment far away from the nose is due to the fact that the flow is here fully attached.

Both the experimental and the computed results show large-magnitude negative values of pressure coefficient at the top roof and the corner edge (shoulder) of the nose. This observation may be qualitatively confirmed using, for example, flow visualisation tests which are presented in chapter four.

Effect of yaw angle

Most of the changes in pressure coefficient with yaw angle occurred on the nose of the train, becoming insignificant far away from the nose. Most of the changes at the individual tappings occurred on the tappings close to the side edge of the nose, implying the onset of vortex behaviour from the sides at yaw.

The test results show an increase in the magnitude of the high negative values of the pressures in the lee side of the train as the yaw angle increases and the associated increased adverse pressure gradient on this side may lead to the expectation of possible separation and occurrence of wake vortices in the lee side of the train which can be investigated using flow visualisation tests.

Effect of Ground Clearance and Ground Simulation

From the test results it was established that, for the present configuration, all ground effects were of second order magnitude only. The nose, especially the top roof and corner edge "shoulder", were the regions most sensitive to changes in ground clearances and ground simulations, presumably due to small changes in separated flow occurring in this region in the presence of the ground. Far away from the nose the effect of ground clearance and ground simulation become negligible.

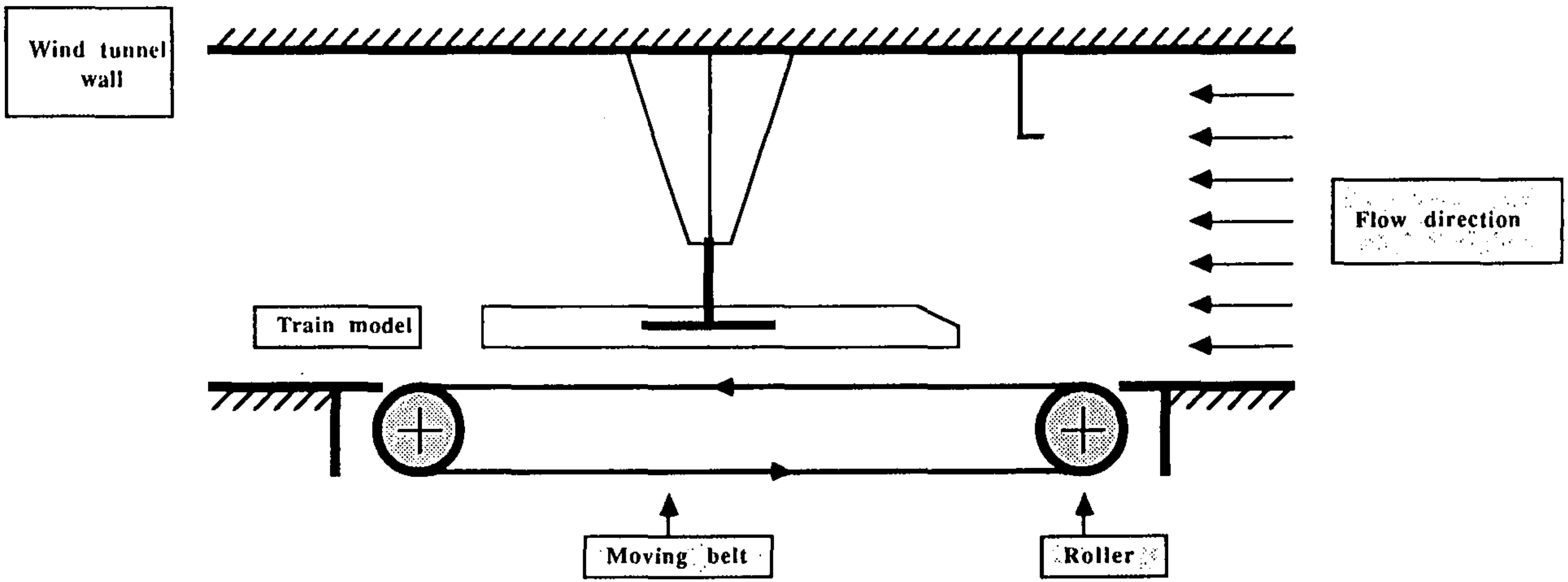

Figure 3-1 Layout of the working section of the environmental wind tunnel

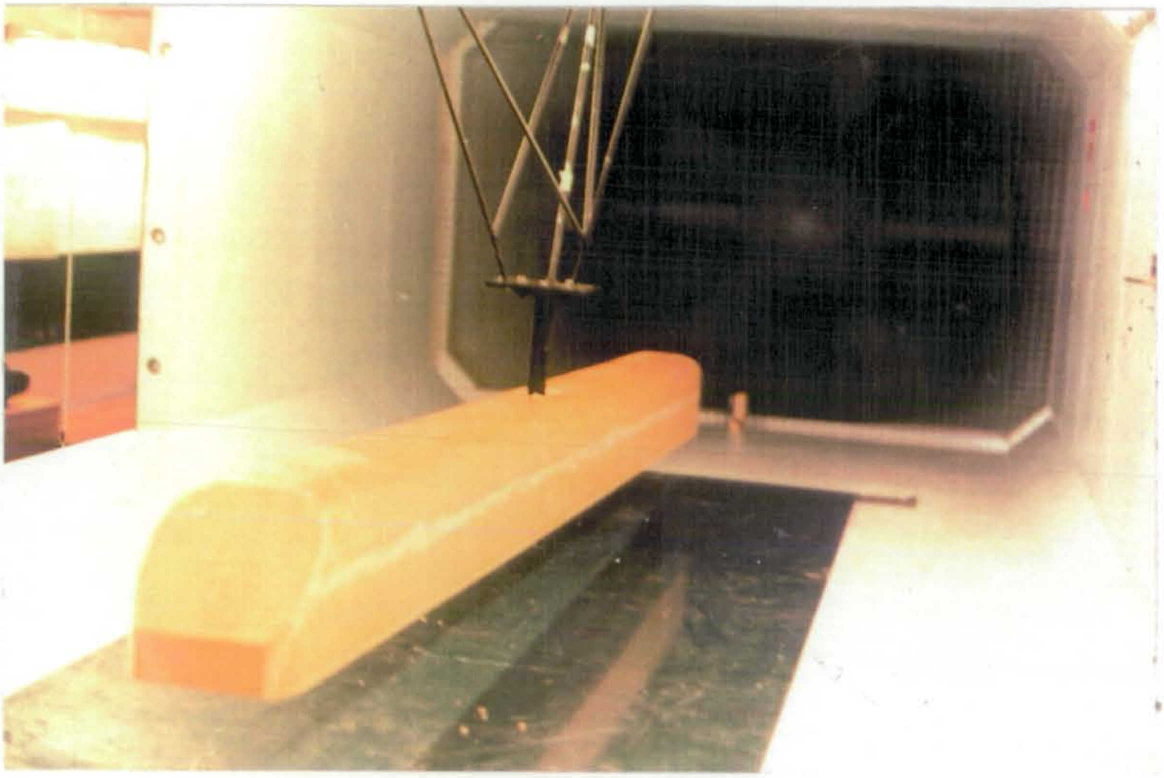

Figure 3-2 A tapped EMS train model in an Environmental wind tunnel

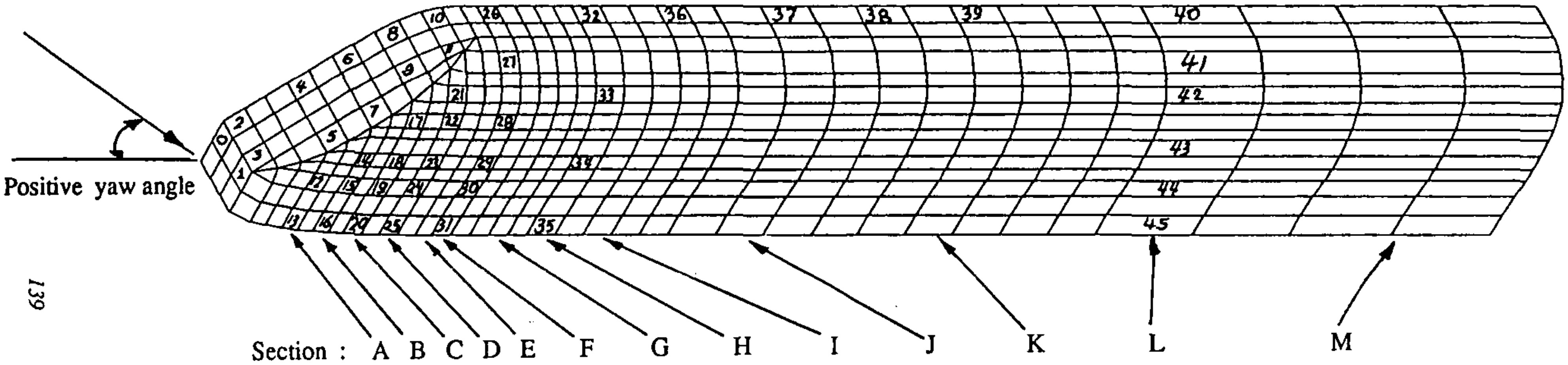

Figure 3-3 Locations of pressure tappings on the surface of an EMS train model, (see Figure 2-22, Table 2-1

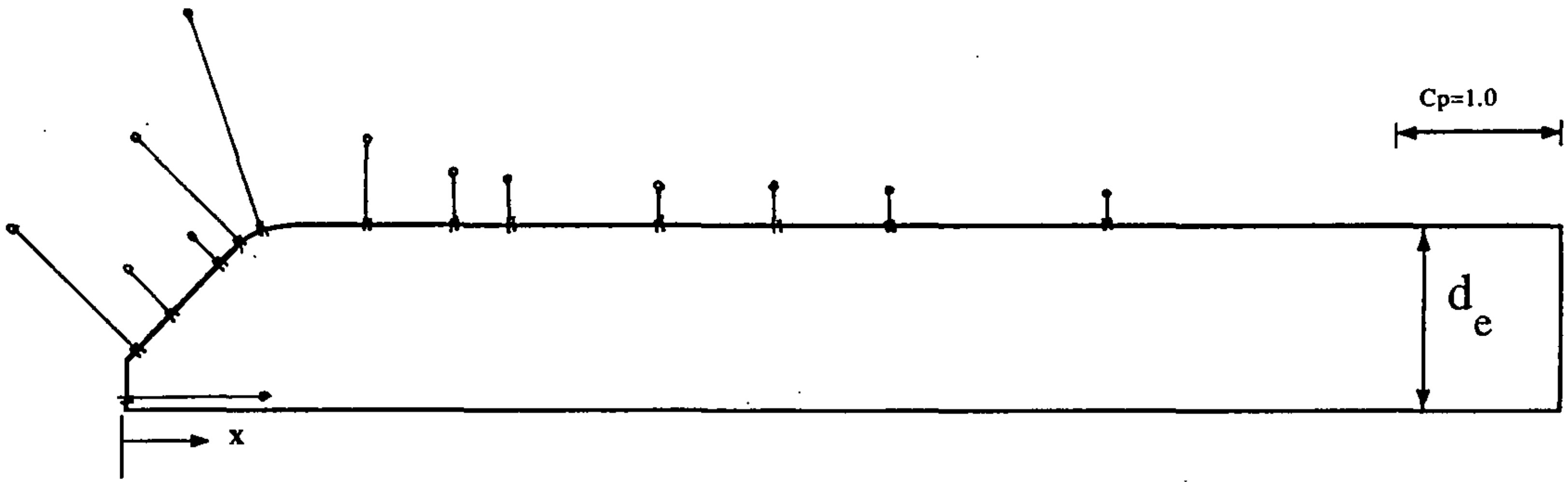

Figure 3-4 Pressure coefficient distribution close to the centre-line of an EMS train model with zero yaw angle and ground clearance Z/de=0.125

|| Indicate location of pressure tapping

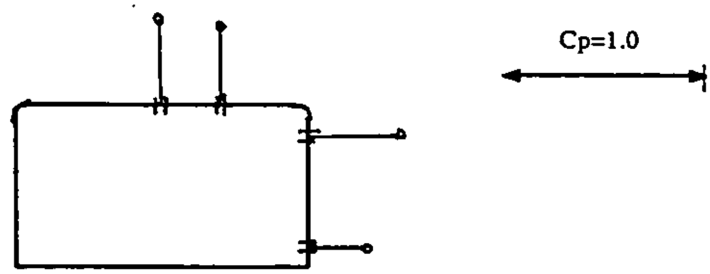

Cross section A

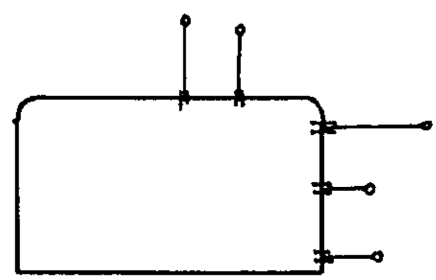

Cross section at section B

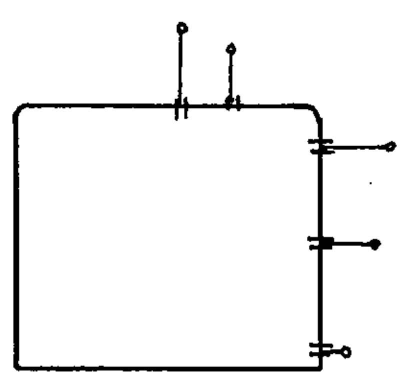

Cross section at section C

Figure 3-5 Circumferential pressure distribution for an EMS train model on sections A, B and C at zero yaw angle (see Figure 2-22).

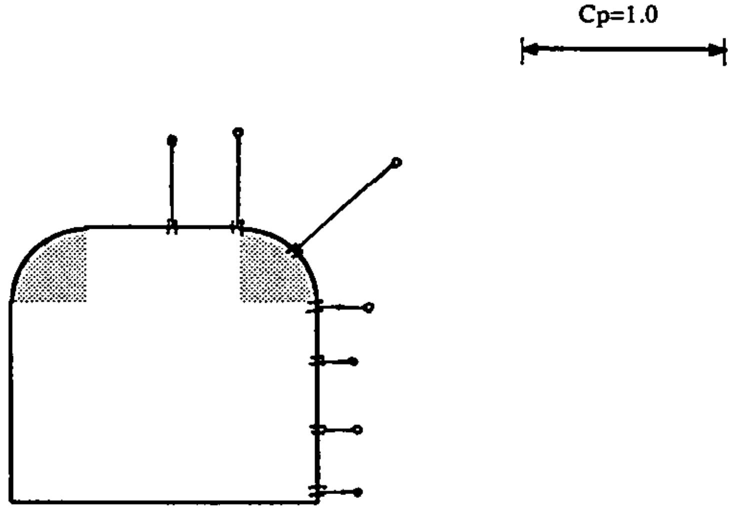

Cross section at section D

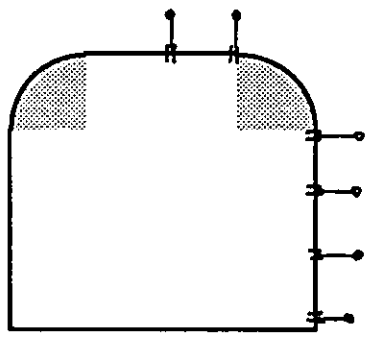

Cross section at section F

Figure 3-6 Pressure coefficient distribution for sections D and F at zero yaw angle and ground clearance Z/de=0.125.

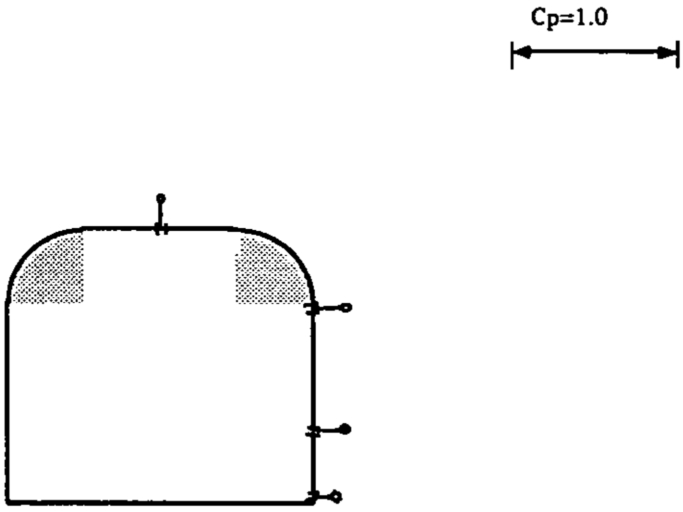

Cross section at section H

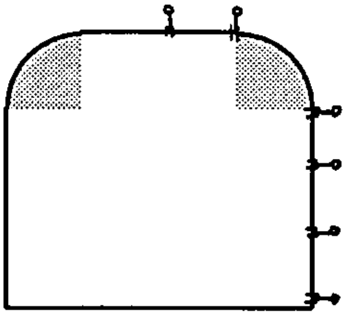

Cross section at section L

Figure 3-7 Pressure coefficient distribution for sections H and L, at zero yaw angle and ground clearance Z/de=0.125.

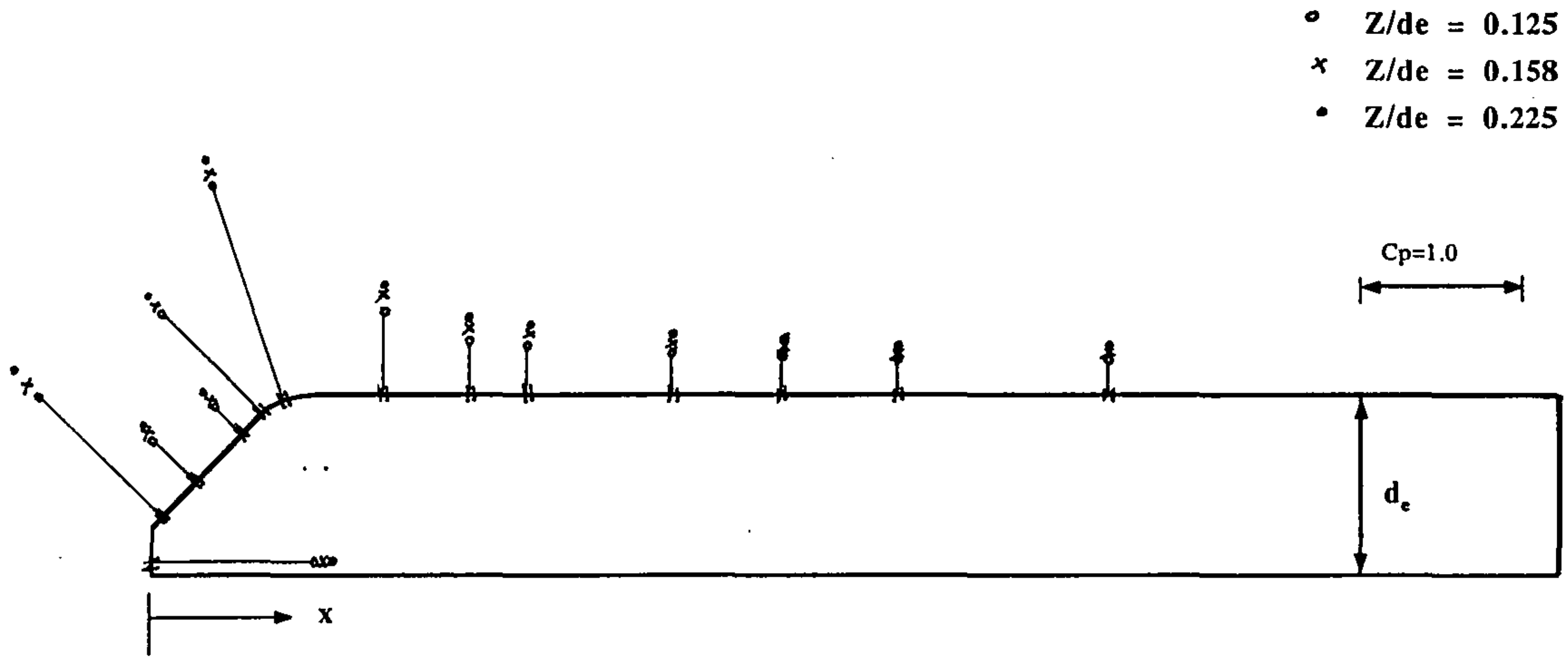

Figure 3-8 Effect of ground clearance on pressure coefficient close to the centre-line of an EMS train model at zero yaw angle

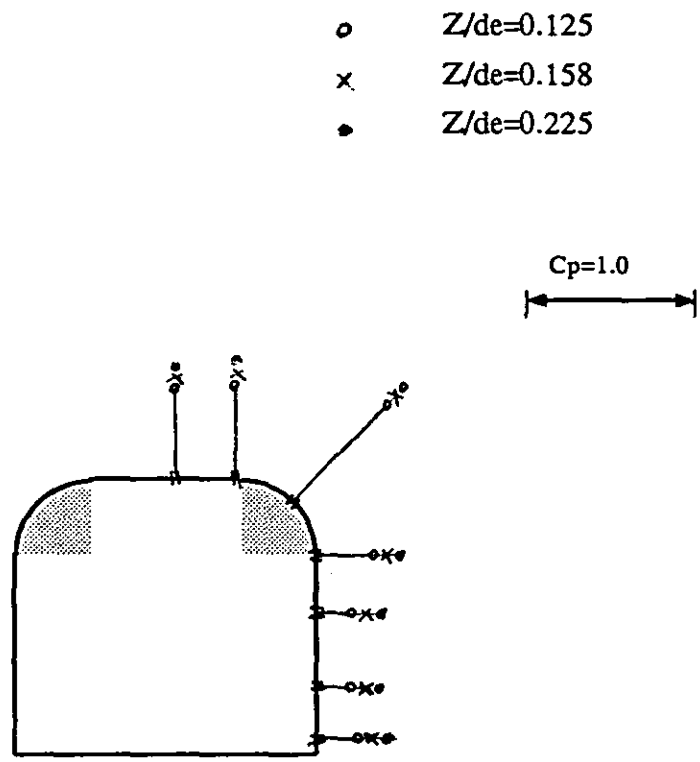

Cross section at section D

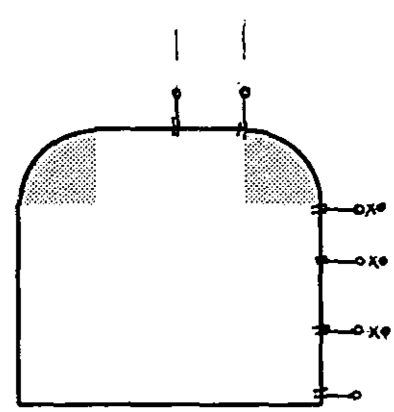

Cross section at section F

Figure 3-9 Effect of ground clearance on pressure coefficient for sections D and F at zero yaw angle.

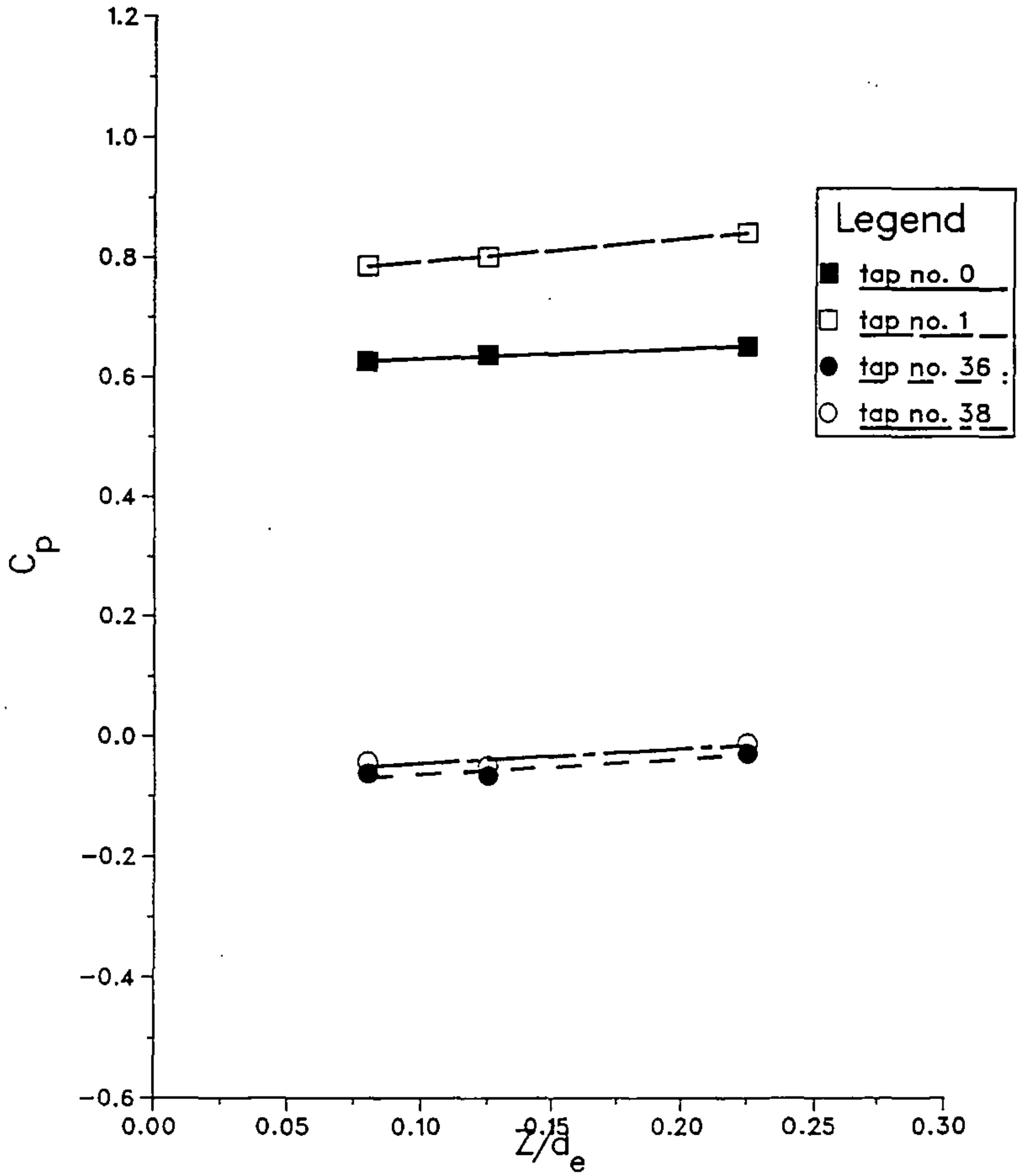

Figure 3-10 Effect of ground clearance on the individual tapping at zero yaw angle, (see Figure 3-3)

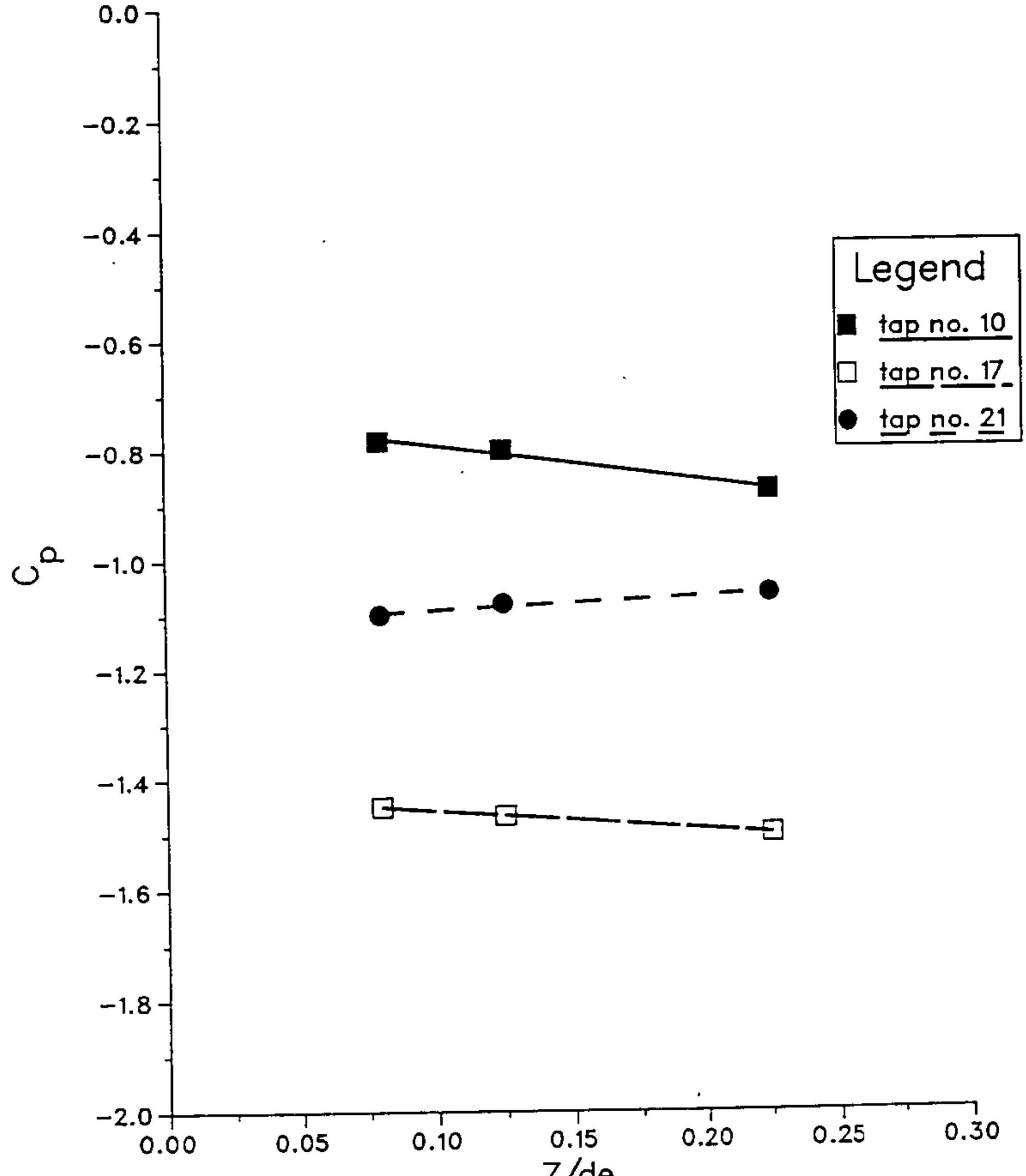

Figure 3-11 Effect of ground clearance on the individual tapping at zero yaw angle, (see Figure 3-3)

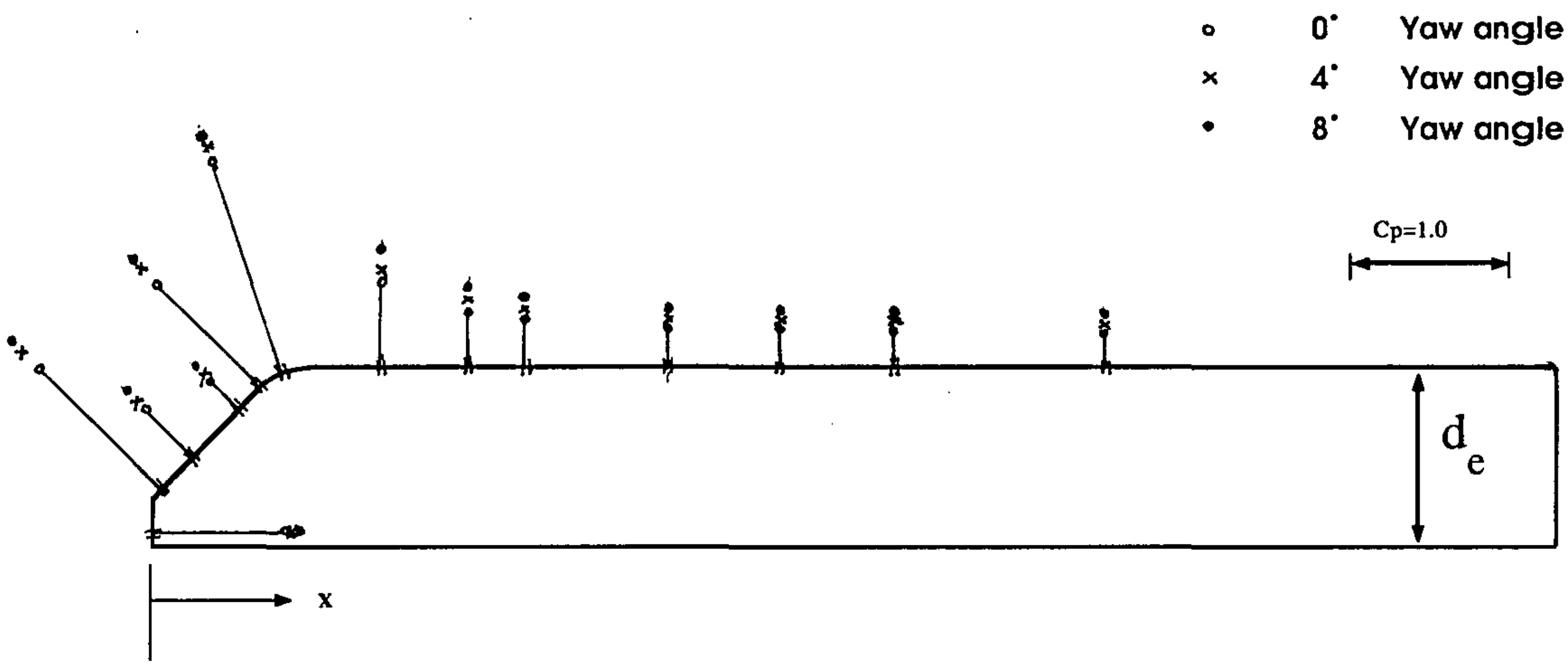

Figure 3-12 Effect of yaw angle on pressure coefficient close to the centre-line of an EMS train model at ground clearance Z/de=0.125

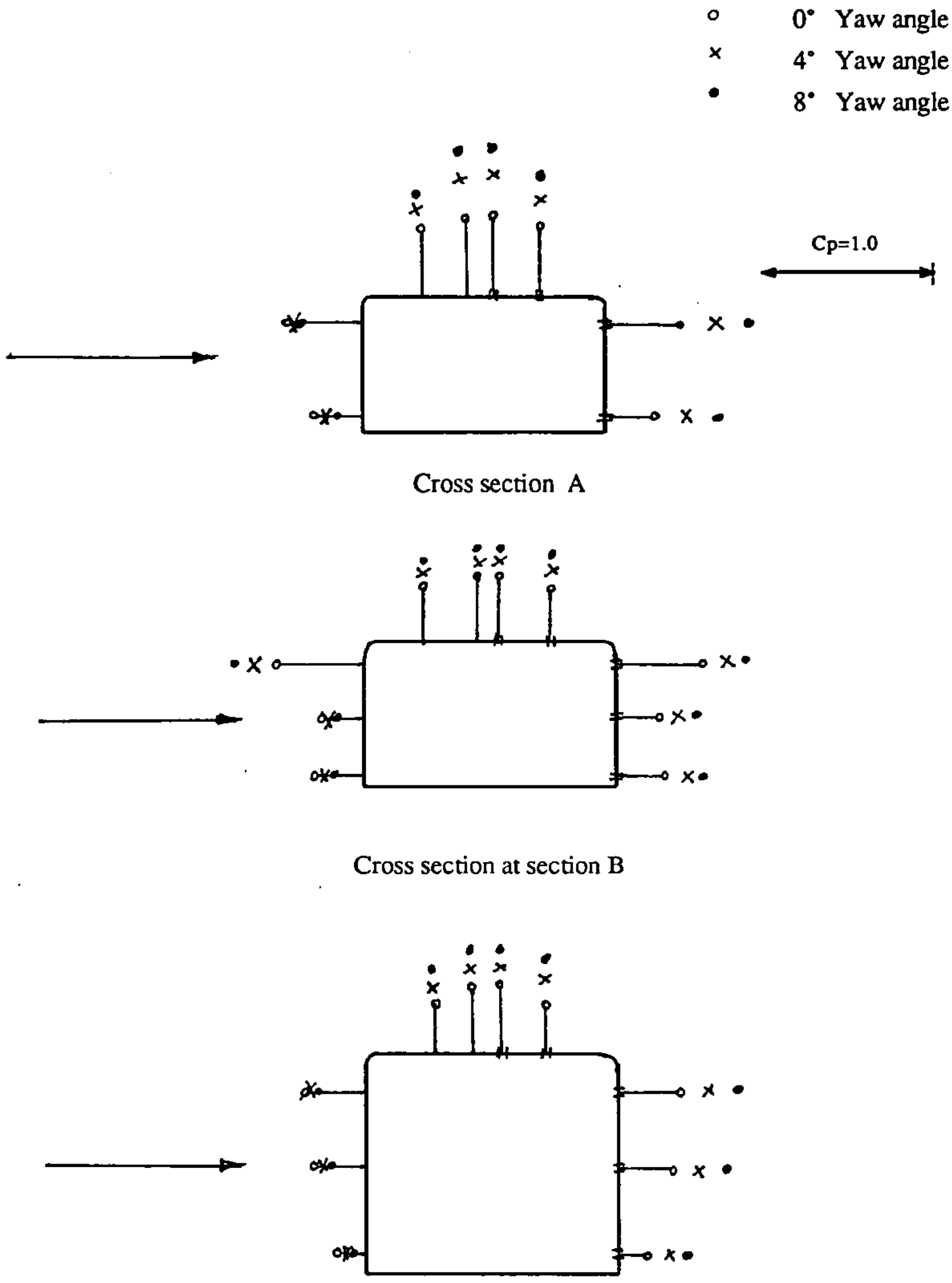

Figure 3-13 Effect of yaw angle on pressure coefficient distribution for sections A, B and C and ground clearance Z/de=0.125.

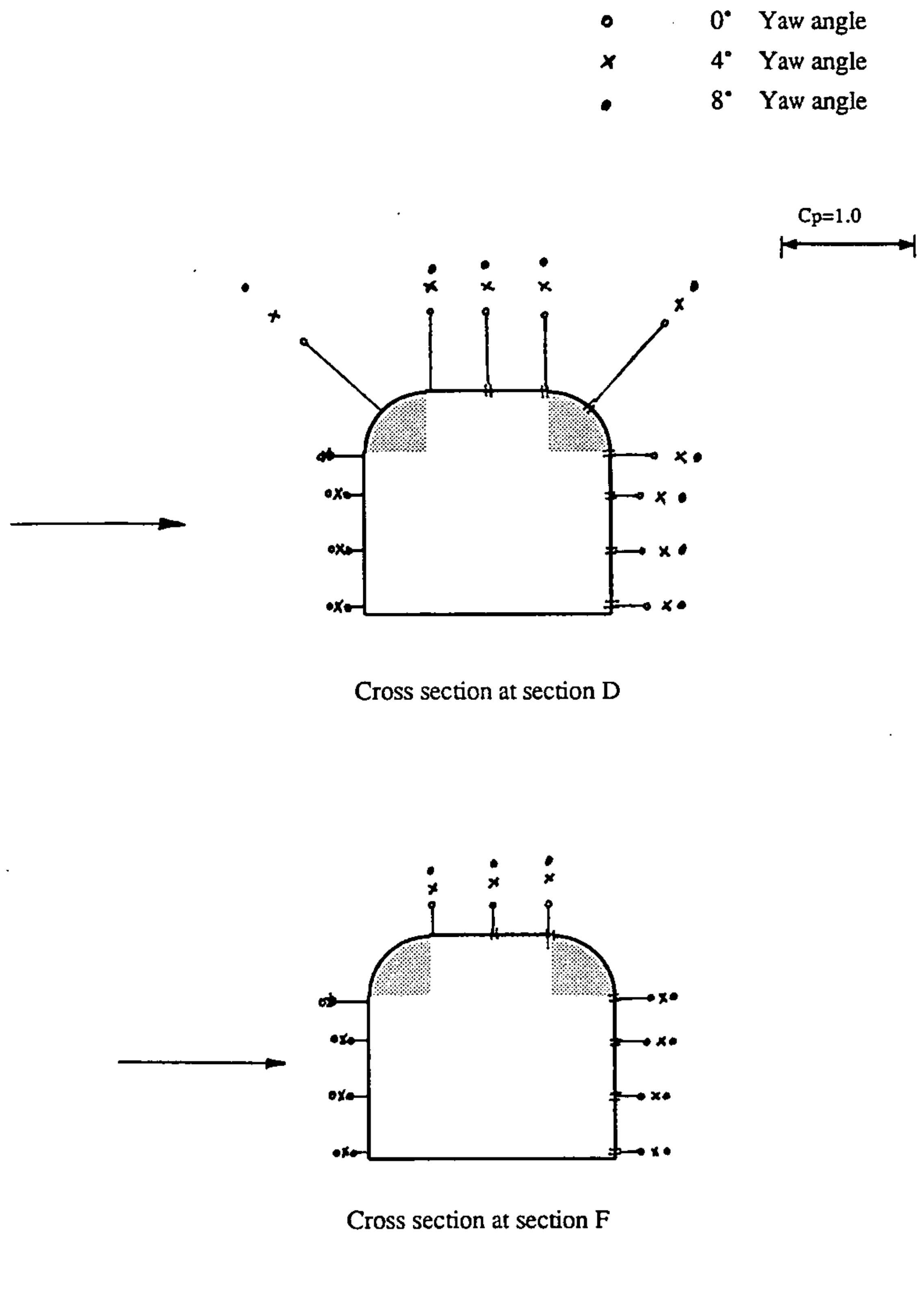

Figure 3-13a Effect of yaw angle on pressure coefficient for sections D and F at Z/de=0.125.

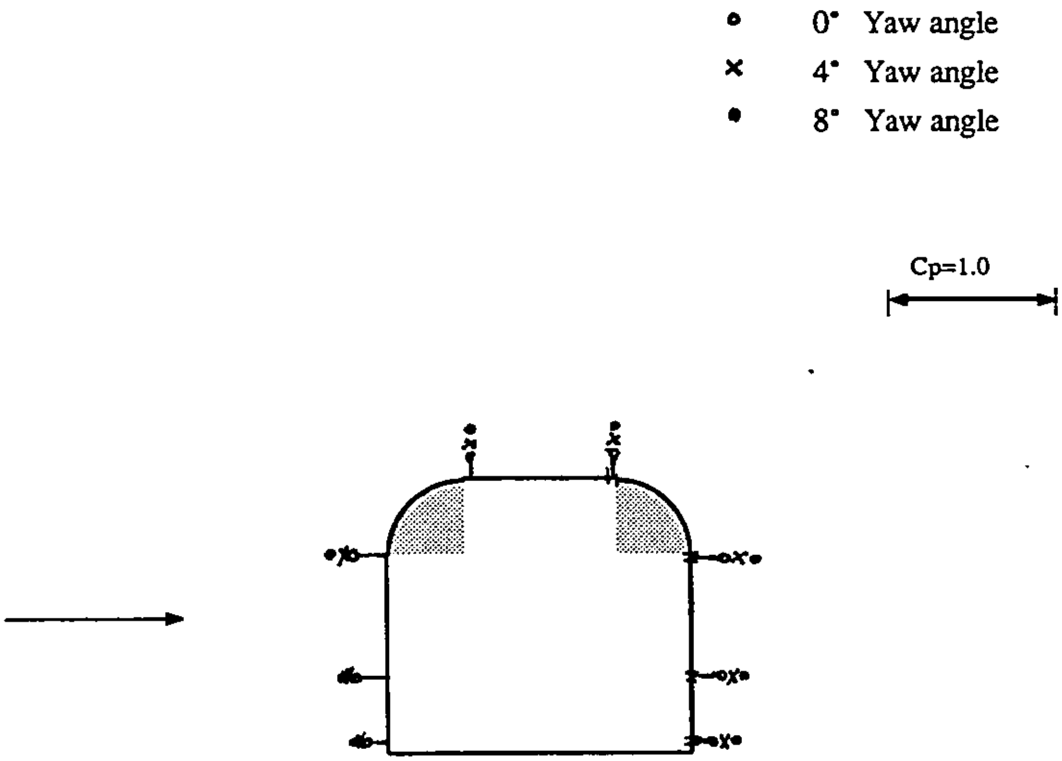

Cross section at section H

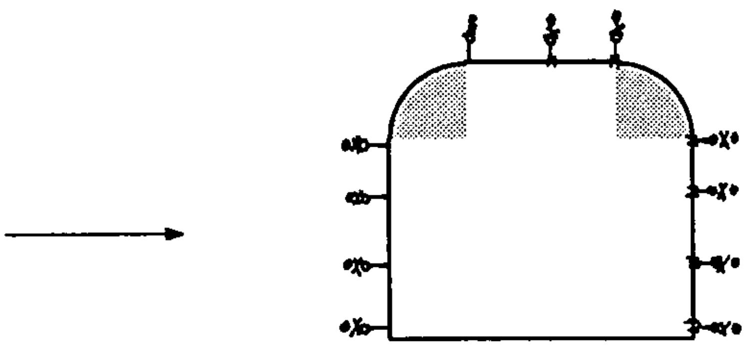

Cross section at section L

Figure 3-14 Effect of yaw angle on pressure coefficient for sections H and L at ground clearance Z/de=0.125.

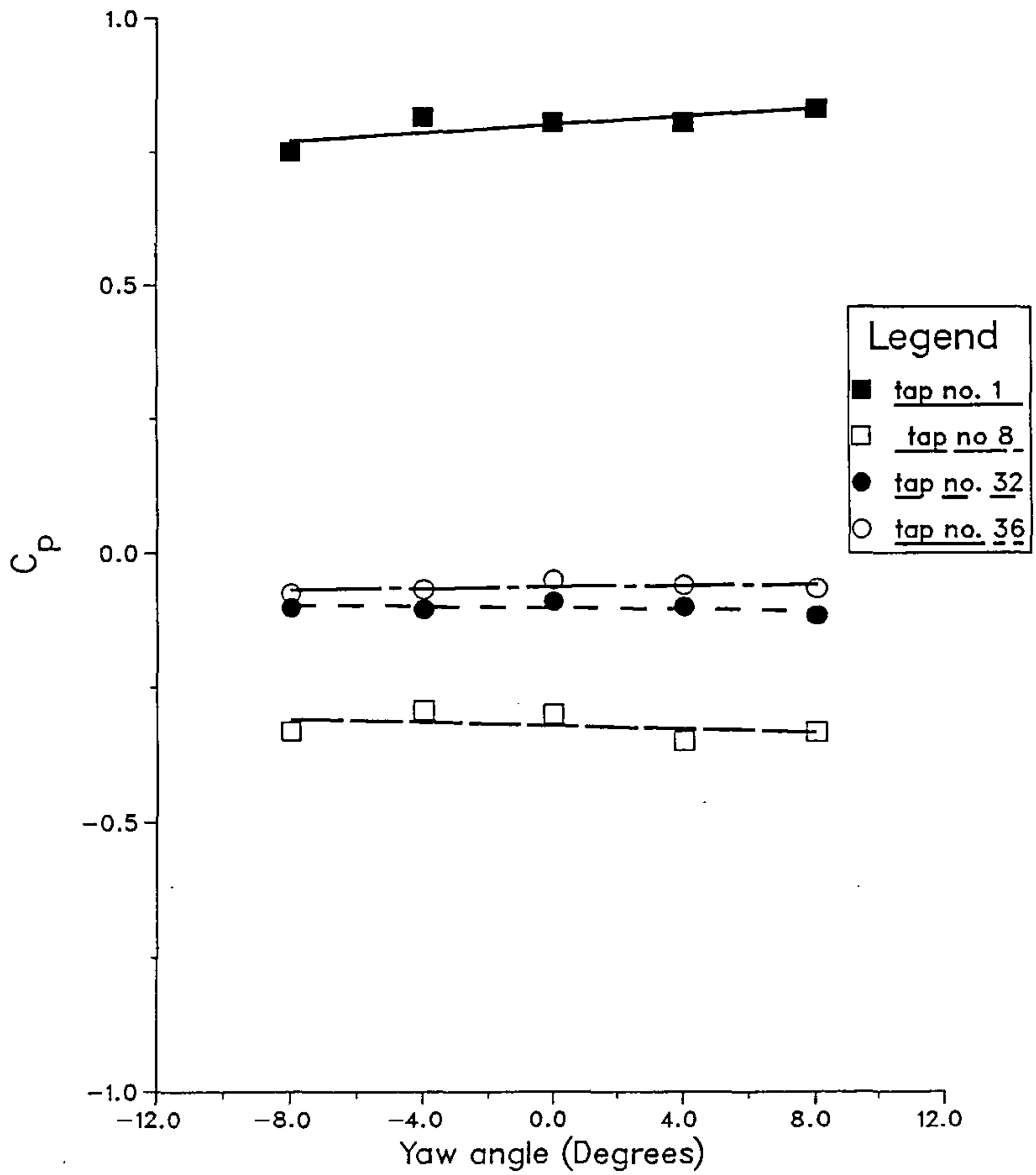

Figure 3-15 Effect of yaw angle on the individual tapping at ground clearance Z/d_e=0.125, (see Figure 3-3)

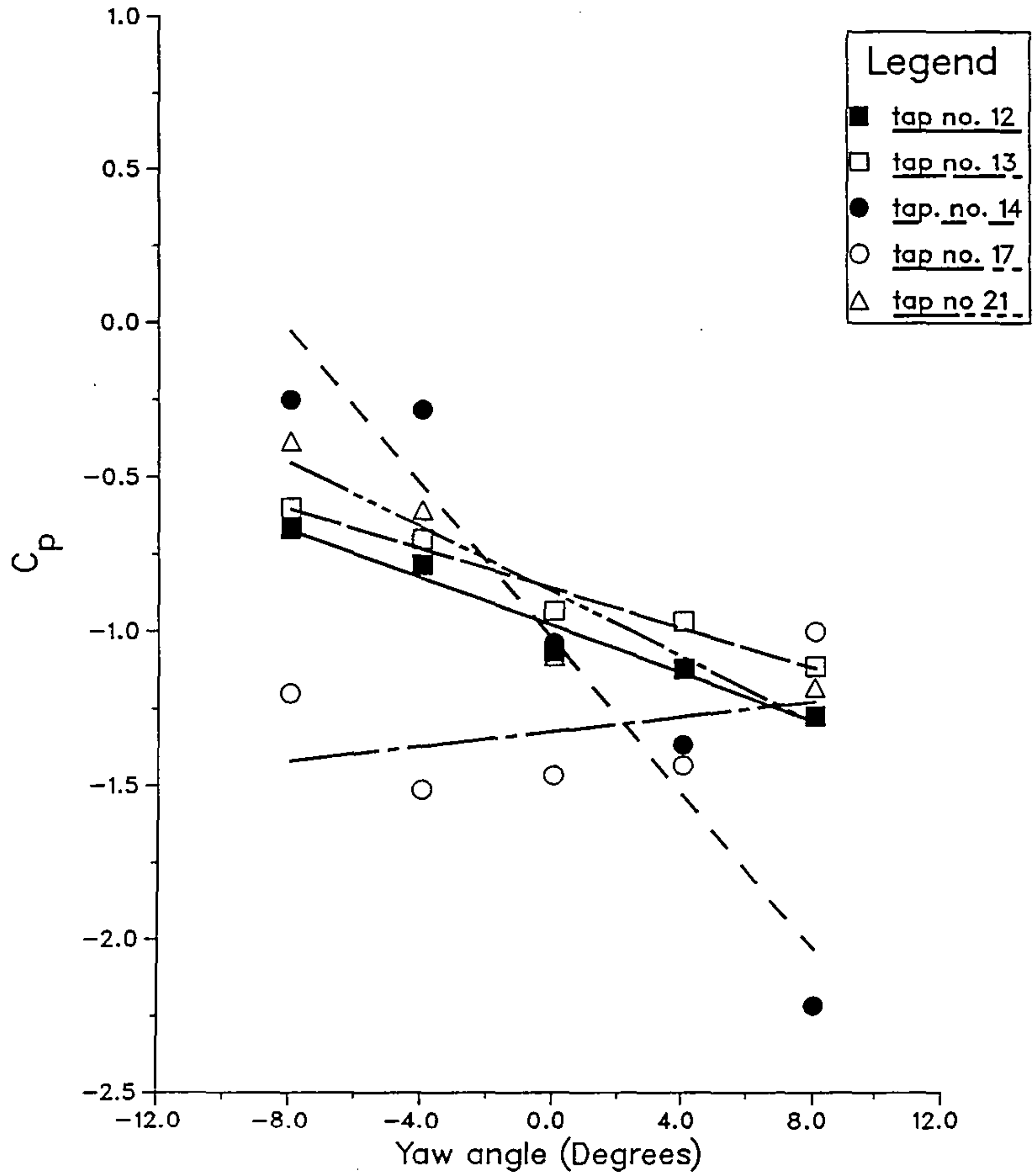

Figure 3-16 Effect of yaw angle on the individual tappings at ground clearance Z/d_e=0.125, (see Figure 3-3)

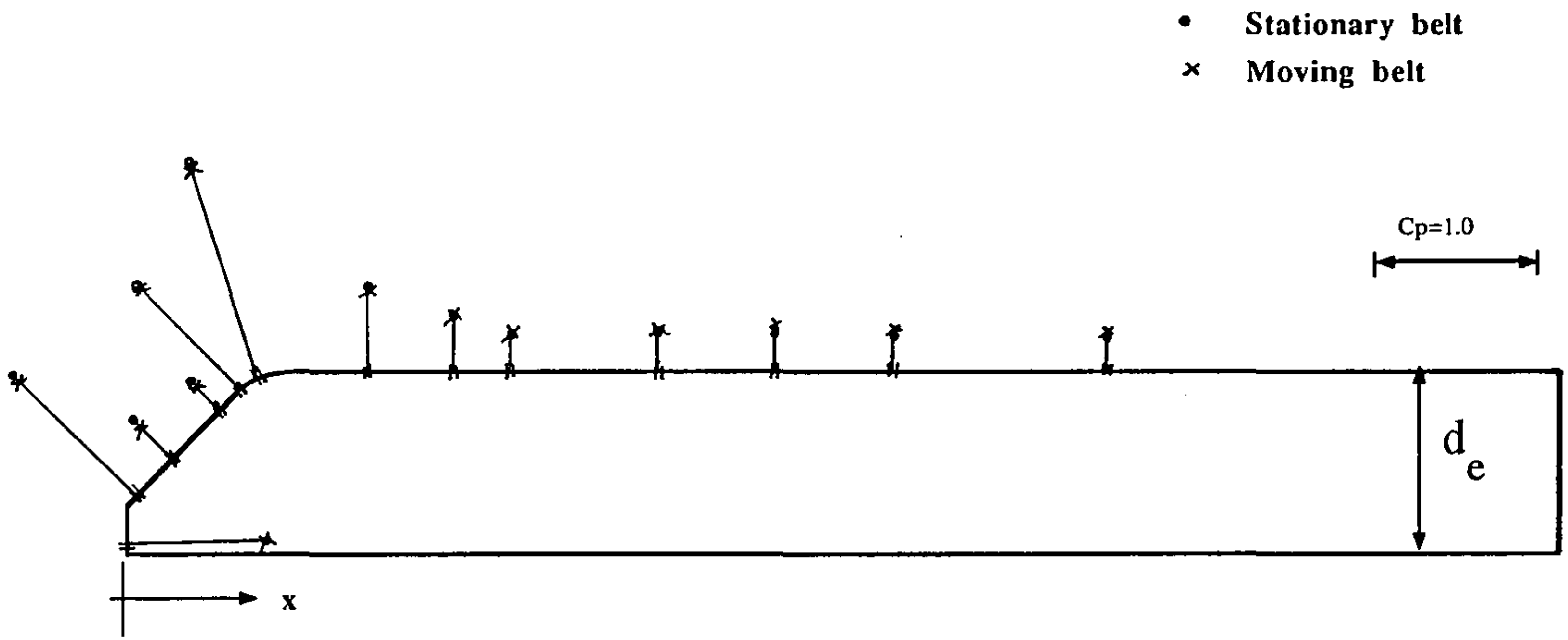

Figure 3-17 Effect of ground simulation on pressure coefficient close to the centre-line of an EMS train model with zero yaw angle and ground clearance Z/de=0.125

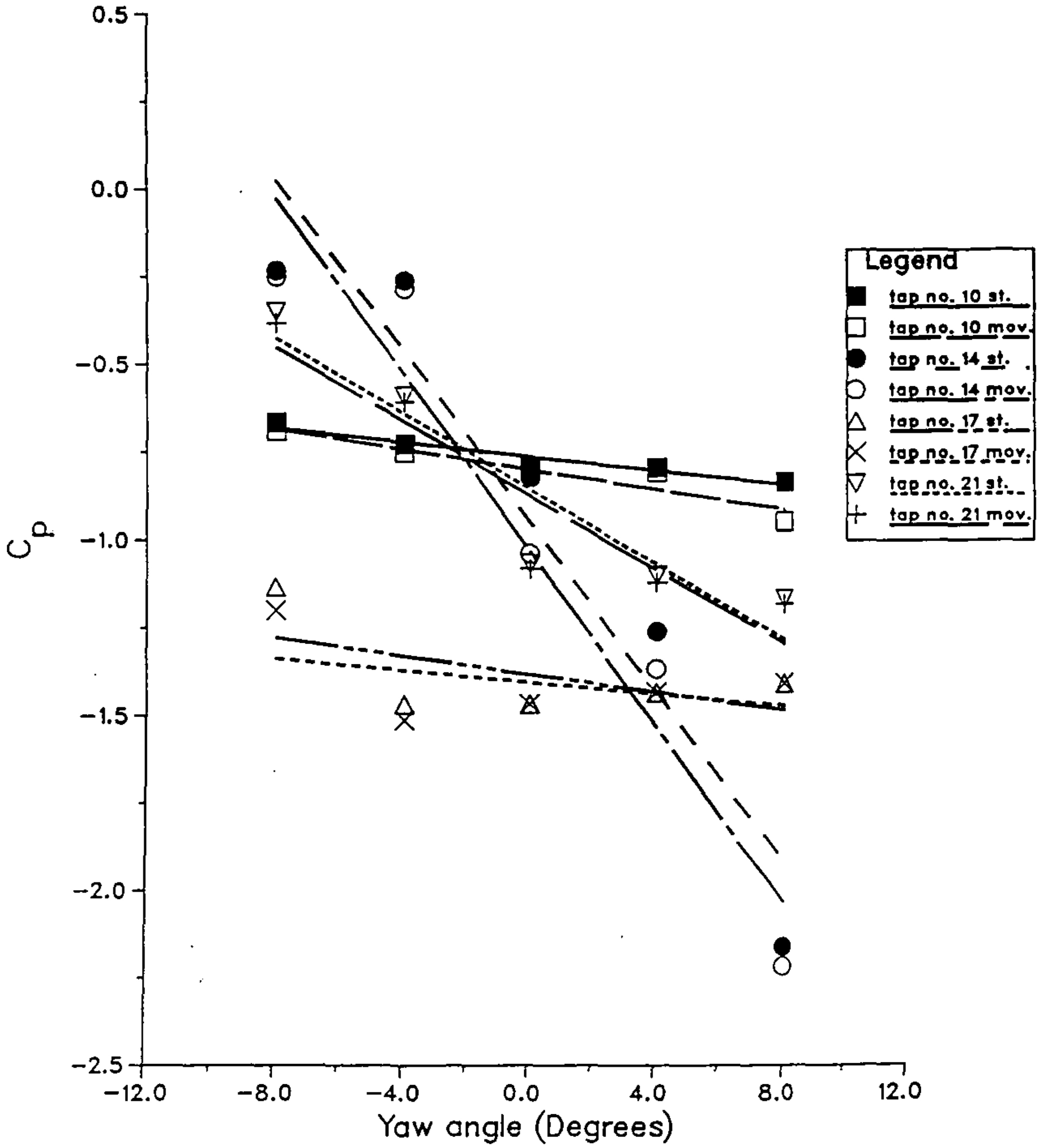

Figure 3-18 Effect of yaw angle on the individual tappings at ground clearance Z/d_e=0.125, (see Figure 3-3)

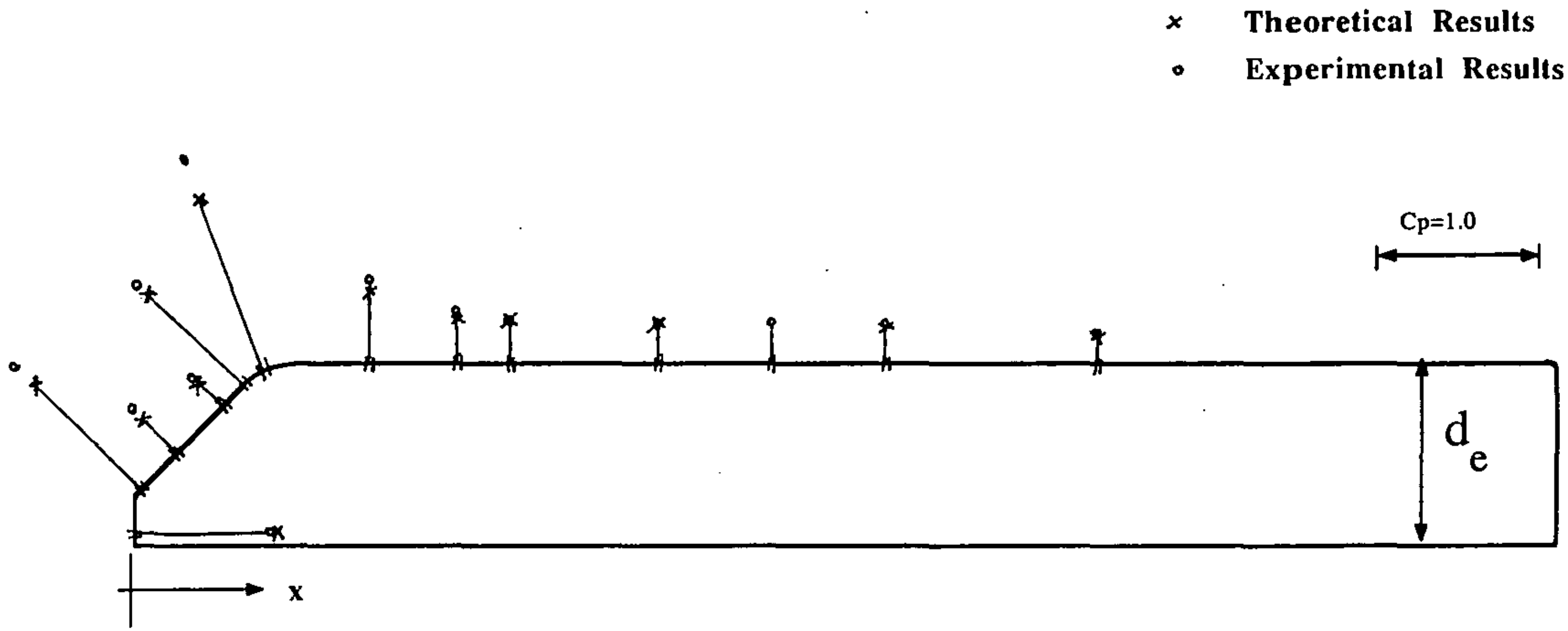

Figure 3-19 Comparison of the experimental results with their theoretical potential flow prediction for pressure coefficient distribution, close to the centre-line, for zero yaw angle and ground clearance Z/de=0.125

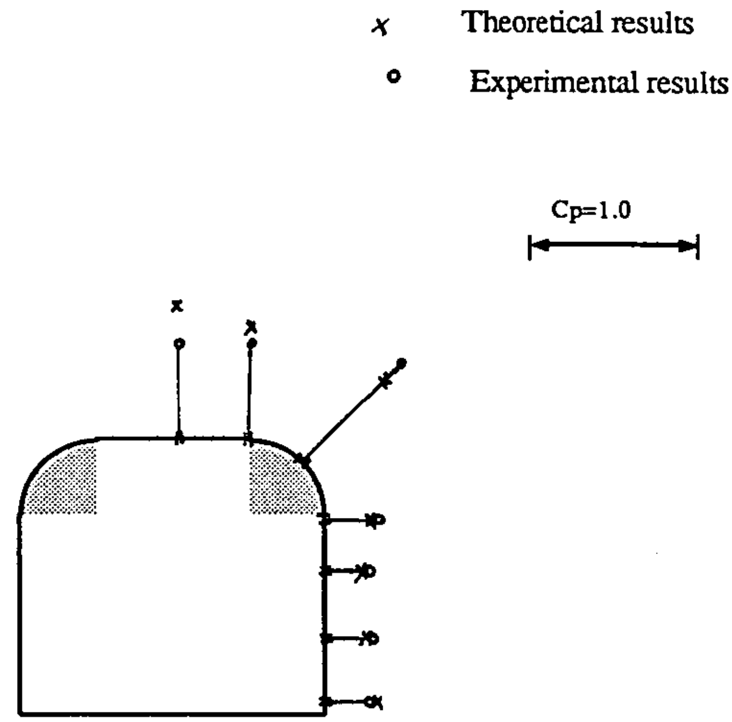

Cross section at section D

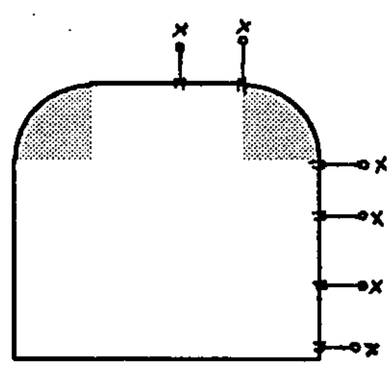

Cross section at section F

Figure 3-20 Comparison of the experimental results with their theoretical poptential flow prediction for sections D and F, zero yaw angle and ground clearance Z/de=0.125.

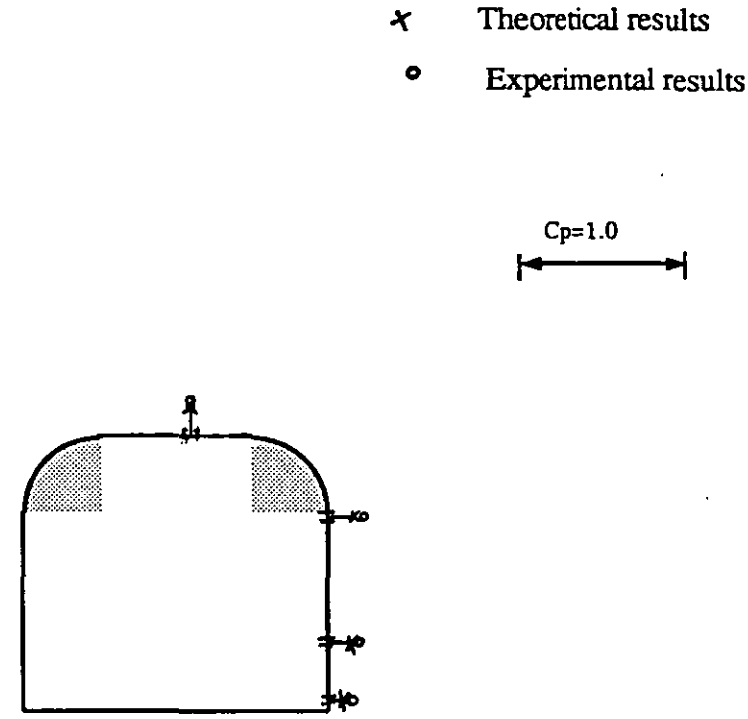

Cross section at section H

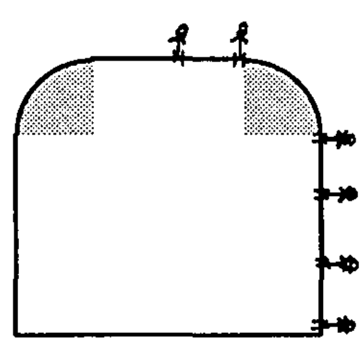

Cross section at section L

Figure 3-21 Comparison of the experimental results with their theoretical poptential flow prediction for pressure coefficient distribution for sections H and L, zero yaw angle and ground clearance Z/de=0.125.

CHAPTER 4

WIND TUNNEL FLOW VISUALISATION TESTS ON AN EMS TRAIN MODEL

4.1 Introduction

A series of wind tunnel flow visualisation tests were carried out on EMS train models to provide supporting evidence to add to the pressure distributions over the model surface obtained in chapters two and three. The tests were performed at different angles of yaw, with and without ground simulation to determine the effect of the ground clearance on the form of the flow around the train.

Wake vortices in the lee side of the train affect the pressure distribution and hence the overall aerodynamic forces. Therefore, flow visualisation on the lee side was also performed to study the vortex wake, for the train at yaw, to help assess its influence on the measured aerodynamic forces and moments which are presented in chapter five.

The remainder of the chapter is in five sections. Section 4.2 provides a summary of the flow visualisation techniques employed in the tests. This is followed by section 4.3 which provides an outline of the test programme carried out using an open-jet and a small smoke wind tunnel. Section 4.4 presents details of the two EMS train models i.e. 1/25 and 1/63 scale models. The test results are discussed in section 4.5 and the chapter ends with concluding remarks in section 4.6.

4.2 Flow Visualisation Techniques

The air-flow visualisation test programme on EMS train models employed three standard techniques, namely : tuft and spinner probes; oil suspension; and smoke.

In the tuft and spinner technique , the tuft probe was a metal rod 670 mm in length with a 130 mm long tuft at its end. This was used to investigate the attached flow, flow direction and separated flow regions around, behind or far from the model. A vortex probe made from a metal rod 765 mm in length with a small spinner at its end was employed to study vortices in the flow, the flow direction and the steadiness of the flow.

The oil suspension technique used titanium dioxide powder added to silicone fluid and stirred to produce a uniform white mixture suitable for painting over the model surface. If the mix is too light the flow pattern is likely to be unclear and if the mix is too thick the details of the flow are lost.

The smoke technique employs a smoke-jet nozzle, which issues white smoke, and is fitted ahead of the model in a low velocity smoke tunnel.

4.3 Outline of the Test Programme

4.3.1 Open-jet Wind Tunnel

The two basic techniques (tuft and spinner, and oil suspension) were carried out in the open-jet wind tunnel, as this allows a larger model to be used and provides more space around the model. A fixed board was used to simulate the ground. The tests were carried out at a Reynolds Number (based on the free stream velocity and the equivalent diameter of the train cross-section) of 4.37×10^5 as in the pressure survey studies. Figure 4-1 shows the general layout of the open-jet wind tunnel.

Tunnel working section

cross section	: 1.06 m wide × 0.91 m high
length	: 1.37 m
maximum speed	: 30 m/s
longitudinal turbulence	: 0.45–0.6% at the measurement section [82]
Ground board	: 0.91 m × 0.91 m

4.3.2 Smoke Wind Tunnel

The smoke wind tunnel is a low speed-wind tunnel with a jet nozzle positioned ahead of the model to supply a white smoke of vapourised oil pressurised by nitrogen. A fan is fixed to the other end of the tunnel to accelerate the smoke. The yaw angle and plane of the smoke is controlled manually. The tunnel is supplied with eight high-wattage bulbs to make photography easy and to keep the working section clear. Figure 4-2 shows features of the layout of the smoke wind tunnel. The tunnel speed is 0.5 m/sec, giving a Reynolds number (again based on the mainstream velocity and the equivalent diameter) of 2.06×10^4. At this low Reynolds number a reasonable impression of the wake vortices in the lee side of the train can be obtained although the points of which flow separation occur will be different at the higher Reynolds number associated with a real train. At best therefore, the smoke tunnel results give a qualitative impression of the vortex formation present in the higher Reynolds number tests of the other flow visualisation work and the pressure measurements.

Tunnel working section

Height : 0.452 m

Width : 0.475 m

Length : 1.42 m

4.4 EMS Train Models

The flow visualisation tests were applied to one of two EMS train models according to the size of the working section of the test tunnels used; these models were :

Model 1

A 1/25 scale model, shown in Figure 4-3 in the open jet wind tunnel with the following dimensions :

Height : 0.149 m

Width : 0.151 m

Length : 2.25 m

The model is made in two identical front and rear parts, both halves are identical both internally and externally.

Model 2

This model is an a 1/63 scale and is shown in Figure 4-4. It is a solid wooden model of the front half of the train made to fit the smoke tunnel working section. The model's centre was fixed in the tunnel by a metal rod attached to allow its yaw angle to be varied. The model dimensions were.

Height : 0.06 m

Width : 0.061 m

Length : 0.45 m

4.5 Test Results

The flow visualisation tests were carried out on both EMS train models with and without the presence of the ground board at different yaw angles namely, 0°, 10°, 22°, 45°, and 90°. The main results are presented in the next sub-sections. It is noted that the flow visualisation tests were carried out at larger yaw angles than those used for the panel method prediction and pressure measurements. This was done in order to study the wake vortices which dominated the lee side of the train and affect the side force at high yaw angle. Thus, at least some experimental information has been provided for an EMS train model at high yaw angles, even though the prediction procedure of chapter two is invalid under these conditions.

4.5.1 0° Yaw Angle

The flow pattern at the surface of the model (see Figure 4-5) was deduced by use of the tuft and spinner technique in the absence of the ground simulation. The Figure shows the direction of the local flow and indicates that the flow is attached over most of the model's surface except for the side corner edge of the nose and the front of the roof. Figure 4-6 shows the flow direction and region of separation in the presence of the ground simulation using the same flow visualisation technique. This Figure shows that the ground board has a significant effect, deflecting the flow upwards over the train. With respect to the flow of Figure 4-5 the region of separation at the roof front grows as well as extending the strips of of separation on the roof corners. This is because the ground simulation changes the nature of the flow underneath the model : the flow velocity is decreased, this together with the introduction of a turbulent boundary layer on the ground simulator leads to an increased flow angle over the front face of the train.

Figure 4-7 comprises two photographs which show the flow pattern using the smoke technique. Each photograph represents the flow at a particular flow plane. Thus the top photograph is for the flow over the roof of the train. The other photograph is for the flow approximately mid-way between the roof and floor of the train. Figure 4-7 shows (1) a separated flow region on the upper side corners, i.e. the "shoulder", at both sides of the nose of the model ; (2) separated flow and vortices appear on the roof of the train ; and (3) the flow elsewhere returns back to a steady attached flow, after a short distance downstream of the nose. Both the tuft and spinner eviedence as well as the smoke technique (see Figure 4-6 and Figure 4-7) suggest the existence of two regions of vorticity at each side of the train roof downstream of the nose (see Figure 4-8).

Figure 4-9 comprises two photograph for the same flow conditions which show the flow pattern using the oil suspension technique, in this separation lines appear on both side corner edges of the nose.

In passing, it is important and interesting to compare here qualitatively these flow visualisation results with the results from the three-dimensional potential flow prediction (chapter two) and the measured pressure distribution (chapter three). The flow visualisation results, at 0° yaw angle, are consistent with the calculated and measured pressure coefficient distribution. For example, the flow visualisation results at 0° yaw angle show separated flow regions on the side corner edges of the train nose and the front of the roof of the train : these regions coincide with the adverse pressure gradient zones observed in both prediction and pressure survey. This also explains the observed exessive negative values predicted for the pressure coefficient since separation will tend to relieve these pressures.

4.5.2 10° Yaw Angle

The flow pattern at this yaw angle using the tuft and spinner technique in the absence of the ground simulation is shown in Figure 4-10. The Figure shows that on the lee side there is a strong wake vortex, with another wake vortex on the front roof and a small strip along the corner edge of the roof. The flow over the rest of the model remains attached except for a small region of disturbance at the top of the corner on the windward side (see marked zone in Figure 4-16). Figure 4-11 shows the flow direction and separation region using the the tuft and spinner technique in the presence of the ground simulation. The Figure shows that in comparison with the zero ground effect case the top view separated flow region is again lengthened due to the upwards deflection of the onset flow, although less than at zero yaw. At this yaw angle the formation of a ground vortex is a further significant difference induced by the ground flow.

Figure 4-12 shows the corresponding flow pattern using the smoke technique. The Figure shows the wake vortex and separated flow on the lee side of the model and separated flow on the front of the roof. The flow direction on the roof of the train is seem to be deflected more than the yaw angle perhaps due to the wxessive effect of the lateral pressure gradient on the slow moving fluid near the train roof. The Figure also shows that two wake vortices occur in the lee side of the train. One originates from the ground floor as indicated in Figure 4-11 and the other from the roof of the train.

4.5.3 22° Yaw Angle

Figure 4-13 shows the flow pattern at yaw angle 22° using the tuft and spinner technique in the absence of the ground simulation. The Figure shows a wake vortex on the lee side corner and another wake vortex at the bottom of the lee side while the flow over the windward side of the model remains predominantly attached. The ground vortex is shorter on the lee than on the windward side. Figure 4-14 shows the flow pattern in the presence of the ground simulation. It shows that the wake vortex in the lee side is larger in size than at yaw angle 10° (see Figure 4-11) and there is now a vortex that takes the form of a long strip along the bottom of the model. The flow angles are increased (in comparison with the flow in Figure 4-13) and a vortex region now appears over the nose roof. The roof side shows a separated flow region and a strip shaped vortex wake in the lee side. The flow over the windward side remains attached. Figure 4-15 consists of two photographs which show two wake vortices along the length of the train, one from the ground and the other from the roof. The wake vortices are nearly double the size (as measured by the vortex correlation factor, see Figure 4-24) of those which occur at 10° yaw angle (see Figure 4-12). The flow on the windward side of the model remains attached.

Figure 4-16 presents of two photographs which show the flow direction and flow separation lines in the lee side and on the roof of the model using the oil suspension technique. The Figure shows a separation line starting at the beginning of the inclination of the nose along the front edge, see arrow labelled A. There is another line starting from the same point, making a small angle with the first flow separation line mentioned above (arrow labelled B). Flow separation lines also appear in the roof of the nose, indicated by arrows labelled C and D.

The flow visualisation tests described here for 22° yaw angle show that there are two wake vortices in the lee side of the train, one from the ground side and the other from the roof side and the vortices move away downstream along the length of the train. Thus the flow visualisation methods used give consistent results. Figure 4-17 shows the two vortices along the train and their locations with respect to the cross section on the train.

4.5.4 45° Yaw Angle

Figure 4-18 shows the flow pattern using the tuft and spinner technique. The Figure shows that there is a flow disturbance region and a wake vortex on the lee side. There is a strip shaped disturbance region and and a wake vortex along the top edge of up to more than half of the tested length of the model which is larger than those occuring at 10° and 22° because at 45° yaw angle the adverse pressure gradient is higher. There is also another strip shaped flow disturbance region at the bottom of the lee side. In the front of the nose the flow starts a steady rotation and the roof shows a separation in the front and a strip of disturbance along the side of the lee side. The flow in the windward side is fully attached.

Figure 4-19 shows the flow pattern in the presence of the ground simulation using tuft and spinner technique. The strengthing and lengthing of the separation region observed at other yaw angles when introducing the ground board is also present here.

Figure 4-20 comprises two photographs which show the flow pattern using the smoke technique. The Figure shows again two wake vortices along the length of the train, as in the case for yaw angles 10° and 22° (see Figure 4-12 and Figure 4-15). The wake vortices for 45° yaw are larger in size and dominate most of the lee side of the model. The flow over the windward side remains fully attached.

4.5.5 90° Yaw Angle

Figure 4-21 shows the flow pattern using the tuft and spinner technique. The existence of two vortices one over the roof and the other underneath the model are the single feayures dominate. The flow in the windward side of the model remain fully attached. Both the flow direction and the disturbance regions are deflected away from the bottom of the train.

Figure 4-22 shows the flow direction and separation lines using the oil suspension technique. The Figure shows a flow separation lines indicating the flow has separated at the windward corner but re-attached before separating again. This may well be due to low Reynolds number effect.

4.6 Concluding Remarks

The main concluding remarks from the series of flow visualisation tests undertaken in this study may be summarised as follows :

1. The flow visualisation test results from the three techniques, at 0° yaw angle, are all in agreement that the corner edge sides and the roof of the nose of the train are regions of flow separation. These flow visualisation results support deductions made from both the predictions for the pressure coefficient and the measured pressure coefficients. The flow visualisation of flow separation occurs in regions indicated by both predicted and measured pressure field as adverse pressure gradient zones. The separation zones are relatively small and localised, supporting the use of an inviscid method for the zero yaw case. This encouraging conclusion suggests that the panel method may be useful for calculating the aerodynamic forces and moments by integrating the pressure distribution over the surface of the model. Similarly the flow velocities calculated by the panel method can be used as main stream velocities for the turbulent boundary layer prediction (at least away

from separation zones), a possibility which is considered later in this thesis.

2. For the train at yaw, there are two wake vortices in the lee side of the train along its length, one originating from the ground and the second from the roof of the train. This leads to the expectation of adverse pressure gradients on this side of the model and explains the negative values of the pressure coefficient and the rapid velocity changes observed in the panel method predictions and measured pressure coefficient. The observed wake vortices can have a significant effect on the aerodynamic forces and moments, specifically by influencing the pressure drag. The effect of the wake vortices needs to be confirmed by experimental tests to measure the aerodynamic forces and moments as presented also in a later chapter.

   From the the results of smoke-based flow visualisation tests, the angle between the roof side wake vortex and the ground wake vortex has been measured. This angle may be called the vortex correlation factor. The available results suggests a linear relation between the yaw angle and the corresponding vortex correlation factor, see Figure 4-25. This linear relation which is probably associated with the generated normal force suggests that the vortex correlation factor is about half the value of the corresponding yaw angle.

3. A fixed board was used to simulate the ground effect on the flow around the model. This simulation shows that the ground effect causes the flow pattern, particularly the region of flow separation and wake vortices to be increased in length relative to their counterparts without ground simulation due to increased flow onset angle.

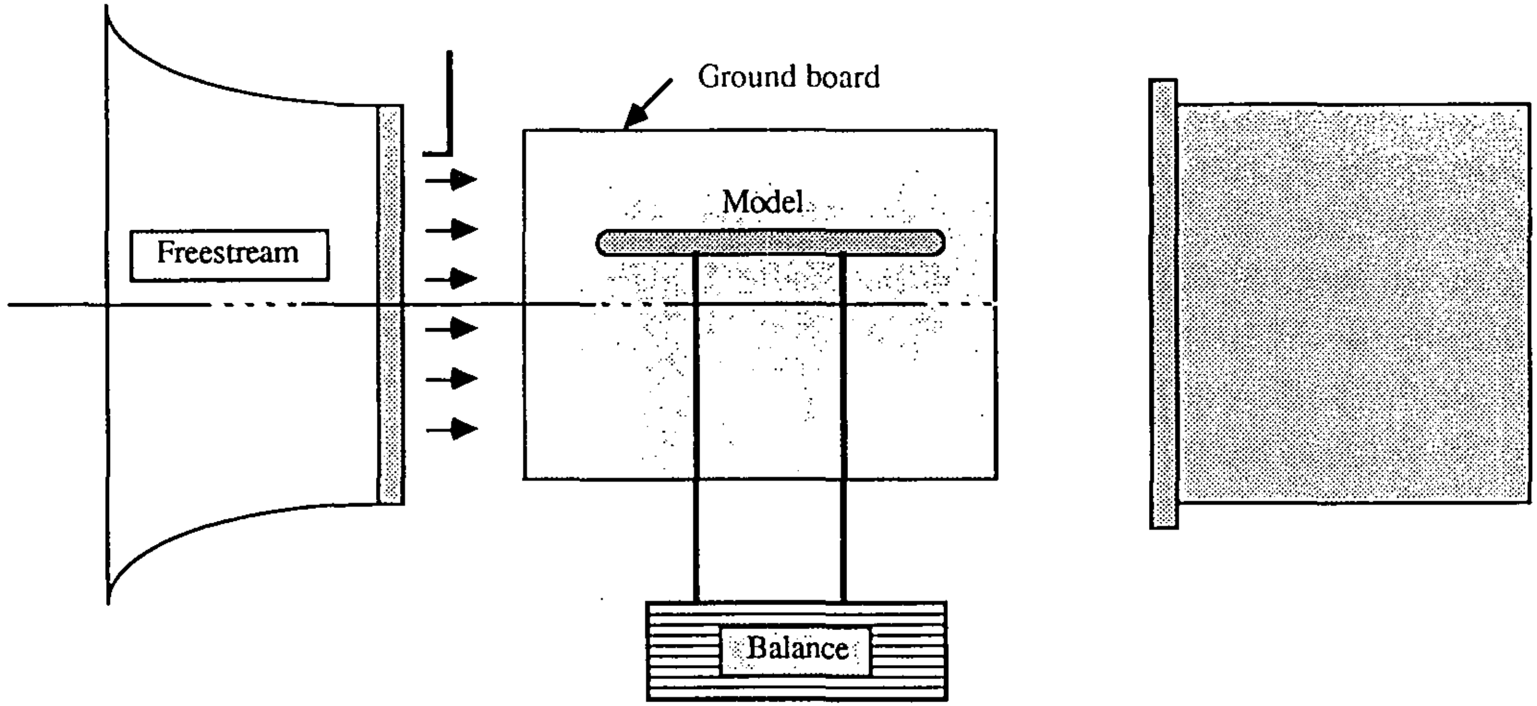

(a) Side view

Figure 4-1 General layout of the open-jet wind tunnel

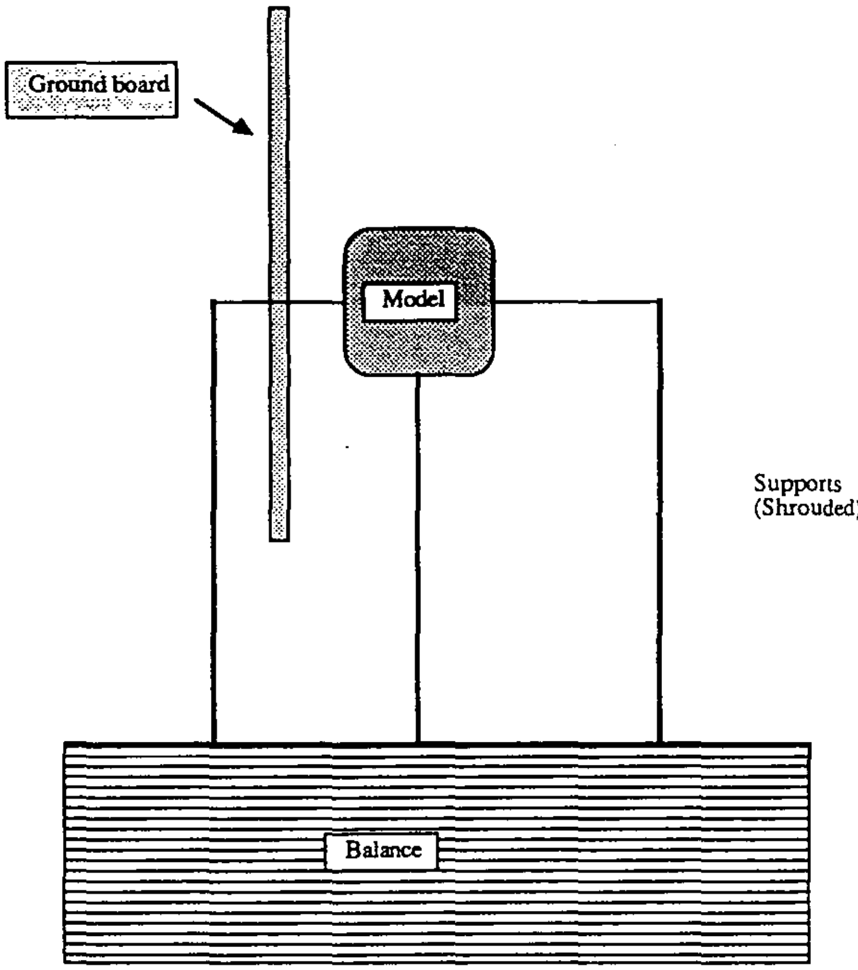

(b) Front view looking downstream

Figure 4-1 Cont.

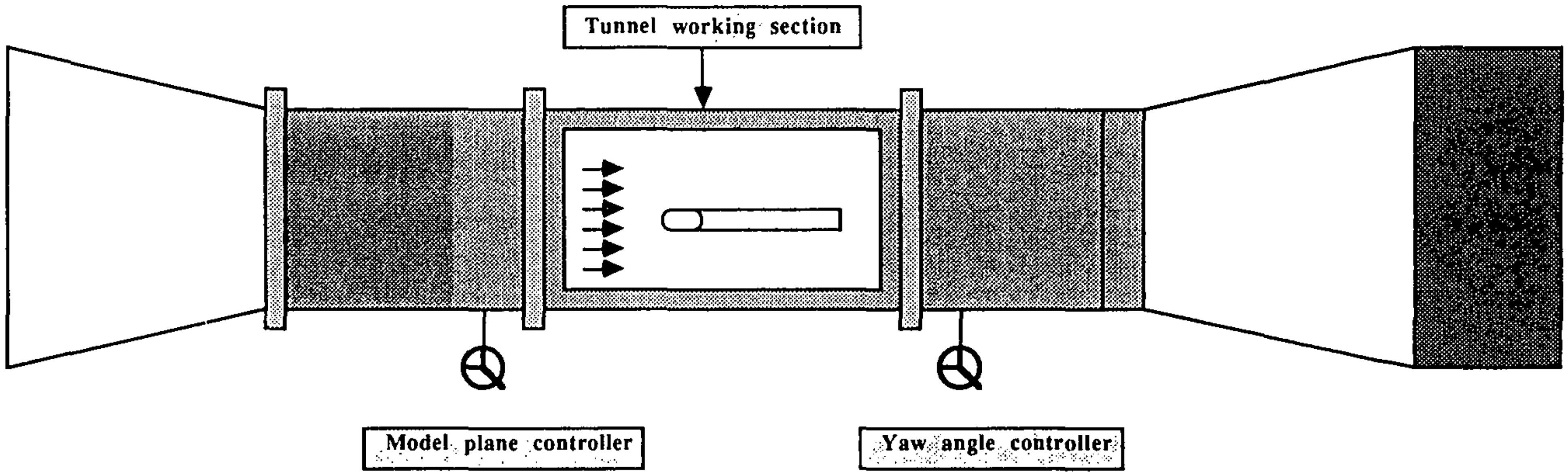

Figure 4-2 General layout of the smoke wind tunnel

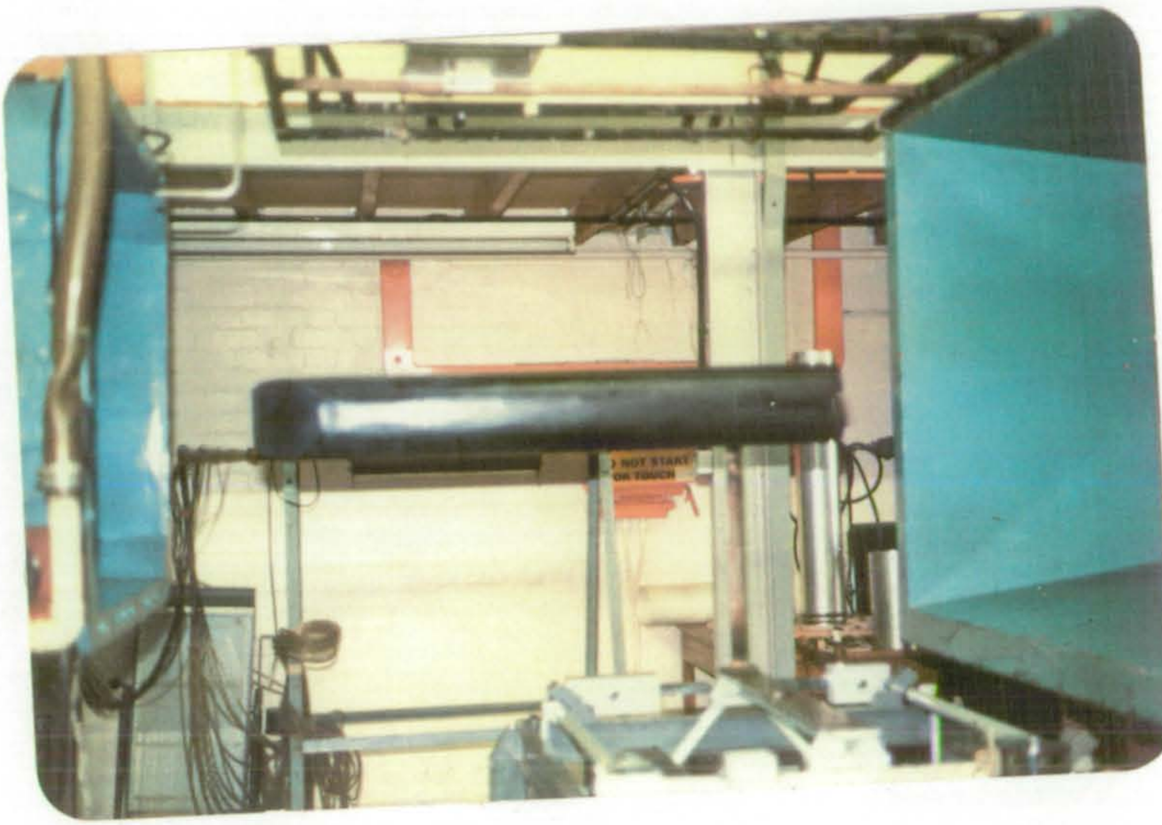

Figure 4-3 EMS train model in the open-jet wind tunnel

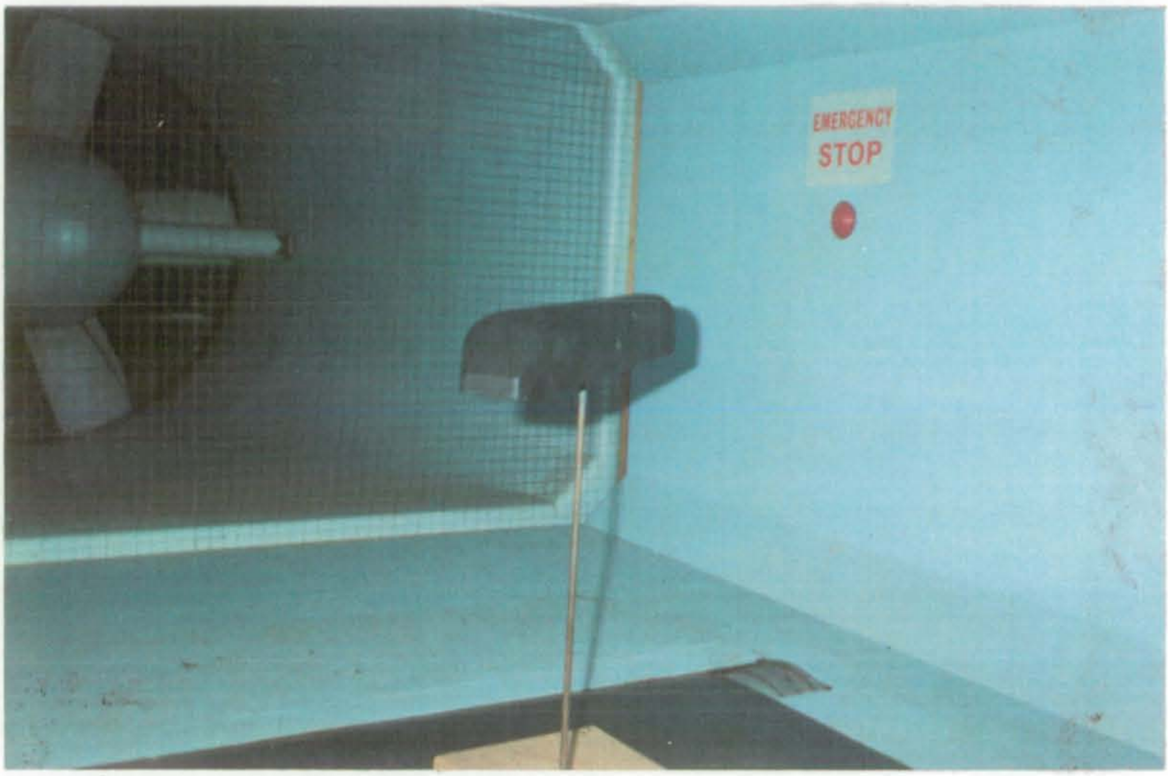

Figure 4-4 EMS train model for wind tunnel tests

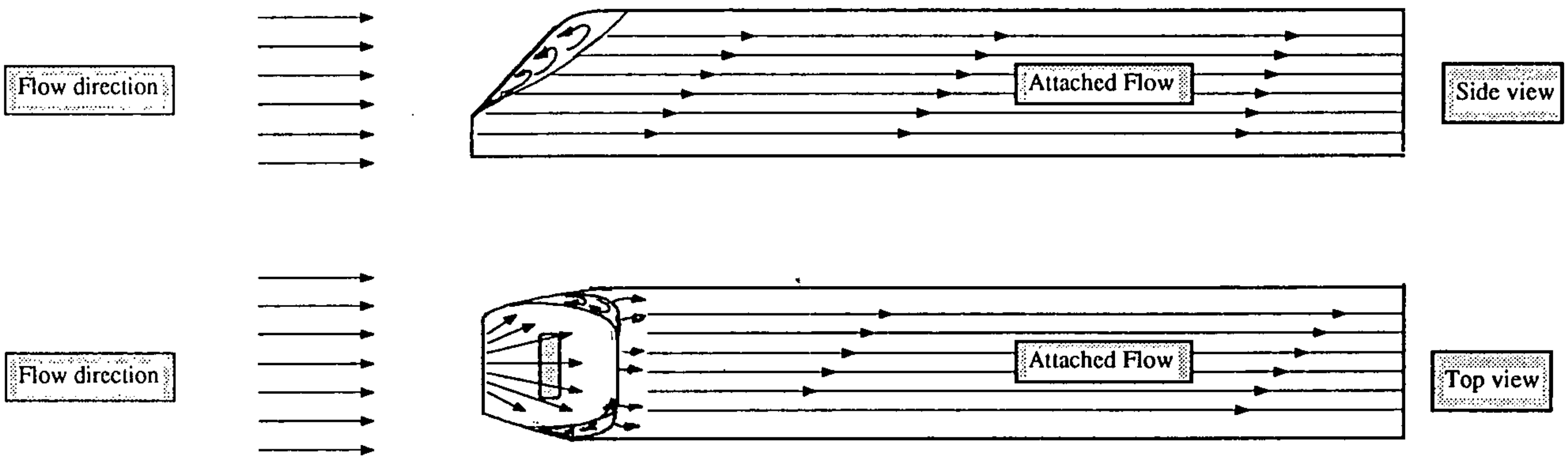

Figure 4-5 Flow pattern at 0° yaw angle in the absence of the ground simulation, using tuft and spinner technique,
$Re = 4.37 \times 10^5$

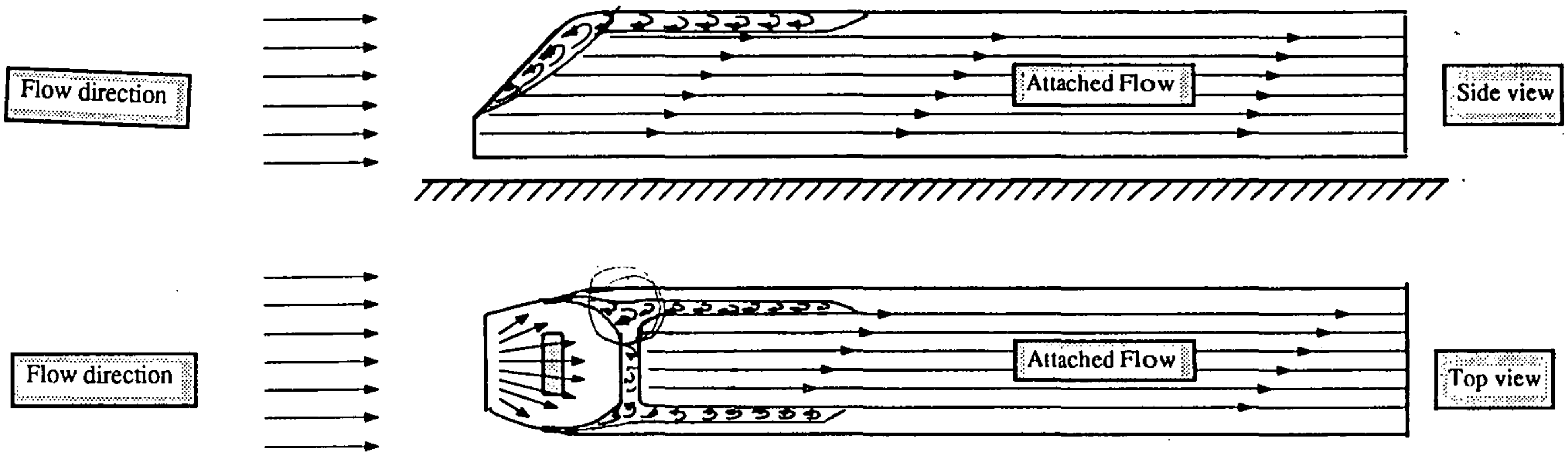

Figure 4-6 Flow pattern at 0° yaw angle in the presence of the ground simulation, using the tuft and spinner technique,
$Re = 4.37\times10^{5}$

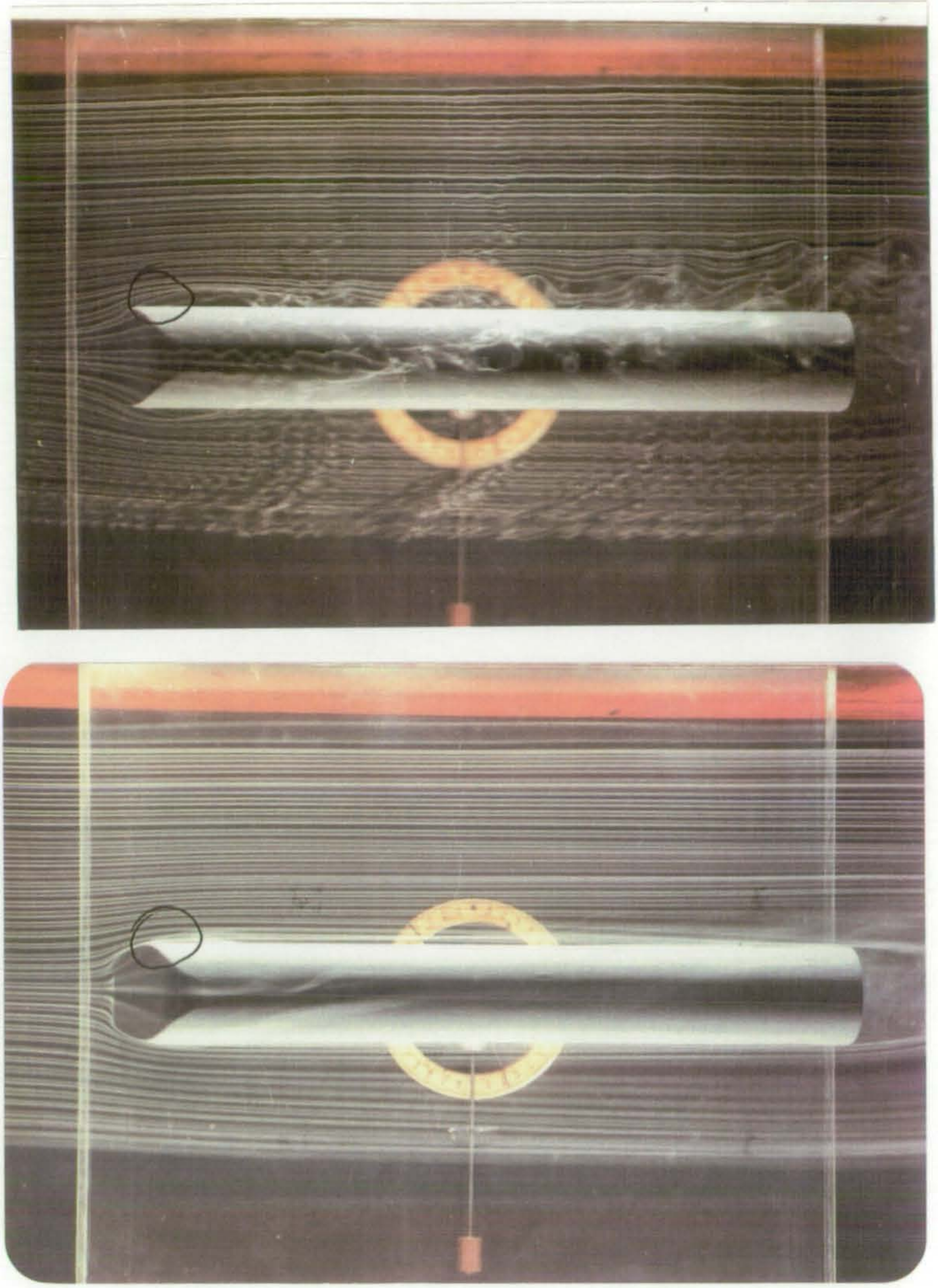

Figure 4-7 Flow pattern at 0° yaw angle in the absence of the ground simulation, for two different planes of flow, using the smoke technique.

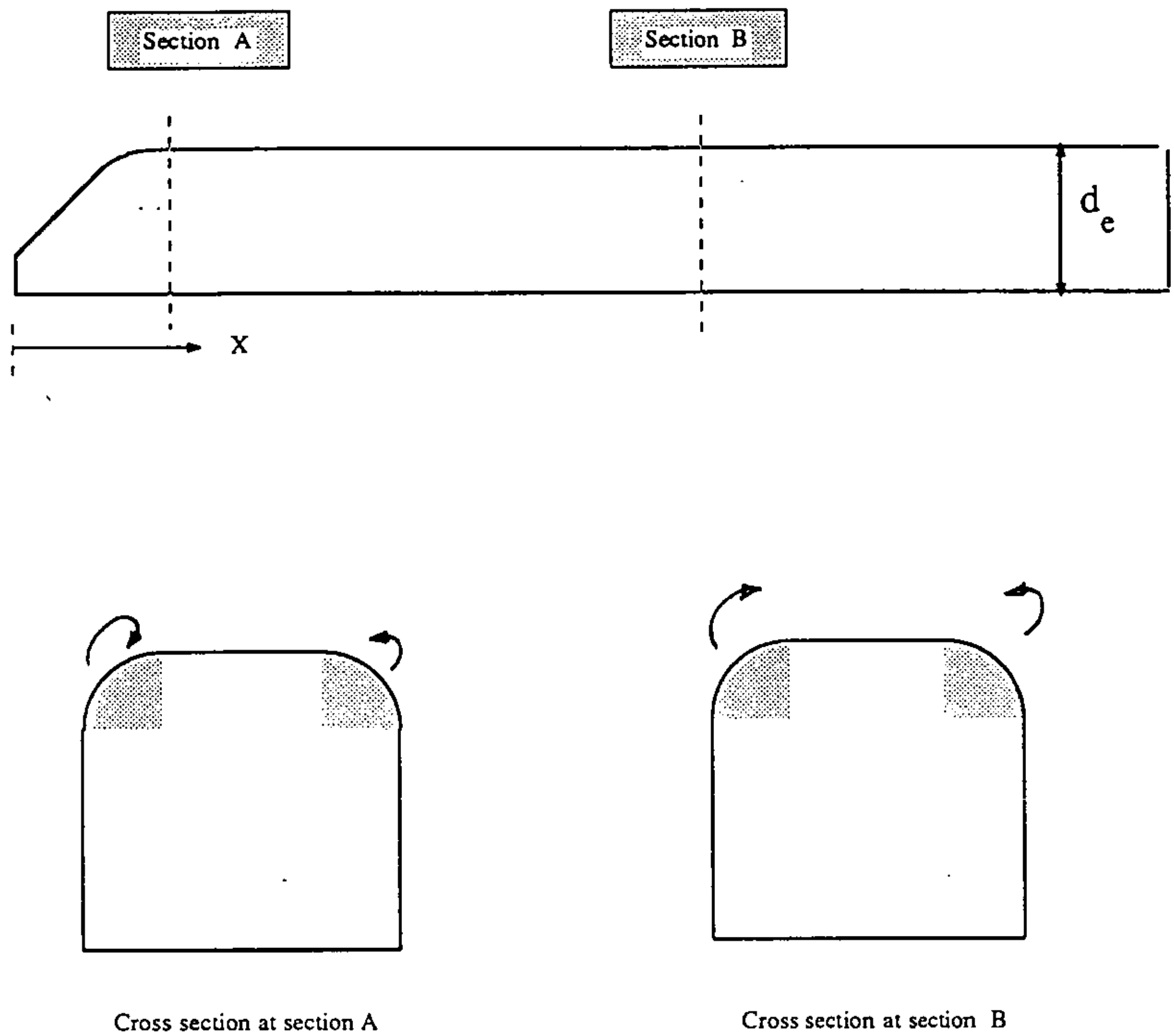

Figure 4-8 Two vortices on two cross sections of an EMS train model at zero yaw angle

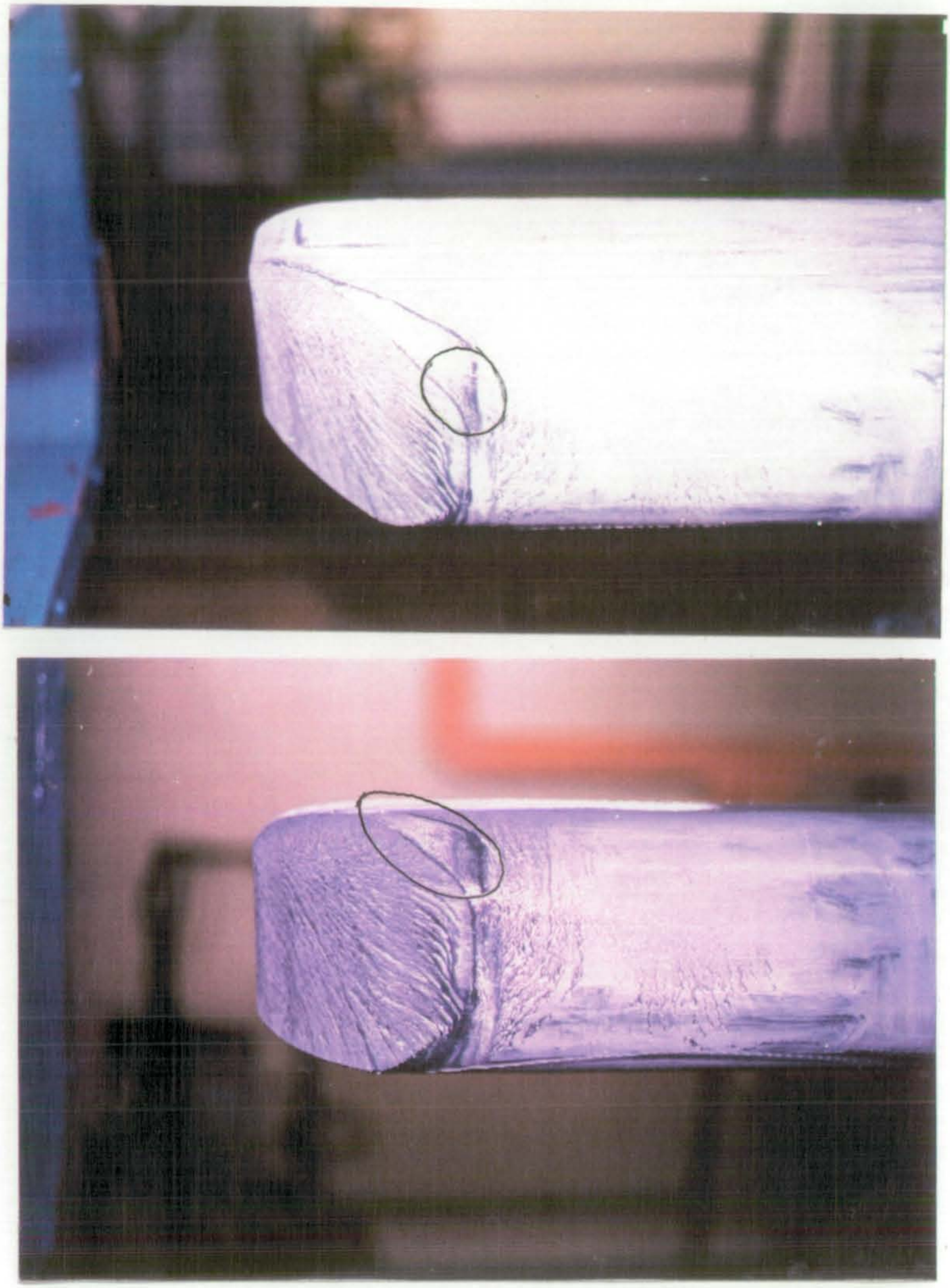

Figure 4-9 Flow pattern at 0° yaw angle in the absence of the ground simulation, using the oil suspension technique, Re=4.37×10^5.

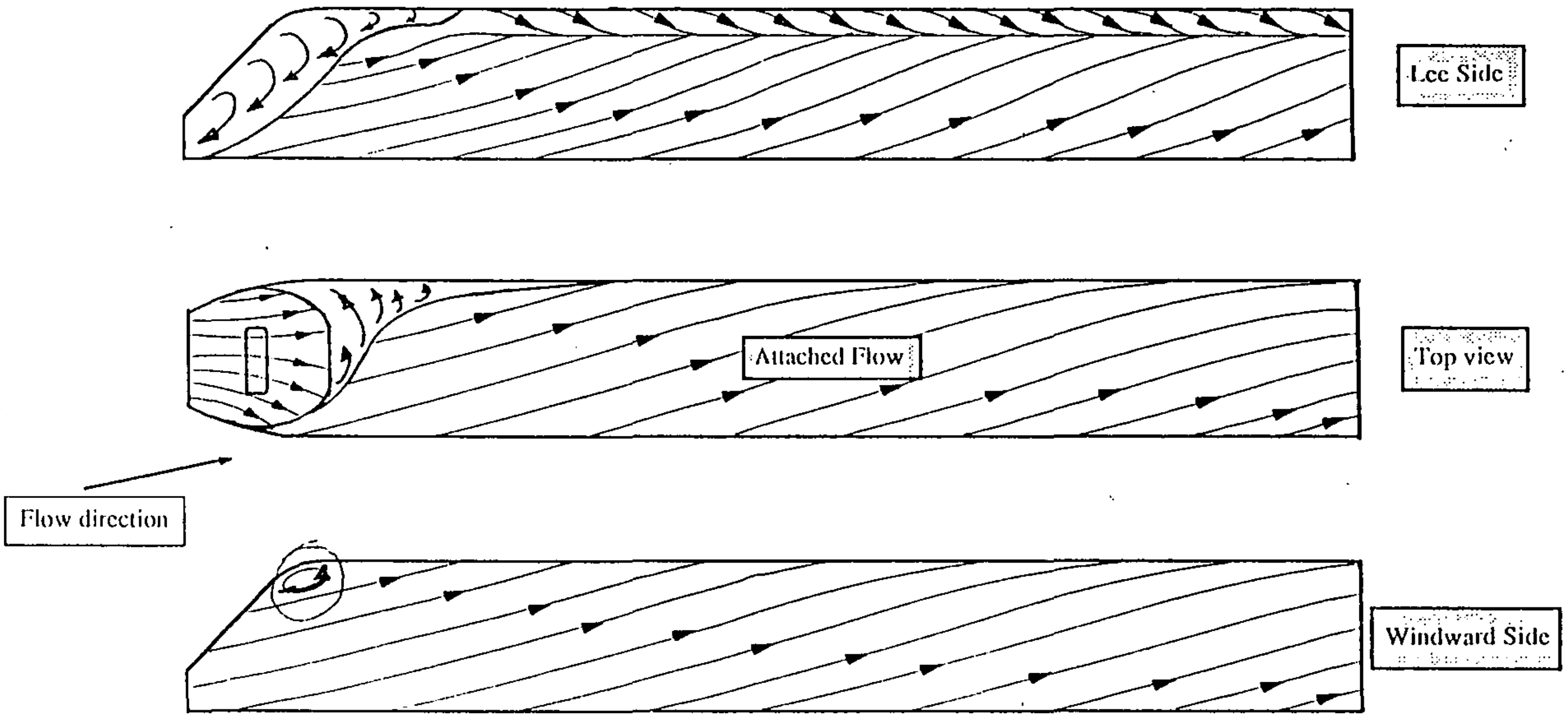

Figure 4-10 Flow pattern at 10° yaw angle in the absence of the ground simulation, using tuft and spinner technique,
$Re = 4.37 \times 10^5$

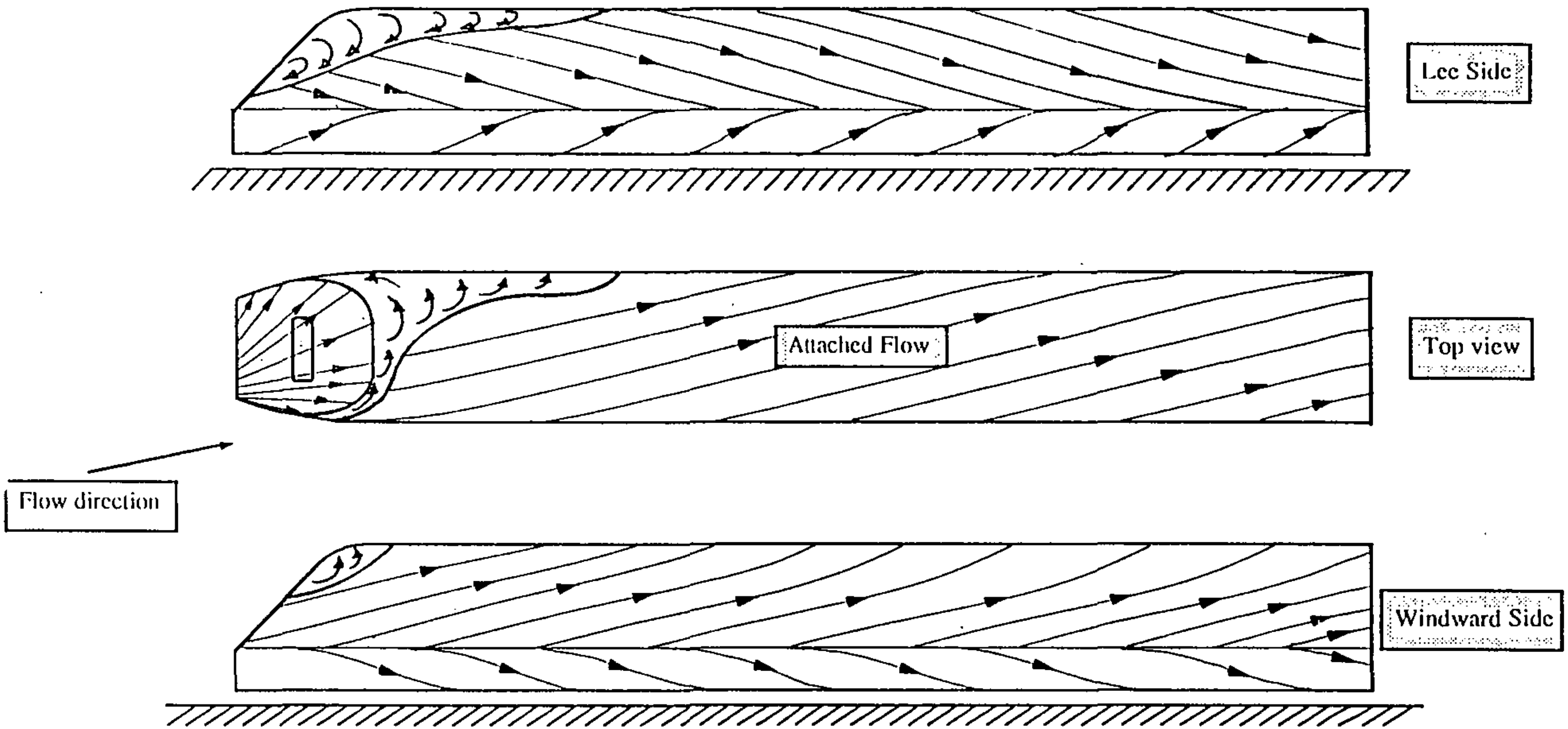

Figure 4-11 Flow pattern at 10° yaw angle in the presence of the ground simulation, using tuft and spinner technique,
$Re = 4.37\times10^5$

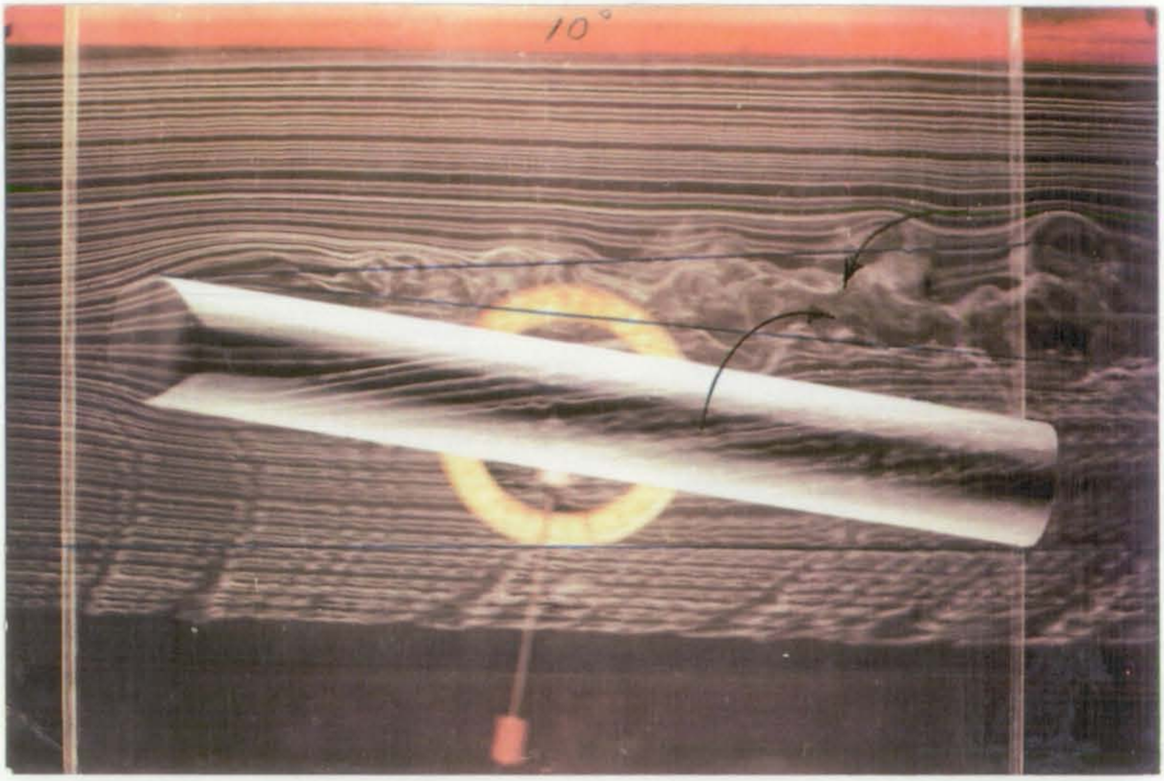

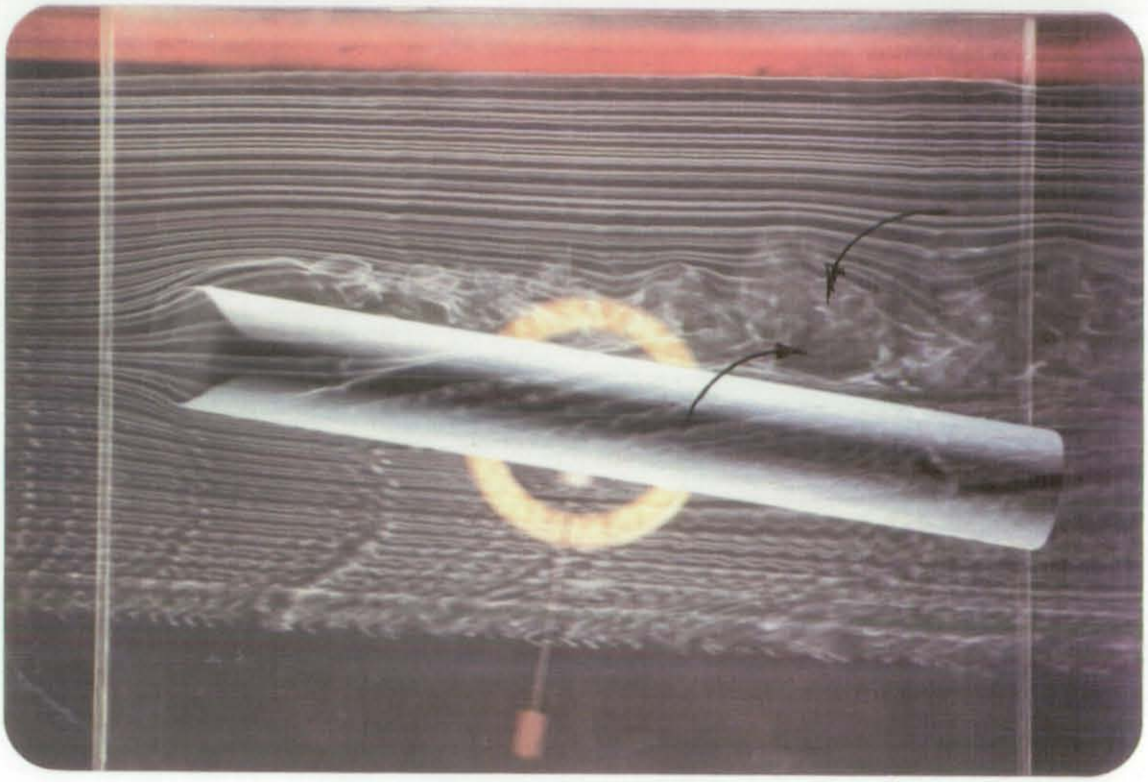

Figure 4-12 Flow pattern at 10° yaw angle in the absence of the ground simulation, for two different planes of flow, using the smoke technique.

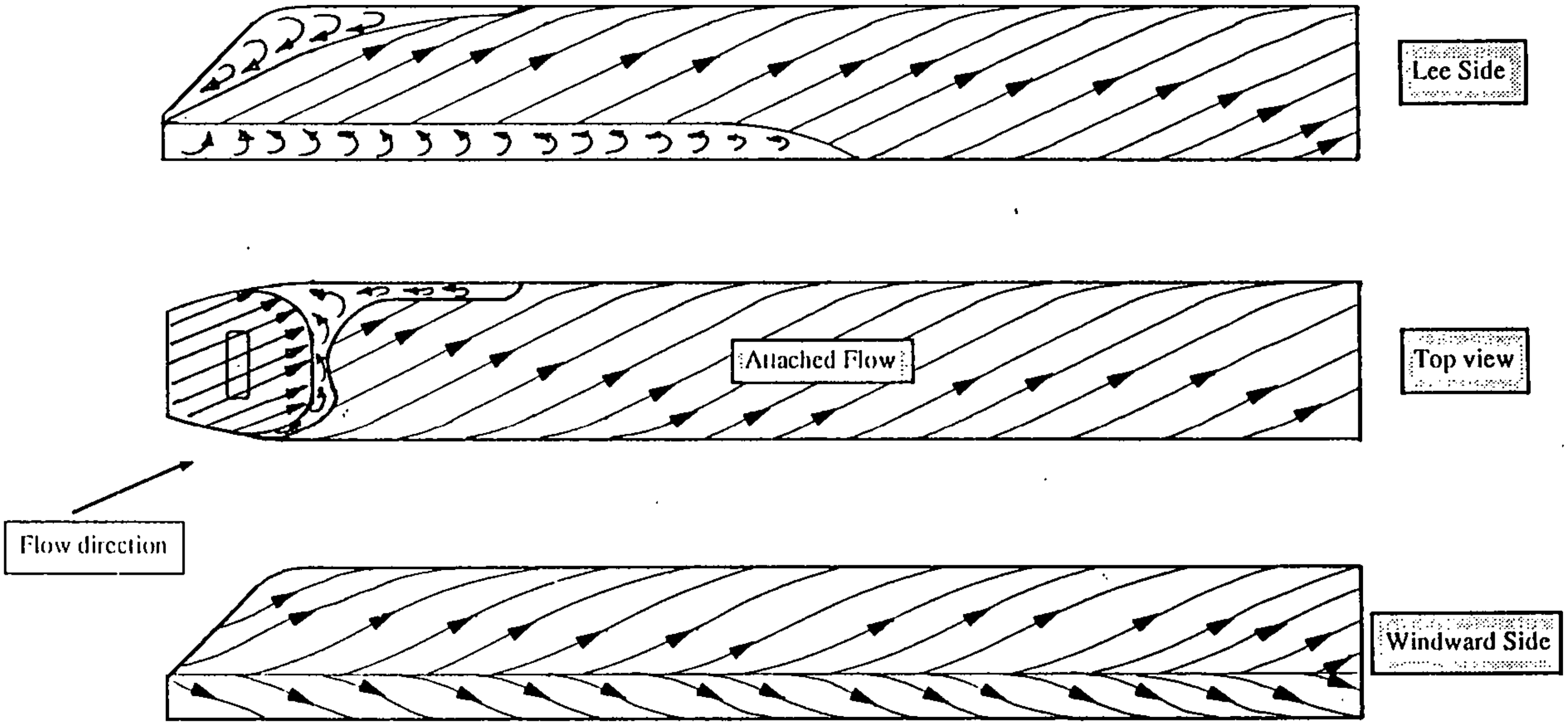

Figure 4-13 Flow pattern at 22° yaw angle in the absence of the ground simulation, using tuft and spinner technique,
$Re = 4.37\times10^{5}$

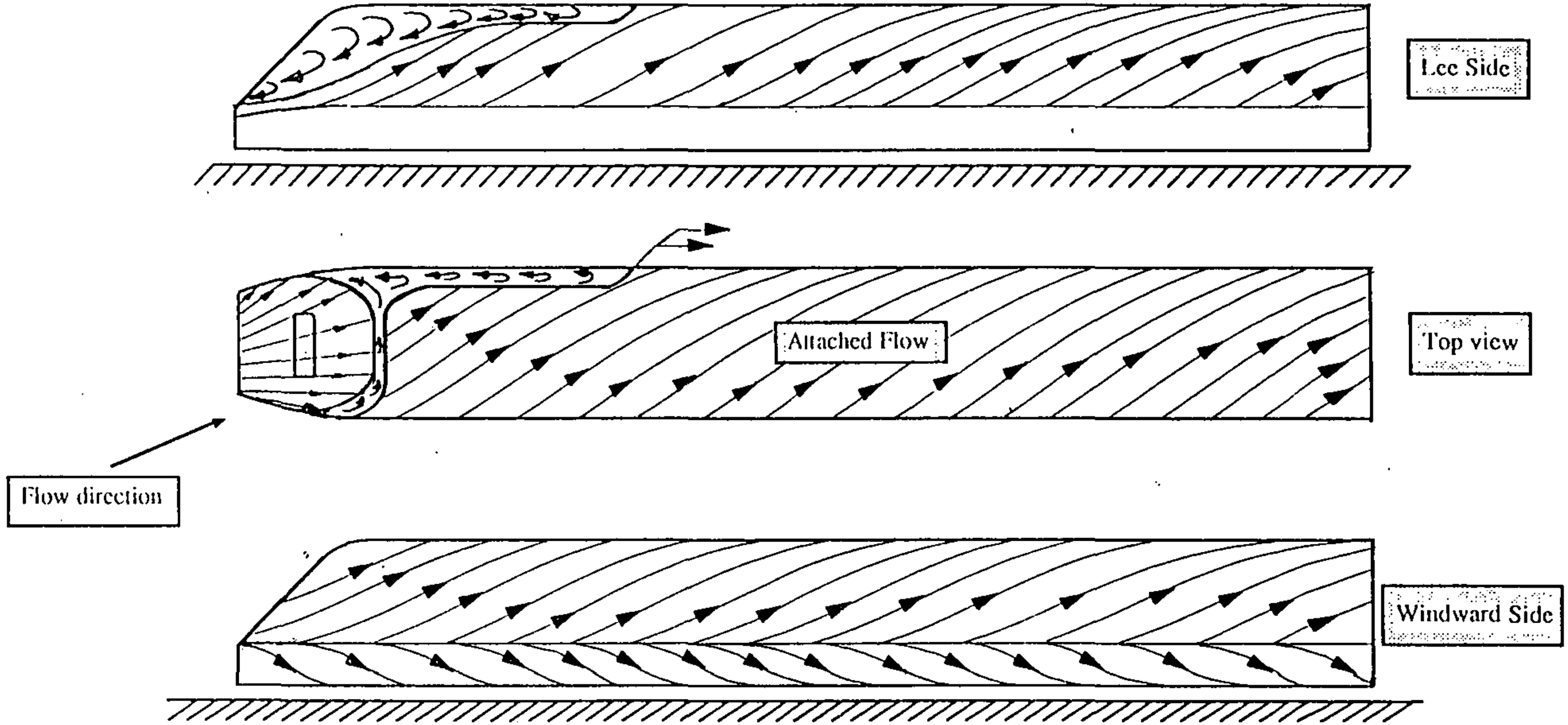

Figure 4-14 Flow pattern at 22° yaw angle in the presence of the ground simulation, using tuft and spinner technique,
$Re = 4.37 \times 10^5$

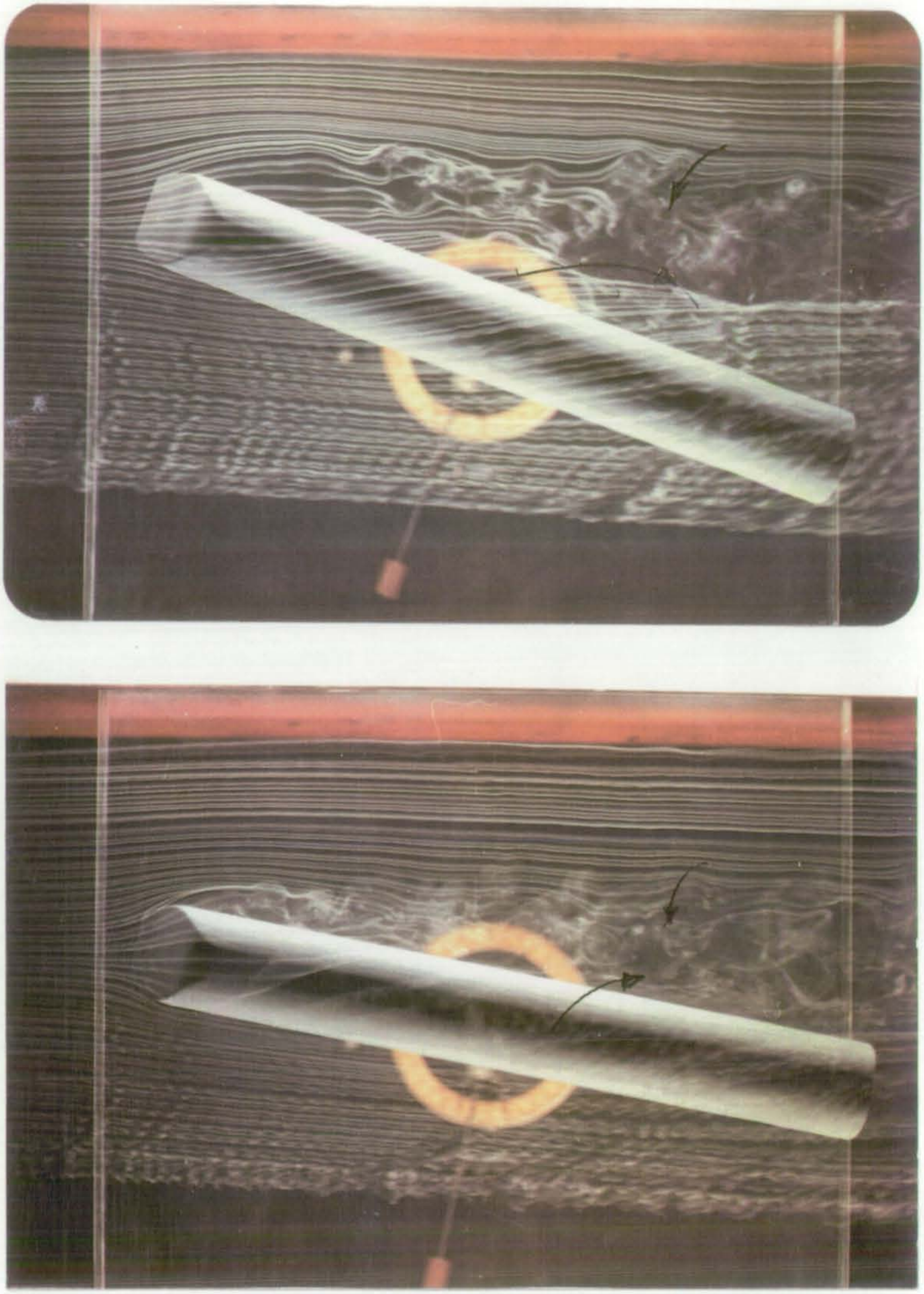

Figure 4-15 Flow pattern at 22° yaw angle in the absence of the ground simulation, for two different planes of flow, using the smoke technique.

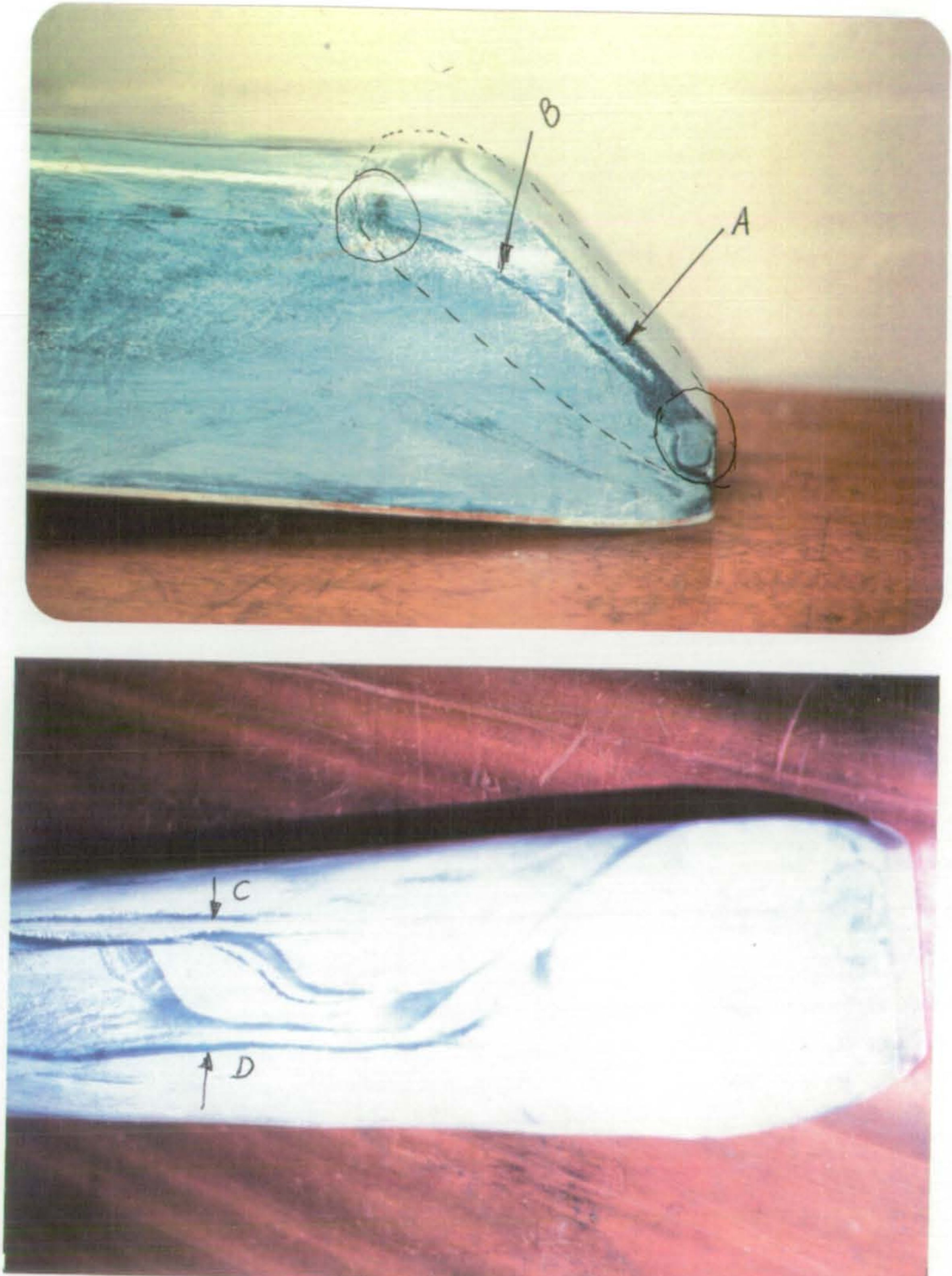

Figure 4-16 Flow pattern at 22° yaw angle in the presence of the ground simulation, using the oil suspension technique, $Re=4.37\times10^5$.

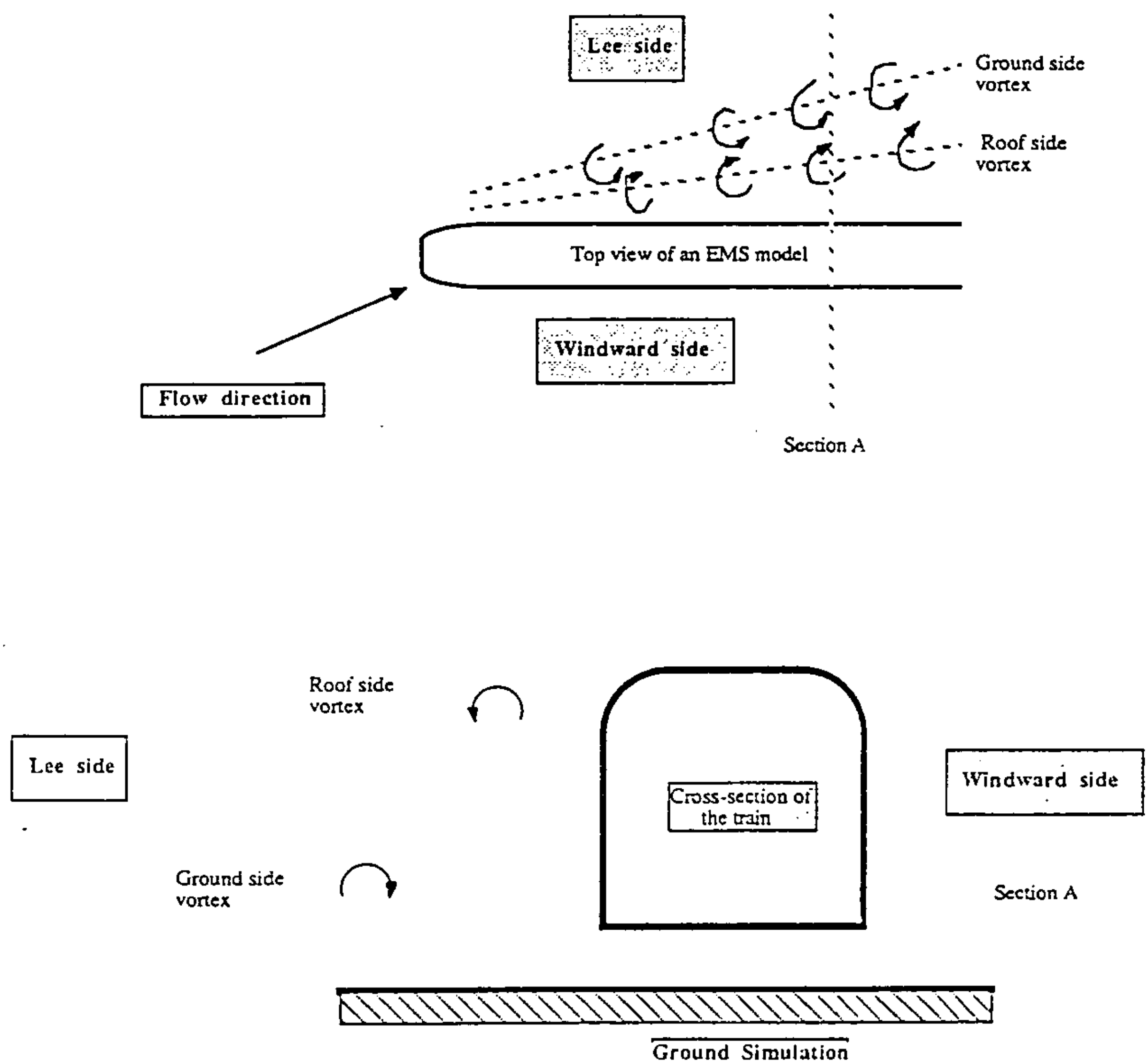

Figure 4-17 Two vortices in the lee side of the train at a yaw.

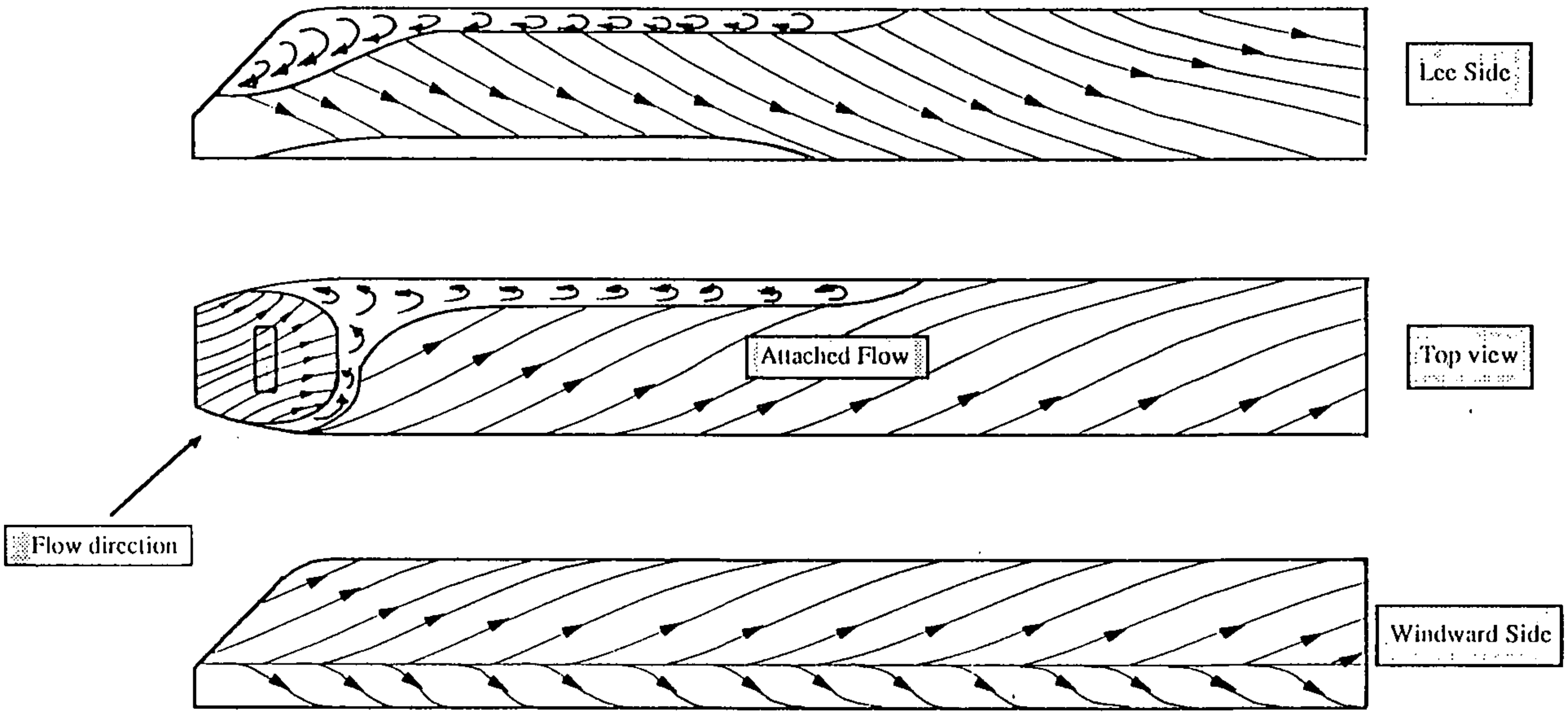

Figure 4-18 Flow pattern at 45° yaw angle in the absence of the ground simulation, using tuft and spinner technique,
$Re = 4.37 \times 10^{5}$

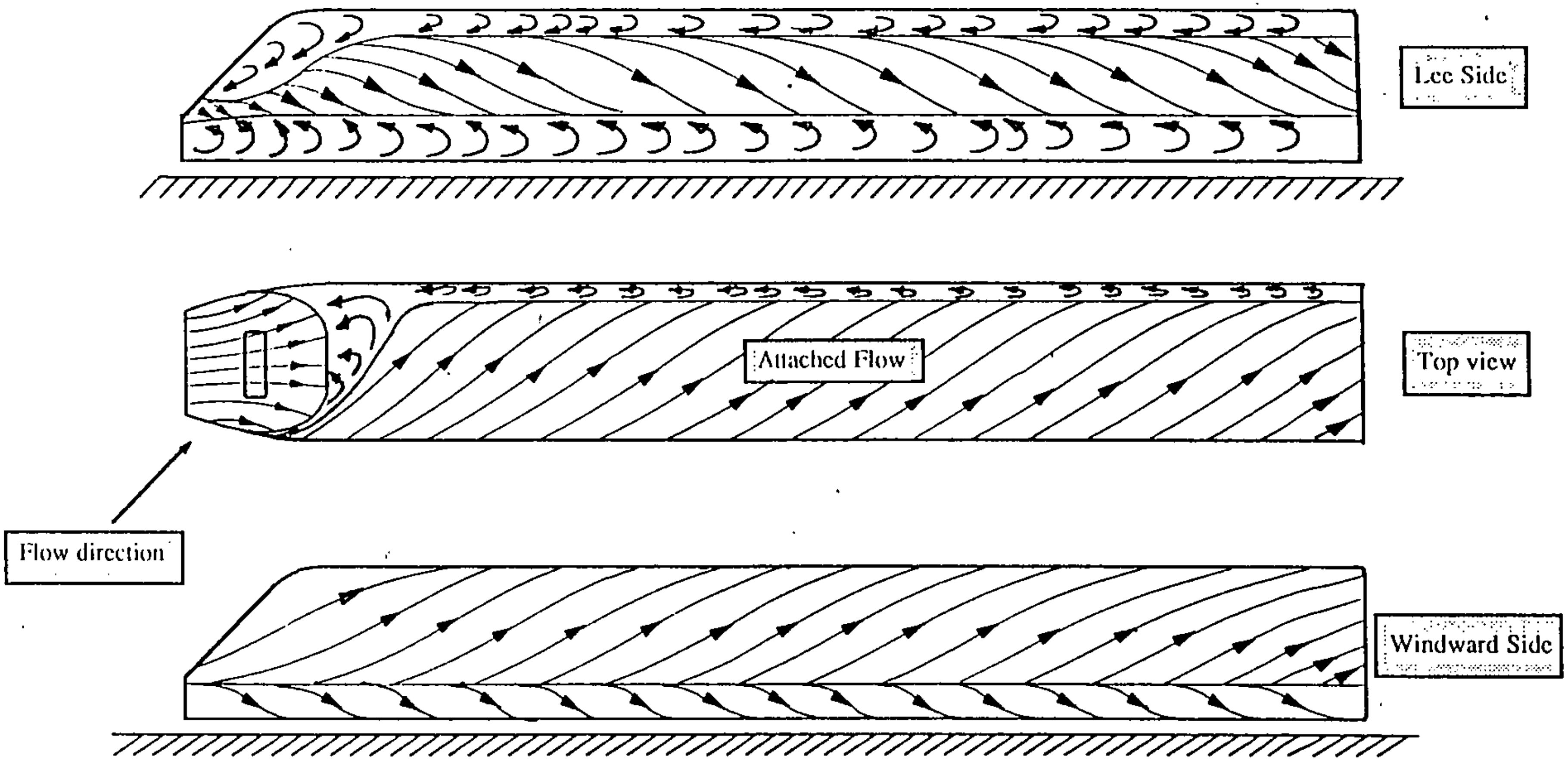

Figure 4-19 Flow pattern at 45° yaw angle in the presence of the ground simulation, using tuft and spinner technique,

$$Re = 4.37 \times 10^5$$

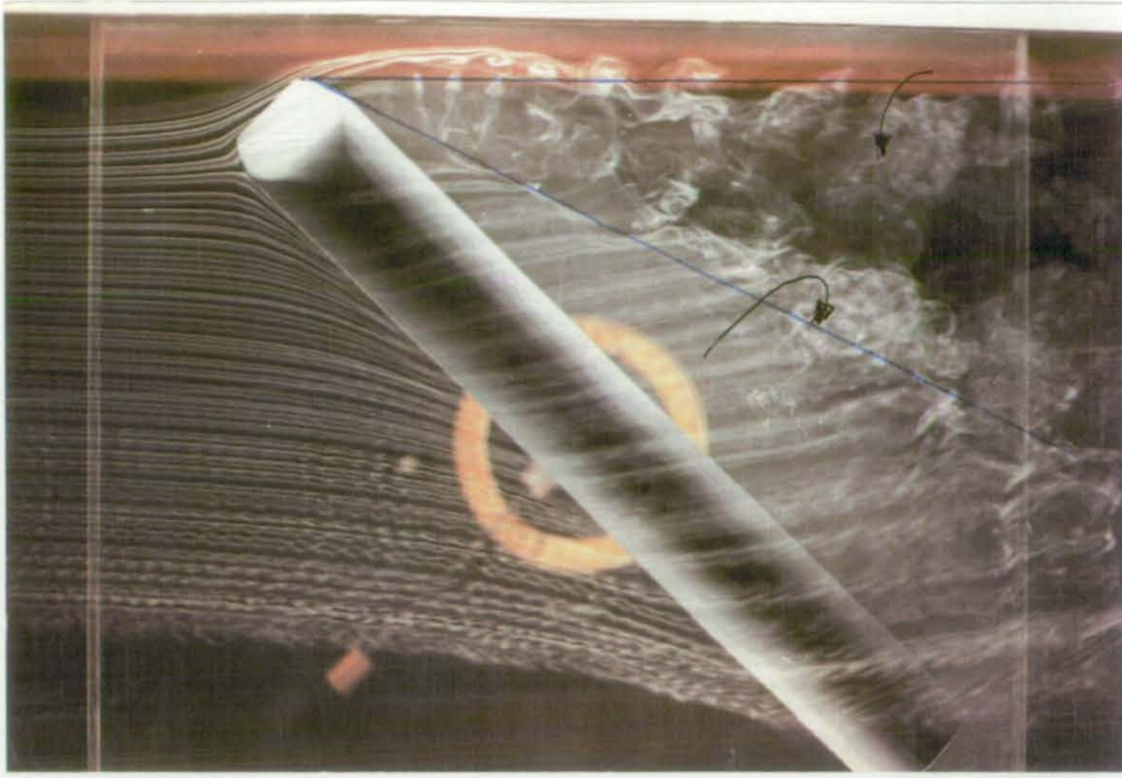

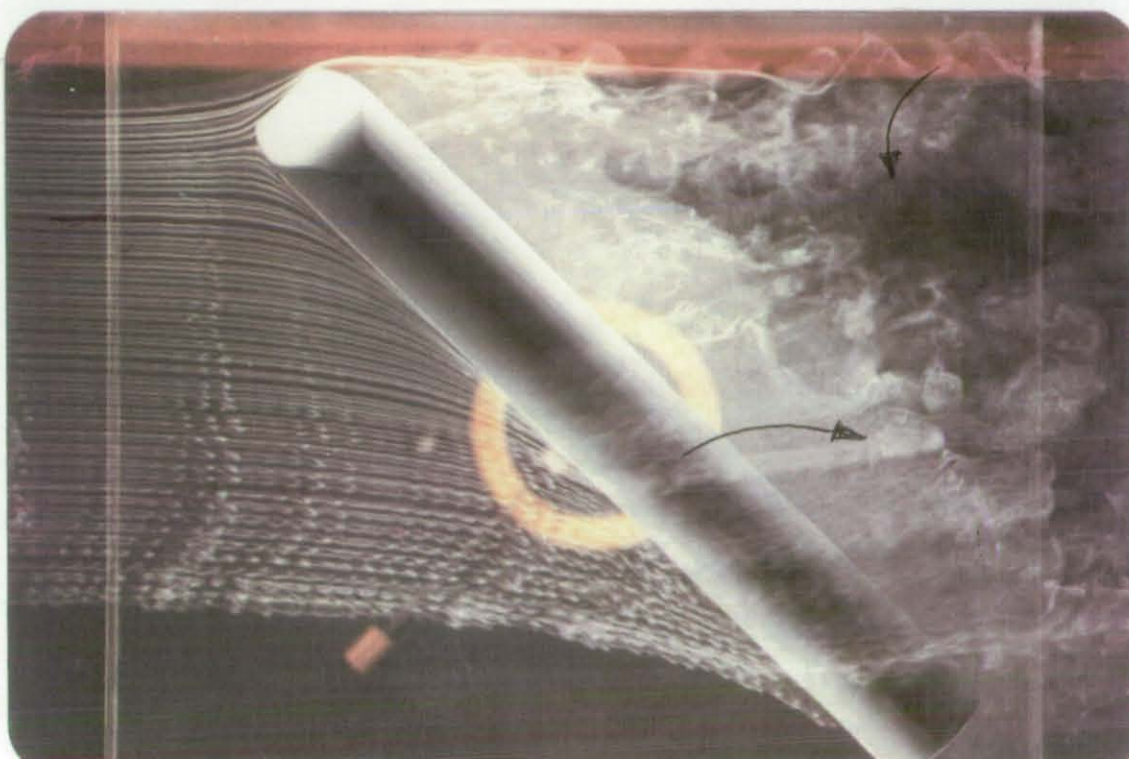

Figure 4-20 Flow pattern at 45° yaw angle in the absence of the ground simulation, for two different planes of flow, using the smoke technique.

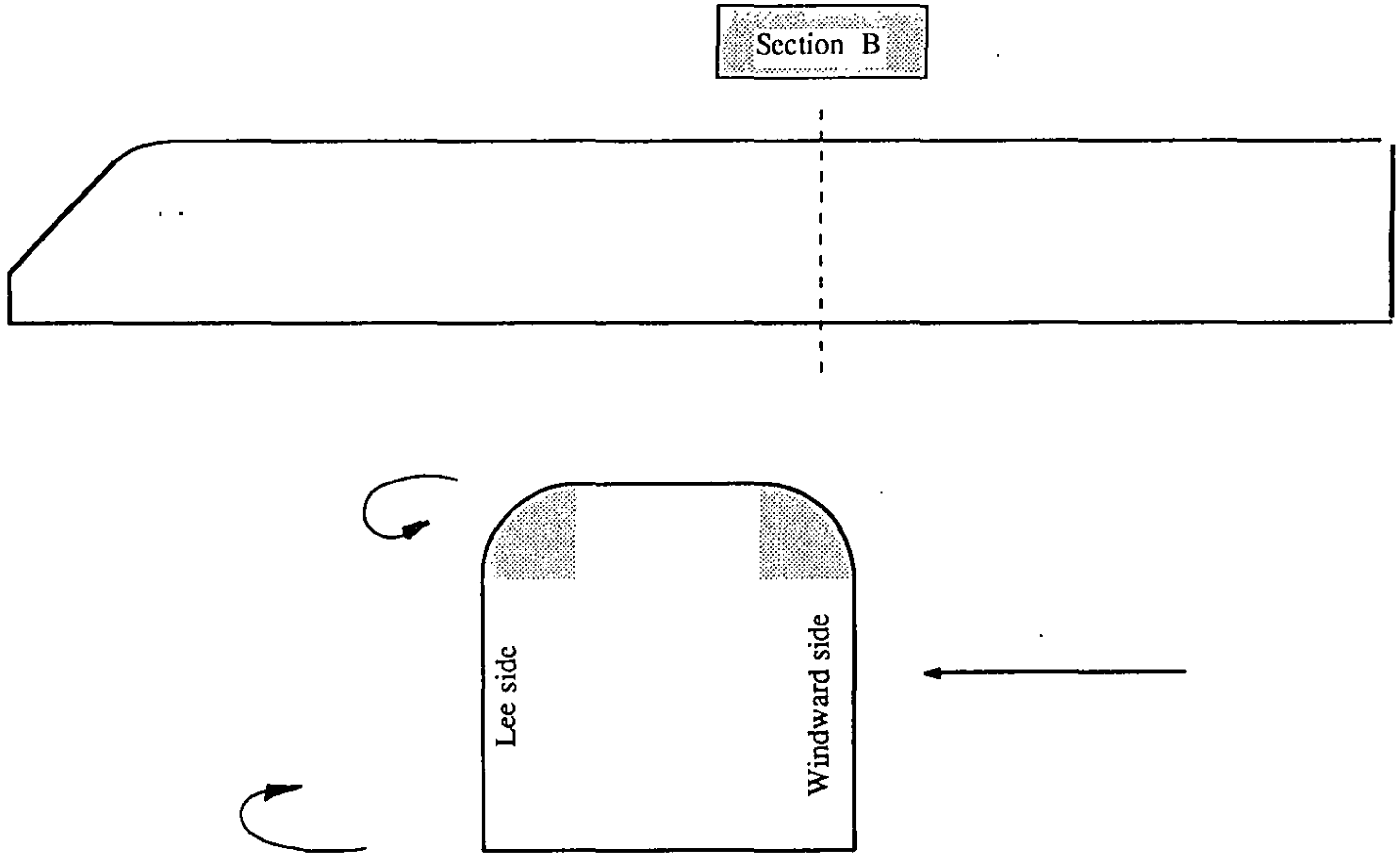

Cross section at section B

Figure 4-21 Flow pattern at 90° yaw angle in the absence of the ground simulation, using tuft and spinner technique,

$$Re = 4.37 \times 10^5$$

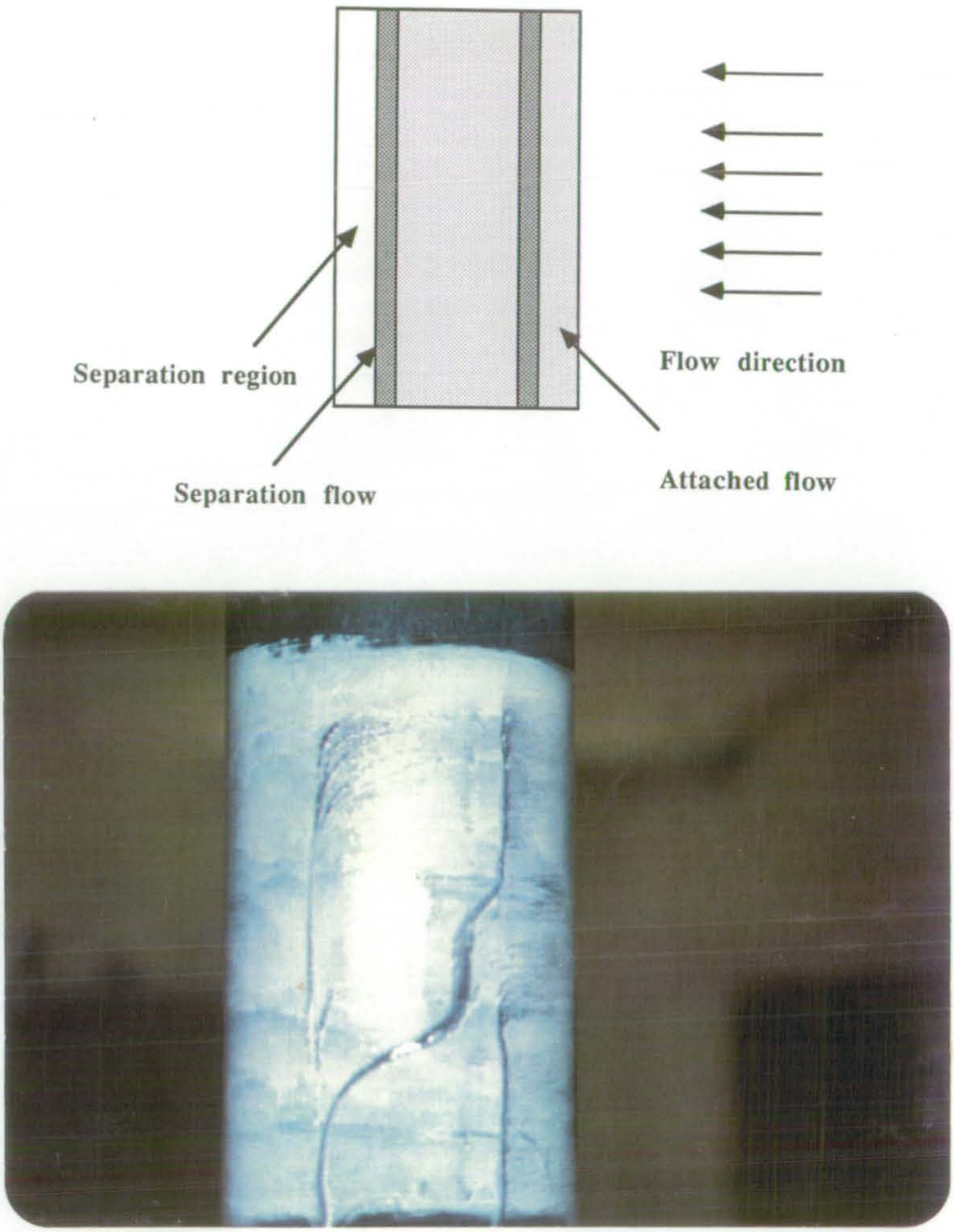

Figure 4-22 Flow pattern at 90° yaw angle in the absence of the ground simulation, using the oil suspension technique, Re=4.37×10^5.

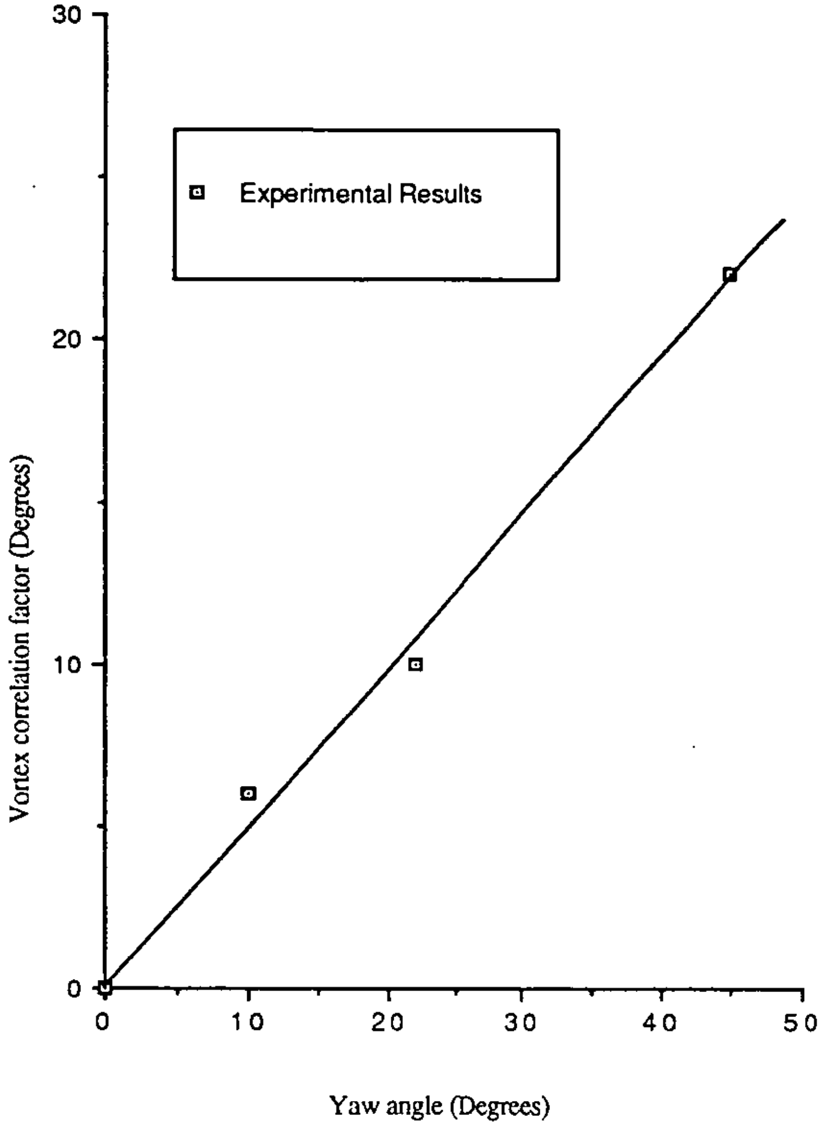

Figure 4-23 Vortex correlation factor and yaw angle.

CHAPTER 5

WIND TUNNEL AERODYNAMIC FORCES AND MOMENTS TESTS ON AN EMS TRAIN MODEL

5.1 Introduction

This chapter is concerned with wind tunnel tests to investigate and measure the aerodynamic forces and moments acting on an EMS train for design purposes, these may be used to provide supporting information for consistency checks on the pressure measurements and the qualitative results of the flow visualisation tests. The tests examine the effects of yaw angle and the presence of the ground on the aerodynamic forces.

The rest of the chapter comprises five sections. Section 5.2 defines the aerodynamic forces and moments of interest—lift, drag, side force and yawing moment. Blockage corrections used in wind tunnel testing are discussed and presented in section 5.3 and section 5.4 describes the EMS train test model. Section 5.5 concerns the test programme and section 5.6 presents the results. Concluding remarks are then made in section 5.7.

5.2 Definitions of Aerodynamic Forces and Moments

When a vehicle moves in air the pressure distribution and the viscous shear over its surface result in aerodynamic forces and moments. It is conventional to separate the resultant force and moment into three components. Thus, for the resultant force : lift is the component acting perpendicular to the direction of the freestream ; drag acts in the opposite direction to the vehicle motion ; and the side force acts perpendicular to both the lift and drag forces as shown in Figure 5-1. The moment components are : yawing moment which is the moment that tends to rotate the body about the axis that forms lift direction , see Figure 5-1 ; pitching moment which acts in the plane of the lift and drag; and rolling moment which acts to roll the the body about the direction of the motion of the body.

Aerodynamic forces and moments are normally represented by non-dimensional coefficients.

Drag coefficient, C_D ; lift coefficient, C_L ; and side force coefficient, C_S , are expressed as

$$C_D = \frac{D}{\frac{1}{2}\rho V^2 A} \qquad 5\text{-}1$$

$$C_L = \frac{L}{\frac{1}{2}\rho V^2 A} \qquad 5\text{-}2$$

$$C_s = \frac{S}{\frac{1}{2}\rho V^2 A} \qquad 5\text{-}3$$

where :

L : lift force,

D : drag force,

S : side force,

A : projected area,

V : freestream velocity, and

ρ : Air mass density

Aerodynamic moments are also usually defined as non-dimensional coefficients e.g. for yawing moment.

$$C_Y = \frac{Y}{\frac{1}{2}\rho V^2 A x} \qquad 5\text{-}4$$

where :

Y : Yawing moment

x : Reference length

5.3 Blockage Corrections

The presence of a large model in the working section of a wind tunnel makes it necessary for the measured aerodynamic forces to be corrected to compensate for the increase in the velocity of the local flow caused by the blockage.

The 1/25 scale EMS train model which has been used to measure the aerodynamic forces in the environmental wind tunnel has an area much less than the area of the wind tunnel test section. In this case the geometry blockage ratio B (model area/test section area) of the model at 0° yaw is 0.014. Thus the blockage correction factor (see ref. [83, 84] which increases the effective B by about a factor of 2, would lead to a correction multiplication for drag coefficients of 0.973 or a correction of approximately 3%. This is sufficient small that no blockage correction has been applied to the test results for aerodynamic forces reported herein (the tests were carried out for small angles of yaw in the range 0°—8°).

5.4 EMS Train Model

The test EMS train model was to a 1/25 scale, constructed from wood and was 2.25 m long, 0.149 m high and 0.151 m wide. A hole was made at the centre of the model roof to fit a strain gauge balance with support in the wind tunnel wall, see Figures 5-2 and 3-2, the bottom of the model was covered by a removable wood panel to help the insertion of the strain gauge balance.

5.5 The Test Programme

The test programme was performed in the environmental wind tunnel of the Department of Transport Technology, Loughborough University of Technology. The ground was simulated using a stationary and moving belt and a calibrated strain gauge balance was fixed inside the model to measure the aerodynamic forces and moments.

Two series of tests were performed, the first series tested the model at a fixed yaw angle and four ground clearances of $Z/d_e = 0.08$, 0.125, 0.158 and 0.225. The second series of tests were performed at a fixed ground clearance of $Z/d_e=0.125$ but for yaw angles of $0°$, $2°$, $4°$, $6°$, and $8°$.

The tests were carried out with a flow Reynolds number of 4.375×10^5. This Reynolds number is the same as that used in the pressure coefficient measurements of chapter three and the flow visualisation tests of chapter four (to avoid the influence of Reynolds number on the results). The tests measured lift, drag, side force and yawing moment with both stationary and moving ground planes.

5.6 Test Results

5.6.1 Drag

Figure 5-3 shows the variation in drag coefficient with yaw angle for both the stationary and moving belt. It is seen that the moving belt always results in a drag coefficient higher than that of the stationary belt. In the case of a moving belt more air will flow between the body and ground and this leads to reduced pressure underneath the train. In addition, the presence of the moving belt removes the boundary layer on the ground simulation and thereby changes the position of the separation points and the lee side vortex formation process. The amount of drag experienced by a train vehicle is related to the structure of flow in its wake. The flow around a train dominated by a lee side votex which grows from a separation line near the top lee side corner. As yaw increases the adverse pressure gradients grow and the associated flow separation increases. Also since drag is defined to be in a direction parallel and opposite to the vehicle motion (as shown in Figure 5-1), yaw will contribute a flow component in the same direction and thereby increase the apparent effect. These influences are observed in the flow visualisation tests (Figure 5-3) and provide an explanation for the large increase in C_D as yaw angle increases. The difference between the two curves is small at the lower yaw angles and increases as the yaw angle increases. Figure 5-4 shows the drag coefficient variation with ground clearance for three different yaw angles (0°, 2° and 4°). The Figure shows again that the moving belt gives a drag coefficient higher than the stationary belt, and that the difference between the two curves decreases (except 0° yaw) as the ground clearance increases, although this effect is minor over the range of ground clearance measurements.

5.6.2 Lift

The variation of the lift coefficient, when a stationary and moving belt are employed, for different yaw angles at a ground clearance $Z/d_e = 0.125$ is shown in Figure 5-5. The Figure shows that the stationary belt ground simulation always gives a negative lift that is (algebraically) slightly higher than the negative lift of the moving belt simulation. The action of the moving belt is to draw more air underneath the train thus lowering the pressure beneath the train and hence increasing the downforce which contributes to negative lift.. The values for both types of ground simulation decrease as the yaw angle increases. Figure 5-6 shows the variation of the lift coefficient with ground clearance for five different yaw angles (0°, 2°, 4°, 6° and 8°). The Figure indicates that as the ground clearance increases the lift coefficient for the stationary belt initially decreases and then increases slightly, but is fairly constant for the moving belt. The difference in lift between the stationary and moving belt is higher at small ground clearances and decreases as the ground clearance increases. As the yaw angle increases the mean levels of both the curves for the stationary and moving belt decrease. It should be noted that all these lift coefficients are almost are order of magnitude smaller that the drag measured on the train.

5.6.3 Side Force

The main problem for a moving train in a high crosswind is the effect of side force on the stability of the train because this force can cause the train to be blown over, particularly in exposed locations such as an embankment.

Figure 5-7 shows the side force variation versus the yaw angle. The Figure shows that the magnitude of the the side force increases rapidly as the yaw angle increases, due to the high effective length/diameter ratio of the model. The almost linear change with yaw angle is related to the linear change of the vortex correlation factor observed in the flow visualisation tests. The moving belt does not seem to influence the value of the measured side force and this may be due to the fact, that the increasing velocity in the underbody region has no major effect on the formation of the vortices or the separation region in the lee side of the train.

Figure 5-8 shows the variation of the side force with ground clearance for a stationary and moving belt. The Figure shows that the ground clearance does not have a great effect on the side force except when the model is very close to the ground. Once again moving belt measurements are not significantly different from the corresponding stationary belt measurements.

5.6.4 Yawing Moment

Figure 5-9 shows that, in close proximity to the ground, the yawing moment decreases in magnitude as the ground clearance increases. The moving belt seems to give a negative yawing moment which is higher than that measured for the stationary belt. Figure 5-10 shows as expected that the yawing moment increases as the yaw angle increases since, as yaw increased, the pressure on the windward side of the train was increased and lowered in the lee side of the train especially on the nose. The effect of the moving belt decreases as the ground clearance increases.

5.7 Concluding Remarks

The main concluding remarks from the results of the measurements of the aerodynamics forces and moments may be presented as follows :

1. The drag coefficient increases substantially as the yaw angle increases. This is due to the increase in the size of the wake vortices which became stronger in the lee side of the train as the yaw angle increases.

2. The flow visualisation tests of chapter six show that the wake vortices are stronger and bigger in size in the presence of the ground simulation . This can explain the increase of the drag observed in the presence of the ground simulations.

3. It was not possible to alter the direction of the moving belt to be the same as the yaw angle of train during the measurements of the forces. This may have some effects on the results for the train at yaw angle with moving belt.

4. It was found that the stationary belt always provided a negative lift that is algebraically higher than that for the moving belt and that for both moving and stationary belts the lift increases as the ground clearance reduced. The moving belt simulation exhibited a drag higher than that of the stationary belt and (for both belts) the drag increased as the yaw angle increased. The effect of the ground is not significant for drag, especially at 0° yaw angle. These results indicate, of course, that for both lift and drag the effect of the moving belt is reduced as the ground clearance increases and the effect of the ground simulation is then not so significant.

5. The measurements of side force showed that the side force increased rapidly and almost linearly with yaw angle and that the moving belt had no effect on the measurements. This result is consistent with the panel method predictions and measured pressure distribution which exhibit negative values of high magnitude for the pressures in the lee side of the train at yaw.

6. The yawing moment increased as the ground clearance increased and the effect of the moving belt was not significant on the yawing moment. Thus in general , the moving belt has affected the lift and drag and has no

significant effect on the side force and yawing moment.

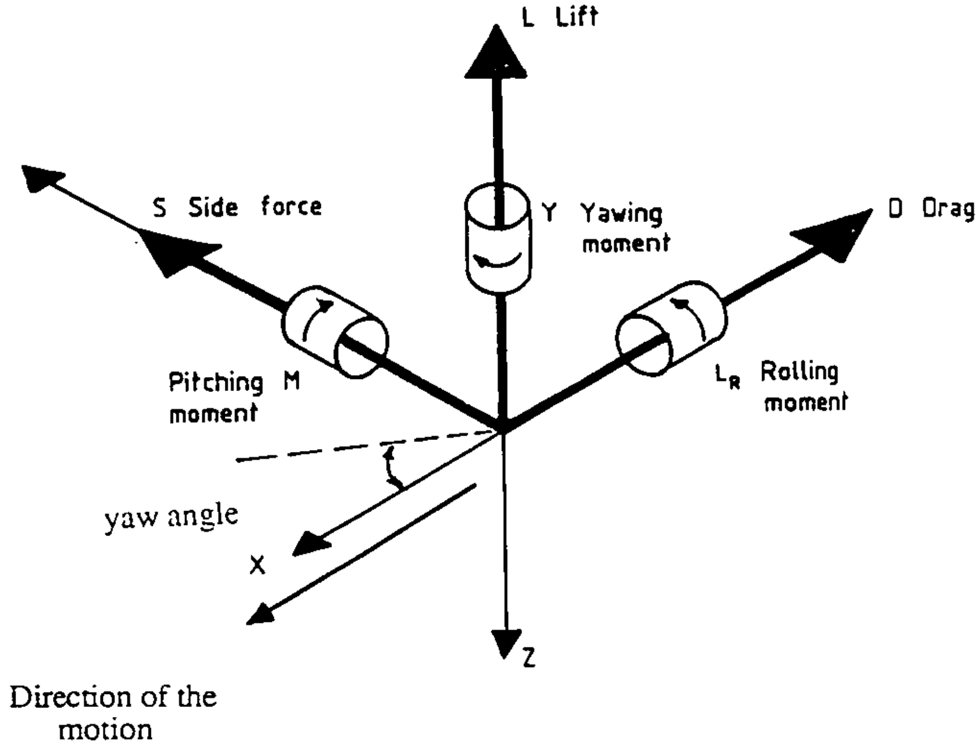

Figure 5-1 The systems of force and moment components

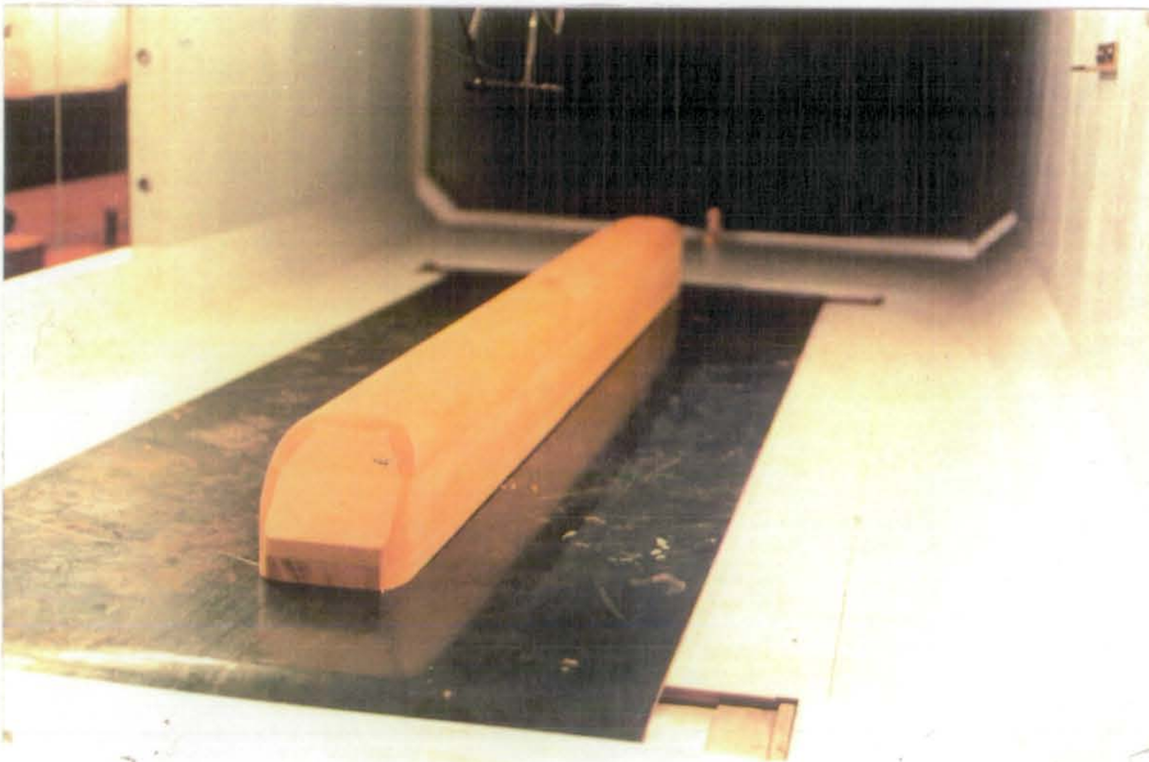

Figure 5-2 EMS train model in the environmental wind tunnel

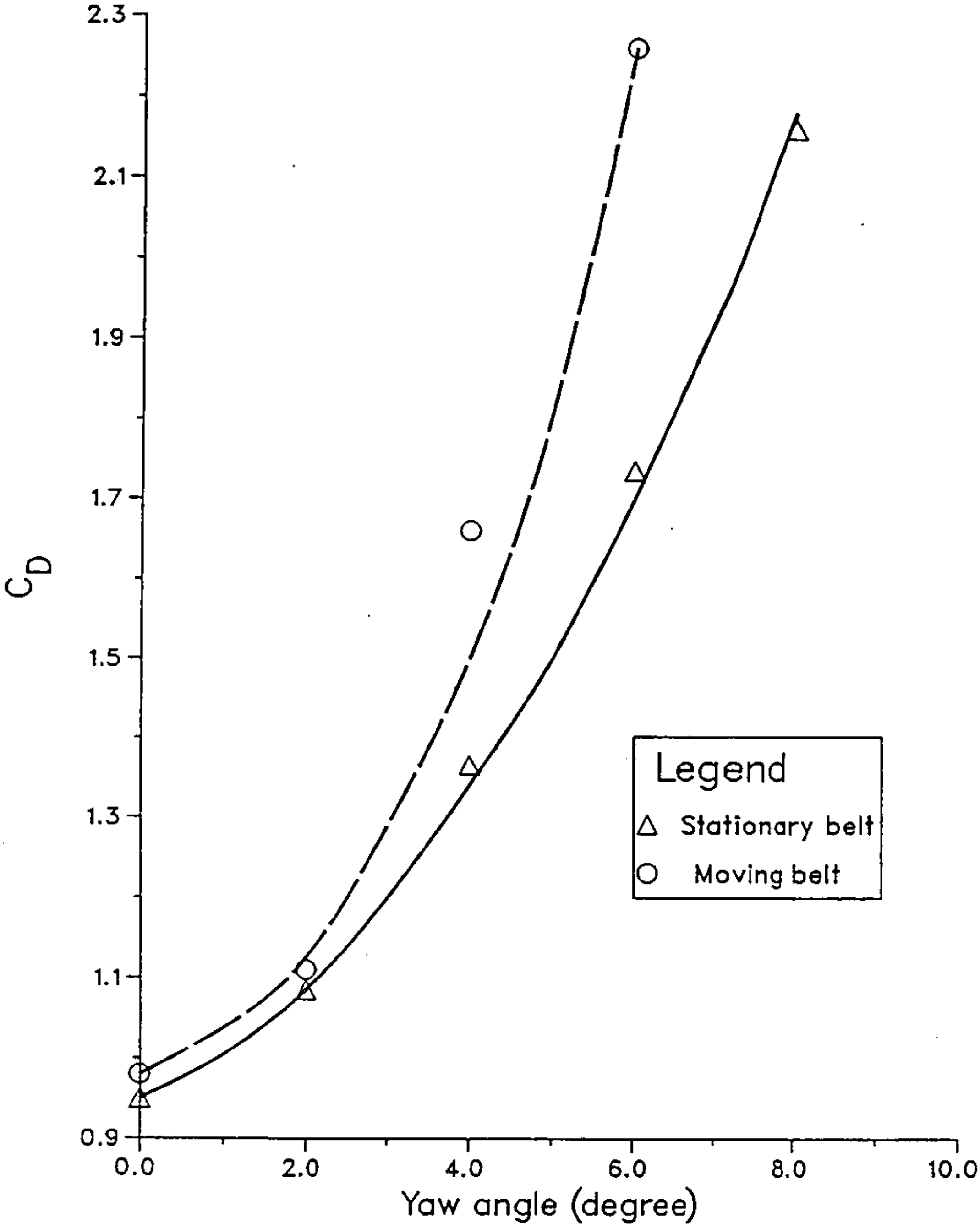

Figure 5-3 Drag coefficient variation with yaw angle at ground clearance $Z/d_e=0.125$

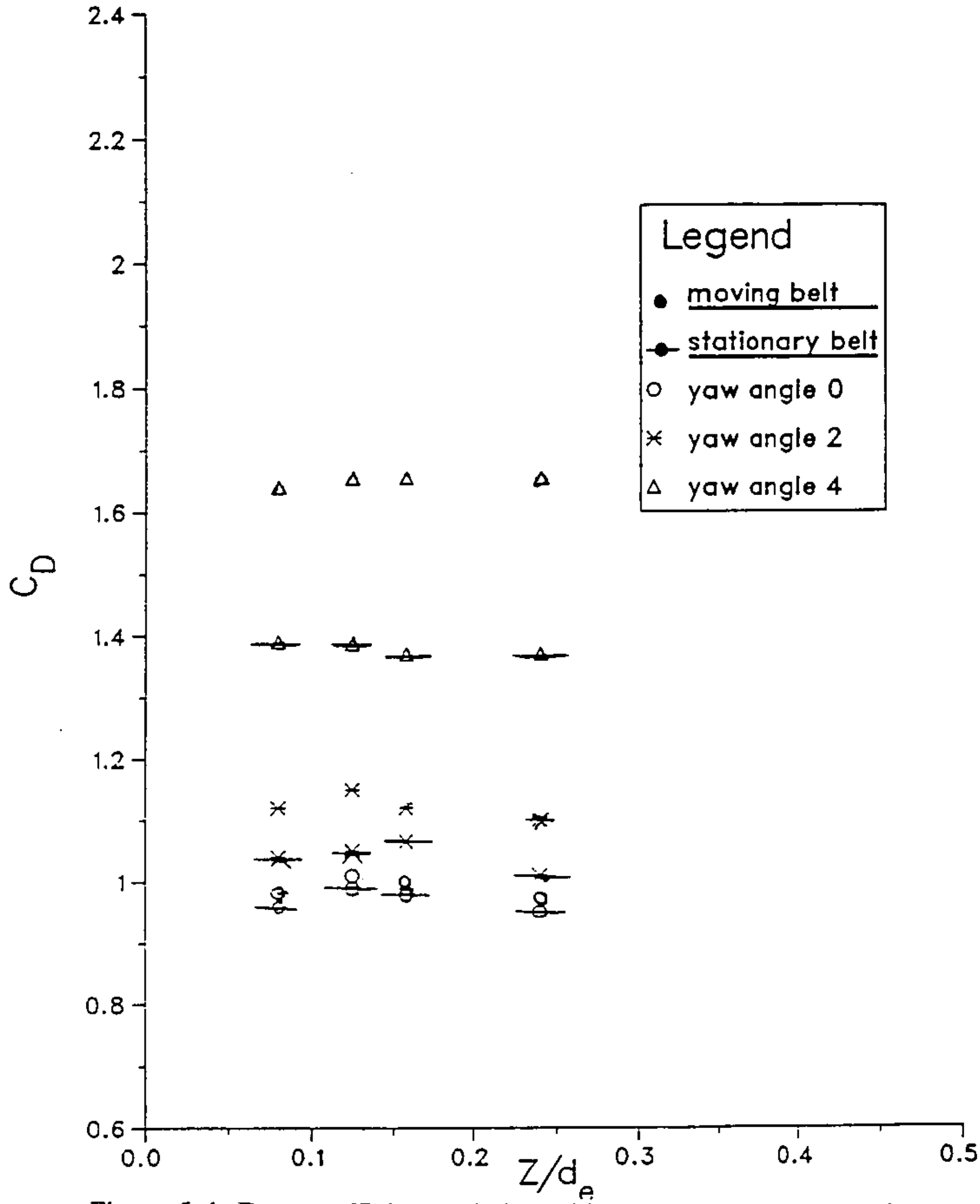

Figure 5-4 Drag coefficient variation with ground clearance at various yaw angles

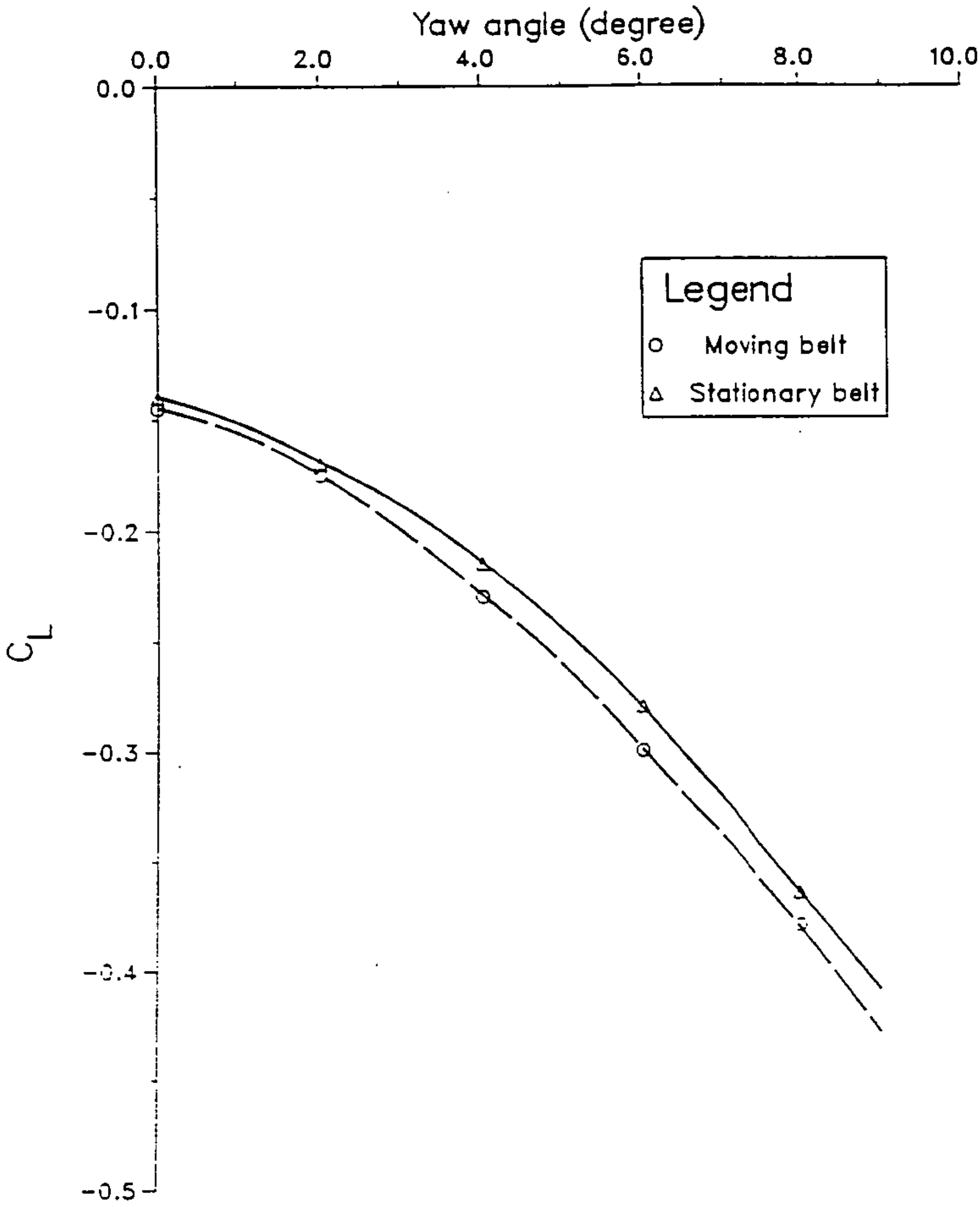

Figure 5-5 Lift coefficient variation with ground clearance at various yaw angles

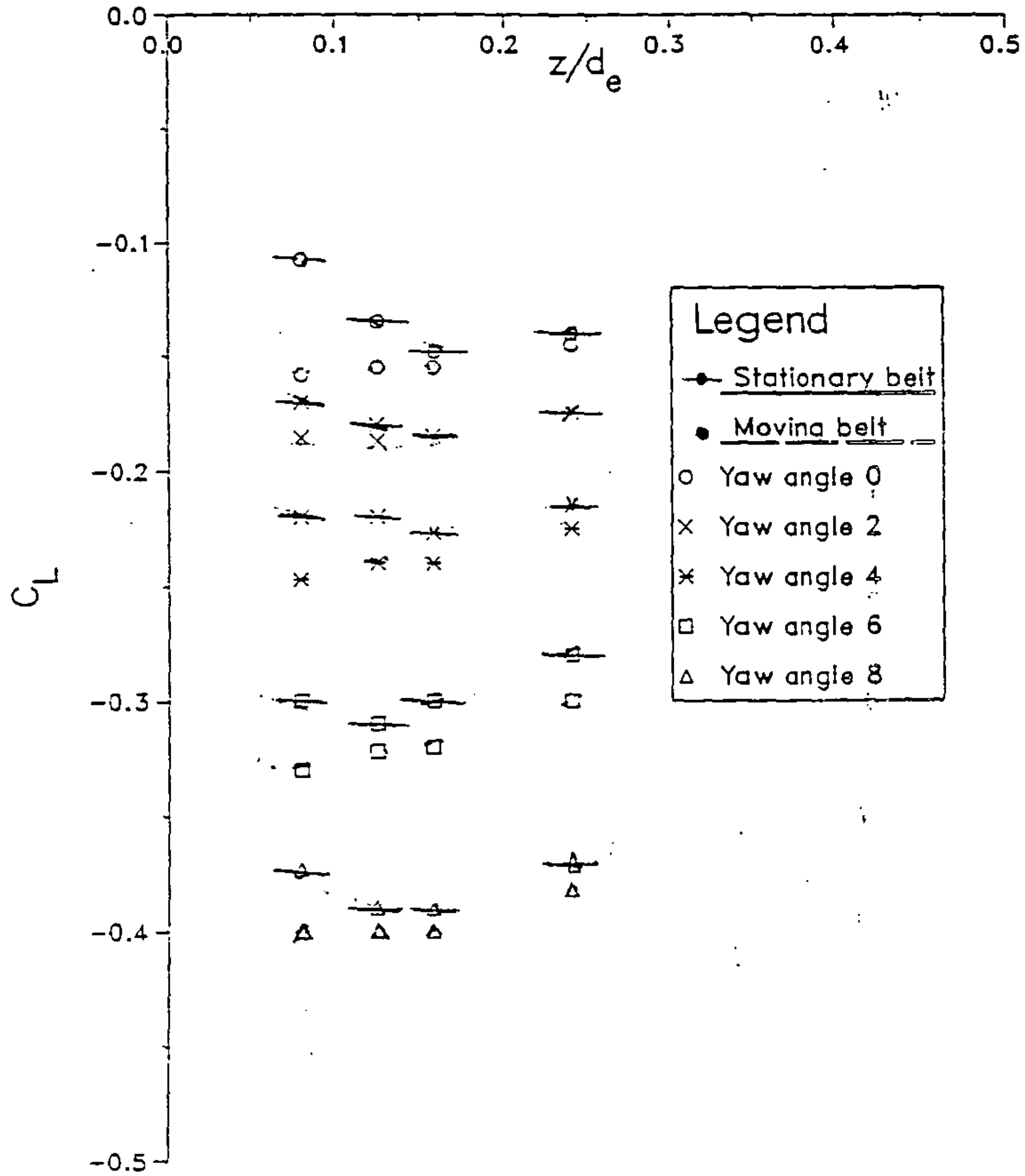

Figure 5-6 Lift coefficient variation with ground clearance at various yaw angles

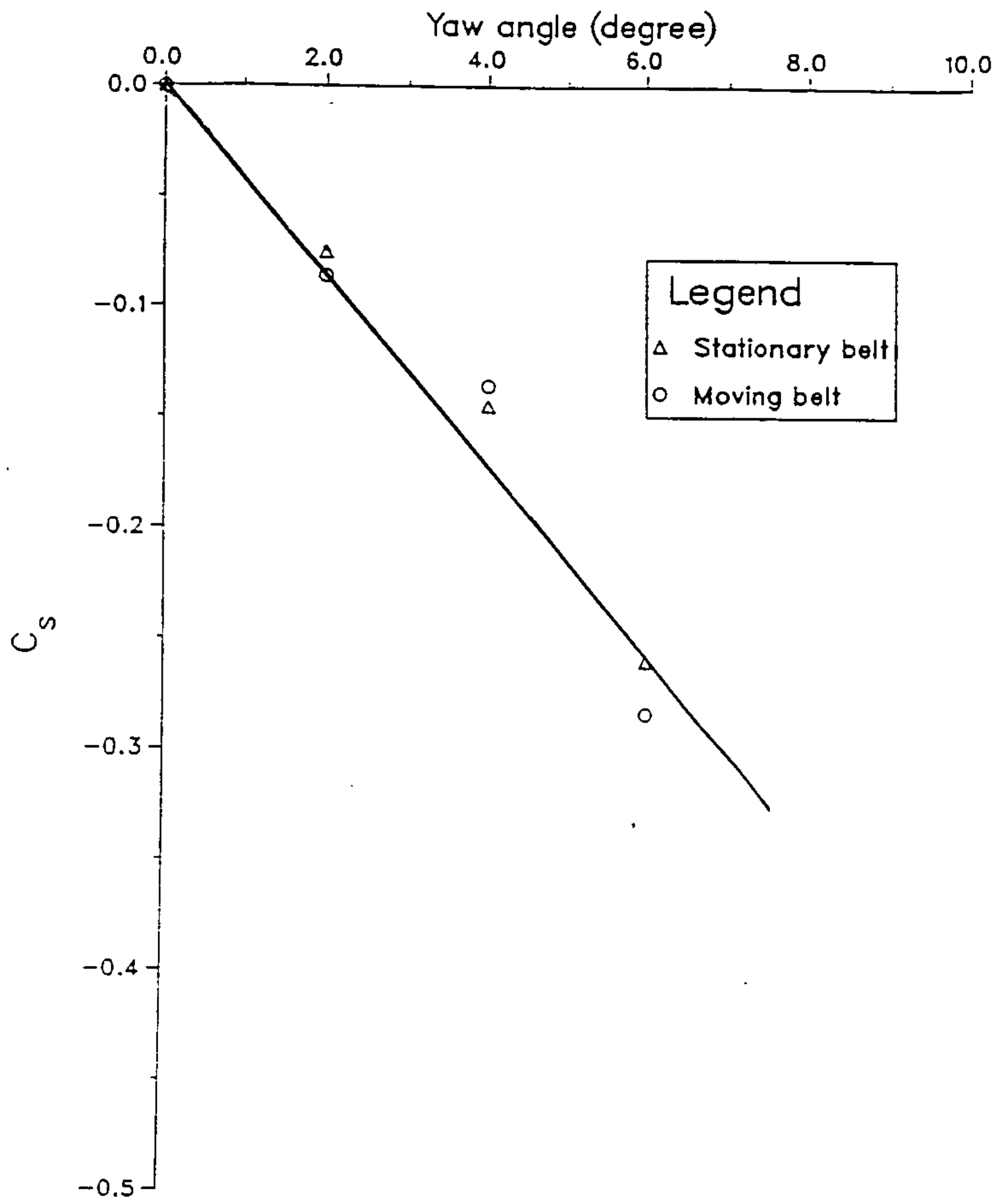

Figure 5-7 Side force coefficient variation with yaw angle at ground clearance $Z/d_e=0.125$

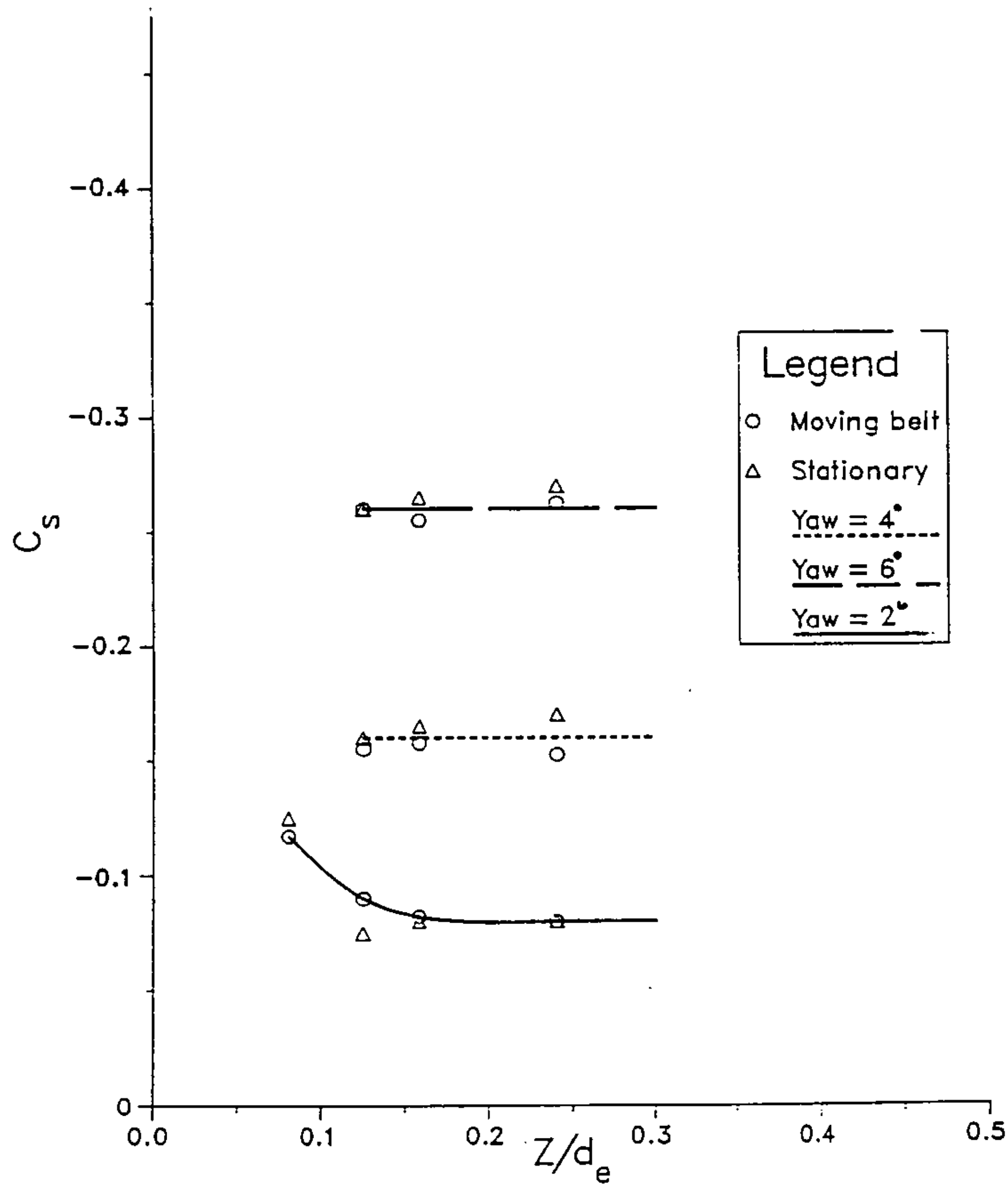

Figure 5-8 Side force coefficient variation with ground clearance at various yaw angles

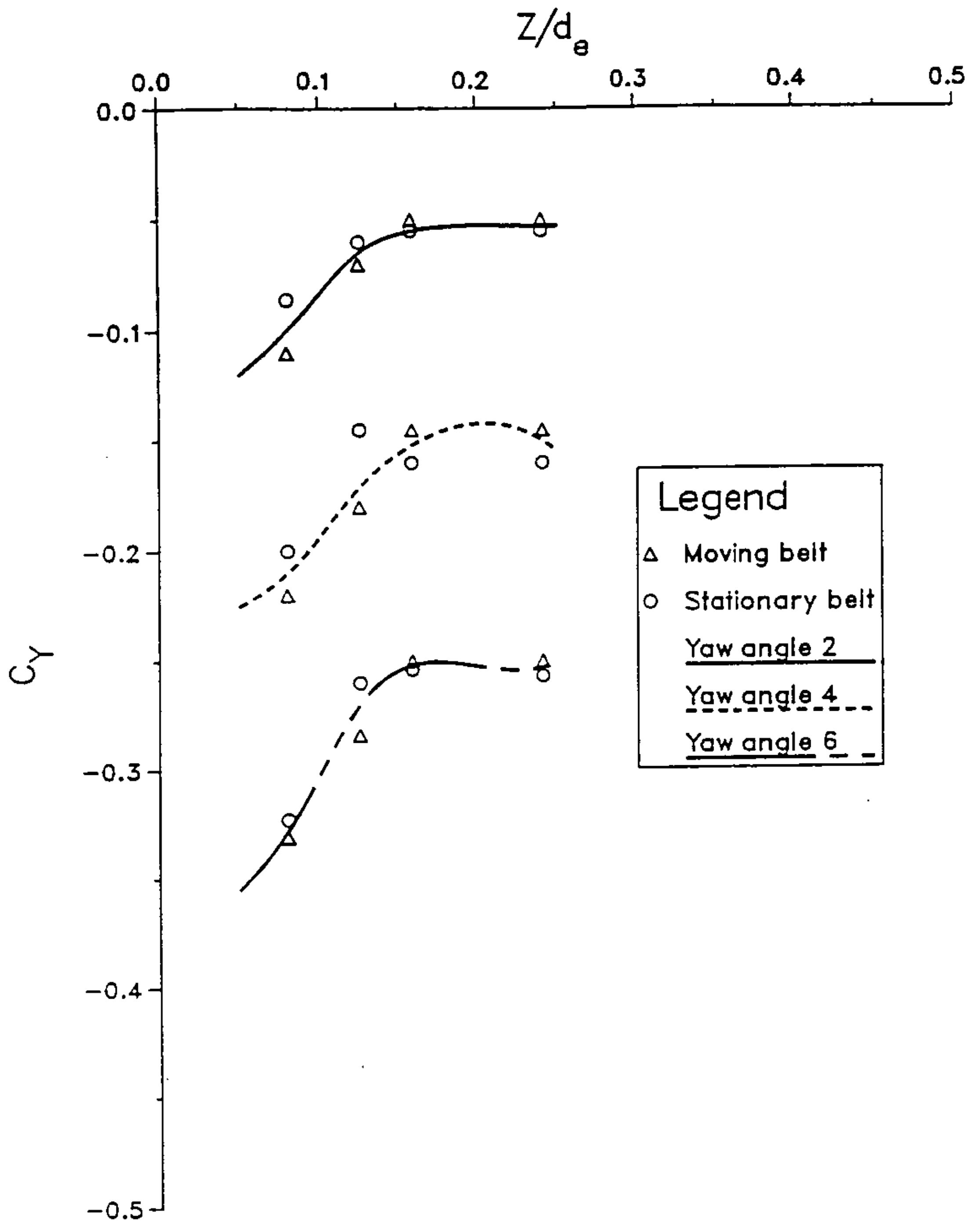

Figure 5-9 Yawning moment coefficient variation with ground clearance at various yaw angles

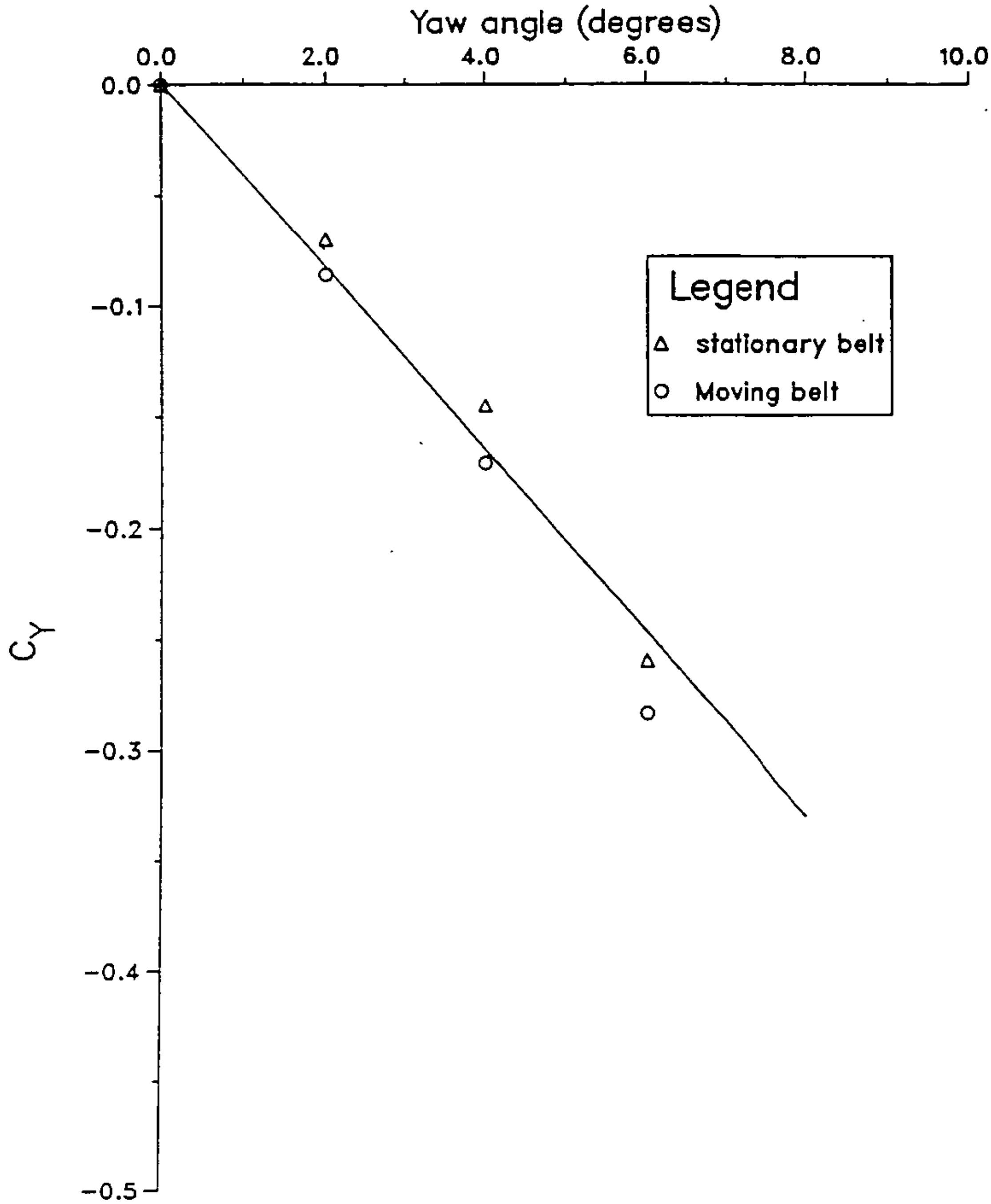

Figure 5-10 yawning moment coefficient variation with yaw angle at ground clearance Z/d_e=0.125

PART III : TURBULENT BOUNDARY LAYERS PREDICTIONS ON EMS TRAIN

PART III

TURBULENT BOUNDARY LAYERS PREDICTION ON EMS TRAIN

In part I an inviscid flow prediction for pressure distribution has been carried out. In part II a series of wind tunnel experimental test has been carried out on the EMS train models to provide the qualitative comparison with the inviscid flow prediction and to study flow in the lee side of the train. In reality the flow over the train model as well as on the real train is viscous therefore a numerical technique suitable to predict the turbulent boundary layer is needed. The prediction of the three-dimensional turbulent boundary layer at yaw, on the central part of the train in cross wind and on the nose of the train at 0° yaw angle (no cross wind) is presented in this part.

In the nose and tail regions both the flow and vehicle geometry are more complicated and require an increase in the sophistication of the analytical approach. Ideally, in order to be able to cope with vehicle geometries met in industrial aerodynamics design practice, an approach is needed which allows for both the specification of the governing equations for three-dimensional turbulent boundary layers over arbitrarily shaped surfaces and can also represent, or sensibly approximate, the geometry of these surfaces for use during the solution process for the turbulent boundary layers.

CHAPTER 6
PREDICTION OF THREE-DIMENSIONAL TURBULENT BOUNDARY LAYERS ON AN EMS TRAIN

6.1 Introduction

In practice flow over trains is always viscous and this influence on the aerodynamic forces and moments, particularly drag, needs to be taken into account to design a safe and efficient vehicle. For the time being, it appears that routine practical design methods incorporating viscous flow effects on three-dimensional surfaces moving in a fluid are likely to be limited to those which combine an inviscid flow calculation with a turbulent boundary layer computation [85,86]. In this study only the development of three-dimensional turbulent boundary layers is considered because of the high Reynolds number ($Re>10^5$) involved. The discussion here provides only a summary of the principal ideas involved in turbulent boundary layer analysis, rather than a detailed discussion of the theory underlying the turbulent boundary layer [87] — which is beyond the scope of this thesis. The goal of the chapter is to attempt to estimate the skin friction drag particularly on the complex shaped nose section of an EMS type train.

The popular practical methods for calculating the development of three-dimensional turbulent boundary layers may be divided into finite-difference or integral methods depending on the form of the governing equations. In finite-difference schemes the flow characteristics are calculated at a set of points distributed over the boundary layer thickness thickness. The appeal of this technique is that no assumption is made on the shape of the velocity profile, although a model of the flow physics in the form of a turbulence model for shear stresses [85] is required. This makes such methods to be, potentially, of general use. Substantial computing time is however required in comparison with integral methods. The principal reason for this is that integral methods predict only integrated properties of the boundary layer and thus reduce the number of independent space variables by one. However, integral methods require assumptions to be made about velocity profiles and so the accuracy of such approaches is limited by the validity of the assumed velocity profiles to the flow situation under analysis [85]. However, for routine design analyses the faster integral equation method is a natural choice, provided the profile shape assumption remains valid. In this thesis the integral method has been employed to demonstrate how to predict three-dimensional boundary layers on the EMS train model.

The usual assumptions for boundary layer theory apply to the method used here; it is therefore taken that for the high Reynolds number flows of interest the following hold:

1. viscous effects of the fluid are limited to the immediate vicinity of the surface of a body in the fluid, and inviscid flow conditions exist beyond the outer-edge of this boundary layer.

2. a no-slip condition exists for the boundary layer flow at the body surface and the flow velocity increases with increasing distance from the surface, finally reaching the velocity of the enclosing inviscid flow at the outer-edge.

3. the boundary layer flow is fully attached and its interaction with the enclosing inviscid flow is only weak.

4. the thickness of the boundary layer is small compared with the local curvature of the body surface.

5. The state of motion within the boundary layer may be expressed in terms of a mean-flow governing the large scale motion of the fluid, and a fluctuating-flow governing the turbulent "mixing" effect.

Limitation (3) above confines the adopted method to fully attached flows and the observed flow separation, vortices and viscous wake effects (see chapter two) can not be investigated. The inability of the inviscid flow analysis to provide reliable flow data to the method for yaw angles larger than about 15° further reduces the scope of the analysis. The main attraction of the approach adopted is to allow predictions of the friction drag on an EMS type train at small yaw angles, including, for the first time, the drag on the complex nose shape. An attempt is also made to investigate criteria that suggest the onset of flow separation, by studying the behaviour or solution trends of the predicted boundary layer, within the restrictions just mentioned above.

The rest of the chapter comprises five sections. Section 6.2 concerns the governing equations and numerical solution scheme for three-dimensional turbulent boundary layers on arbitrary shaped vehicle surfaces. Section 6.3 looks at a simplified approach to boundary layer analysis suitable for the train central body, far from the nose and tail, to be used in pure cross flow problems. The governing equations are given, a computer programme developed to implement the approach is described, and results of applying the programme to a test problem and the EMS train central body in a crosswind are provided. Section 6.4 returns to the more general case and describes the computer programme written to compute the boundary layer development over the train nose. Section 6.5 then discusses the results of applying the programme to the nose at 0° yaw. The chapter ends with the concluding remarks of section 6.6

6.2 Three-dimensional Turbulent Boundary Layer Analysis Scheme for Arbitrary Vehicle Shape

In order to cope with the variety of vehicle surface shapes arising in industrial aerodynamic design practice, the equations governing three-dimensional turbulent boundary layer flow are usefully specified in an arbitrary co-ordinate system (here referred to as the boundary layer co-ordinate system) which is defined in terms of a surface fitted to the vehicle of interest. This approach allows the routine generation of the boundary layer co-ordinate system from vehicle engineering drawings, using standard numerical methods for surface geometry interpolation, allowing direct evaluation of the numerical (geometric) parameters needed in the system of equations required to compute the development of the boundary layer.

Myring [88] and Cousteix [89] have derived the governing equations for three-dimensional turbulent boundary layers in a general non-orthogonal curvilinear co-ordinate system. This gives designers an alternative co-ordinate system for representing the flow and/or geometry of the vehicle surface, rather than being restricted to, for instance, the traditional system defined by the streamlines of the external flow(here referred to as streamline co-ordinate system). Although the boundary layer equations are expressed in an arbitrary non-orthogonal curvilinear co-ordinate system, the assumed velocity profiles in two mutually orthogonal directions (which are of course required in any integral method) are often still conveniently defined in a streamline co-ordinate system. Myring [88] has resolved this conflict by providing the necessary transformation relationships required to make the transition from the streamline to the arbitrary curvilinear co-ordinate system. Further, Cousteix [89] has developed an integral method which can be employed to generate suitable families of streamline and crossflow velocity profiles. Finally, Hirschel et al. [90] and Hirschel [46] have described a technique to construct a boundary layer co-ordinate system for definition of both the surface geometry of realistic vehicle bodies and the associated governing equations of the turbulent boundary layer. Hirschel has successfully used this to compute the turbulent boundary layer on a transport aeroplane [45], helicopter fuselage and on a fighter [46], in addition Hirschel et al. [47]

have applied the idea to car bodies.

The scheme adopted in this thesis is therefore based on the integral method developed by Cousteix [89] for predicting three-dimensional boundary layers combined with the concept of the boundary layer co-ordinate system of Hirschel et al. [90] to form a procedure capable of calculating the turbulent boundary layer on the nose of the EMS train. The techniques themselves are adequately described in references [88,89], details are included here to explain how they have been applied to the EMS train shape.

6.2.1 Governing Equations for Three-dimensional Turbulent Boundary Layer in Streamline Co-ordinate System

This section quotes the system of integral equations which govern the steady incompressible and subsonic three-dimensional turbulent boundary layers of interest. The equations are initially defined in the traditional streamline co-ordinate system in which the assumed velocity profiles in two mutually orthogonal directions are ultimately defined as families of streamwise and crossflow profiles [89]. This co-ordinate system, defined with reference to an external streamline is shown in Figure 6-1.

The general momentum integral and entrainment equations for steady three-dimensional subsonic incompressible flow may be written as [89,42] with streamline co-ordinate system, ξ, η Figure 6-1 :

— Longitudinal momentum equation

$$\frac{\partial \theta_{11}}{\partial \xi} + \frac{1}{U_e h_2}\frac{\partial}{\partial \eta}(\theta_{12}) + \frac{1}{U_e}\frac{\partial U_e}{\partial \xi}(2\theta_{11} + \delta_1) - \frac{1}{U_e}K_1(\theta_{11} - \theta_{22}) = \frac{\tau_{01}}{\rho U_e^3} \qquad 6\text{–}1$$

— Transverse momentum equation

$$\frac{\partial \theta_{21}}{\partial \xi} + \frac{1}{U_e h_2}\frac{\partial \theta_{22}}{\partial \eta} + \frac{2}{U_e}\frac{\partial U_e}{\partial \xi}\theta_{21} + \frac{1}{h_2 U_e^2}\frac{\partial U_e}{\partial \eta}(\theta_{11} + \theta_{22} + \delta_1) - \frac{2}{U_e}K_1\theta_{21} = \frac{\tau_{02}}{\rho U_e^3} \qquad 6\text{–}2$$

- Entrainment equation

$$U_e \frac{\partial}{\partial \xi}(\delta - \delta_1) - \frac{1}{h_2}\frac{\partial \delta_2}{\partial \eta} = F(H_{\delta-\delta_1}) - (\delta - \delta_1)\left(\frac{1}{h_1 h_2}\frac{\partial h_2}{\partial \xi} + \frac{\partial U_e}{\partial \xi}\right) \qquad 6\text{-}3$$

where

ξ,η,ζ	:	streamline co-ordinate system
τ_{01}, τ_{02}	:	skin friction components in the ξ, η directions respectively
$\theta_{11},\theta_{12},\theta_{21},\theta_{22}$	:	momentum thicknesses
δ_1, δ_2	:	displacement thicknesses
δ	:	boundary layer thickness
ρ	:	the density of the fluid
h_1,h_2	:	metric coefficients in the ξ, η co-ordinate system
H	:	streamwise shape factor
$H_{\delta-\delta 1}$	:	$\delta-\delta_1/\theta_{11}$ shape parameter used in entrainment theory
K_1,K_2	:	geodesic curvature in the ξ and η directions respectively
U_e	:	resultant velocity just outside the boundary layer

Equations (6-1), (6-2) and (6-3) are the underlying governing equations applied indirectly to the EMS model ; for convenience of application, these need first to be expressed in an arbitrary surface-fitting boundary layer co-ordinate system ; this is described next.

6.2.2 A Surface-Fitting Boundary Layer co-ordinate System

The geometry of the EMS train model shown in Figure 6-2 is most straight forwardly described with reference to a cartesian co-ordinate system ($X^{1'}$, $X^{2'}$, $X^{3'}$). The boundary layer co-ordinate system (X^1, X^2, X^3) is then arranged in such a way that the X^2 ordinate lines are on the surface of the body, i.e., these ordinates are lines on the surface of the body where X^1 is constant as shown in Figure 6-2, and are defined by cross sections parallel to the $X^{2'}$ - $X^{3'}$ plane. The X^2 ordinate is measured along the circumference of these cross sections and the upper symmetry line of the train serves as a datum line for the circumferential direction with $X^2 = 0$ at the upper symmetry line; $X^2 = 0.5$ at the lower symmetry line; and $X^2 = 1$ at the upper symmetry line having having traversed the entire train periphery. The X^1 co-ordinate, is measured along the $X^{1'}$ axis with $X^1 = 0$ at the nose and $X^1 = 1$ at the rear of the train.

The basic relationships which connect the two co-ordinate systems are [90]

$$X^{1'} = L_{x^1} X^1 \qquad \text{6–4}$$

$$X^{2'} = X_0^2(X_1) + L_{x^2}(X^1)\int_0^{x^2} \cos\alpha_c(X^1,X^2)dX^2 \qquad \text{6–5}$$

$$X^{3'} = X_0^{3'}(X^1) - L_{x^2}(X^1)\int_0^{x^2} \sin\alpha_c(X^1,X^2)dX^2 \qquad \text{6-6}$$

where

L_{x^1} is the longitudinal length of the body ;

$L_{x^2}(X^1)$ represents the circumferential length of the section at the ordinate X^1 ;

$X_0^{2'}(X^1), X_0^3(X^1)$ are the ordinates of the datum line at the ordinate X^1 for boundary layer co-ordinate axis direction 2 and 3 respectively ;

α_c is the contour angle (see Figure 6-2)

The expression for the transformation of a position vector of a point defined in the cartesian $X^{j'}$ co-ordinate system to its corresponding position vector in the boundary layer $X^{i'}$ system is, in matrix form [90]

$$\begin{bmatrix} \dot{X}^1 \\ \dot{X}^2 \\ \dot{X}^3 \end{bmatrix} = \mathbf{B} \begin{bmatrix} X^1 \\ X^2 \\ X^3 \end{bmatrix} \tag{6-7}$$

where the elements of the matrix **B** possess non-linear position dependent terms (full details of B are given in [90]. A Fortran subroutine to generate the boundary layer co-ordinate system for the EMS train surface has been purpose-written for this study. The subroutine is supplied with the cartesian co-ordinates (deduced from blue-print drawing using a digitiser) of transverse sections (see Figure 6-2) at the points where they intersect the longitudinal grid lines. The interpolating cubic splines providing precise, complete definition of each transverse section are then computed and the position of the normalised axial distance of the transverse section stored—this then allows the coefficient matrix **B** as well as other co-ordinate transformation parameters to be computed for use later in the analysis.

6.2.3 Three-dimensional Governing Equations for Boundary Layer on Arbitrary Vehicle Shape

The momentum integral and entrainment equations defined in streamline co-ordinates (ξ,η) in section 6.2.1 can be expressed in an arbitrary curvilinear co-ordinate system , such as that defined by the X^2 and X^3 axes shown in Figure 6-3, i.e. the boundary layer co-ordinates on the surface of the body, by a suitable transformation process.

Following references [89,88] the momentum integral and entrainment equations may be written in the boundary layer co-ordinate system in the form (for details see Appendix C, section C.1).

— longitudinal and transverse momentum equations

$$\frac{\partial \Theta_{11}}{\partial X^1} = F_1 (\Theta_{11}, \frac{\partial \Theta_{12}}{\partial X^2}, \Theta_{12}, \Delta_1, \Delta_2, \Theta_{22}, c_{fx}1) \quad 6\text{-}8$$

$$\frac{\partial \Theta_{21}}{\partial X^1} = F_2 (\Theta_{21}, \frac{\partial \Theta_{22}}{\partial X^2}, \Theta_{22}, \Delta_1, \Delta_2, \Theta_{11}, c_{fx}2) \quad 6\text{-}9$$

— Entrainment equation;

$$\frac{\partial}{\partial X^1}(\frac{\delta U_1}{U_s} - \Delta_1) = F (\frac{\partial}{\partial X^2}(\frac{\delta W_1}{U_e} - \Delta_2), \frac{\delta U_1}{U_e} - \Delta_1, \frac{\delta W_1}{U_e} - \Delta_2, G, \gamma_s) \quad 6\text{-}10$$

where

$c_{fx}1$, $c_{fx}2$, : skin friction coefficient in X^1, and X^2 co-ordinates

Θ_{11}, Θ_{12}, Θ_{21}, Θ_{22} : momentum thicknesses

Δ_1, Δ_2 : displacement thicknesses

Figure 6-4 shows the surface (domain) over which the solution of equations are required and bounded by

$$X_1^1 \leq X^1 \leq X_m^1 \text{ and } X_1^2 \leq X^2 \leq X_n^2$$

in the boundary layer co-ordinate system. To formulate the problem in a discretised form suitable for solution this region is subdivided into a grid by the set of of lines X_j^1=constant and X_i^2=constant then expressions corresponding to the governing equations are written for a fixed value, say, X^2_j of the variable x and for all the associated values $X^2_1, X^2_2, \ldots X^2_i, \ldots X^2_n$ of X^2 using finite difference expressions for the derivatives with respect to X^2. The derivatives of Θ_{12}, Θ_{22}, $(\delta W_1/U_e - \Delta_2)$ with respect to $X^2$are expressed in discrete form by using the values of Θ_{12}, Θ_{22}, $(\delta W_1/U_e - \Delta_2)$ at adjacent points and the system of equations (6-8) to (6-10) can then be written for fixed values X^1_j of X^1 for all the values of X^2_i in the range $X^2_1 \leq X^2_i \leq X^2_n$.. Following this procedure the resulting system of equations (6-8) to (6-10) form a set of coupled ordinary differential equations for which the independent variable is X^2 and may be integrated using Runge-Kutta numerical scheme. These equations form the basis of a method applicable to the EMS shape.

6.3 Simplified Boundary Layer Analysis for Train Central Body

Before the above system of equations was applied to the calculation of the boundary layer development on the EMS train nose, a simplier but still practically relevant problem was considered.

The train central body forms a significant proportion of the train length and the magnitude of the aerodynamic forces it experiences, in particular with regard to the train's stability against toppling in a strong crosswind, are of interest. The central body does not requitre the full complexity of the equations derived in the previous section, since it is possesses a simple shape, i.e. a cylinder-like body with a fixed transverse section. In aircraft performance studies, the successful use of finite length yawed slender body models suggests that the adoption of finite length cylinder-like shape to model the train central body may be useful. Representing the central portion of a train by cylindroid with a fixed but arbitrary cross-section shape means that significant simplification can be made to the analysis of section 6.2 by incorporating the unchanging shape directly into the governing equations for the boundary layer specified in the streamline co-ordinate systyem.

The method employed in this section to predict the three dimensional turbulent flow in the central sections of the train for crossflow condition, see Figure 6-5, is therefore based on the following references. Cumpsty et al. [43] who developed a method for calculating the three-dimensional turbulent boundary layer using momentum integral equations in conjunction with an entrainment equation for application to an infinite swept wing. Everitt [44] who closely follows the above work and that of Smith [91] to study three-dimensional turbulent flow on an infinite length, yawed, cylindrical body.

6.3.1 Governing Equations

To express the momentum integral equations in a form suitable for use with an infinite length cylindroid body, the equations for the development of the turbulent boundary layer along a generic circumferential periphery of the cylindroid are desired.

Thus, the momentum integral and entrainment equations as conventionally defined in a three-dimensional streamline co-ordinate system (e.g. equations 6-1 - 6-3 of section 6.2) are converted by projection so that they are in terms of an orthogonal set of streamwise (s_1) and transverse (n_1) co-ordinates that are defined on the surface of the cylindroid (see Figure 6-6), with origin at the top symmetry line of the train roof. Details of this transformation are given in reference [44]. These are then further transformed using the component of the velocity in the spanwise and (s) direction outside the boundary layer so that only a chordwise (x) co-ordinate along the circumferential periphery remains. At this point the various assumptions for the velocity profiles of the flow are made and a set of three simultaneous first-order non-linear differential equations result. The unknowns are the derivatives, with respect to the chordwise co-ordinate, of the streamwise momentum thickness (θ_{11}) and shape factor (H) and the angle between limiting external streamlines (β) at the analysis point. The approach for the governing equations of this section follows the suggestions of Everitt [44], except for the use of the assumed crossflow velocity profile and the derivation of the coefficients for the set of simulataneous governing equations which the present work has contributed from researching other sources e.g. [92].

It can be shown [44] that the longitudinal (f_1), transverse (f_2) momentum and entrainment (f_3) equations respectively for the turbulent boundary flow in the chordwise co-ordinate system (x) of the cylindroid may be expressed in the forms

$$f_1(h_2,U_1,V_1,U_e,H,\theta_{11},\theta_{22}, d\theta_{11}/dx\ d\theta_{22}/dx, du_e/dx, dh_2/dx)=1/2cf_1 \qquad 6\text{-}11$$

$$f_1(h_2,U_1,V_1,U_e,H,\theta_{11},\theta_{21},\theta_{22},d\theta_{21}/dx,d\theta_{22}/dx,du_e/dx,dh_2/dx)=1/2cf_2 \qquad 6\text{-}12$$

$$f_1(h_2,U_1,V_1,U_e, \delta-\delta_1, d(\delta-\delta_1)/dx, d\delta_2/dx, du_e/dx, dh_2/dx =F \qquad 6\text{-}13$$

where

$\theta_{11}, \theta_{12}, \theta_{21}, \theta_{22}$ integral thicknesses defined in the list of symbols and abbreviation

δ_1, δ_2 displacement thicknesses

U_e is resultant mean flow velocity in the direction of the external streamwise co-ordinate just outside the boundary layer

U_1, V_1 are chordwise and spanwise velocity components respectively just outside the boundary layer.

H is the streamwise shape factor given by

$$H = \frac{\delta_1}{\theta_{11}}$$

c_{f1}, c_{f2} are the skin friction coefficients in the s and n directions respectively

F is the entrainment function

To solve equations (6-11) to (6-13), the assumed velocity profiles (see Figure 6-7) in the streamwise direction used for the three-dimensional turbulent boundary layer are similar to those for the two-dimensional turbulent boundary layer case, the simplest form that may be taken is the power law formula [44]

$$\frac{u}{U_e} = \left(\frac{\zeta}{\delta}\right)^{n_1} \tag{6-14}$$

with

u : the velocity component inside the boundary layer in the streamwise direction

$$n_1 = \frac{H - 1}{2}$$

For the assumed crossflow velocity profile Johnston [92] proposed the following formula

$$\frac{v}{U_e} = a[1 - \frac{u}{U_e}] \qquad 6\text{-}15$$

with

$$a = \tan\beta \frac{\sqrt{c_{f1} \cos\beta}}{[0.1 - \sqrt{c_{f1} \cos\beta}]}$$

and

v : the velocity component inside the boundary layer in the crossflow direction

β : angle between limiting and external streamlines.

Expressions for the skin friction coefficients c_{f1} and c_{f2} that occur on the right-hand sides of equations (6-11) and (6-12) may be obtained, following [44] from the relationship known as the Ludwieg-Tillman empirical formula for the streamwise skin friction coefficient, given by

$$c_{f1} = 0.246 \exp(-1.561H)\, R_{\theta 11}^{-0.268} \qquad 6\text{–}16$$

where

$R_{\theta 11}$ is the Reynolds number based on the momentum thickness θ_{11}

and for the case of an infinite length body it can be shown that the following holds

$$c_{f2} = c_{f1} \tan\beta \qquad 6\text{–}17$$

The entrainment function F may be written in the form [44]

$$F = 0.025H - 0.022 \qquad 6\text{-}18$$

Using equation (6-14) for the assumed streamwise velocity profile and equation (6-15) for the assumed crossflow velocity profile, integral thicknesses ($\theta_{21}, \theta_{22}, \theta_{12}, \delta_2$

occuring in equations (6-11) to (6-13)) may be evaluated in terms of θ_{11}, H, and β for flow with $R_{\theta 11} > 10^4$ [44]. Substituting the latter relationships into equations (6-11) to (6-13) results in three governing equations for the turbulent boundary layer as used in the numerical solution procedure employed by the computer programme to predict the flow, in the form

$$C_{11}\frac{d\theta_{11}}{dx} + C_{12}\frac{d\beta}{dx} + C_{13}\frac{dH}{dx} = G_1 \qquad 6\text{-}19$$

$$C_{21}\frac{d\theta_{11}}{dx} + C_{22}\frac{d\beta}{dx} + C_{23}\frac{dH}{dx} = G_2 \qquad 6\text{-}20$$

$$C_{31}\frac{d\theta_{11}}{dx} + C_{32}\frac{d\beta}{dx} + C_{33}\frac{dH}{dx} = G_3 \qquad 6\text{-}21$$

where the coefficients C_{ij} and right hand side G_i are non-linear functions of θ_{11}, β and H and other terms. The full expressions for the terms C_{ij} and G_i are not supplied by Everitt [44] but have been evaluated for this study and are provided below : -

$$C_{11} = C_1 - C_2(H-1)(a - \theta_{11}C_3)$$

$$C_{12} = - C_2C_4\,\theta_{11}(H - 1)$$

$$C_{13} = - C_2\theta_{11}(C_5 - (H - 1) + a)$$

$$C_{21} = a\,(H-1)(aC_2 + 2\theta_{11}C_3) + C_1(a + C_3\theta_{11})$$

$$C_{22} = C_4\quad [(C_1+2a(H-1)]$$

$$C_{23} = C_2\,a^2\theta_{11} + C_5\,\theta_{11}\,[C1+ 2aH-1)]$$

$$G_1 = \frac{1}{2}c_{f1} - \frac{C_1\theta_{11}}{U_e}\frac{dU_e}{dx}\left[(2 + H) + (\frac{C_2}{C_1})^2\,(1 - a^2(H - 1))\right] - C_2\theta_{11}(H - 1)C_6$$

$$G_2 = \frac{1}{2}c_{f2} - \frac{1}{U_e}\frac{dU_e}{dx}\theta_{11}\left[a^2C_2(H - 1) + C_2(H + 1) + 2C_1a(1 + (\frac{C_2}{C_1})^2\right]$$

$$+ \theta_{11}(C_1 + 2a(H - 1)C_6$$

6.3.2 Computer Programme for Boundary Layer in Crossflow Condition

A FORTRAN programme, called TURBCEN, has been written as part of this study to predict the development of a three-dimensional turbulent boundary layer for the central part of an EMS train. The block diagram for programme TURBCEN is shown in Figure 6-8 and results from this programme include : the streamwise momentum thickness (θ_{11}), the streamwise shape factor (H) and the angle between the external streamline and the surface streamline (β). Data defining the periphery of the cross section of the central part of the model is supplied to the programme as a set of points specified in a two-dimensional cartesian co-ordinate system oriented in the plane of the train cross-section. Other input data also includes the external resultant velocity for inviscid flow at these points and the boundary conditions for the boundary layer (i.e. initial values for θ_{11}, H and β) at the initial point of the section. (The inviscid flow field for the section was of course obtained using the programme POTOFLO — described in chapter two — which computes the potential flow velocity on the section subject to the freestream velocity of interest.)

Cubic spline interpolation functions, employing NAG [93] library routines E02BAF and E02BCF, have been used to fit the geometry of the section defined by the input data to generate boundary layer co-ordinates in the chordwise direction. Similarly, cubic spline interpolation functions are used to represent the variation of the resultant inviscid flow velocity at the edge of the boundary layer ; from this fit the derivative of the velocity is also obtained. Several GINOGRAF [94] graphics subroutines are then called to plot both the input data points and their associated curve fits, to verify that the input data is correct and that the interpolations are satisfactory. The governing equations are then formed numerically using a subroutine named FUN1 which employs the governing equations (6-19) to (6-21) given in section 6.3.1 and a subroutine named UEIN computes the values and derivatives of the external resultant inviscid velocity.

In essence the governing equations, a system of three first-order ordinary differential equations, may be expressed in matrix form as

$$\mathbf{C}\frac{dy}{dx} = \mathbf{g}$$

where :

y	is a 3×1 vector, the components of which are the variables whose values are to be calculated, specifically θ_{11},β,H
x	is the chordwise co-ordinate
C and **g**	are a matrix and a vector respectively of coefficients which are nonlinear functions of θ_{11},β,H and x, (see equations (6-19), (6-20) and (6-21)).

The subroutines FUN1 and UEIN calculate the terms of **C** and **g** and the equations are then represented in the form

$$\frac{dy}{dx} = \mathbf{C}^{-1}\mathbf{g}$$

where : $\mathbf{C}^{-1}$ is the matrix inverse of **C** and is obtained using a NAG [93] matrix inversion routine F01AAF. The resulting matrix equation is then in a form suitable for solution by the NAG [93] routine D02BAF which uses a Runge-Kutta method.

6.3.3 Calculations for Train Central Body in a Crossflow Condition

6.3.3.1 Test Problem

Programme TURBCEN has been thoroughly tested by assessing its ability to predict three-dimensional turbulent boundary layer development for a problem for which satisfactory experimental results exist. The experimental study reported by Smith [91], which is briefly summarised next, is considered to be the type of problem that the programme should be expected to predict adequately.

Smith has studied, using a wind tunnel, the development of a three-dimensional turbulent boundary layer over a flat plate swept at 26.5° and mounted horizontally between false vertical walls. Immediately beneath this was placed a porous circular cylinder, swept at the same angle as that of the plate, and fitted with a Thwaites flap with suction applied to its surface to prevent the separation of flow from the plate surface. Smith carried out a series of experiments on this apparatus, which was designed to simulate the case of an infinite yawed wing for various flow regimes. The computer programme TURBCEN was tested by numerically simulating the infinite yawed wing conditions corresponding to the results for 'Run 1' of the tests reported by Smith. The input pressure distribution, experimentally measured and computer predicted streamwise momentum thickness (θ_{11}), the angle between the external and surface streamline (β) and the shape factor (H) are plotted against the distance normal to the leading edge and shown in Figures 6-9, 6-10, 6-11 and 6-12 respectively. The computer programme was tested using a starting distance $x = 0.11$ m from the leading edge of the flat plate where the following values for the boundary layer parameters and freestream velocity were known : θ_{11}=0.0010 m, β =5.05°, H=1.27 and U_e =27.8 m/sec. The degree of agreement between the experimental and predicted results shown in these Figures was considered to be sufficiently encouraging to justify further use of the computer programme to predict the three-dimensional turbulent boundary layer development on the central portion of the train. In particular, the ability of the method to predict the rapid growth of the boundary layer when subjected to a strong adverse pressure gradient is most encouraging.

6.3.3.2 Computed Results for Crossflow on an EMS Train

This section presents the results obtained from an application of the computer programme TURBCEN to the prediction of the turbulent boundary layer along the chordwise co-ordinate, for an EMS train shape. For this problem the EMS train model was taken to be travelling at 15° yaw and subject to an incident freestream flow with a velocity 30 m/s.

The inviscid velocity distribution predicted by the computer programme POTOFLO for three-dimensional potential flow prediction, (see chapter two) on the surface of the EMS train at 15° yaw angle for the region of the train well downstream of the nose was used as input data to the computer programme TURBCEN. It should be remembered that this potential flow prediction has been obtained using a source only method, so no vortex formation nor side force is possible ; 15° served therefore the absolute limit at which crossflow prediction could be carried out. The calculation has been started a distance x=0.16 m downstream of the nose tip and with initial boundary conditions chosen θ_{11}=0.0024 m, H=1.7 and β=-2°). These estimates for the initial conditions are different to those used in the test case and were chosen after consideration of the results of the flow visualisation tests on the EMS train (chapter four). These gave a good indication of the approximate regions of attached and separated flow on the model train, to guide where the 'central portion' calculation might be relevant as well as the fact that the value of H appears to vary between 1.3 to 1.8 for turbulent boundary layers far away from the nose and far away from the separation [22]. An initial guess of β=-2° and θ_{11}=0.0024m and H=1.7 therefore served reasonable [22].

Figure 6-13 shows the variation of the streamwise momentum thickness (θ_{11}) along the chordwise surface distance co-ordinate measured across the train roof. Thus, it is predicted that the momentum thickness should increase slowly at the beginning of the development of the boundary layers and then increase sharply in the neighbourhood of the train lee side corner which is therefore an expected separation point as also confirmed by the flow visualisation study reported earlier.

In Figure 6-14 the variation of the shape factor (H) along the chordwise co-ordinate is shown. It can be seen that the shape factor at the start of the development of the boundary layer decreases slightly but then starts to increase again, followed by a sharp increase near the (assumed) point of separation.

Finally, Figure 6-15 shows the variation of the angle between the limiting and external streamlines (β) along chordwise surface distance co-ordinate. It shows an increase in this angle at the beginning of the development of the boundary layer, then decreases slightly and is followed by a sharp increase near the (assumed) separation point.

The trends predicted in Figures 6-13,6-14 and 6-15 occurs may be compared with those predicted by the model of Copley [22] for an APT shape at 25°, see Figure 6-16. Even though there are differences between models and at different yaw angles, the trend of the curves are similar implying that flow on long body shape has a similar structure at a low yaw angles.

The observed behaviour of the curves in Figures 6-13 to 6-15 occurs because the circumferential pressure gradient on the train roof away from the corners and far away from the nose is small and consequently the boundary layer on the train roof changes in thickness only slowly until close to the separation line. Because the axial pressure gradient is also small, then the curvature of the streamlines within the boundary layer is also small, as observed in the flow visualisation tests.

6.4 A Computer Programme for Boundary Layer Analysis on Train Nose

For boundary layer prediction close and on the nose of the train, the full set of the equations must be used.

A computer programme, called TURBNOS, has been developed to compute the three-dimensional turbulent boundary layer on an EMS train model and can, with a modest degree of change, be adopted for any other model, e.g aircraft fuselage or motor car body. The block diagram of the computer programme TURBNOS is shown in Figure 6-17.

The geometry of the EMS train is supplied to the programme as a set of points on the model surface in cartesian co-ordinates. At each such point the inviscid flow velocity (expressed as a magnitude and angle) is also given as calculated in a prior analysis using the potential flow programme, POTOFLO. Output from the programme includes computed skin friction coefficient and momentum thickness in the boundary layer co-ordinate system.

Programme TURBNOS may be divided into two functional parts. The first part is a one-time only generation of a boundary layer co-ordinate system data set, from the supplied body surface geometry, followed by a step-by-step equation solution process for the the turbulent boundary layer. Cubic spline interpolation functions, employing NAG [93] subroutines have been used to fit the supplied geometry points which lie in each transverse section to define the boundary layer co-ordinate system. Once the cubic spline equation for a given circumferential section is known the circumferential boundary layer co-ordinate X^2 may be calculated. These cubic spline fits allow the numerical evaluation of all boundary layer, cartesian and streamline co-ordinate transformation parameters required for the solution process as mentioned in section 6.2.3. For the overall calculation method to succeed one must ensure that the cubic spline fits for the EMS train transverse sections are satisfactory, thus, the programme plots the fitted curve for each section so that these may be checked.

The equation solver process for the turbulent boundary layer involves a repetitive cycle following the sequence : (i) form the system of equations for a boundary line (transverse section) on the body surface ; (ii) solve the equations; (iii) proceed to the next boundary line. To form the system of equations a number of terms which occur on the right-hand side must be derived from the solution or initial conditions for the terms on the left-hand side. This is because all the terms appearing in the system of equations (6-7), (6-8) and (6-9) cannot be expressed directly in the boundary layer co-ordinates but are related in a known way to a set of terms in the streamline system, see reference [88,89] for details. Two subroutines have been written to relate terms in the boundary layer and streamline co-ordinate system. A subroutine called THSTR computes all the necessary terms in the streamline co-ordinate system from the solution of the boundary layer equations while the other subroutine, called THCURV, is employed to transform these streamline co-ordinate system terms to the boundary layer co-ordinate system. Three-purpose written subroutines, namely EQ1, EQ2 and EQ3, then form the equations to be solved. The equations generated have the form of a system of first-order differential equations, which may be written as

$$\frac{dY_i}{dt} = F_i(t, Y_1, Y_2, Y_3, \ldots, Y_N) \qquad \text{where } i = 1,2,3,\ldots, N$$

A NAG library subroutine called D02BAF [93], which employs a Merson [93] form of the Runge-Kutta method, has been used to solve the equations numerically.

6.5 Predicted Distribution of Skin Friction Coefficient on EMS Train Nose

The computer programme TURBNOS was used to predict the development of the three-dimensional turbulent boundary layer on the nose of an EMS train traveling at a constant velocity in still air. For this zero yaw situation , the source only potential flow method should predict a reasonable free stream velocity. Further, the flow around the nose, as observed in the experimental work (see chapters three and chapter four), is attached apart from small regions of separation at the side edge corners and at the top of the nose. As separation represents a discontinuity in the attached flow it can be anticipated to result in numerical instability as the computational procedure for the boundary layer approaches these regions. However, meaningful predictions for the flow prior to these regions can be obtained. Thus, this calculation provides a useful application of the programme as regards both the trends to expect of the flow and the detail provided of the skin friction behaviour of the flow over the nose. Even this calculation has brought to light many problems which can hinder such an analysis. These problems may be summarised as follow :

1. Boundary conditions — programme TURBNOS requires values for the momentum thicknesses Θ_{11}, Θ_{21} and the term $(\delta U_1/U_e - \Delta_1)$ at each point of the initial cross section. These are difficult to find theoretically.

2. The initial cross-section at the very front of the nose presented problems because of the sharp corners and the attendant separation of flow that these can cause. Furthermore sharp corners may cause spurious geometric shapes or programme errors to occur during the curve fitting phase used to generate the boundary layer co-ordinate system, see Figure 6-18. In this Figure a cubic spline fit for a cross-section with a sharp corner is shown. The Figure shows the failure of the cubic spline to represent the correct shape of the cross-section and this of course would lead to a failure in generating an acceptable boundary layer co-ordinate system. It was therefore essential to check the quality of fit

before proceeding with the calculation. Perhaps the practicality of using a cross-section further from the front could be investigated, possibly with the aid of experimental data to define the necessary initial conditions for the boundary layer parameters.

Nevertheless, successful solutions were derived to overcome the above problems. The difficulty with obtaining reasonable estimates for initial conditions for the boundary layer thicknesses etc. has been overcome by using the so-called von Karman-Pohlhausen [95] method to estimate the initial conditions for the turbulent boundary layer analysis.

This method (as presented in ref [95]) provides a table to find the values for laminar boundary layer parameters along the surface of a body. The table provides values for the parameters Λ, λ, H, $F(\lambda)$, and $J(\lambda)$ which are defined as

$$\Lambda = \frac{\Delta^2}{\nu} \frac{dU_1}{dX^1}$$

$$\lambda = \frac{\Theta^2}{\nu} \frac{dU_1}{dX^1}$$

$$H = \frac{\Delta_1}{\Theta}$$

$$F(\lambda) = \frac{\Delta\Theta^2}{\nu} \frac{U_1}{\Delta X^1}$$

$$J(\lambda) = \frac{\tau_\omega \Theta}{\mu U_1}$$

It is noted that the parameters λ, H, F and J may all be expressed in terms of Λ. Thus the table characterised by the von Karman-Pohalhausen method provides the numerical values of all parameters for a set of values of Λ.

For a body with a bluff nose the method takes the stagnation point as its starting point. The velocity at this point is zero and from the above relationship $F(\lambda)$ is zero. Using this value of $F(\lambda)$ the values of Λ, λ, H, $J(\lambda)$ can be found from the table provided for the method and these new values can be used as initial conditions for the computation of the development of the laminar boundary layer. The solution procedure then continues as follows.

A series of values of distance X^1 along the surface of the body are chosen to give small values of ΔX^1 between consecutive points. At all chosen points the values of the flow velocity and its derivatives are computed using the potential flow prediction computer programme POTOFLO. For each step ΔX^1 the value of Θ^2/v is calculated, where Θ is the value computed at the end of the previous step. This value for the term Θ^2/v enables the corresponding value of λ to be found and from this the values of $F(\lambda)$, H, Λ and $J(\lambda)$ can then be found from the table. Then, taking the value to of $F(\lambda)$ for the step the value of $\Delta\Theta^2/v$ can be calculated using the expression for $F(\lambda)$ given above. Knowledge of $\Delta\Theta^2$ allows the value of Θ^2 and hence Θ at the end of the step to be calculated. This two-stage calculation involving the terms Θ^2/v and $\Delta\Theta^2/v$ is then repeated for subsequent steps until the point where we expect the flow to become turbulent (as suggested by, say, flow visualisation tests for the body under consideration). The values at this point can then be used as estimates for the initial condition for a turbulent boundary layer prediction and it is then possible to calculate the values of Θ_{11}, H and Δ.

The above procedure has been applied to two planes of flow on the EMS train nose. The first of the planes was a vertical plane passing through the centre line of the nose and the second plane was perpendicular to the first (at the base) but was both at and parallel to the base of the EMS model. This allowed initial values to be calculated for the turbulent boundary layer parameters Θ_{11}, H and Δ at two points on the circumferential periphery of a transverse cross-section of the train nose. One of these points is the intersection of the periphery of this transverse cross-section with the first plane on the nose roof centreline. The second point is one at the base of the nose. The initial values along the periphery of this transverse section between the two points were then obtained by linear interpolation for each parameter Θ_{11}, H and Δ. After the calculation of the initial values along the periphery, an interpolation was required to find the intermediate points as explained earlier.

The second problem, (item 2 above) was overcome by simply using more points in the corner edges of the train cross-sections so as to have more realistic representation of the local geometry, see Figure 6-19. Figure 6-19 shows a cubic spline fit for a cross-section with a sharp corner, but in this case more points were added on the sharp corner to smoothen the curve in this region.

Following the resolution of the above difficulties, the computer programme TURBNOS could then be applied to the EMS train. The train was taken to be at 0° yaw angle and subjected to an incident freestream velocity of 30 m/s. The calculation for the boundary layer was started at a transverse cross-section at the nose of the train at a distance x=0.8 m from the tip of the nose this being sufficient to avoid the small separation at the blunt nose. With the estimated initial values for Θ_{11}, H and Δ along the circumferential periphery of this section being known, the calculation for the three-dimensional turbulent boundary layer was started and proceeded downstream.

Figure 6-20 shows the variation of the predicted local skin friction coefficient with the circumferential co-ordinate for section B, see Figure 3-3. This result is plausible and consistent with the attached flow regimes observed in the flow visualisation tests for this region of the nose of the train. The increase observed for the coefficient at the sharp corner (points 10-15) is due to the sharp changes in the pressure gradients on this side of the nose. Some of the scatter in the results in Figure 6-20 may be due to the method of starting the solution, as described above.

Figure 6-21 shows the distribution of local skin friction coefficient on the train centre-line for three computed sections. The Figure shows that the local skin friction coefficient increases almost linearly with longitudinal distance, which is a consequence of the increase in velocity in this region as the flow accelerate over the nose.

6.6 Summarising Remarks

6.6.1 Summary Remarks for Turbulent Boundary Layer Predictions on the Nose Of the EMS Train

A theoretical analysis suitable for the prediction of the development of the three-dimensional turbulent boundary layer on the surface of bodies in practical aerodynamic design has been presented. This analysis has been obtained by reviewing and combining analytic and numerical methods employed in aerodynamic studies within the aerospace and automotive industries to derive a method appropriate for high-speed vehicles such as the EMS train. The analysis scheme is based on an integral equation method specified in a general curvilinear co-ordinate system and associated momentum and entrainment equations. The potential of the analysis was demonstrated by applying it to predict the turbulent boundary layers on the nose of an EMS train.

In developing the computer programme TURBNOS to predict the turbulent boundary layer over the train surface. Two principal difficulties were encountered. The first involved the lack of reliable data for the specification of the initial conditions for the calculation. The second difficulty was due to the existence of sharp edges in the basic geometric model used as data to the programme. These could cause spurious geometric shapes or programme errors to occur during the curve fitting phase used to generate the boundary layer co-ordinate system. It was therefore essential to check the quality of fit before proceeding with the calculation. Unsatisfactory fits were improved by increasing the number of points in the region of the rapid geometric changes in the body shape. The initial condition problem was overcome by using the von Karman-Pohlhausen method.

The computed results for the local skin friction drag on the centre line of the roof of EMS train nose and along the circumferential periphery of a test transverse section through the nose were examined and found consistent with the results of the flow visualisation studies for these regions of the train. These results suggest some potential for the programme, although increased effort to establish more realistic initial conditions is certainly desirable.

6.6.2 Summary Remarks for Turbulent Boundary Layer Predictions on the Central Body in a Crosswind

1. A computer programme called TURBCEN was written by the author to predict the development of the turbulent boundary layer on the central section of the train far from the nose. The use of an infinite cylindroid to model the train allowed simplifications to be made in the derivation of the governing equations. The programme predicts the development of the boundary layer along the periphery of a generic cross-section of the central portion of the train. In short, this program was intended for turbulent boundary layer computations involving uniform sections with simple, smooth geometries and subject to uniform freestream flows. The results from the programme suggest it is suitable for predicting the boundary layer for the simple flow regimes and geometries of the central section of the train.

2. The quality of the computed results for the momentum thickness (θ_{11}), shape factor (H) and the angle between the limiting and external streamlins (β) along the periphery of the EMS train model are good far away from separation and poor in the separation region.

3. The flow visualisation tests for an EMS train at yaw shows a separation of the flow on the side corner of the lee side of the train and this is consistent with the turbulent boundary layer prediction which shows a sharp rise in and susequent high values of the shape factor H in the same region. Both of these results, flow visualisation and turbulent boundary layer prediction, are also consistent with the wind tunnel measured pressure coefficient which have negative values of high magnitude on the lee side of the train.

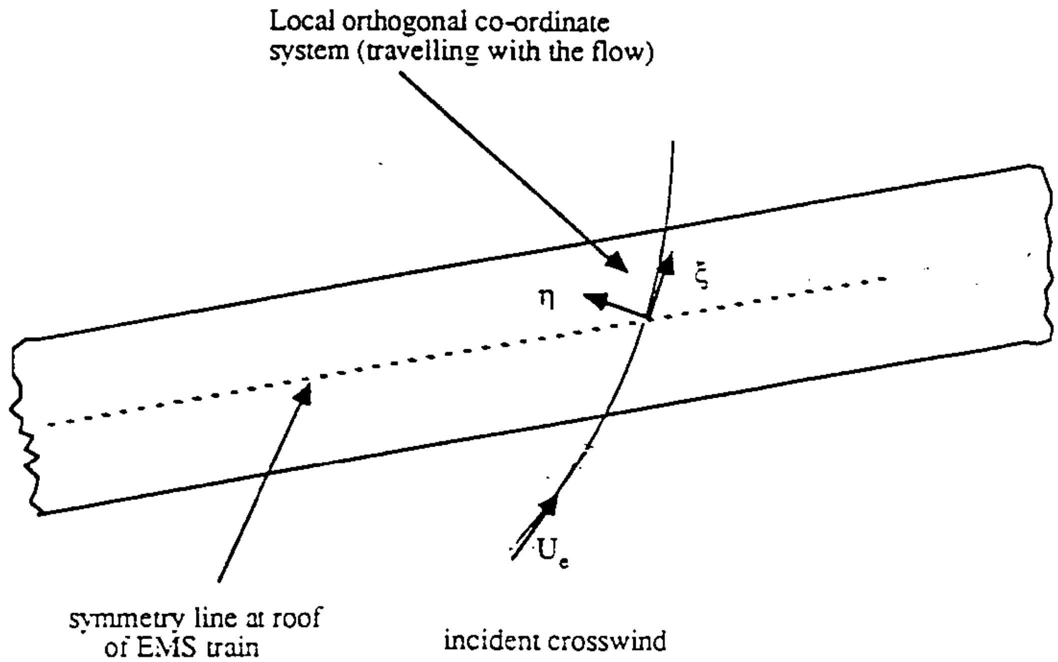

Figure 6-1 Streamline co-ordinate (ξ,η) system

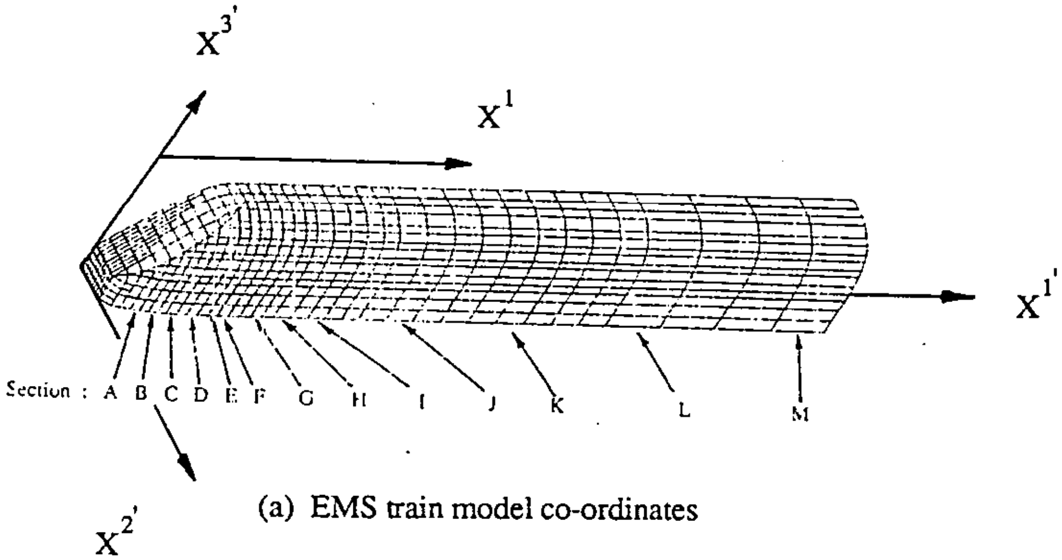

(a) EMS train model co-ordinates

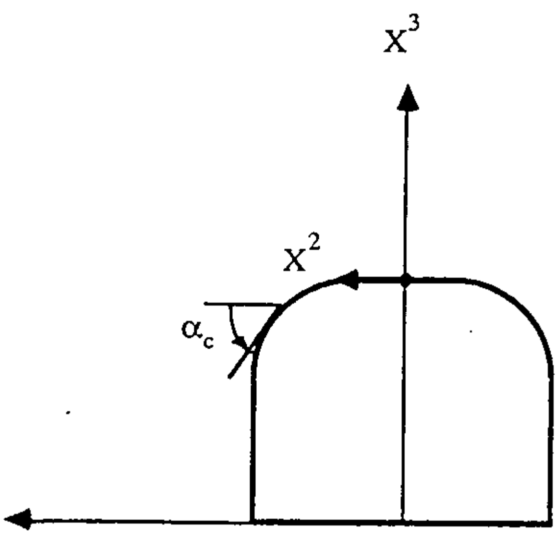

(b) section at $x^{1'} = l_0$

Figure 6-2 The cartesian co-ordinate system and the surface-oriented boundary layer co-ordinate system.

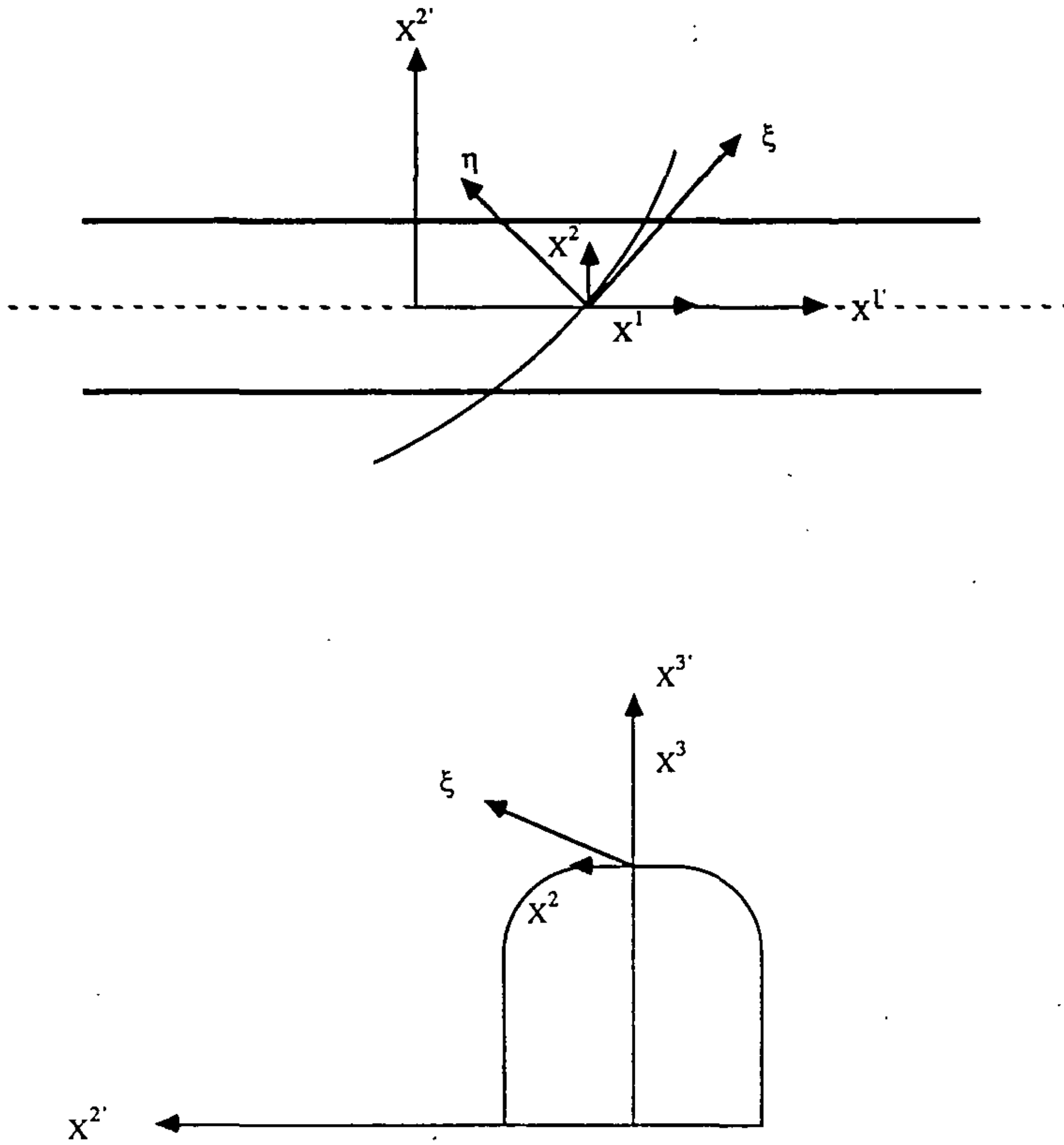

Figure 6-3 Boundary layer and cartesian co-ordinate systems

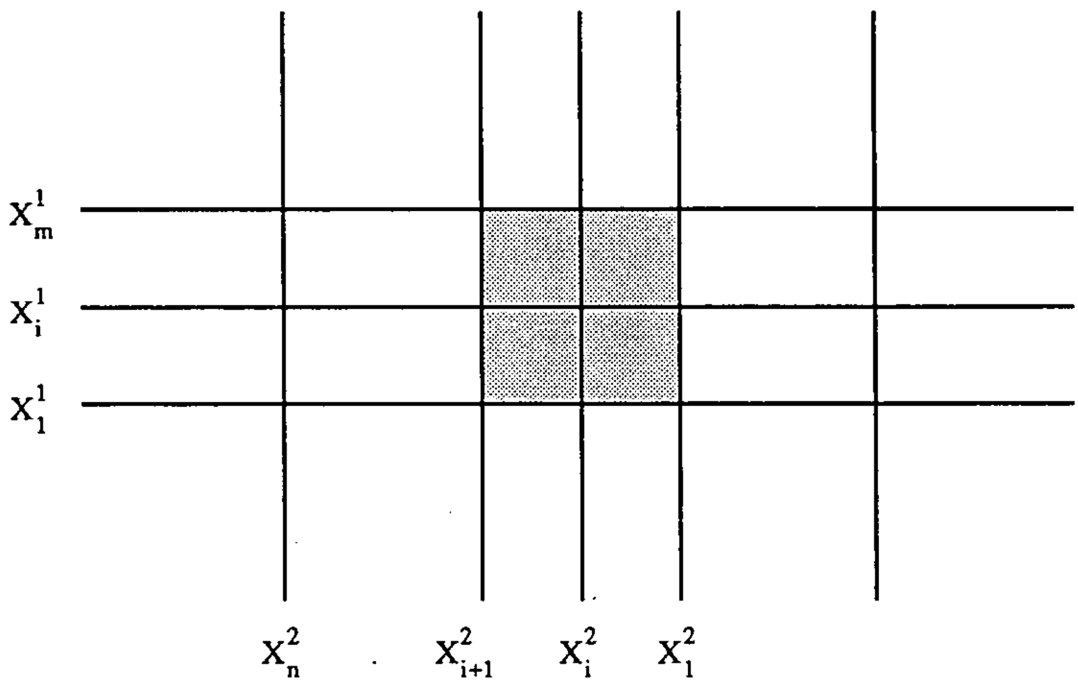

Figure 6-4 A sample Grid for the method of lines

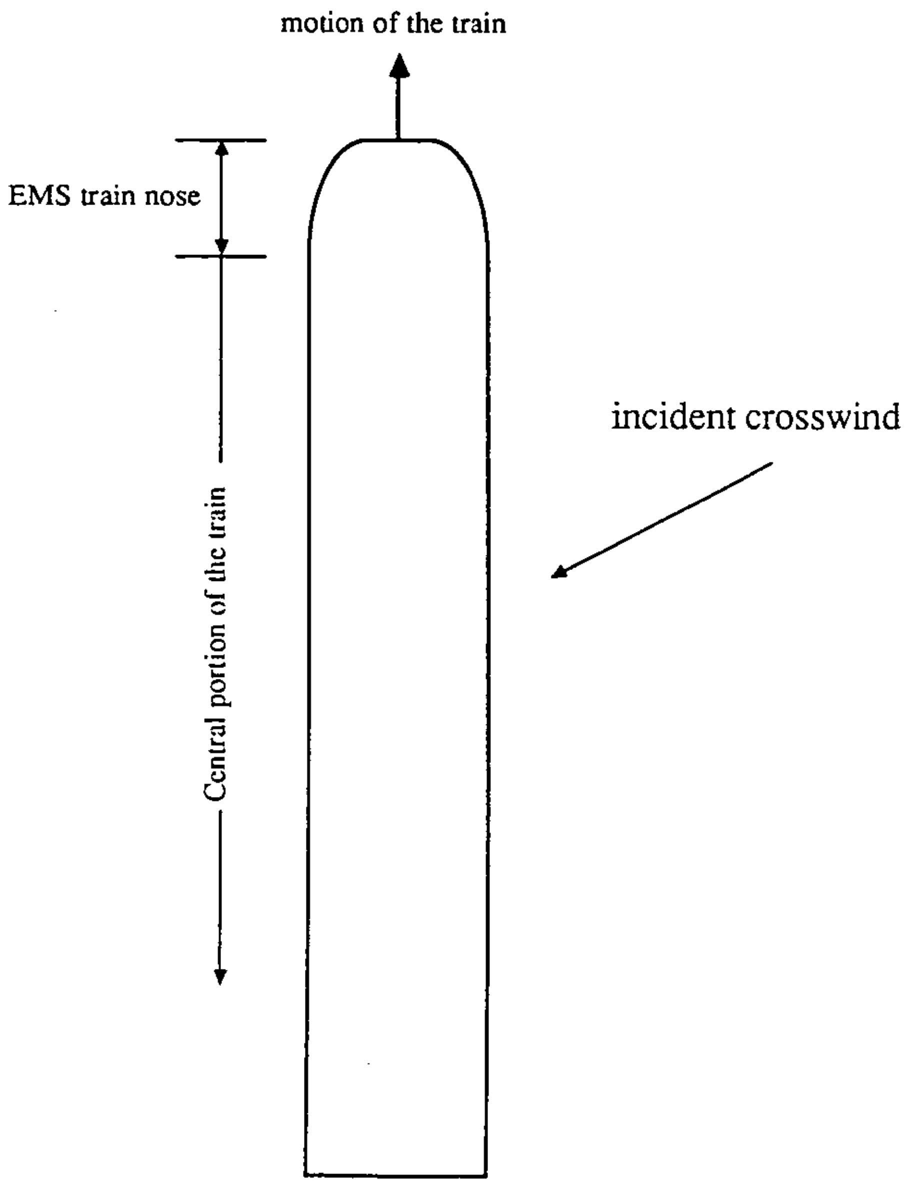

Figure 6-5 Three-dimensional turbulent boundary layer analysis on the central portion of the EMS train in a crosswind

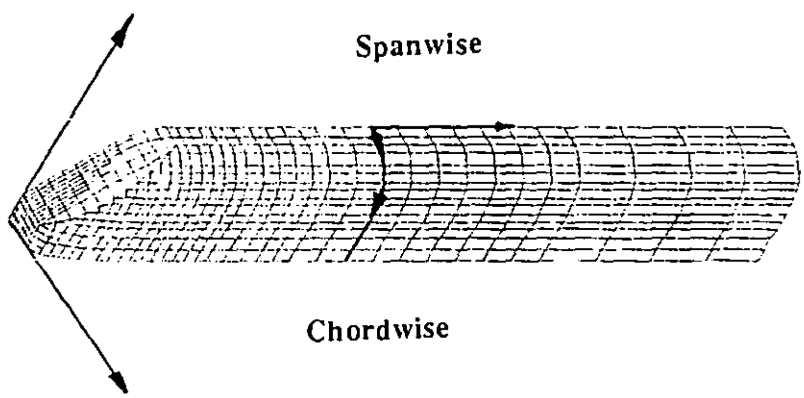

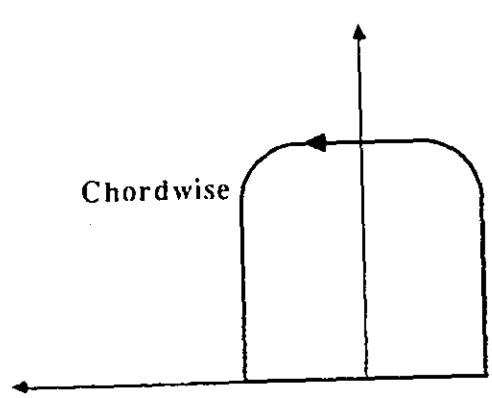

Figure 6-6 Streamwise and spanwise directions in EMS train model

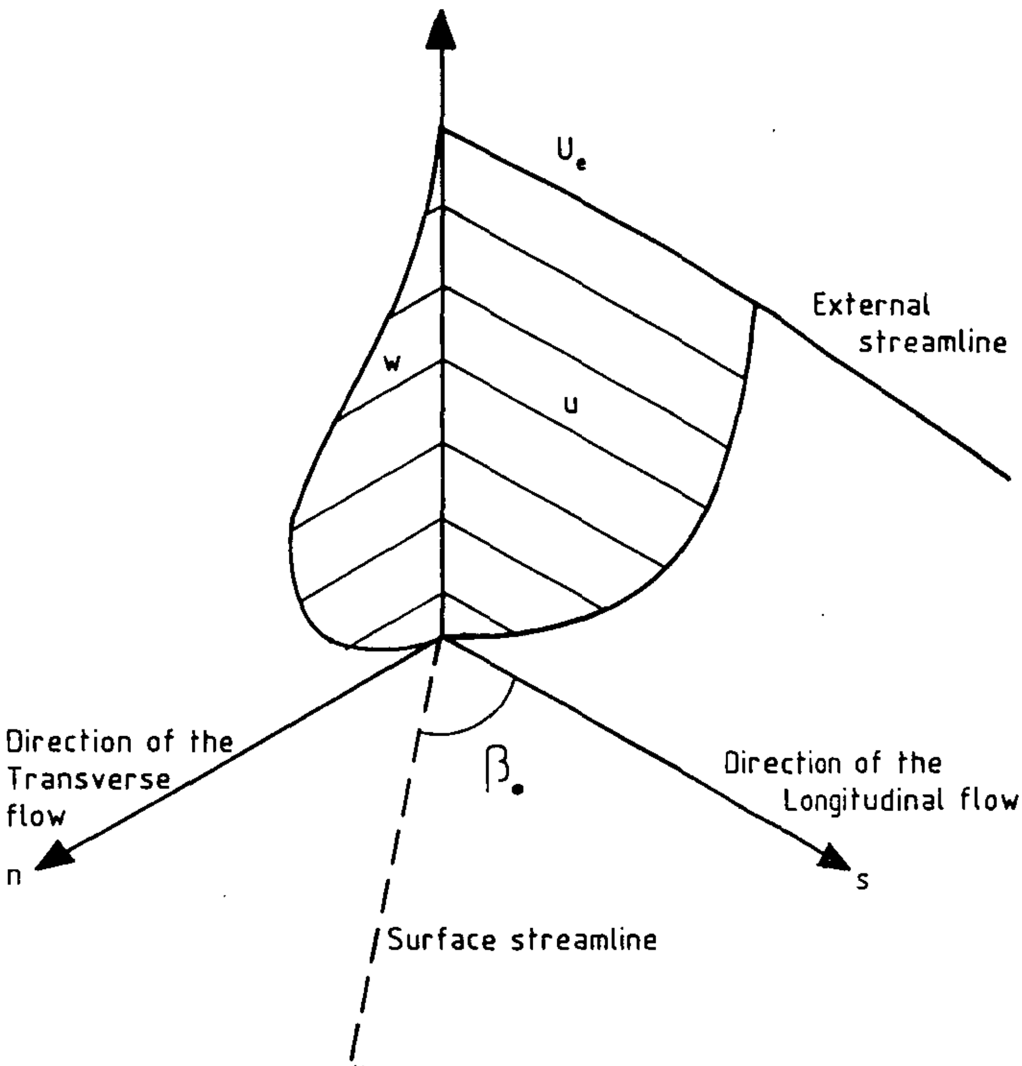

Figure 6-7 Three-dimensional velocity profiles for longitudinal (u) and transverse flow (w)

START

DATA PREPARATION

A. GEOMETRY OF CROSS-SECTION FROM CENTRE OF BODY

1. Read cartesian co-ordinate of the reference points defining the periphery cross-section from uniform central part of the body

   - draw the geometry as a check

2. Fit cubic spline curve through the perifery of the cross-section from step A.1 above

   - draw splined periphery as a check on quality of fit

3. Generate chord- and spanwise co-ordinate system for cross-section using the cubic spline fit from step A.2 above

   - draw chord- and spanwise co-ordinate of cross-section as a check

B. CHORDWISE EXTERNAL POTENTIAL VELOCITY

1. Read chordwise external potential velocity for periphery of cross-section of step A.1 above

2. Fit cubic spline through the external potential velocity

C. INITIAL BOUNDARY CONDITIONS

1. Specify the values for the terms H, θ β (see section 6.3 equation (6-19, 6-20 and 6-21) for initial reference point on the periphery of cross-section

1

1

GENERATION AND SOLUTION OF GOVERNING EQUATIONS

D. GENERATE GOVERNING EQUATIONS

1. For the current reference point

   (a.) using the spline fit for chordwise potential velocity in step B.2 evalute external potential velocity U_e and the space derivative $\frac{dU_e}{dx}$ at this point

   (b.) compute values of the coefficients C_{ij} and right-hand side G_i , i,j=1,3 of equations (6-19),(6-20) and (6-21) as nonlinear functions of , θ_{11}, β, H .

   (c.) Assemble results of the step D.1.(b.) above to form the system of governing equaations

E. SOLVE GOVERNING EQUATIONS AND WRITE RESULTS

1. Solve system of equations from step D.1.(b.) above to obtain H, θ_{11}, β at a new point, chosen by NAG routine D02BAF on periphery of cross-section
2. If the current point is not one of those specified in the DATA PREPARATION steps A.1 and A.2 go to step D above, otherwise go to the next step below
3. Write the results for the flow at the current reference point i.e H θ_{11}, β
4. If more reference point remain go to step D, otherwise STOP

STOP

Figure 6-8 Block diagram for the programme TURBCEN

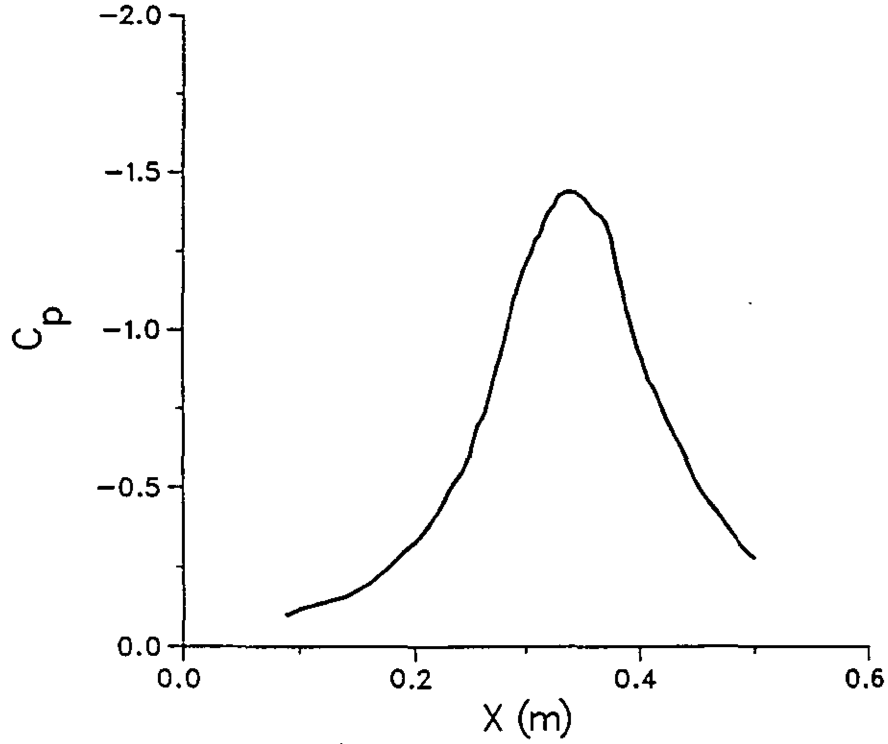

Figure 6-9 Pressure distribution on flat plate for the test case

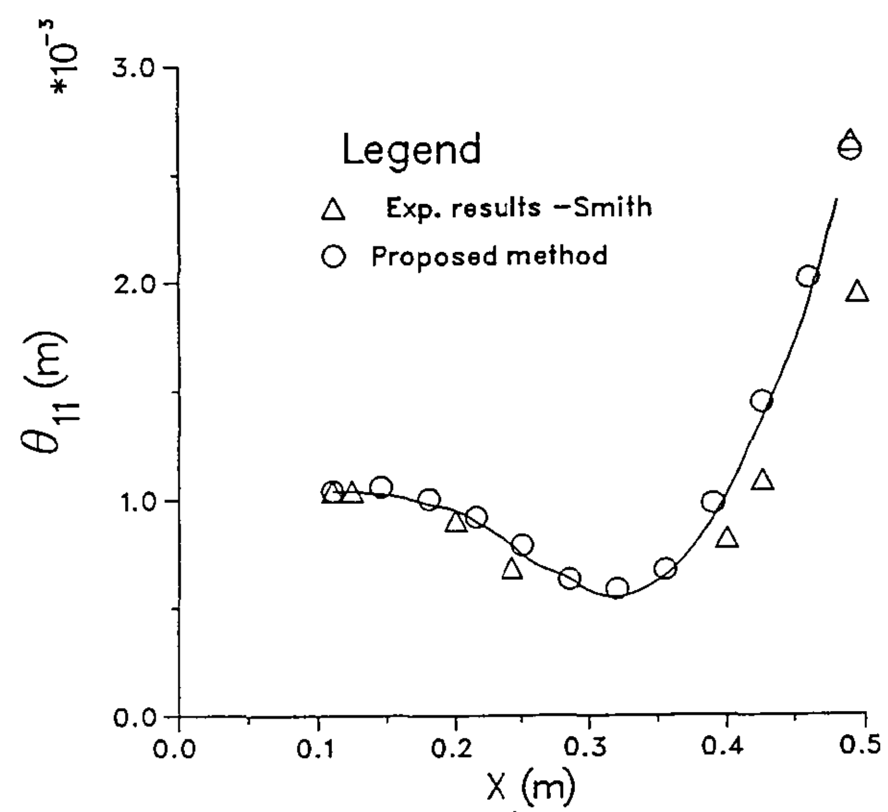

Figure 6-10 Variation of stream momentum thickness

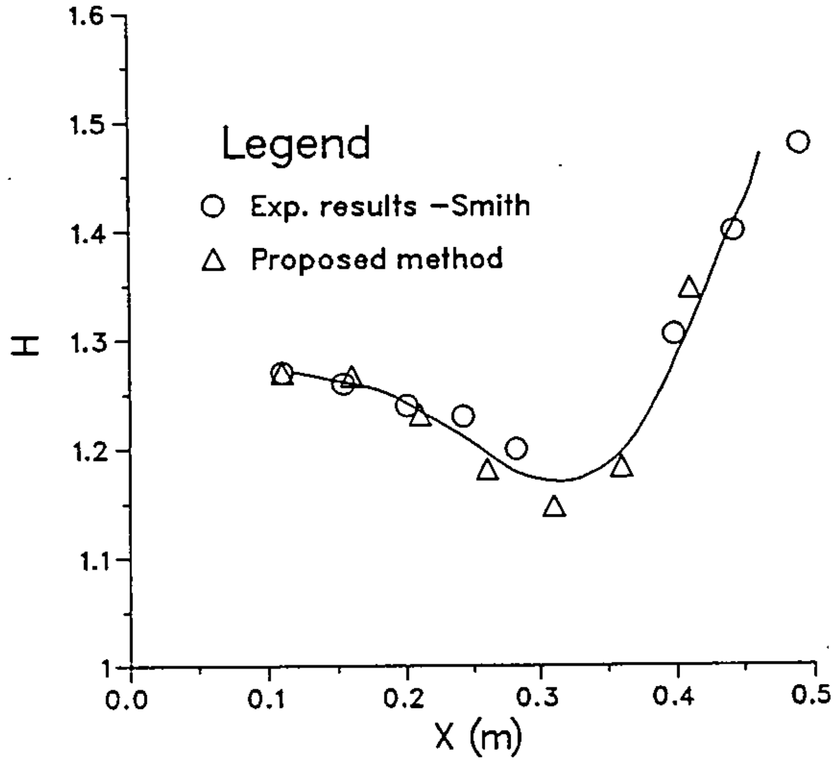

Figure 6-11 Variation of streamwise shape factor

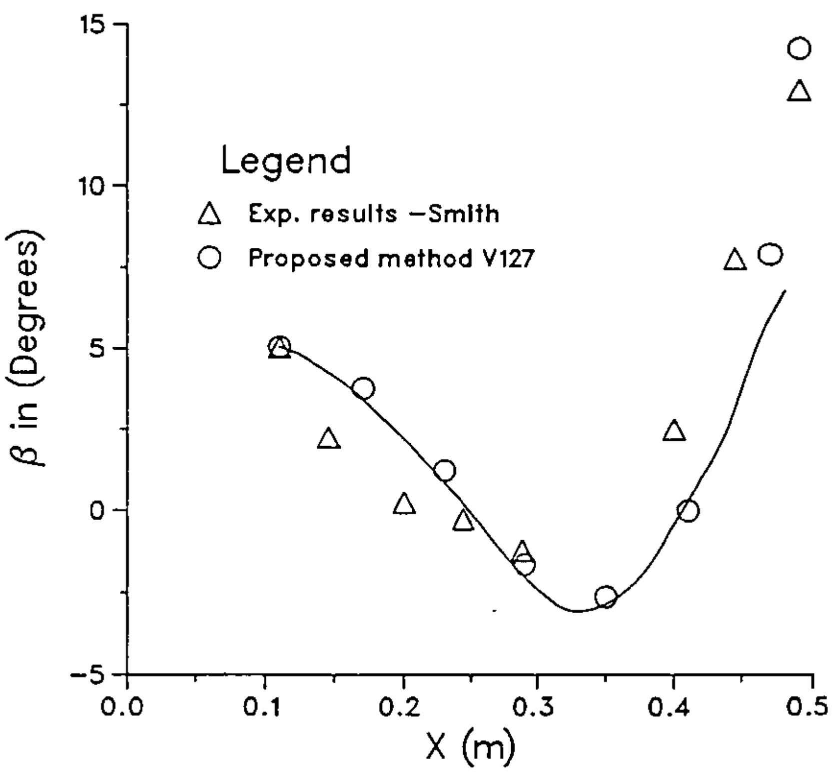

Figure 6-12 Variation of angle between limiting and external streamlines

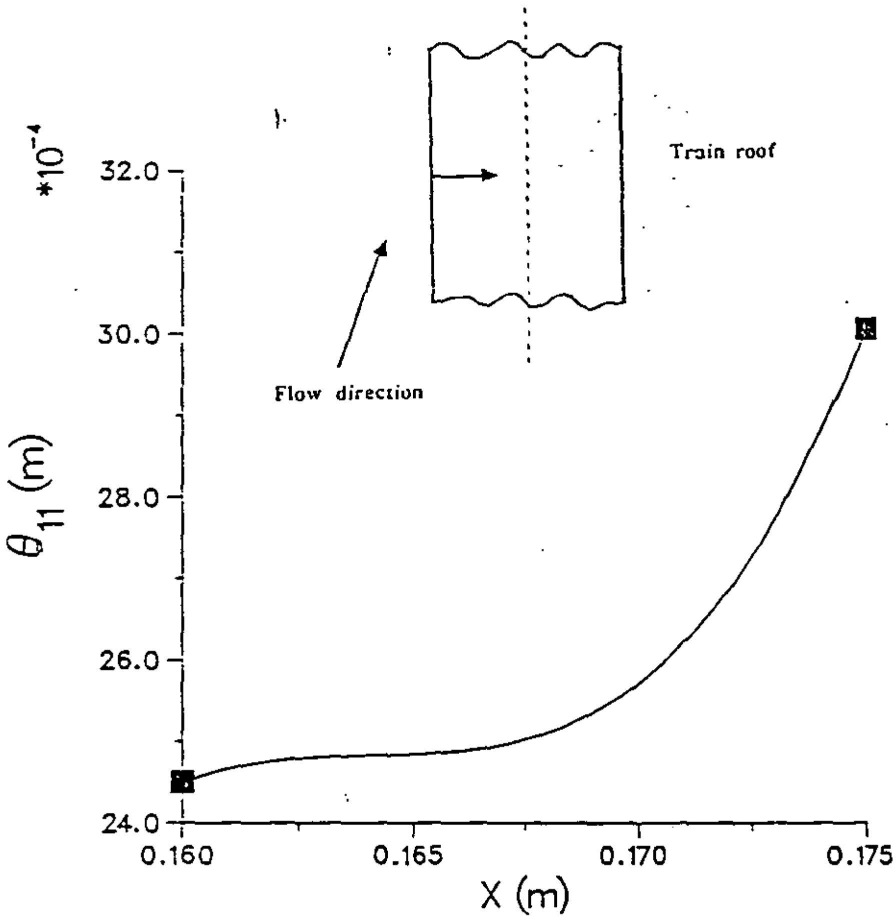

Figure 6-13 Variation of the momentum thickness along the chordwise surface distance

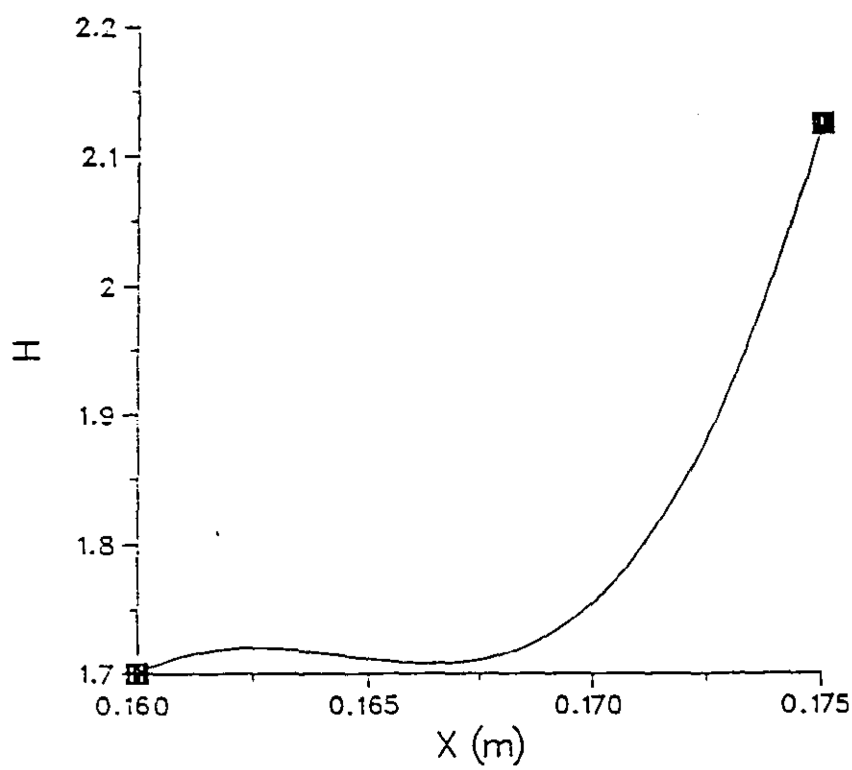

Figure 6-14 Variation of the shape factor along the chordwise surface distance

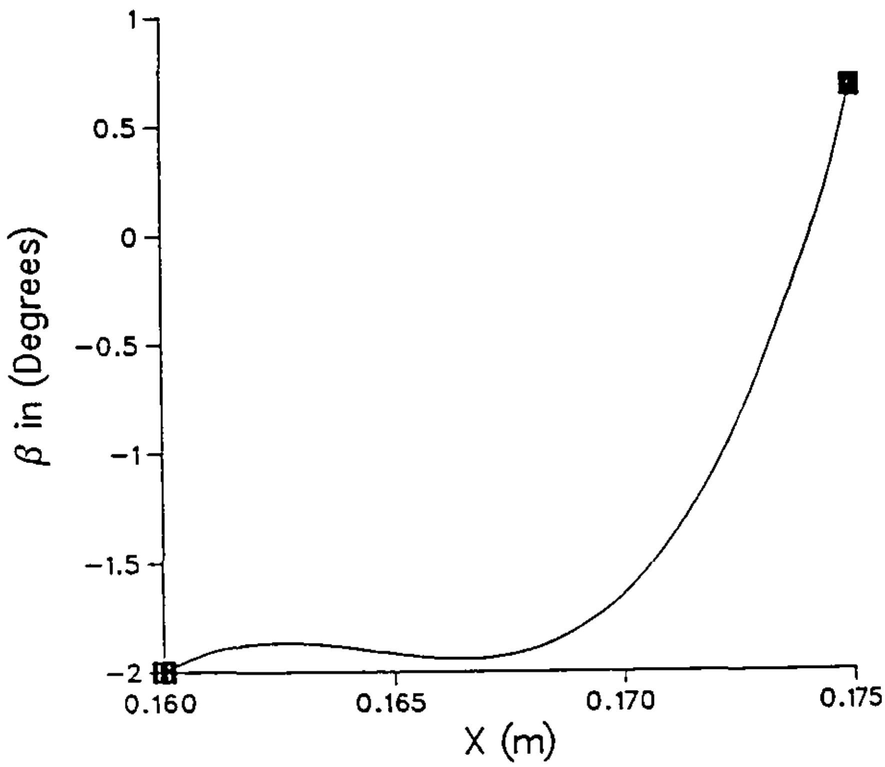

Figure 6-15 Variation of angle between limiting and external streamlines along the chordwise surface distance

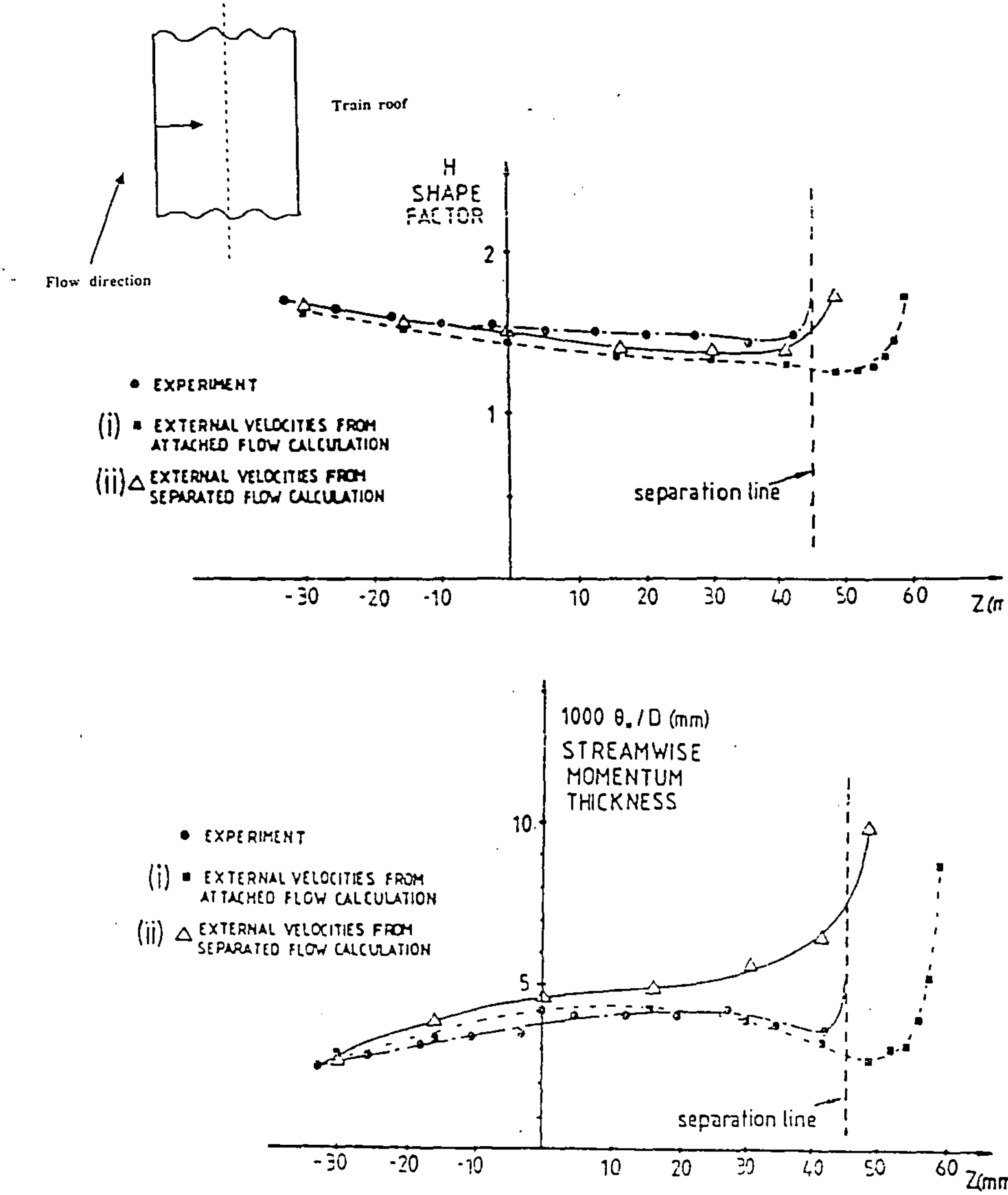

Figure 6-16 Measured and calculated shape factor and momentum thickness for APT at yaw angle 25° [ref. 20]

START

DATA PREPARATION

A. GEOMETRY OF BODY SURFACE

1. Read cartesian co-ordinates of reference points defining geometry of body surface
   - draw the geometry as a check
2. Fit cubic splines through each cross-section of body surface
   - draw cross-sections to check on quality of fit
3. Generate boundary layers co-ordinate system for spline fitted body surface
   - use co-ordinate transform concepts given in section 9.3.
   - generate database to allow any cross-section of the body between any two consecitive sections supplied as data in steps A.1 and A.2 above to be generated by interpolation
   - draw body surface in boundary layer system as a check

B . SPECIFICATION OF EXTERNAL VELOCITY

1. Read external velocity (in streamline system) over body surface and transform this velocity to the boundaru layer system
2. Fit cubic spline to B.L. external velocity and hence allow for the determination of the space partial derivative of external velocity $\frac{dU_e}{dx}, \frac{\partial h_1}{\partial z}, \frac{\partial h_2}{\partial x}, \frac{\partial}{\partial x}(\frac{q}{h_1})$ through the body surface

C. INITIAL BOUNDARY CONDITION FOR FIRST SECTION

1. Specify the parameters Θ_{11}, Θ_{12} and $(\delta U_1/U_e - \Delta_1)$ for each reference point on the initial cross-section

1

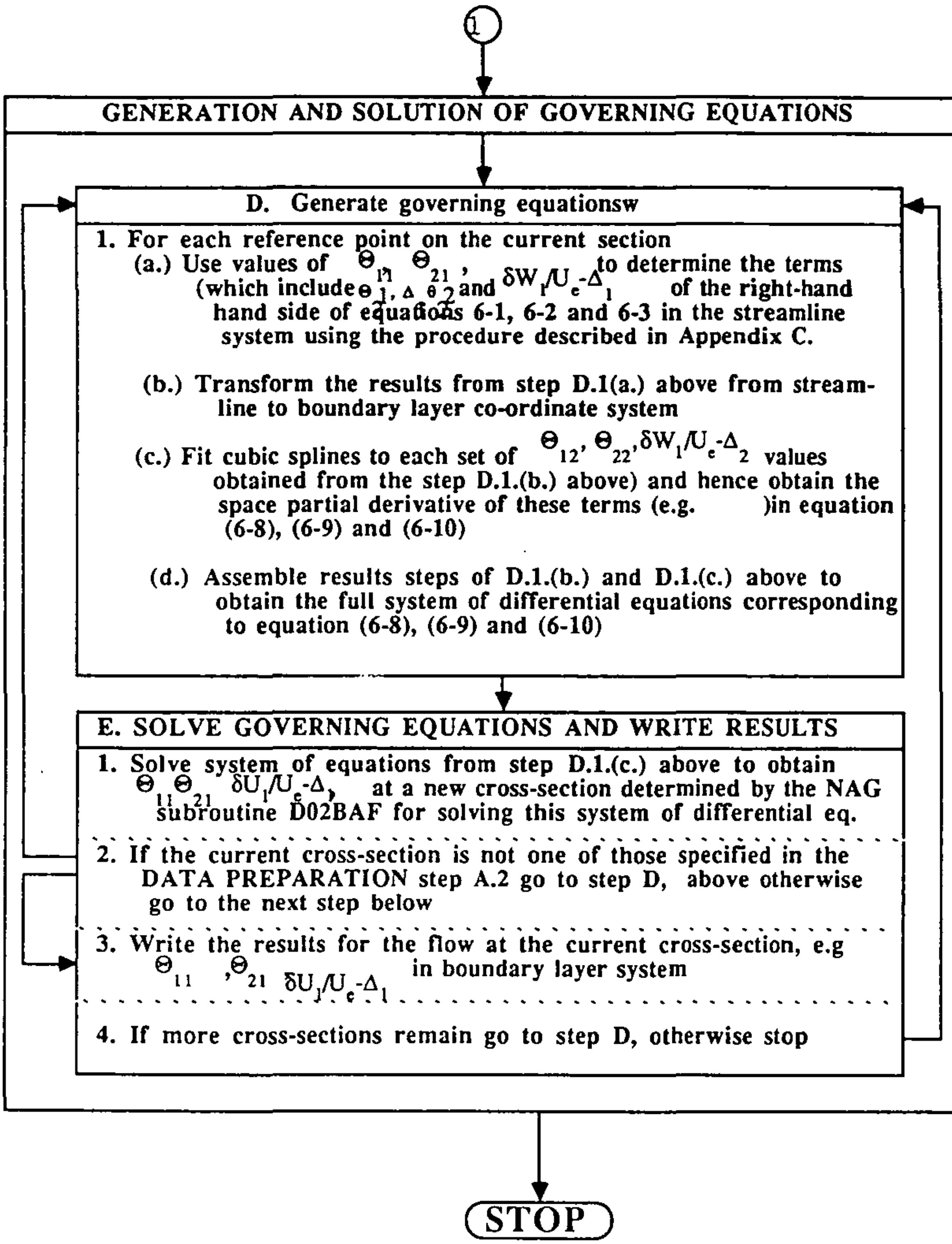

Figure 6-17 Block diagram for the programme TURBNOS

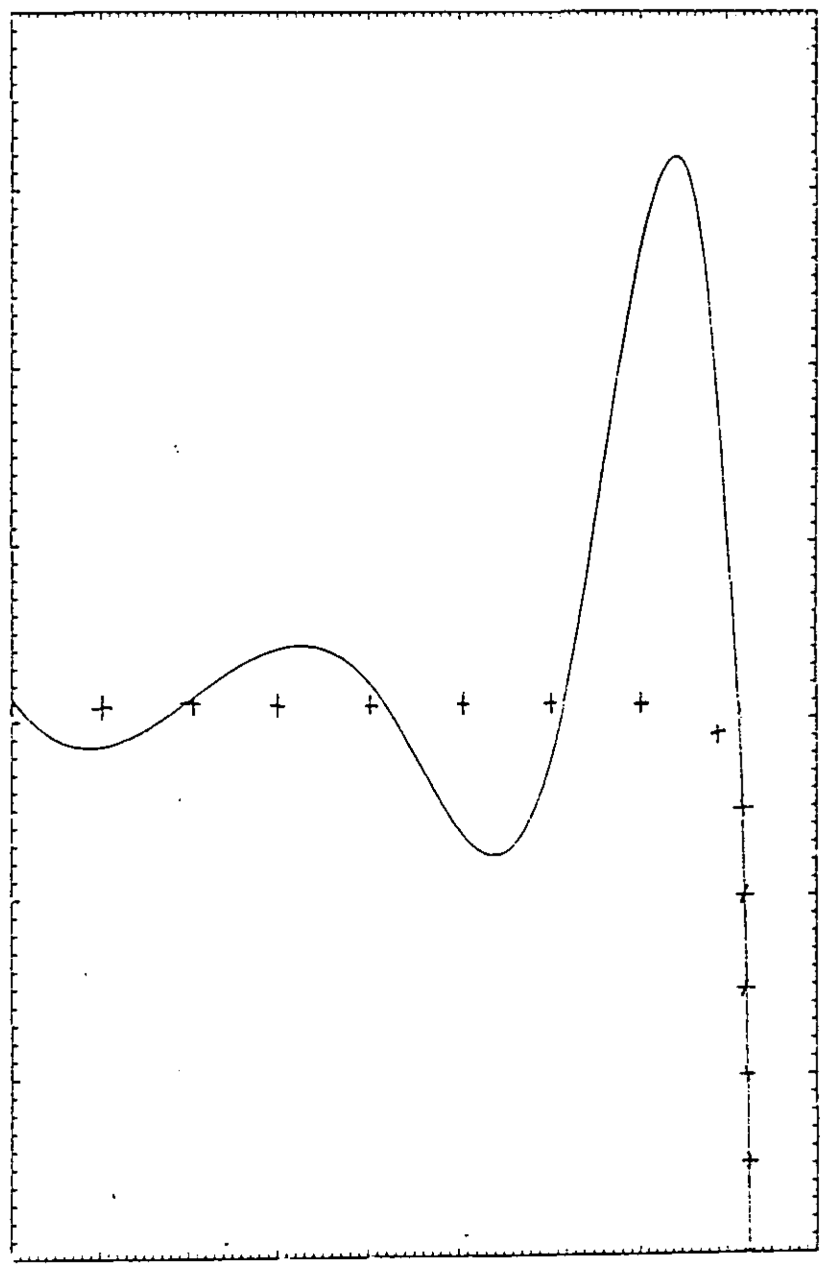

Figure 6-18 Cubic spline fits in an EMS train cross-section with a sharp corner

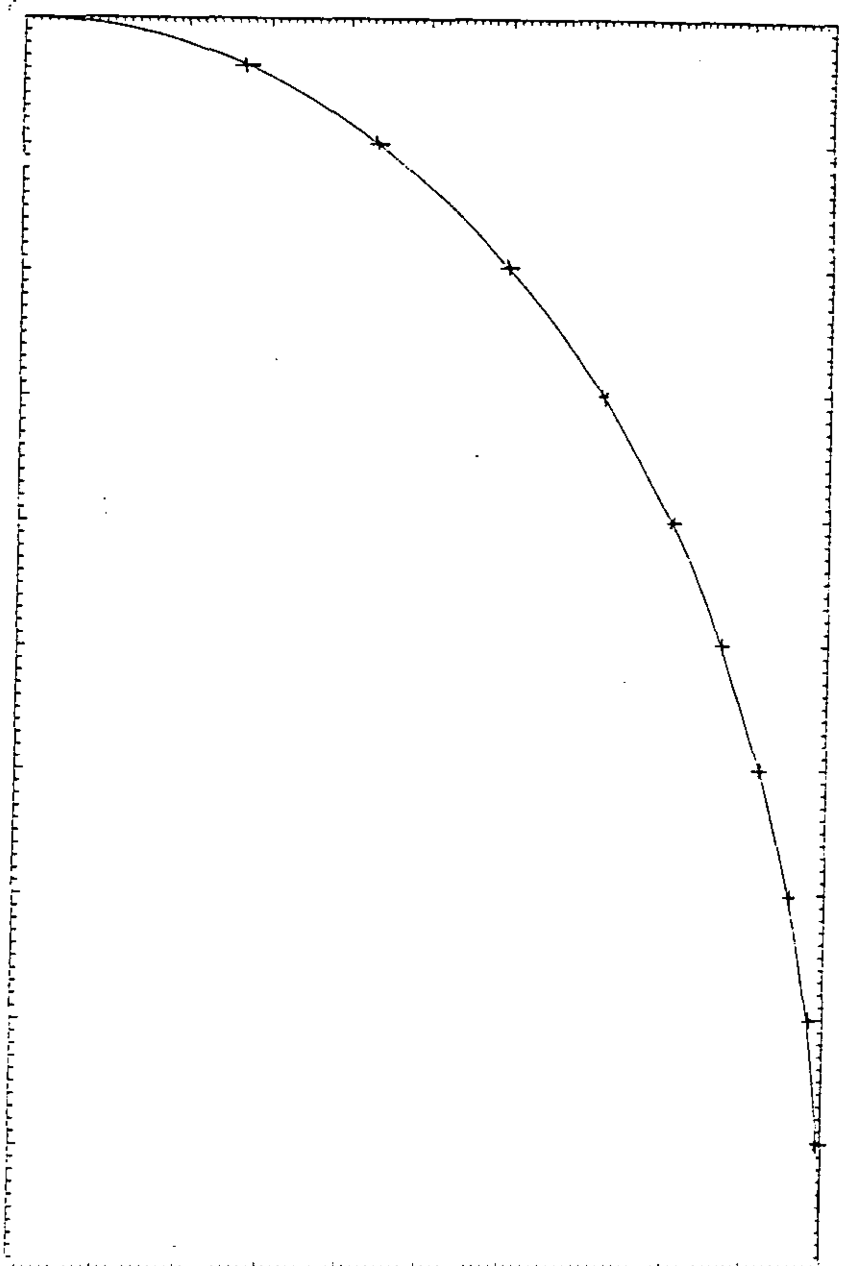

Figure 6-19 Cubic spline fits in an EMS train cross-section with a smooth corner

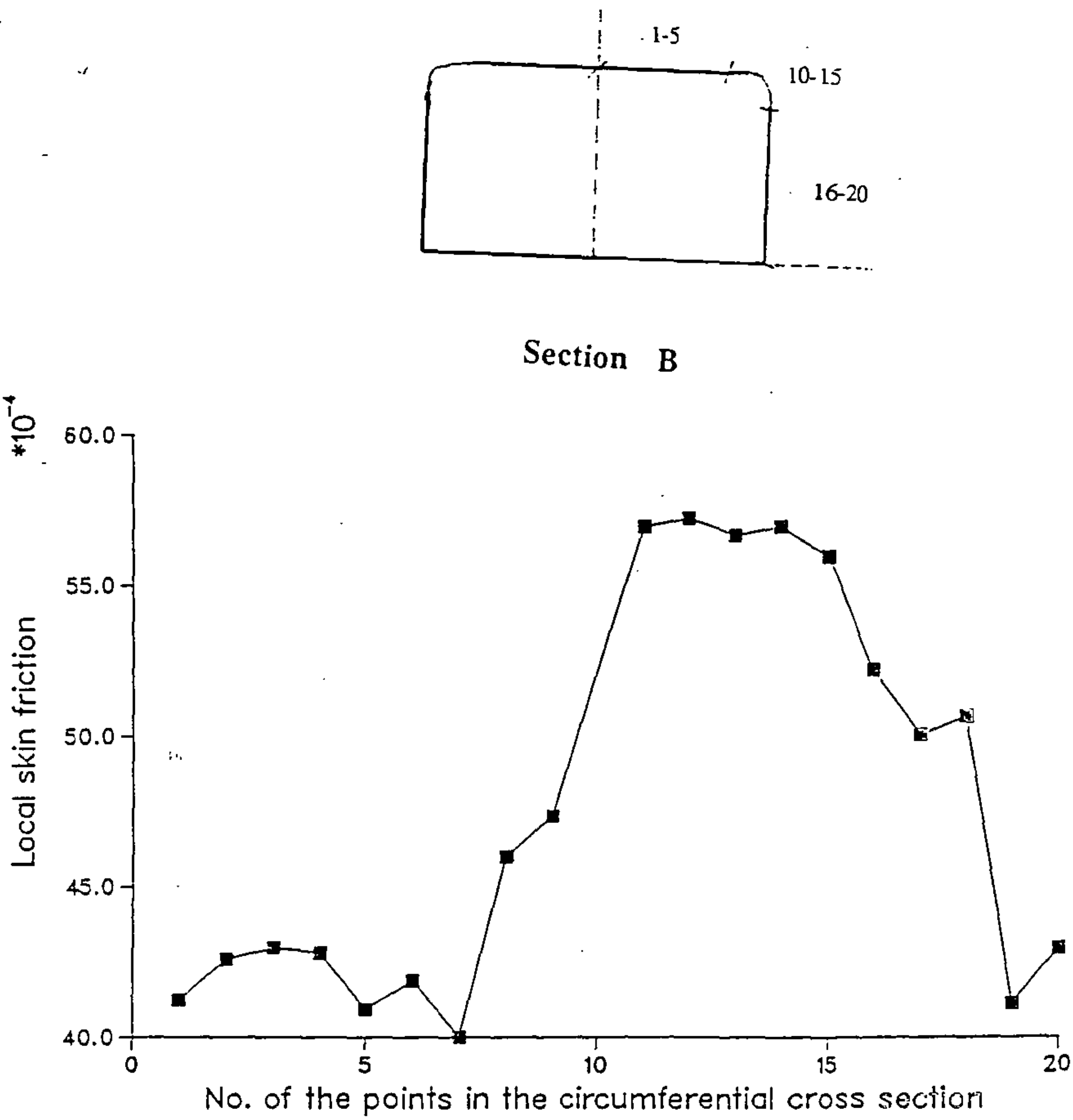

Figure 6-20 Local skin friction coefficient variation along circumferential cross-section

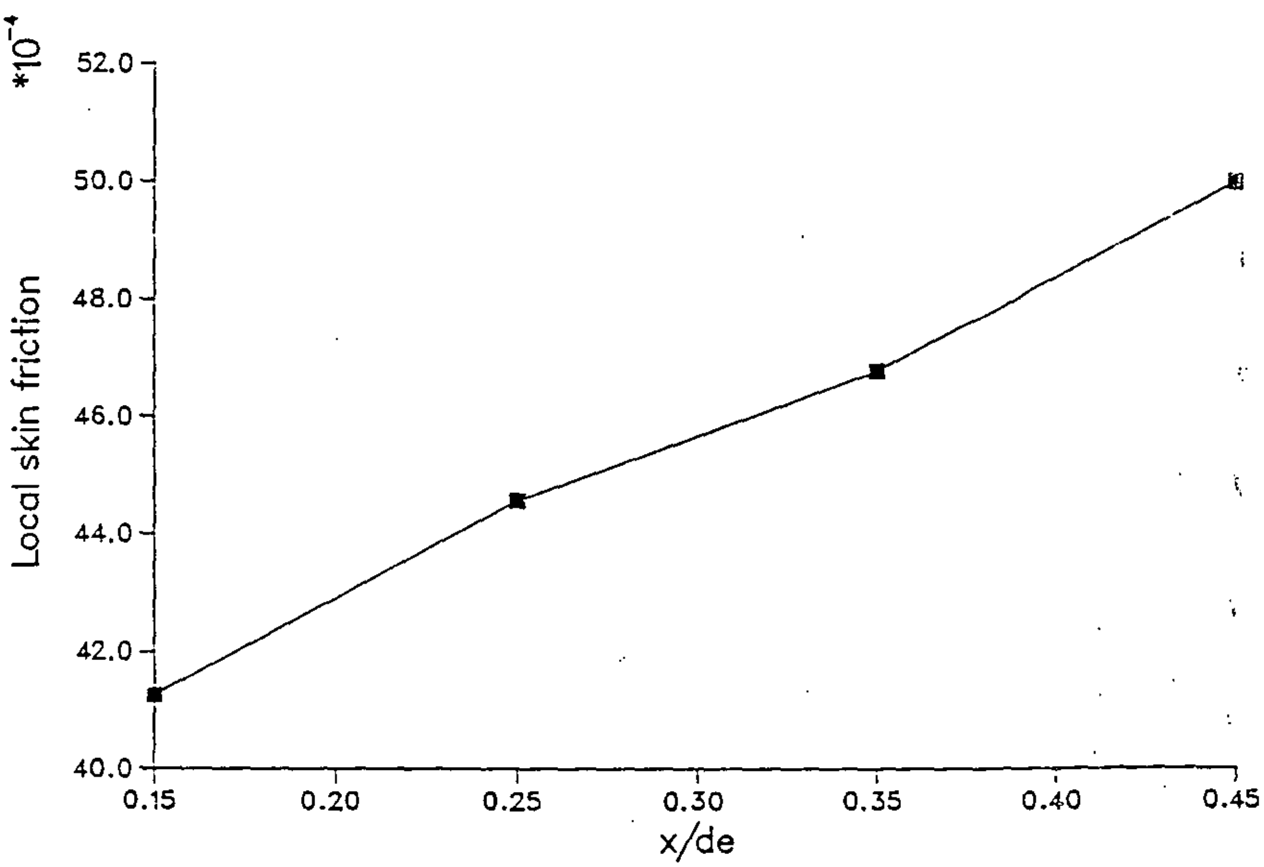

Figure 6-21 Local skin friction coefficient variation along centre-line of the EMS train model

CHAPTER 7

CONCLUSIONS AND SUGGESTIONS FOR FURTHER WORK

7.1 Introduction

This chapter presents the outcome of the research programme described in this thesis on a theoretical and experimental study of the flow around high-speed EMS train models. The aim of the theoretical part of the work was to develop computer programmes with capabilities for aerodynamic analysis in routine engineering design for evaluation of high-speed train aerodynamics. The goals of the experimental research programme were three-fold. The first was to provide validation data to aid the development of the computer programmes developed during the theoretical work. The second goal was to conduct a wind-tunnel investigation of the influence of the type of ground simulation and its proximity on the air flow around an EMS train model. The third goal was to collect a body of data for some aerodynamic forces and moments relevant to the high-speed train shape of interest here, data not so far available in the open literature.

The remainder of this chapter consists of two sections. Section is 7.2 presents the main conclusions, while section 7.3 provides suggestions for further work.

7.2 Conclusions

7.2.1 Nose of the EMS Train

The main conclusions for this region were as follows :

1. The results of the three-dimensional potential flow prediction indicated that the distribution of the static pressure coefficient possessed suction values of high magnitude on the top of the nose/roof junction and the corner-side edge (shoulder) of the nose. At the nose of the EMS train model, the experimentally measured pressure coefficient showed similar trend, but also some disparity with those obtained from the potential flow prediction, in particular in the high suction region mentioned above. These differences were largely due to neglect of viscous effects in the theoretical method.

2. The flow visualisation tests on EMS train models at zero yaw angle using three different techniques (i.e. tuft and spinner, oil suspension, and smoke) all consistently showed that the front roof and the side-corner edge (shoulder) of the nose were regions of separation in the flow. These results were consistent with the predicted and measured pressure distributions which both showed adverse pressure gradient regions of high magnitude in the high suction zones. At finite yaw angles, the predicted and measured pressure coefficients showed suction values of high magnitude also on the lee side of the train. The flow visualisation tests implied that the flow was attached on the windward side of the train but separated in the lee side.

3. The initial predicted results for the three-dimensional turbulent boundary layer growing on the train nose were encouraging. The results showed an increase in the local skin friction drag along the circumferential periphery of transverse sections of the nose. These results gave useful indications of the magnitude of skin friction on the complex nose shape, not previously available, but were certainly difficult to obtain with the integral method used since starting from the complex front and side edge region of the nose

7.2.2 Main Body of the EMS Train

The main conclusions drawn for this region are were follows :

1. The three-dimensional potential flow predictions showed that the values of the calculated pressure coefficients, along the upper roof symmetry line train decreased slightly with longitudinal distance away from the nose of the train. There was no significant change in the form and magnitude of the axial and circumferential pressure gradients for the main body of the train far away from the nose. These results suggest that the flow is attached far away from the nose. Results from wind tunnel tests to measure the pressure coefficient for this

portion of the EMS train model were found to be in good agreement with the corresponding values predicted using potential flow theory. This agreement with potential flow theory also supports the expectation of attached flow .

2. The flow visualisation tests agreed qualitatively with the above providing direct evidence that at points on the train far away from the nose the flow is attached

   For the EMS train model at yaw, the flow visualisation tests showed that the flow was attached on the windward side and separated on the lee side of the main body of the train. These results were qualitatively consistent with the predicted and measured pressure coefficient for the main body of the train.

7.2.3 Ground Effect on an EMS Train Model

Ground Clearance Effect.

1. The measured aerodynamic forces for a simulation using a stationary ground plane showed that the lift and drag coefficients increased as the amount of ground clearance was reduced until about Z/d_e=0.15, where they began decreasing slightly. For a moving belt ground simulation, changes in the magnitude of clearance had less effect.

2. The influence of the size of ground clearance on the side force coefficient was not significant when the train model was set at small yaw angle. At high yaw angle changing ground clearance had a much larger effect on these forces. The measured yawing moment coefficient increased with the amount of ground clearance at all angles of yaw.

3. Pressure coefficient distribution measurements made in the wind tunnel showed that the amount of ground clearance did not have a significant effect on the measured pressure coefficients for parts of the upper train surface far away from the nose. However, the amount of ground clearance has a significant effect on pressure coefficients measured on the front roof and corner-side edge of the nose i.e, where separation of flow had been observed. This was limited to the observation that changes in ground clearance induced small changes in the angle of the onset flow over the nose, which could reflect most strongly in the size of the separated flow regions.

Effect of Ground Simulation type

1. The ground simulation using a stationary belt always provided a negative lift which was algebraically greater than the case when a moving belt was employed to simulate the ground. The measurements also showed that the type of ground simulation did not have a significant effect on the measured yawing moment.

2. The moving belt simulation provided a value of aerodynamic drag higher than that observed with the stationary belt. For both types of belts, the drag increased as the yaw angle increased.

3. Wind tunnel flow visualisation on the EMS train model showed that the wake vortices were stronger and larger in size in the presence of a ground simulation. This observation contributed to the explanation for the measured increase of the side force coefficients in the presence of the ground simulations.

7.2.4 Vortex Correlation Factor

Using the results of the flow visualisation tests the form of the vortex wake on the lee side of the train was investigated in an attempt to relate a vortex correlation factor (the projected angle, in a horizontal plane, between the centre lines of the observed lee side wake vortices) to the yaw angle of the train — the conclusions of this investigation were :

1. The flow visualisation tests showed that there were two wake vortices generated on the lee side of the train which moved away along the length of the train. One of these vortices originated from the flow beneath the floor of the train and the second was generated from the train roof. As the train's yaw angle increased the lee side wake vortices increased in size. This lead to the expectation of an increase in drag due to the reduced pressure on the rear of the train associated with the pressure change produced by the vortex. This hypothesis was confirmed by the wind tunnel measurements of the drag.

2. The smoke flow visualisation tests on the EMS train model showed that the vortex correlation factor and the train yaw angle were related linearly : the value of the correlation factor was always half that of the yaw. This observation has not previously been reported in the literature on train aerodynamics.

7.2.5 Aerodynamic Forces and Moments on an EMS Train

1. The wind tunnel measurements of the drag showed that as the train yaw angle increased the drag coefficient increased sharply. These results were consistent with : (1) the results of the flow visualisation tests which show that the wake vortex size increased as the yaw angle increased; (2) the trends in the pressure coefficients. These latter results showed that the pressure coefficient possessed

negative values of high magnitude at the lee side of the train ; the magnitude of these negative values increased as the train yaw angle increased.

2. The tests showed that the use of a moving belt to simulate the ground resulted in higher observed values for the measured aerodynamic forces and moments than was the case when the stationary belt is employed. An important conclusion for general wind tunnel tests on future train designs.

3. The measured lift coefficient, which was negative, increased in magnitude as the train yaw angle increased.

4. The measured yawing moment, which had negative values, also increased in magnitude as the train yaw angle was increased.

5. The measured value for side force coefficient increased rapidly with train yaw angle, as expected.

6. The size of the lee side wake vortex region increased as the train yaw angle was increased, but on the windward side the flow was essentially always attached. This combination of attached flow on the windward side of the train with the (increasing) size of the lee side wake vortex region, was explanation for the sharp increase in the wind tunnel measured side force with an increase in the train yaw angle.

7.2.6 Turbulent Boundary Layer Prediction

Turbulent Boundary Layer Prediction on the nose

1. The developed computer programme gave plausible results for the three-dimensional turbulent boundary layer on the nose of the train. As mentioned above, the results suggested that (for a train at zero yaw angle and a cruising speed of 30 m/s) the local skin friction coefficient increased around the periphery of transverse sections of the nose of the train.

Turbulent Boundary Layer on the Central Part of the Train.

A simplified form of the general three-dimensional turbulent boundary layer analysis was developed for the central part of the train, the principal conclusions resulting from use of this simplified model was :-

1. For a train moving at yaw at a cruising speed of 30 m/s the computed streamwise shape factor, streamwise momentum thickness, integral boundary layer thickness and the angle between limiting and external streamlines (i.e. θ_{11}, H and β respectively) increased slowly with increased distance along the longitudinal length of the train starting from the beginning of the top side of the roof on the windward side. However these same parameters increased sharply near the sharp corner on the lee side of the train. This observation suggested the possibility of a separation of the transverse flow on the sharp corner consistent with the experimentally measured pressure distributions and with the flow visualisation tests, all of which suggested attached flow on the windward side and a region of flow separation on the lee side.

7.2.7 Unsteady Pressure Pulses Due to the Passage of an EMS Train

1. Substantial progress was also achieved by extending the potential flow method to allow the consideration of unsteady flow and the prediction of pressure pulse distributions for some practical railway engineering applications. The main examples considered were an EMS train passing a railway station and an EMS train passing the central part of another EMS train. In both cases the ability to predict the unsteady interaction caused by train passage was demonstrated.

7.3 Recommendations for Further Work

The main recommendations for further work are placed into the three categories: potential flow, experimental work, and turbulent boundary layer predictions.

7.3.1 Potential Flow

1. The panel method used in this work employed a source distribution only, therefore improvement to the programme POTOFLO can be achieved by adding a vortex distribution to allow the prediction of a nett lift force at right angles to the onset flow.

2. The Unsteady aspect of the computer programme POTOFLO should be utilised by applying it to the analysis of further important railway engineering problems, for example the calculation of the pressure pulses due to the passage two different types of trains on adjacent tracks.

7.3.2 Experimental Work

1. The present aerodynamic forces and moment were restricted to small yaw angles. It would be useful to carry out an experimental investigation of higher yaw angles.

2. The smoke flow visualisation tests indicated that the vortex correlation factor had a linear relationship with the yaw angle of the train and was always half the corresponding yaw angle. A further series of flow visualisation tests needs to be performed for other train shapes to examine whether this fact can be generalised. It would also be informative to study the effect of the nose shape on the formation of the two vortices and whether this affects this simple relationship.

3. The side corner edge of the nose is known to significantly affect the vehicle flow field, therefore even small modifications in this region might produce results which improve the aerodynamic performance and this should be investigated further.

4. A satisfactory measurement programme for the turbulent boundary layer and flow separation at the nose of the train has not been completed and this therefore requires further experimental work.

5. A series of experimental tests should be carried out on the circumferential periphery of a transverse section on the nose of the EMS train model. These should measure the characteristics of the turbulent boundary layer for use as data to completely specify the initial boundary conditions for application in more reliable predictions of the development of the turbulent boundary layer.

7.3.3 Turbulent Boundary Layer

The developed computer programme TURBNOS should be used for simpler shape such as the APT train which has a smoother nose shape, and in particular no sharp edges.

REFERENCES

1. Marshall, D., and John, D.,

The Shape of the aviation business in the 21st century

International Journal of Vehicle Design, Vol. 7, Nos. 3/4, pp. 213-230, 1986.

2. Rahn, T., and Spohrer, W.,

Development of new high-speed motor train units to be operated on the German Federal railway network

Railway Engineer, Institution of Mechanical Engineers, Vol. 202, No. D2, pp. 9-23, 1988.

3. Heinrich, K.,

Development and first in-service use of automatic people movers in the federal republic of Germany, with special reference to the magnetic levitation system M-Bahn

Automated People Movers, Engineering and Management in Major Activity Centres, Proceedings of a conference, Edited by Neumann, E.S., and Bondada, M.V.A., Published by the American Society of Civil Engineers, pp. 288-302, 1985.

4. Rhodes, R.G.,

Magnetic levitation and its future prospects in transport

Institution of Mechanical Engineers, C391/1984, pp. 1-8, 1984.

5. Hara, T., Kawaguti, M., Fukuchi, G., and Yamamoto, A.,

Aerodynamics of high-speed trains

Monthly Bulletin of the International Railway Congress Association, Vol. XLV, No. 2, pp. 121-145, 1968.

6. Howarth, P. J.,

APT resistance and performance estimation

Internal Memorandum, IMPS 11, ISSUE A, British Railways Research Department, Advanced Projects Division, 1970.

7. Gawthorpe, R. G.,

Aerodynamics of trains in the open air

Aerodynamics in Railway Engineering, Institution of Mechanical Engineers, Railway Engineer International, Vol. 3, No. 3, pp. 7-12, May/June 1978.

8. Peters, J.L.,

Aerodynamics of very high speed trains and maglev vehicles : State of the art and future potential

International Journal of Vehicle Design, Technological Advances in Vehicle Design Series, SP3, Impact of the Aerodynamics on Vehicle Design, pp. 308-341, 1983.

9. **Aerodynamic Drag Mechanisms of Bluff Bodies and Road Vehicles, Published Symposia, Sovran, G., Morel, T., and Mason, W., Editors, Plenum Press, 1978.**

10. **Impact of Aerodynamics on Vehicle Design, Proceedings of the International Association for Vehicle Design, Technological Advances in Vehicle Design, Editor-in-Chief, Dorgham, M.A., SP3, 1983.**

11. **Railway Aerodynamics Symposium, University of Nottingham, Nottingham, 1984.**

12. Automotive Aerodynamics : an Update, SP-706, International Congress and Exposition, Society of Automotive Engineers, Michigan, 1987.

13. Research in Automotive Aerodynamics, Society of Automotive Engineers, SP747, 1988.

14. Proceedings of the Fifth International Conference on Wind Engineering, Fort Collins, Colorado, USA, July, 1979.

15. Proceedings of the Joint ASME-CSME Applied Mechanics, Fluid Engineering and Bioengineering Conference on Aerodynamics of Transportation, Nagara Falls, New York, June 18-20, 1979.

16. Gawthorpe, R.G.,

Train drag reduction from simple design changes

International Journal of Vehicle Design, Vol. 3, No. 3, pp. 263-274, 1982.

17. Marshall, D.C.F.,

The resistance of express trains

The Railway Engineer, Vol. 147, Part 1, pp. 155-277, 1901.

18. Nock, O.S.,

The railway engineers

B.T. Batsford Ltd., London, 1955.

19. Ellis, H.,

British railway history

George Allen and Unwin Ltd, London, 1954.

20. Stewart, A.J.,

Flow around slender bodies at yaw

Ph.D. Thesis, Department of Engineering, University of Cambridge, 1977.

21. Mair, W.A., and Stewart, A.J.,

The flow past yawed slender bodies with and without ground effects

Journal of Wind Engineering and Industrial Aerodynamics, Vol. 22, pp. 301-327, 1985.

22. Copley, J.M.,

The Three-dimensional flow around railway trains

Ph.D. Thesis, Department of Engineering, University of Cambridge, 1985.

23. Baker, C.J.,

Wind effects in the railway environment

Railway Aerodynamics Symposium, University of Nottingham, Nottingham, 1984.

24. Baker, C.J.,

The determination of topographical exposure factors for railway embankments.

Journal of Wind Engineering and Industrial Aerodynamics, Vol. 21, pp. 89-99, 1985.

25. Gawthorpe, R. G.,

Aerodynamic of trains in tunnels

Aerodynamics in Railway Engineering, Institution of Mechanical Engineers, Railway Engineer International, Vol. 3, No. 3, pp. 7-12, May/June 1978.

26. Gawthorpe, R.G.,

Aerodynamic problems with overhead line equipment

Aerodynamics in Railway Engineering, Part II, Railway Engineer International, Institution of Mechanical Engineers., Vol. 3, No. 4, pp. 38-40, July/August 1978.

27. Hess, J.L., and Smith, A.M.O.,

Calculation of non-lifting potential flow about arbitrary three-dimensional bodies.

Douglas Aircraft Company, Aircraft Division, Report No. E.S. 40622, March 1962.

28. Tinoco, E.N., Ball, D.N., and Rice, F.A.,

PAN AIR analysis of a transport high-lift configuration

Journal of Aircraft, Vol. 24, No. 3, pp. 181-187 , March 1987.

29. *Computational methods in potential aerodynamics*

Morino, L., Editor, Springer-Verlag, Berlin, A Computational Mechanics Publication, Oxford University Press, Oxford, 1985

30. Hess, J.L.,

Review of the historical development of surface source methods

Computational Methods in Potential Aerodynamics, Morino, L., Editor, Springer-Verlag, Berlin, A Computational Mechanics

Publication, University Press, Oxford, pp. 21-37, 1985.

31. Hess, J.L.,

Review of the source panel technique for flow computation

Proceedings of Innovative Numerical Methods in Engineering, 4th International Symposium, Georgia Institute of Technology, Atlanta , A Computation.Mechanics Publication, Spring-Verlag, pp. 192-210, 1986.

32. Ahmed, S.R., and Hucho, W.H.,

The calculation of the flow field past a van with the aid of a panel method

Society of Automotive Engineers, No. 770390, pp. 1672-1692, 1977.

33. Mahomedali, F.,

Two-dimensional potential flow calculations applied to train cross-section

Internal Memorandum, IM AERO 67, British Railways Board, Research and Development Division, Aerodynamics Section, 1973.

34. Johnston, G.W., Seshagiri, B.V., and Ellis, N.D.,

Aerodynamic interference of high speed ground vehicles

UTIAS Report, No. 185, CN 0082-5253, 1976.

35. Copley, J.M.,

The Three-dimensional flow around railway trains

Railway Aerodynamics Symposium, University of Nottingham, Nottingham, 1984.

36. Copley, J.M.,

The Three-dimensional flow around railway trains

Journal of Wind Engineering and Industrial Aerodynamics, Vol. 96, pp. 21-52, 1987.

37. Morrow, T.B.,

Prediction of the pressure distribution on vehicles moving near the ground

Department of Transport Technology, Loughborough University of Technology, Report No. TT72R05, 1972.

38. Maccabee, F.G., Morrow, T.B., and Parmar, B.M.,

Wind-tunnel measurements of aerodynamic characteristics of model trains of APT-type including pressure distributions

Department of Transport Technology, Loughborough University of Technology, TT74R04, 1974.

39. Lock, R.C. and Firmin, M.C.P.,

Survey of techniques for estimating viscous effects in external aerodynamics

Royal Aircraft Establishment, Technical Memorandum, Aero 1900, April 1981.

40. Smith, P.D.,

A calculation method for the turbulent boundary layer on an infinite yawed wing in compressible, adiabatic flow

Royal Aircraft Establishment, Current Paper No. 1268, September 1972.

41. Ashill, P.R., and Smith, P.D.,

An integral method for calculating the effects on turbulent boundary-layer development of sweep and taper

Aeronautical Journal, Paper No. 1241, pp. 43-53, February 1985.

42. Smith, P.D.,

An integral prediction method for three-dimensional compressible turbulent boundary layers

RAE, TR 72228, 1973.

43. Cumpsty, N.A., and Head, M.R.,

The calculation of three-dimensional turbulent boundary layers part 1 : Flow over the rear of an infinite swept wing

The Aeronautical Quarterly, Vol. 1, pp. 55-84, 1967.

44. Everitt, K.W.,

The calculation of three-dimensional turbulent boundary layers on infinite yawed bodies

Internal Memorandum, IM AERO 66, ISSUE A, Dynamics Group, Research and Development Division, British Railways Board, April 1973.

45. Hirschel, E.H.,

Three-dimensional boundary layer calculations in design aerodynamics

Proc. IUTAM-Symposium on Three-dimensional Turbulent Boundary Layers (H. Fernhdz and E. Krause, eds.), Springer Verlag, Berlin, Heidelberg-New York, pp. 353-365,1982.

46. Hirschel, E.H.,

Computation of three-dimensional boundary layers at fuselages

AIAA, 83-0455, 1983.

47. Hirschel, E.H., Bretthauer, N., and Rohe, H.,

Theoretical and experimental boundary-layer studies of car bodies

International Journal of Vehicle Design, Vol. 5, NO. 5, pp. 567-584, 1984.

48. Howell, J.P.,

Aerodynamic response of maglev train models to a crosswind gust

Journal of Wind Engineering and Industrial Aerodynamics, Vol. 22, pp. 205-213, 1986.

49. Howell, J.P., and Everitt, K.W.,

The response of high-speed ground vehicles to crosswind gusts

Department of Engineering, University of Warwick, SERC Grant No. GR/A 9659/5, 1983.

50. Howell, J.P.,

The influence of ground simulation on the aerodynamics of high-speed trains

Report GR/A 1828, Department of Engineering, University of Warwick, June 1980.

51. Howell, J.P.,

Maglev aerodynamics

Railway Aerodynamics Symposium, University of Nottingham, April 1984.

52. Cooper, R.K.,

Wind-tunnel tests on a 1/25 scale APT-P model

Technical Memorandum, Report TM AERO 43, Research and Development Division, British Rail, March 1982.

53. Cooper, R. K.,

The effect of cross-winds on trains

Journal of Fluid Engineering, Transportations of the ASME, Vol. 103, pp. 170-178, March 1978.

54. Everitt, K.W.,

Preliminary notes on flow visualisation tests

Internal Memorandum, IM AERO 23 (ISSUE A), British Railway, Research Department, Advanced Projects Division, August 1971.

55. Maccabee, F.G., and Parmar, B.M.,

Results of wind tunnel tests on model trains of APT-type : Surface flow visualisation

Department of Transport Technology, Loughborough University of Technology, TT74R05, 1974.

56. Baker, C.J., and Watson, A.S.,

Flow visualisation experiments on a Derby lightweight DMU

Technical Memorandum, Report No. TM AERO 67, British Railway, Research and Development Division, April 1982.

57. Butler, S.F.J., and May, B.A., and Pound,T.N.,

A moving belt rig for simulation at low speed wind tunnels

Aeronautical Research Council, Reports and Memoranda, No. 3451, 1963.

58. Bagley, J.A.,

The pressure distribution on two dimensional wings near the ground

Aeronautical Research Council, Reports and Memoranda, No. 3238, 1961.

59. Bearman, P.W.,

Some effects of free-stream turbulence and the presence of the ground on the flow around bluff bodies

Aerodynamic Drag Mechanisms of Bluff Bodies and Road Vehicles, Published Symposia, Sovran, G., Morel, T., and Mason, W., Editors, Plenum Press, pp. 95-114, 1978.

60. Diuzet, M.,

The moving-belt of the I.A.T. long test section wind tunnel

Journal of Wind Engineering and Industrial Aerodynamic, Vol. 22, pp. 237-244, 1986.

61. Gawthorpe, R. G.,

Specification of a generalised vehicle shape for aerodynamic research

Appendix 3, pp. 36-41, The Aerodynamic Problems of Advanced Ground Transport, Report by the Aerodynamics Group of AGT Panel, SERC, Stollery, J.L. (Ed.), College of Aeronautics, Cranfield, 1978.

62. Mason, W.H., Balhaus, W.F., Mackenzie, C., Frick, J., and Sterin, M.,

An automated procedure for three-dimensional transonic flow over a wing-body combinations including viscous effects

Report AFFDL-TR-77-122, Vol. 1, Feburary 1977, Available from NTIC as AD-A055899.

63. Street, C.L.,

Viscous-invscid interaction for transonic wing-body configuration including wake effects

AIAA Paper 81-1266, Presented at AIAA 14th Fluid and Plasma Dynamics Conference, Palo Alto, CA, pp. 22-24, June 1981.

64. Hess, J.L., and Smith, A.M.O.,

Calculation of potential flow about arbitrary bodies,

Progress in Aeronautical Sciences,Vol. 7, pp. 1-138, 1967.

65. Ahmed, S.R., Gawthorp, R.G., and Mackdrodt, P.A.,

Aerodynamics of roads and rail vehicles

Vehicle System Dynamics, Volume 14, pp. 319-392, 1985

66. Anderson, J.D., Jr.,

Fundamentals of aerodynamics

McGraw-Hill Book Company, pp. 166-175, 1984.

67. Bauer, A.B., Smith, A.M.O, and Hess, J.L,

Potential flow and boundary layer theory as design tools in aerodynamics

Canadian Aeronautics and Space Journal, Volume 16, pp. 53-69, February 1970.

68. Hess, J.L., and Smith, A.M.O.,

Calculation of non-lifting potential flow about arbitrary three-dimensional bodies,

Journal of Ship research, Vol. 8, pp. 22-44, September 1964.

69. Petrie, J.A.H.,

Development of an efficient and versatile panel method for aerodynamic problems

Ph.D. Thesis, University of Leeds, March 1979.

70. Lamb, H.,

Hydrodynamics

Cambridge University Press, Sixth Edition, 1932.

71. Rubbert, P.E., and Sarris, G.R.,

A General Three-dimensional Potential Flow Method Applied to V/STOL Aerodynamics

Paper No. 680304, S.A.E., Transactions, 1968, pp. 945-957.

72. Maskew, B.

Calculation of Three-dimensional Potential Flow around Lifting Non-Planar Wings and Wing-Bodies Using a Surface Distribution of Quadrilateral Vortex-Rings,

Department of Transport Technology, Loughborough University of Technology, TT7009; 1970.

73 Giesing, J.P.,

Non-linear interaction of two lifting bodies in arbitrary unsteady motion

Trans. ASME, Journal of Basic Engineering, September 1968, pp. 387-394.

74. Christopher, P.A.T., Deo, H.S., and Shaw, C.T.,

A Ring Source Method for Predicting the Aerodynamic Characteristics of Bodies of Revolution

College of Aeronautics, Cranfield Institute of Technology, Report 8409, March 1984.

75. Kellogg, O.D.,

Foundations of potential theory

Frederick Ungar Publishing Company, New York, pp. 222, 1929.

76. Henshell, R. D., (ed.)

Data Preparation, User Manual, Level 6.1

PAFEC Ltd., Nottingham, United Kingdom, 1984.

77. Vallentine, H.R.,

Applied Hydrodynamics , second edition,

Butterworth and Co. Ltd. , London 1967.

78. Kawaguti, M.,

The flow of a perfect fluid around two moving bodies

Journal of the Physics Society of Japan, Volume 19, Number 8, pp. 1409-1415, May 1964.

79. Gould, R.F.W.,

Passenger train coach in direct side winds.

Nat. Maritime Inst. Rep. Proj., No. 89/0294, 1976.

80. **Journal of Wind Engineering and Industrial Aerodynamic, Volume, 22, 1986.**

81. Gross, D.S., Sekscienski, W.S.,

Some problems concerning wind tunnel testing of automotive vehicle

SAE Transaction, 660385, pp. 593-607, 1966.

82. Stevens, C.J.,

Ground effects on advanced ground vehicles

Department of Transport Technology, Loughborough University of Technology, Internal Report, 1982.

83. Sykes, D.M.,

Blockage corrections for large bluff bodies in wind tunnels,

Advances in Road Vehicle Aerodynamics, B.H.R.A pp. 311-321, Cranfield,1973.

84. Garry, K.P.,

Wind tunnel techniques for reducing commercial vehicle aerodynamic drag

Ph.D. thesis, College of Aeronautics, Cranfield Institute of Technology, pp. 238-240, 1982.

85. Johnston, L.J.,

A solution method for the three-dimensional compressible turbulent boundary-layer equations

Aeronautical Journal, April 1989.

86. Humpherys, D.A., and Lindhout, J.P.F.,

Calculation methods for three-dimensional turbulent boundary layer

Progress in Aerospace Sciences, Vol. 25, pp. 107-129, 1988.

87. Schlichting, H.,

Boundary layer theory

McGraw-Hill Book Company, Sixth Edition, LOndon, 1968.

88. Myring, D.F. ,

An integral prediction for three dimensional turbulent boundary layers in incompressible flow

Royal Aircraft Est. , Technical Report No. 70147, pp18, Aug. 1970.

89. Cousteix, J.,

Theoretical analysis and prediction method for a three-dimensional turbulent boundary layer

Ph.D. Thesis, University of Paris, France. ONERA Publication No. 157, 1974.

90. Hirschel, E.H., and Kordulla, W.,

Shear flow in surface-oriented coordinate

Vieweg Verlag, Braunschweig ,Vol 4 of Notes on Numerical Fluid Mechanics, 1981.

91. Smith, P.D.,

Calculation methods for three-dimensional turbulent boundary layers

Aeronautical Research Council Report and Memoranda No. 3523, 1968.

92. Johnston, J.P.,

On three-dimensional boundary layers generated by secondary flow

Journal of Basic Engineering, Transactions of the American Society of Mechanical Engineers, Series D in Vol. 82, 1960.

93. Numerical Algorithms Group, Oxford, UK.

NAG FORTRAN library

Mark 11 , Jan. 1985.

94. Computer Aided Design Centre, Cambridge U.K.

GINOGRAF

April 1976.

95. Houghton, E.L., and Boswell, R.P.,

Further aerodynamics for engineering students

E. Arnold, 1969.

96. Michel, R., Quemard C., and Durant, R.,

Hypotheses on the mixing length and application of the turbulent boundary layer

Computation of turbulent boundary layer, 1968. AFOSR- IFP. STANFORD conference , Vol. 1, Methods, Predictions, Evaluation and flow structure, G. Sovran, D.J. Cockrell.

APPENDICES

APPENDIX A
TWO-DIMENSIONAL POTENTIAL FLOW PREDICTION METHOD

A.1 Introduction

A description of a two-dimensional panel method for predicting potential flow is presented in this Appendix. This represents the background theory of the two-dimensional computing exercise made prior to the development of the three-dimensional panel method of Chapter 2. In the case of two-dimensional potential flow, the body surface is approximated by line elements rather than by flat panels. Thus, for (closed) two-dimensional bodies, which are conventionally represented by a single profile curve or contour such as shown in Figure A-1, its approximation by the panel method takes the form of an inscribed polygon as indicated. Thus, for two-dimensional bodies the approximating surface elements are simply plane strips of infinite extent in the dimension normal to the plane of the figure. The control point has been chosen to lie at the centre of the line element.

The detailed assumptions and associated limitations of the panel method employed here are presented in full in section 2.1, they are summarised briefly here for reference.

- i. Flow is assumed to be non-viscous and irrotational
- ii. only applicable to non-lifting potential flow, since only a distribution of source density assumed.
- iii. Predicted source densities on adjacent panels are uniform, but not necessarily the same.
- iv. Predictions of the flow velocity and pressure on the approximating body satisfy the boundary conditions only at panel control point.
- v Panel control points are not necessarily on the body contour

It is emphasised again that the use of a source method, leading to no lift predictions introduces some restriction on the application of the method. Assuming that the flow is non-viscous means that predictions in or in the neighbourhood of regions of thick boundary layers, flow separation or wakes (for high-speed trains these are typically at the train nose and trailing end) are invalid. The limitations denoted by (iii)— (v) inclusive are due to the division of the vehicle body into a finite number of panels. The disparities that are caused by this discretisation process can be reduced by increasing the number of panels.

The remainder of this Appendix comprises two sections. Section A.2 describes the numerical procedure for the two-dimensional panel method. Section A.3 then presents a few details of a computer programme, based on this approach. The application of this programme to test problems is presented in Chapter 2.

A.2 Two-dimensional Panel Method

The description provided here for the two-dimensional method provides the basic steps necessary to solve a two-dimensional potential flow problem.

A.2.1 Basic Theory

This section describes the basic equations required to compute the velocity and pressure distribution on the surface of a body immersed in an external field flow.

Lamb [81] and Kellogg [82] show that the potential function at an external field point may be represented by the surface integral of a distribution of sources. Thus the potential at any external field point p due to a source distribution around a body surface S can be written as [41], see Figure A-2.

$$\phi_p = \oiint_S \frac{\sigma(s)}{r_{(p,q)}} dS \qquad \text{A-1}$$

where

$\sigma(s)$ is the source strength at an arbitrary point q on the surface s,

$r_{(p,q)}$ is the distance between the field point p (x,y,z) in the cartesian and the source point q at (ξ,η,ζ) and is given by

$$r^2 = (x-\xi)^2 + (y-\eta)^2 + (z-\zeta)^2 \qquad \text{A--2}$$

It is noted that the above expression differs from that conventionally referred to as the velocity potential by a non-essential factor of $-1/4\pi$.

The velocities in the flow field may be expressed as the appropriate derivative of the resulting potential function. The pressure may then be calculated from Bernoulli's equation. Consider the expression for the potential function, and associated velocities, at a point in the external flow field involving a two-dimensional body with an arbitrary closed contour. Restrict attention to, an arbitrary shell surface area S extending axially from a cartesian z-axis value of $z=-L$ to $z=+L$ with s representing the co-ordinate measured along the contour of the shell. Assume that the source density $\sigma(s)$ does not vary in the z-axis direction since we are to deal ultimately with the two-dimensional case by letting $L \rightarrow \infty$.

We can assume that $z=0$ when evaluating equation (A-1) and this means that the potential ϕ_p can be written as

$$\phi_p = \oint \sigma(s) \int_{-L}^{+L} \frac{d\zeta}{r} \, ds \qquad \text{A-3}$$

or

$$\phi_p = \oint \sigma(s) \, \text{lin} \left[\frac{(\sqrt{a^2 + L^2} + L)^2}{a^2} \right] ds \qquad \text{A-4}$$

where

$$a^2 = (x - \xi)^2 + (y - \eta)^2$$

To avoid the infinite integral that will result in the above in the limiting case as the shell becomes an ideal two-dimensional entity i.e. as $(L \rightarrow \infty)$ we can make use of the fact that the net source strength on the shell is zero, so that

$$\oint \sigma(s) \log(4L)^2 \, ds = 0 \qquad \text{A-5}$$

so subtracting the left-hand side of equation (A-5) from equation (A-4) and re-arranging gives

$$\phi_p = \oint \sigma(s) \log[\frac{\sqrt{a^2 + L^2} + L}{2L}]^2 - \oint \sigma(s) \log(a^2)\, ds \qquad \text{A-6}$$

Now if we let $L \rightarrow \infty$ then

$$\phi_p = - \oint \sigma(s) \log[(x-\xi)^2 + (y-\eta)^2]\, ds \qquad \text{A-7}$$

and the partial derivatives of the potential at point p with respect to the x- and y-ordinate variables are

$$\frac{\partial \phi_p}{\partial x} = -2 \oint \sigma(s) \frac{(x-\xi)}{(x-\xi)^2 + (y-\eta)^2}\, ds \qquad \text{A-8}$$

$$\frac{\partial \phi_p}{\partial y} = -2 \oint \sigma(s) \frac{(y-\eta)}{(x-\xi)^2 + (y-\eta)^2}\, ds \qquad \text{A-9}$$

$\frac{\partial \phi_p}{\partial x}$ and $\frac{\partial \phi_p}{\partial y}$ represent the components of the velocity in the direction of the x- and y- axes respectively

Equations (A-7) — (A-9) inclusive provide a basis for determining, the potential function, and the x- and y-component of velocity at a point p in the external flow due to a source distribution along a contour of an arbitrary two-dimensional body. These expressions are required in the next stage of the panel method to calculate the flow characteristics for the panels which are used to approximate the true body contour as described next.

A.2.2 Co-ordinate Transformation

The basic principle of the two-dimensional panel method involves the approximation of the body by a number of straight-line elements which form an inscribed polygon to the actual body contour, see Figure A-1. Before proceeding to determine the contribution that each line element makes to the potential function at an external field point, it is convenient to obtain the relationship between the global cartesian co-ordinate system used to describe the body and overall flow field and a local cartesian co-ordinate system conveniently aligned with a given panel element. This local co-ordinate system simplifies the subsequent calculations of the contribution of the given panel element to the potential function.

Consider a field point p with global co-ordinate $(x_i,y_i,)$ where the subscript i refers to the i-th field point of interest (Figure A-3). Let s_{ij} and h_{ij} refer to the co-ordinates of the i-th field point in the local co-ordinate system of the j-th element on the contour of the body where s represents the tangential direction (along the element) in the local co-ordinate system and h the normal direction. It is desired to find an expression for the potential function and velocity at point i due to a source distribution in the j-th element in terms of s_{ij}, h_{ij}, and s.

Some Miscellaneous Results Involving Panel Element

From Figure A-3 it is seen that the co-ordinates of the field point $p(x_i,y_i)$ may be written as

$$x_i = x_{oj} + (s_{ij} \cos\alpha_j - h_{ij} \sin\alpha_j) \qquad \text{A-10}$$

$$y_i = y_{oj} + (s_{ij} \sin\alpha_j + h_{ij} \cos\alpha_j) \qquad \text{A-11}$$

where

α_j	is the angle between the x-axis and s-axis as in Figure A-3
x_{oj}, y_{oj}	represents the global cartesian co-ordinates of the origin of the local co-ordinate system for panel j.

For a field point placed on the surface of the element we have $h_{ij} = 0$ and $s_{ij} = s$, substituting these values into equations (A-10) and (A-11) gives the global co-ordinate (ξ,η) of the field point as

$$\xi = x_{oj} + s\cos\alpha_j \qquad \text{A-12}$$

$$\eta = y_{oj} + s\sin\alpha_j \qquad \text{A-13}$$

subtracting equation (A-12) from equation (A-10) and equation (A-13) from equation (A-11) we get respectively

$$x_i - \xi = (s_{ij} - s)\cos\alpha_j - h_{ij}\sin\alpha_j \qquad \text{A-14}$$

$$y_i - \eta = (s_{ij} - s)\sin\alpha_j + h_{ij}\cos\alpha_j \qquad \text{A-15}$$

By squaring equations (A-14) and (A-15) forming the sum of the results

$$(x_i - \xi)^2 + (y_i - \eta)^2 = (s_{ij} - s)^2 + h_{ij}^2 \qquad \text{A-16}$$

using equations (A-14), (A-15) and (A-16), equations (A-7), (A-8) and (A-9) can be written as

$$\phi_i = - \int_{l_j} \sigma(s) \log[(s_{ij} - s)^2 + h_{ij}^2]\, ds \qquad \text{A-17}$$

where

l_j is the length of the j-th element

Then,

$$V_x = \frac{\partial \phi_i}{\partial x} = -2\int_{l_j} \sigma(s) \frac{(s_{ij} - s)\cos\alpha_j - h_{ij}\sin\alpha_j}{(s_{ij} - s)^2 + h_{ij}^2} ds \qquad \text{A-18}$$

$$V_y = \frac{\partial \phi_i}{\partial y} = -2\int_{l_j} \sigma(s) \frac{(s_{ij} - s)\sin\alpha_j + h_{ij}\cos\alpha_j}{(s_{ij} - s)^2 + h_{ij}^2} ds \qquad \text{A-19}$$

Before proceeding further we need to find expressions for s_{ij} and h_{ij} in terms that are known, namely the global co-ordinates of the i-th field point,and the j-th element under analysis, these may be obtained by inverting equations (A-10) and (A-11) to give

$$s_{ij} = (x_i - x_{oj}) \cos\alpha_j + (y_j - y_{oj}) \sin\alpha_j \qquad \text{A-20}$$

$$h_{ij} = -(x_i - x_{oj}) \sin\alpha_j + (y_j - y_{oj}) \cos\alpha_j \qquad \text{A-21}$$

Substitution of the relationships of equations (A-20) and (A-21) into the contribution at the i-th field point to the potential function and to the x- and y- component of velocity given by equations (A-17), (A-18) and (A-19), allow these contributions to be calculated in terms of the co-ordinate values (x_i, x_{oj}, α_j...etc.) in the global co-ordinate system.

A.2.3 Derivation of the Governing Equations

The contribution to the velocity potential and the x- and y-component of the velocities at the field point i due to a source distribution over the j-th element are derived above. If the contour of the body is discretised into N elements (see Figure A-1 for example) then equation (A-17) for the potential function and equations (A-18) and (A-19) for the components of fluid velocity may be written in the form

$$\phi_i = -\sum_{j=1}^{N} \int_{s_j}^{s_{j+1}} \sigma_j(s) \log[(s_{ij} - s)^2 + h_{ij}^2] \, ds \qquad \text{A-22}$$

$$\frac{\partial \phi_i}{\partial x} = -2 \sum_{j=1}^{N} \int_{s_j}^{s_{j+1}} \sigma_j(s) \frac{(s_{ij} - s)\cos\alpha_j - h_{ij}\sin\alpha_j}{(s_{ij} - s)^2 + h_{ij}^2} \, ds \qquad \text{A-23}$$

$$\frac{\partial \phi_i}{\partial y} = -2 \sum_{j=1}^{N} \int_{s_j}^{s_{j+1}} \sigma_j(s) \frac{(s_{ij} - s)\sin\alpha_j + h_{ij}\cos\alpha_j}{(s_{ij} - s)^2 + h_{ij}^2} \, ds \qquad \text{A-24}$$

where s_j and s_{j+1} represent the lower and upper integration limits, respectively, for the local s ordinate of j-th element.

These equations represent the panel method's approximation for the potential function and fluid velocity for the true body of interest. The equations need to be combined with the body surface normal velocity boundary condition to establish the source densities; how this is done is explainedlater.

To integrate equations (A-22), (A-23) and (A-24) a suitable assumption for the source strength distribution over the elements needs to be made. In the present work the assumption of a constant source strength distribution over each element but possibly different from element to element was found to provide satisfactory computed results.

Source density assumed constant over each panel.

If we assume a constant source strength distribution over each element then equations (A-22), (A-23) and (A-24) can be written as

$$\phi_i = -\sum_{j=1}^{N} \sigma_j \int_{s_j}^{s_{j+1}} \log[(s_{ij} - s)^2 + h_{ij}^2]\, ds \qquad \text{A-25}$$

$$\frac{\partial \phi_i}{\partial x} = -2 \sum_{j=1}^{N} \sigma_j \int_{s_j}^{s_{j+1}} \frac{(s_{ij} - s)\cos\alpha_j - h_{ij}\sin\alpha_j}{(s_{ij} - s)^2 + h_{ij}^2}\, ds \qquad \text{A-26}$$

$$\frac{\partial \phi_i}{\partial y} = -2 \sum_{j=1}^{N} \sigma_j \int_{s_j}^{s_{j+1}} \frac{(s_{ij} - s)\sin\alpha_j + h_{ij}\cos\alpha_j}{(s_{ij} - s)^2 + h_{ij}^2}\, ds \qquad \text{A-27}$$

where

σ_j represents the constant source strength for the j-th element.

Equations (A-25)-(A-27) inclusive may be expressed for the convenience of calculation as

$$\phi_i = -\sum_{j=1}^{N} \sigma_j I^o \qquad \text{A-28}$$

$$\frac{\partial \phi_i}{\partial x} = 2 \sum_{j=1}^{N} \sigma_j (J^o \sin\alpha_j + K^o \sin\alpha_j) \qquad \text{A-29}$$

$$\frac{\partial \phi_i}{\partial y} = 2 \sum_{j=1}^{N} \sigma_j (-J^o \cos\alpha_j + K^o \sin\alpha_j) \qquad \text{A-30}$$

where

I^o, J^o and K^o are the analytic solutions of the integrals [83] given by :

$$I^o = \Big[(s - s_{ij}) \ln[(s - s_{ij})^2 + h_{ij}^2] - 2(s - s_{ij}) + 2h_{ij} \tan^{-1}\frac{s - s_{ij}}{h_{ij}} \Big]_{s_j}^{s_{j+1}}$$

$$J^o = \frac{1}{|h_{ij}|} \Big[\tan^{-1}\frac{s - s_{ij}}{h_{ij}} \Big]_{s_j}^{s_{j+1}}$$

$$K^{o} = 0.5 \left[\ln[(s - s_{ij})^2 + h_{ij}^2] \right]_{s_j}^{s_{j+1}}$$

Solution for field velocity and pressure

It is noted that the potential function and the velocity components at the field point i due to all the source points may be written as

$$\phi_i = \sum_{j=1}^{j=N} \sigma_j Z_{ij} \qquad \text{A-31}$$

$$\frac{\partial \phi_i}{\partial x} = \sum_{j=1}^{j=N} \sigma_j X_{ij} \qquad \text{A-32}$$

$$\frac{\partial \phi_i}{\partial y} = \sum_{j=1}^{j=N} \sigma_j Y_{ij} \qquad \text{A-33}$$

where X_{ij},Y_{ij} and Z_{ij} are the matrices of *influence coefficients* (e.g. Z_{ij} represents the influence of the source distribution on the j-th element on the potential of the i-th field point) whose elements are formed from, for example, terms in equations (A-28), (A-29) and (A-30), if a constant source strength within elements is required.

With regard to the boundary condition on the body surface, the normal and tangential velocities induced at the control point on the i-th element by all the sources can then be written respectively as

$$\frac{\partial \phi_i}{\partial n} = \sum_{j=1}^{j=N} \sigma_j \left[-X_{ij} \sin\alpha_i + Y_{ij} \cos\alpha_i \right] \qquad \text{A-34}$$

$$\frac{\partial \phi_i}{\partial s} = \sum_{j=1}^{j=N} \sigma_j \left[-X_{ij} \cos\alpha_i + Y_{ij} \sin\alpha_i \right] \qquad \text{A-35}$$

It is important to note that when evaluating the matrix coefficient for X_{ij} and Z_{ij} (where i and j refer to the control point on the i-th element and the the j-th element respectively) a special case arises when i=j. This results in the integrals becoming undefined and require to be evaluated by approaching this limiting condition correctly.

The normal component of the free stream velocity can be written as

$$V_n = -n.V_\infty \qquad \text{A-36}$$

The boundary condition for potential flow is that the total normal velocity component on the control point is zero, as described in section 2.3.1, and this can be written, as already in equation 2-9 in the form of,

$$\nabla\phi.n|_s = \frac{\partial\phi}{\partial n}\Big|_s = V_\infty \cdot n\,\Big|_s - F \qquad \text{A–37}$$

Equation (A-37) then can be applied to all the panel control points expressed in equation (A-34) as

$$\sum_{j=1}^{j=N} \sigma_j\,[\,-X_{ij}\sin\alpha_i + Y_{ij}\cos\alpha_i] = -n\,.V_\infty + F_i \qquad ,\quad i = 1,2,\ldots,N \qquad \text{A-38}$$

where

F_i is a prescribed magnitude of the normal velocity at the i-th control point which is zero except when there is a suction or blowing etc.

Equation (A-38) is a system of linear algebraic equations and can be solved for the unknown values of source strengths σ_j. If the source densities are known then the tangential velocity, V_T for any element, can be obtained by summing the contribution from the sources along with the contribution from the streamline, that is

$$V_T = \sum_{j=1}^{j=N} \sigma_j (X_{ij} \cos\alpha_i + Y_{ij} \sin\alpha_i) + V_\infty \cos\alpha_i \qquad \text{A–39}$$

The pressure coefficient can then be obtained once the velocity distribution is known. The pressure coefficient is defined as

$$C_p = \frac{P - P_\infty}{\frac{1}{2}\rho V_\infty^2} \qquad \text{A-41}$$

and for incompressible flow

$$P - P_\infty = \frac{1}{2}\rho (V_\infty^2 - V_T^2) \qquad \text{A-42}$$

thus the pressure coefficient can be written as

$$C_p = 1 - \frac{V_T^2}{V_\infty^2} \qquad \text{A-43}$$

If the freestream flow has a magnitude of one unit then C_p may be written as

$$C_p = 1 - (V_T)^2 \qquad \text{A-45}$$

A.3 Computer Programme

A computer programme called TWODP has been written based on the theory described in the previous section and is capable of predicting the two-dimensional incompressible potential flow around arbitrarily shaped contours. The basic input to the programme consists of the geometry for the body surface about which the flow is to be computed. The body is defined by the number of straight-lined elements and a set of input points representing their vertices in a Cartesian co-ordinate system, the points are connected by straight lines to represent the elements. In the present work the input points, for an EMS train model were obtained from the blue-print drawing obtained from British Rail [6]. The co-ordinates of the these points have been generated using a programme for digitising drawings provided by the computer centre of Loughborough University of Technology [84]. It is important to display and inspect the generated sections before proceeding further to use them with TWODP to ensure that all the co-ordinates and the elements generated are correct and well proportioned. This verification has been achieved using a computer graphics package called Tellagraf [85].

TWODP has the capability to determine the source strengths, the velocity and pressure distribution at the flow field points. The computer programme analyses all the elements in turn and for each element the induced velocity at the null point due to the other elements are computed. The block diagram summarising the actions of the computer programme TWODP is shown in Figure A-4.

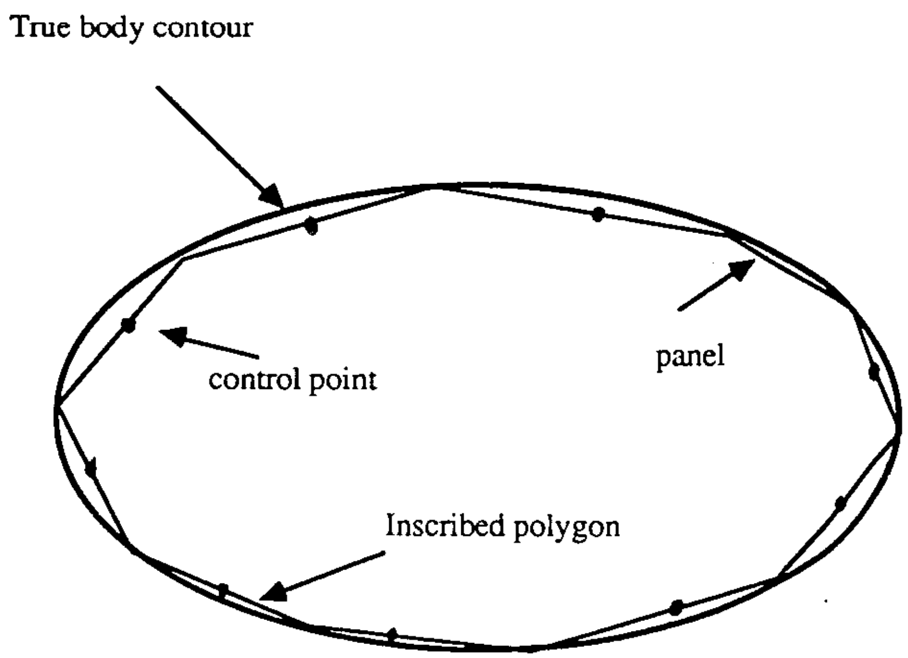

Figure A-1 Panel method approximation of an arbitrary two-dimensional body contour by straight-line surface elements — i.e panels.

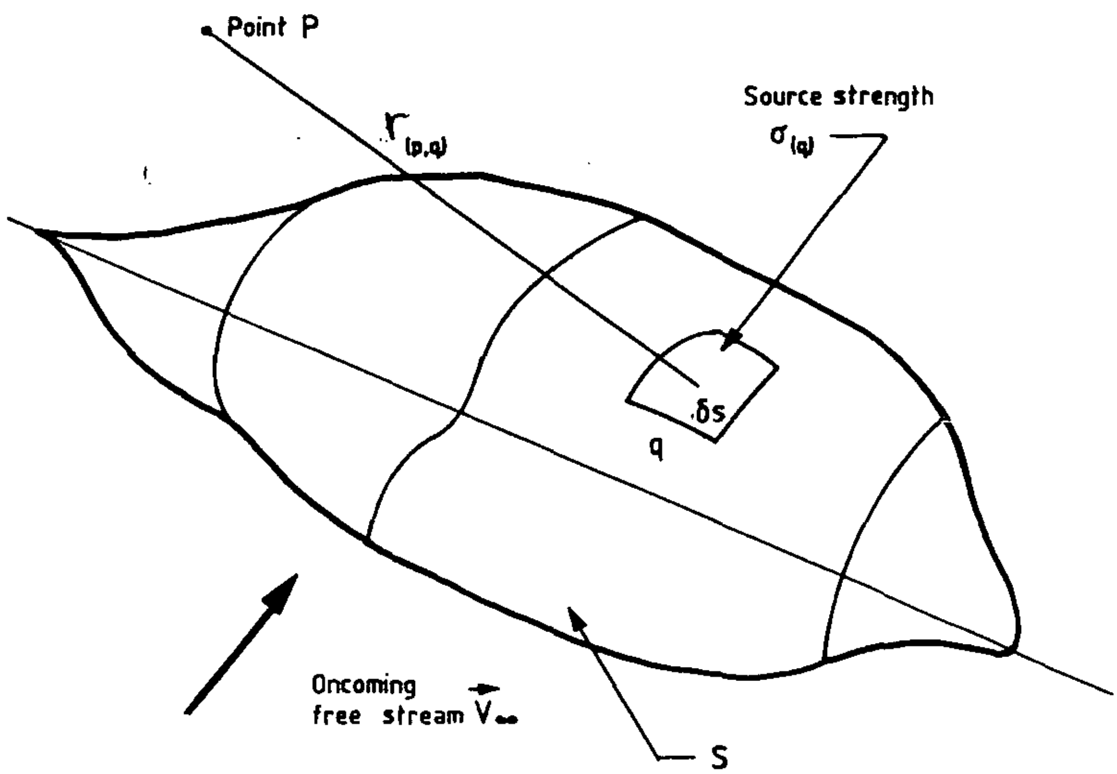

Figure A-2 Elemental surface source distribution, on an arbitrary surface S, inducing a velocity at an external field point p

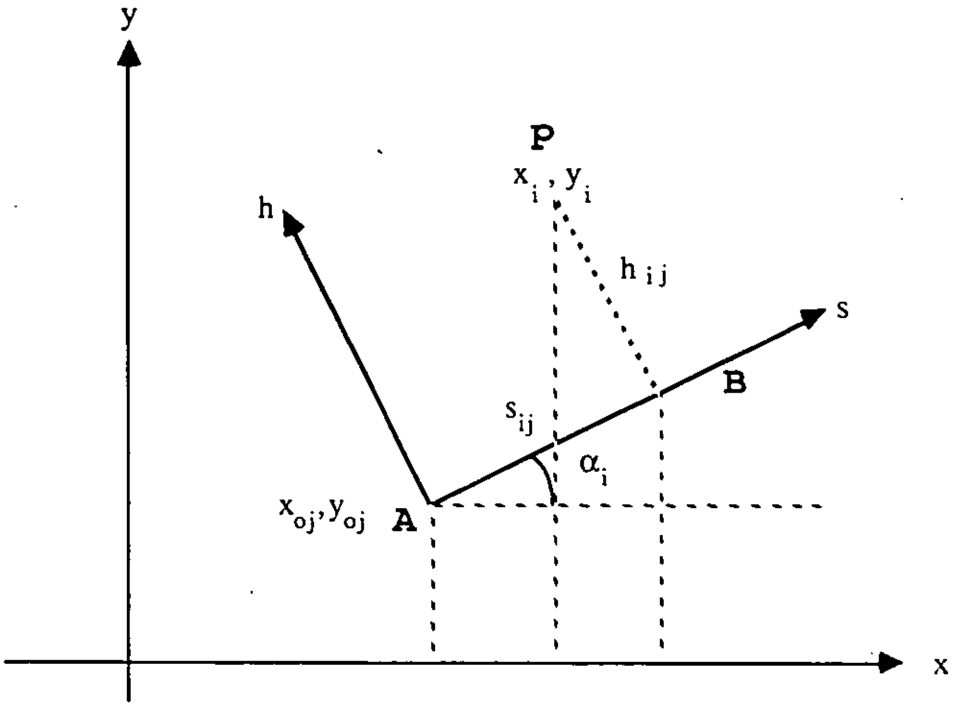

Figure A-3 The Global (x-y) co-ordinate system and a Local (s-h) co-ordinate system for a straight-line panel element AB.

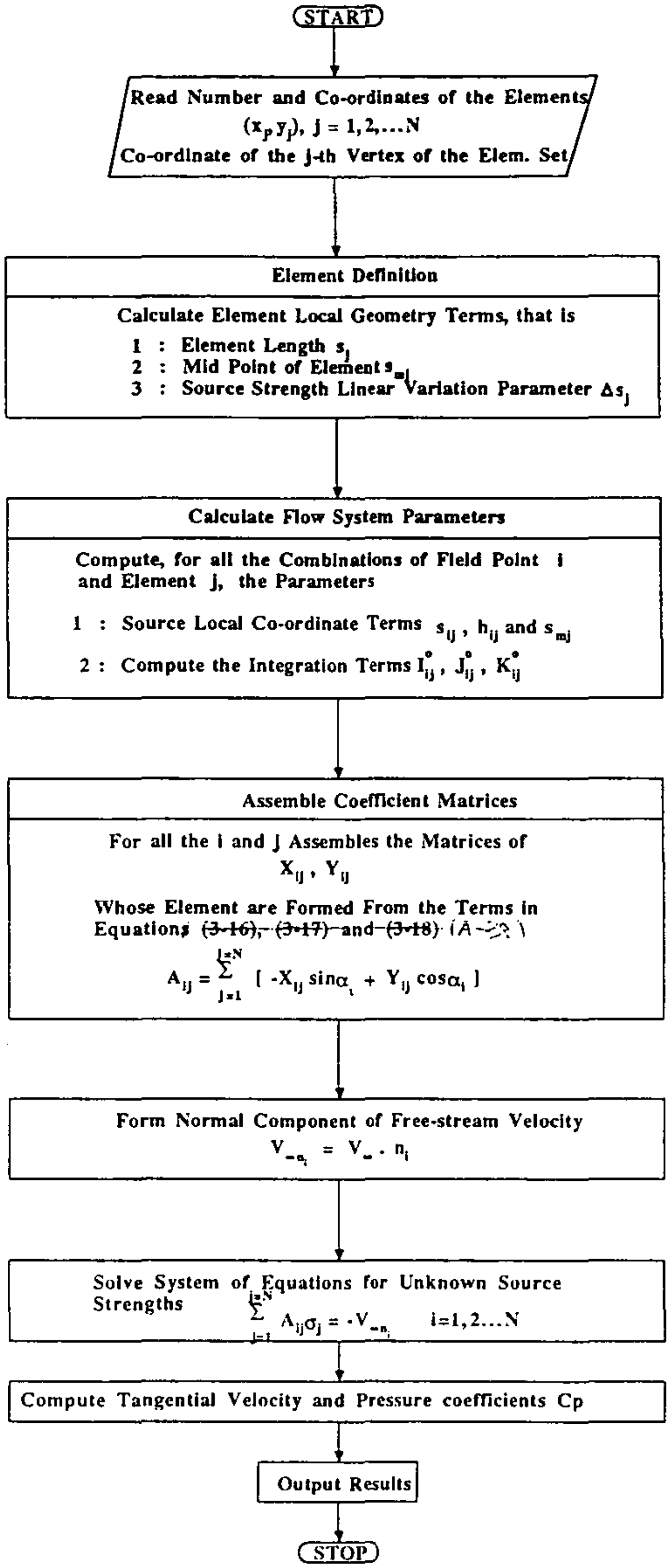

Figure A-4 Block diagram for programme TWODP

Appendix B

A Planar Quadrilateral Panel Element and its Local Co-ordinate System

This Appendix describes briefly the formation of the plane quadrilateral surface panel element used in the approximation of a body's surface and the formation of the transformation matrix required to map points from the global (cartesian) co-ordinate system to the panel element's local (cartesian) co-ordinate system. In order to determine the flow about an arbitrary body it is convenient to employ a single global coordinate system to specify the geometry of the body and its surrounding space and a set of local co-ordinate systems, one for each panel, to specify details local to each panel. The local co-ordinate systems is fixed in the plane surface of its corresponding panel element.

Let the global position vectors of the corners of an arbitrary, say the i-th, element (Figure B-1) be x_{1i}, x_{2i}, x_{3i} and x_{4i}. Then the diagonal vectors $\mathbf{T}_1$ and $\mathbf{T}_2$ of the element, which are used to determine the normal unit vector to the panel element, are, see Figure B-1, given by

$$\mathbf{T}_1 = x_{3i} - x_{1i} \qquad \text{B-1}$$

$$\mathbf{T}_2 = x_{4i} - x_{2i} \qquad \text{B-2}$$

The vector normal to the diagonals is given by the vector cross product as

$$\mathrm{T}_3 = \mathrm{T}_2 \times \mathrm{T}_1 \qquad \text{B-3}$$

and thus the normal unit vector to the plane which is to be associated with the planar quadrilateral panel element is

$$n = \frac{T_3}{|T_3|} \qquad \text{B-4}$$

The plane of the panel element may now be completely defined if a point on it is specified. A convenient point is the centroid of the element's associated four data points and is given by the position vector

$$x_{av} = [\frac{x_{1i} + x_{2i} + x_{3i} + x_{4i}}{4}] \qquad \text{B-5}$$

The panel element vertices are now obtained as projections of the four data points onto the plane of the element along the normal vector. The resulting points are referred to as the corner points of the planar quadrilateral panel element. The signed distance of the k-th such point from this plane is

$$d_k = n.(x_{av} - x_k) \qquad k=1,2,3,4 \qquad \text{B-6}$$

Then the position vectors of the corners in the global co-ordinate system are

$$x_k = x_{av} + n \cdot d_k \qquad k=1,2,3,4 \qquad \text{B-7}$$

The unit vector along the diagonal vector T_1 is

$$t_1 = \frac{T_1}{|T_1|} \qquad \text{B-8}$$

and the vector cross product of the unit diagonal vector t_1 and the unit normal vector is

$$t_2 = n \times t_1 \qquad \text{B-9}$$

The vectors t_1, t_2 and n (see Figure B-1) are the unit vectors parallel to the panel element's local co-ordinate system axes and are expressed in terms of the global co-ordinate systems axis set, the transformation matrix for the co-ordinate systems may be expressed

$$R = \begin{bmatrix} a_{11} & a_{12} & a_{13} \\ a_{21} & a_{22} & a_{23} \\ a_{31} & a_{32} & a_{33} \end{bmatrix} \qquad \text{B-10}$$

where the components of the transformation matrix are derived from the component of the vectors t_1, t_2 and n and may be written as

$$a_{11} = t_{1x} \qquad a_{12} = t_{1y} \qquad a_{13} = t_{1z}$$

$$a_{21} = t_{2x} \qquad a_{22} = t_{2y} \qquad a_{23} = t_{2z}$$

$$a_{31} = n_x \qquad a_{32} = n_y \qquad a_{33} = n_z$$

Hence to transform, for example, a point specified in global co-ordinates to its corresponding value in the panel element's local co-ordinate system, the position vector (in the global system) of the origin (centroid) of the element V_o is required (exactly analogous to the two-dimensional case, see Appendix A). Thus, to transform a point with position vector V_r in the global co-ordinate system to a its corresponding value V_e in a panel element local co-ordinate system requires the calculation

$$V_e = R\,(V_r - V_o) \qquad \text{B-11}$$

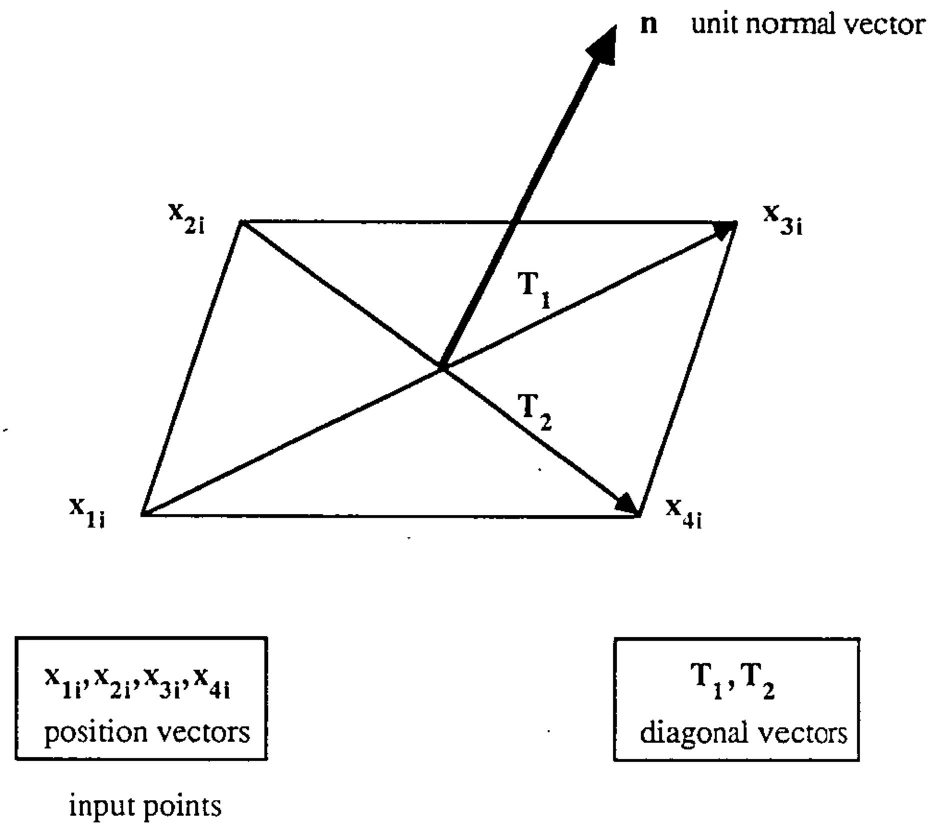

Figure B-1 The formation of a planar panel element from four input points

Appendic C

Computation of the Turbulent Boundary Layer on an EMS Train

Appendic C

Computation of the Turbulent Boundary Layer on an EMS Train

This Appendix quotes the fuller forms of expressions for the governing equations and relationships between turbulent boundary layer parameters defined in the boundary layer and streamline co-ordinate systems employed to solve for the development of the turbulent boundary layer on the nose of an EMS train. The notation for terms in expressions follows that of chapter 6.

C.1 Governing Equations for Three-dimensional Turbulent Boundary Layer in the Boundary Layer Co-ordinate System

The momentum integral and entrainment equations defined in a streamline co-ordinates may be written in an arbitrary curvilinear co-ordinate system defined by the X^1 and X^2 axes shown in Figure 6-1, such as, say the boundary layer co-ordinate system. Following references [88,89] the momentum integral and entrainment equations may be written in the boundary layer co-ordinate system as

— **longitudinal momentum equation**

$$c_{f1}/2 = \frac{1}{h_1}\frac{\partial\Theta_{11}}{\partial X^1} + \Theta_{11}\left[\frac{2}{U_e h_1}\frac{\partial U_e}{\partial X^1} + \frac{1}{q}\frac{\partial}{\partial X^1}\left(\frac{q}{h_1}\right) + K_1\right] + \Theta_{12}\left[\frac{2}{U_e h_2}\frac{\partial U_s}{\partial X^2} + \frac{1}{q}\frac{\partial}{\partial X^2}\left(\frac{q}{h_2}\right) + K_3\right]$$

$$\frac{1}{h_2}\frac{\partial\Theta_{12}}{\partial X^2} + \Delta_1\left[\frac{1}{U_e h_1}\frac{\partial U_1}{\partial X^1} + K_1\frac{U_1}{U_e}\right] + \Delta_2\left[\frac{1}{U_e h_1}\frac{\partial U_1}{\partial X^2}\varepsilon + K_2\frac{W_1}{U_e} + K_3\frac{U_1}{U_e}\right] + \Theta_{22}K_2$$

C-1

— **Transverse momentum equation**

$$\frac{c_{fx2}}{2}=\frac{1}{h_1}\frac{\partial\Theta_{22}}{\partial X^1}+\Theta_{21}\left[\frac{2}{U_e h_1}\frac{\partial U_e}{\partial x}+\frac{1}{q}\frac{\partial}{\partial X^1}\left(\frac{q}{h_1}\right)+l_3\right]+\frac{1}{h_2}\frac{\partial\Theta_{22}}{\partial X^2}+\Theta_{22}\left[\frac{2}{U_e h_2}\frac{\partial U_e}{\partial X^2}\right.$$

$$\left.+\frac{1}{q}\frac{\partial}{\partial X^2}\left(\frac{q}{h_2}\right)+l_2\right]+\Delta_1\left[\frac{1}{U_e h_1}\frac{\partial W_1}{\partial X^1}+l_1\frac{U_1}{U_s}+l_3\frac{W_1}{U_e}\right]+\Delta_2\left[\frac{1}{U_e h_2}\frac{\partial W_1}{\partial X^2}\right.$$

$$\left.+l_2\frac{W_1}{U_e}\right]+\Theta_{11}l_1 \qquad \text{C-2}$$

— **Entrainment equation;**

$$\frac{1}{h_1}\frac{\partial}{dX^1}\left(\frac{\delta U_1}{U_e}-\Delta_1\right)+\left(\frac{\delta U_1}{U_e}-\Delta_1\right)\left[\frac{1}{U_e}\frac{1}{h_1}\frac{\partial U_e}{\partial X^1}+\frac{1}{q}\frac{\partial}{\partial X^1}\left(\frac{q}{h_1}\right)\right]+\frac{1}{h_2}\frac{\partial}{\partial X^2}\left(\frac{\delta W_1}{U_e}-\Delta_2\right)$$

$$+\left(\frac{\delta W_1}{U_e}-\Delta_2\right)+\left[\frac{1}{U_e h_2}\frac{\partial U_e}{\partial X^2}+\frac{1}{q}\frac{\partial}{\partial X^2}\left(\frac{q}{h_2}\right)\right]=P(G)\gamma \qquad \text{C-3}$$

where

c_{fx1}, c_{fx2}	:	skin friction coefficient in X^1, and X^2 co-ordinates
h_1,h_2,h_3	:	metric unit
K_1,K_2,K_3	:	geodesic curvature
U_e	:	resultant velocity just outside the boundary layer
Θ_{11}, Θ_{12},	:	momentum thicknesses
Θ_{21},Θ_{22}		
Δ_1,Δ_2	:	displacement thicknesses

The method used to express the equations (C-1), (C-2) and (C-3) in a form suitable for numerical solution is an integration scheme combined with the method of lines which is a technique lying midway between analytical and grid methods and based on the substitution of finite differences for the derivatives with respect to one independent variable and retaining the derivatives with respect to the remaining variables. This strategy replaces a given differential equation by a system of differential equations with a smaller number of independent variables [108].

Thus consider Figure 6-4 which shows the domain over which the solution of the equations are desired and defined by the bounds

$$X^1_1 \leq X^1 \leq X^1_m \quad \text{and} \quad X^2_1 \leq X^2 \leq X^2_n$$

in the boundary layer co-ordinate system. This region is subdivided into a grid by the set of of lines

$$X^1_j = \text{constant} \quad \text{and} \quad X^2_i = \text{constant}$$

then expressions corresponding to the equations are written for a fixed value , say, $X^1{}_j$ of the variable X^1 and for all the associated values

$$X^2_1, X^2_2, \ldots X^2_i, \ldots X^2_n \quad \text{of} \quad X^2$$

and put into a discretised form, using finite difference expressions for the derivatives with respect to X^2. Equations (C-1), (C-2) and (C-3) may be, after some manipulation, written in the general form:

$$\frac{\partial \Theta_{11}}{\partial X^1} = F_1\left(\Theta_{11}, \frac{\partial \Theta_{12}}{\partial X^2}, \Theta_{12}, \Delta_1, \Delta_2, \Theta_{22}, c_{fx1}\right) \qquad \text{C-4}$$

$$\frac{\partial \Theta_{21}}{\partial X^1} = F_2\left(\Theta_{21}, \frac{\partial \Theta_{22}}{\partial X^2}, \Theta_{22}, \Delta_1, \Delta_2, \Theta_{11}, c_{fx2}\right) \qquad \text{C-5}$$

$$\frac{\partial}{\partial X^1}\left(\frac{\delta U_1}{U_e} - \Delta_1\right) = F\left(\frac{\partial}{\partial X^2}\left(\frac{\delta W_1}{U_e} - \Delta_2\right), \frac{\delta U_1}{U_e} - \Delta_1, \frac{\delta W_1}{U_e} - \Delta_2, G, \gamma_s\right) \qquad \text{C-4}$$

C.2 Boundary Layer Parameter Transformation

The boundary layer parameters defined in the streamline co-ordinate, $\theta_{11}, \theta_{21}, \delta-\delta_1$ etc., are related to boundary layer parameters defined in the boundary layer co-ordinate system as follows :

$$\theta_{11} = \frac{-B + \sqrt{(B^2 - 4AC)}}{2A}$$

where A, B, C are given at the end of the following set of expressions

$$\theta_{21} = \frac{c_{12}\theta_{11}\sin\lambda\left[\Theta_{11}\sin\alpha - \Theta_{21}\sin(\lambda-\alpha)\right]}{-c_{12}\theta_{11}\sin(\lambda-\alpha) + c_{22}\left[\theta_{11}\sin(\lambda-\alpha) - \sin\lambda\{\Theta_{11}\cos\alpha + \theta_{21}\cos(\lambda-\alpha)\}\right]}$$

$$\delta-\delta_1 = \frac{\left(\frac{\delta\sin(\lambda-\alpha)}{\sin\lambda} - \Delta_1\right)\sin\lambda - \delta_2\cos(\lambda-\alpha)}{\sin(\lambda-\alpha)}$$

where

α : the contour angle defined in Figure 6-2

λ : the angle between streamwise, and spanwisen co-ordinates

and the coefficients c_2, c_{12}, c_{22}, A, B and C that occur on the right hand sides are evaluated (using an iterative method) from

$$c_2 = \frac{\delta_2}{\theta_{21}}$$

$$c_{12} = \frac{\theta_{12}}{\theta_{21}}$$

$$c_{22} = \frac{\theta_{22}\theta_{11}}{\theta_{21}^2}$$

$$A = (c_{22} - c_{12}) \sin^2 (\lambda - \alpha)$$

$$B = c_{12}\sin(\lambda-\alpha) \sin\lambda[\Theta_{11} \cos\alpha + \Theta_{21}\cos(\lambda-\alpha)] - c_{12}^2 \sin\lambda\cos(\lambda-\alpha)[\Theta_{11}\sin\alpha - \Theta_{21}\sin(\lambda-\alpha)] - 2c_{22}\sin(\lambda-\alpha)\sin\lambda [\Theta_{11}\cos\alpha + \Theta_{21}\cos(\lambda-\alpha)]$$

$$C = c_{22} \sin^2\lambda[\Theta_{11}\cos\alpha + \Theta_{21}\cos(\lambda-\alpha)]^2$$

Knowing the values θ_{11}, θ_{21} and $\delta-\delta_1$, we can then calculate all the necessary turbulent boundary layer quantities relative to the co-ordinate system defined by the external streamlines and in particular to calculate the new values of c_2, c_{12} and c_{22}.
To calculate all the desired quantities in streamline co-ordinate system from a knowledge of θ_{11}, θ_{21}, $\delta-\delta_1$, Michel-Quemard-Durant [96] gives

$$A = 0.5267 - 0.00071[(\frac{\delta-\delta_1}{\theta_{11}} - 4.35)^2 - 0.04(\frac{\delta-\delta_1}{\theta_{11}} - 4.35)^3]$$

$$B = \exp\{2.303[0.9122 - A(0.8239 + \frac{\mathrm{lin}(\frac{\delta-\delta_1}{\theta_{11}} - 4.35)}{2.303}]\}$$

which allow the parameters G and the shape factor H to be calculated as below [89]

$$G = 3.79 + (B - 0.9)(\mathrm{lin}R_{\theta_{11}} - 3.35)$$

$$F_1 = 0.613G - \frac{[3.6 + 76.86(\frac{1}{G} - 0.154)^2]}{G}$$

$$H = \frac{\{\frac{\delta-\delta_1}{\theta_{11}} - 1 - [(\frac{\delta-\delta_1}{\theta_{11}} - 1)^2 - 4\frac{\delta-\delta_1}{\theta_{11}}\sqrt{\frac{G}{F_1} - 1}\,]\}}{\frac{2G}{F_1} - 2}$$

Then to find the skin friction coefficients c_{fs}, c_{fn} the following sequence of calculations [89] are made

$$\delta_2 = \theta_{21}H$$

$$\delta_1 = \theta_{11}H$$

$$\frac{\delta_2}{\theta_{12}} = -\phi_1\frac{H}{H-1}$$

$$\frac{1}{\phi_2} = 1 + 1.65(\phi_1 - 1)$$

$$\gamma = \frac{H-1}{HG}$$

and hence

$$c_{fs} = 2\gamma$$

now proceeding to find c_{fn}, we have

$$K_2 = -\frac{1}{h_1h_2}\frac{\partial h_1}{\partial X^2}$$

$$T = \frac{-\frac{\delta_2}{\gamma}}{K_2}$$

$$\varepsilon_1 = \frac{2F_1}{|T|}$$

$$\alpha_1 = \frac{\sqrt{20.6\,F_1}}{G}$$

$$\alpha_2 = \frac{\varepsilon + 0.317}{(2.21 + 0.423\varepsilon) + 0.85\times 10^{-0.1175\varepsilon^{0.86}}}$$

$$\alpha_3 = \frac{2.18G^2 - 6.3G}{2F_1^{\ 2}}$$

$$\varepsilon = \frac{2F_1}{|T|}$$

$$\varepsilon_2 = \frac{\varepsilon}{\varepsilon + \frac{1}{F_1}}$$

$$\frac{1}{\varepsilon_1} = (\alpha_1(\alpha_2 - 1) + 1)\alpha_3$$

$$\tan\beta_o = \frac{-\frac{\delta_2}{\delta_1}}{\frac{\varepsilon_1}{F1}\frac{GH}{H\text{-}1} - \varepsilon_2}$$

$$c_{fn} = c_{fs}\tan\beta_o$$

Since we now know θ_{11}, θ_{12}, δ_1, δ_2, θ_{21}, c_{fs} and c_{fn} we can calculate the parameters in the boundary layer co-ordinate system [88,89]

$$\Theta_{11} = \frac{\theta_{11}\sin^2(\lambda-\alpha) - (\theta_{12}+\theta_{21})\sin(\lambda-\alpha)\cos(\lambda-\alpha) + \theta_{22}\cos(\lambda-\alpha)}{\sin^2\lambda}$$

$$\Theta_{12} = \frac{\theta_{11}\sin\alpha\sin(\lambda-\alpha) + \theta_{12}\sin(\lambda-\alpha)\cos\alpha - \theta_{21}\cos(\lambda-\alpha)\sin\alpha - \theta_{22}\cos\alpha\cos(\lambda-\alpha)}{\sin\lambda}$$

$$\Theta_{21} = \frac{\theta_{11}\sin\alpha\sin(\lambda-\alpha) - \theta_{12}\cos(\lambda-\alpha)\sin\alpha + \theta_{21}\sin(\lambda-\alpha)\cos\alpha - \theta_{22}\cos\alpha\cos(\lambda-\alpha)}{\sin^2\lambda}$$

$$\Theta_{22} = \frac{\theta_{11}\sin^2\alpha + (\theta_{12} + \theta_{21})\cos\alpha\sin\alpha + \theta_{22}\cos^2\alpha}{\sin\lambda}$$

$$\Delta_1 = \frac{\delta_1 \sin(\lambda-\alpha) - \delta_2 \cos(\lambda-\alpha)}{\sin\lambda}$$

$$\Delta_2 = \frac{\delta_1 \sin\alpha + \delta_2 \cos\alpha}{\sin\lambda}$$

$$c_{fx} = \frac{c_{fs} \sin(\lambda-\alpha) - c_{fn} \cos(\lambda-\alpha)}{\sin\lambda}$$

$$c_{fz} = \frac{c_{fs} \sin\alpha + c_{fn} \cos\alpha}{\sin\lambda}$$

Now all the parameters of the right hand of the equations (C-4), (C-5) and (C-6) have been calculated then we can solve the equations to find the new values of

$$\frac{\partial \Theta_{11}}{\partial X^1}, \frac{\partial \Theta_{21}}{\partial X^1}, \frac{\partial}{\partial X^1}\left(\frac{\delta U_1}{U_e} - \Delta_1\right)$$

and the process is repeated for the next value, if any, of the independent variable x and so on to the completion of an all x values